Failure Mechanisms in Bone – a mechanical and histological study

Matthew Vincent Mercy
MEng & Man

A thesis submitted to the University of Dublin for the degree of

Doctor of Philosophy

Department of Mechanical and Manufacturing Engineering
Trinity College Dublin
&
Department of Anatomy
Royal College of Surgeons in Ireland

July 2006

Supervised by Prof. D. Taylor
&
Prof. T.C. Lee

Declaration

I declare that the present work has not previously been submitted as an exercise for a degree at this or any other University.

The thesis consists entirely of my own work except where references indicate otherwise.

The library of the University of Dublin, Trinity College, may lend or copy this thesis upon request.

M. V. Mercy

Acknowledgements

From the outset this project has been conducted as a collaborative exercise between Trinity College and the Royal College of Surgeons in Ireland and as such I have benefited from the support of both institutions. I would particularly like to thank the Research Committee of the Royal College of Surgeons in Ireland for grant support.

From day one I have enjoyed the support and guidance of my supervisors Professors Clive Lee and David Taylor, without whom this project would never have come to fruition. I would particularly like to thank them for their continued support and understanding in recent months, which has helped enormously.

To the two Peter's messrs. Kelleghan and O'Reilly, I owe them both huge thanks. Peter Kelleghan was always willing to help in the somewhat unpleasant task of specimen preparation, not many people would be quite so generous with their time. Peter O'Reilly. Always ready to lend a hand, and remarkably understanding, despite having to put up with the frustrations of many a student. I am also grateful to everyone in the bone research group, both past and present. Particular thanks are due to Dr. Fergal O'Brien for establishing many of the protocols used in this study. I would also like to acknowledge the Electron Microscope Unit in Trinity College for making a Scanning Electron Microscope available for this work.

I would also like to thank my friends and also my colleagues in the Critical Parts Lifing & Integrity group Rolls – Royce Plc. I must of course also thank my parents Vincent & Kathleen.

Matthew Mercy

July 2006

Table of Contents

List of Tables

List of Figures

Summary

Repeated loading causes the development of microdamage in bone and may lead to failure by fatigue. Microdamage in the form of microcracks occurs naturally in bone due to the loads experienced during day-to-day activities, and unless such damage is repaired it can play a major role in the development of fragility and stress fractures. In order to maintain structural integrity this damaged bone must be replaced and it has been postulated that microdamage in bone acts as a stimulus for bone remodelling. The development of microdamage can be associated with the mechanisms of creep and fatigue. This study examined the effects of creep and fatigue, quantified the damage caused by these processes and considered the interaction between them. The influence of temperature on the damage caused by creep and fatigue was also investigated.

Using established methods (O'Brien et al, 2003), a series of fatigue studies were conducted on specimens of fresh bovine tibiae, over a range of fatigue stresses associated with physiological conditions. Testing was conducted at both room temperature and elevated temperatures, fatigue damage was labelled using a series of fluorochrome dyes. The mechanisms by which fatigue induced microdamage accumulates in bone at physiological stresses are different to those observed at higher stresses. This change in behaviour may be attributable to a threshold mechanism for damage accumulation in compact bone, as identified elsewhere in the literature.

This study has found that in normal bone tissue in vitro fatigue failure of compact bone is unlikely to occur under physiological loading. At fatigue stresses consistent with physiological levels there is a natural population of microcracks that will develop in such a way that will not have a detrimental effect on the structure of bone. In conjunction with the rate of damage accumulation, this damage target level is seen to increase with increasing stress. Models have been developed to describe damage accumulation in compressive fatigue over a range of stresses from physiological loading levels, to those associated with overload conditions.

The majority of microcracks formed in vivo have been shown not to be dangerous as they are unlikely to propagate to failure and it is proposed that failure will be dominated in fatigue by the propagation of a small number of individual microcracks.

Increasing the operating temperature for fatigue specimens to 50°C was observed to more than halve the fatigue life. A combined fatigue–creep model enables such differences to be compared to a reduction in fatigue strength of up to 12%. Considerable increases in microcrack density have also been identified as a result of testing at elevated temperatures; microcrack density increased by a factor of 10.38.

Examination of creep in compact bone consisted of both mechanical and histological results. The creep behaviour of bone was characterised by a non-linear reduction in time to failure with increasing stress. Examination of the creep fatigue interaction using a cumulative damage model demonstrated that the contribution of creep during cyclic loading is insignificant when compared to the damage caused by fatigue. The process of fatigue has been shown to be far more significant than creep at physiological loading levels where time dependent effects will be negligible. Significantly less microdamage is caused by creep than fatigue loading and it has been identified that creep induced microdamage is less dangerous than fatigue induced microdamage; where microcracks have been shown to grow to much longer lengths in creep without causing failure.

Increasing the operating temperature from room temperature to 50°C was found to reduce the creep life of specimens by a factor of 2.3 at 120 MPa and 25.3 at 130 MPa. Creep rate, a damage accumulation parameter was also seen to rise with increased temperature and hence a higher incidence of microdamage was observed; a 120 fold increase in mean crack density was observed for an engineering stress of 130 MPa.

Both creep and fatigue observed dramatic increases in microcrack density as a result of increasing the operating temperature, nevertheless it has been established that creep causes far less damage than fatigue at in vivo stress levels, despite an operating temperature far greater than human body temperature. This confirms that in vivo, fatigue and not creep will be responsible for the development of microdamage in normal bone where the effects of compressive time dependent loading are likely to be negligible. However, the clinical manifestations of certain bone diseases may reflect a shift in the creep-fatigue transition, so that creep effects begin to dominate during normal activities.

Abbreviations

a	crack length (μm)
da/dN	crack growth rate (mm/cycle)
BMU	basic multicellular unit
Ca	calcium
$Ca_{10}(PO_4)_6(OH)_2$	crystalline hydroxyapatite
CDS	characteristic damage state
CCD camera	charged coupled device camera
CNC	computer numerical control
Cr.Dn	numerical crack density (no. of cracks/ mm^2)
Cr.S.Dn	surface crack density (μm crack length / mm^2)
d_c	damage per loading cycle due to creep
d_f	damage per loading cycle due to fatigue
DPX	mounting medium for histological slides
D_s	generalized damage state
D_f	fatigue damage fraction
D_c	creep damage fraction
D_t	interaction damage fraction
E	Young's modulus, a measure of the stiffness of a material
E_o	initial modulus of a specimen determined prior to testing
ε	strain, percentage change in length
ε_o	initial instantaneous strain in creep
Δε	strain range
dε/dt	steady state creep rate for creep tested specimens
με	microstrain (strain 10^{-3})
FITC	fluorescein isothiocyanate
Jm^{-3}	Joules (energy) per (metre x 10^3) (energy per unit volume)
Hz	hertz (unit of frequency, 1/s)
K	stress intensity
Kc	critical stress intensity
LSCM	laser scanning confocal microscopy
λ	wavelength
m	metre
cm	metre x 10^{-2}
mm	metre x 10^{-3}
μm	metre x 10^{-6}
nm	metre x 10^{-9}
mm Hg	mm of mercury (measure of pressure)
M	molarity (one mole=actual weight/molecular weight of substance)
n	sample size
kN	newtons x 10^3 (measure of force)
N_f	Number of cycles to failure
^{o}	degrees
^oC	degrees celcius
Pa	pascals (measure of stress: 1Pa= $1N/m^2$)
MPa	pascals x 10^6
GPa	pascals x 10^9

P_f	probability of failure
rpm	revolutions per minute
s	seconds
σ	stress, force per unit area
$\Delta\sigma$	stress range
$\Delta\sigma_o$	fatigue strength of a material
$\Delta\sigma_{th}$	fatigue threshold value
σ_m	mean stress in fatigue loading
S.D.	standard deviation
SEM	scanning electron microscope
VPSEM	variable pressure scanning electron microscope
t_f	time to failure (s)
T/T_{melt}	homologous temperature
UV	ultraviolet
WHO	World Health Organisation

1 Introduction

1.1 Introduction to Bone

Bone is a connective tissue. It is composed of cells and an organic matrix, formed from the products of these cells, which is then mineralised. Bone supports the body by providing a structural framework, which protects vital internal organs and serves as levers for movement. Most bones in the skeleton of humans and other animals act as compressive structures to balance the effects of the tensile loading by muscles, tendons and ligaments and to support the skeletal mass.

Bone, along with cartilage, is a supportive connective tissue, which possesses a matrix of highly dense fibres. Bone can be considered as a composite material, with a matrix structure primarily made up of a mineral phase based on calcium salts (crystalline hydroxyapatite $Ca_{10}(PO_4)_6(OH)_2$), which surround collagen fibres. The fibres represent approximately only a third of the matrix. This combination means that the material properties of bone are a compromise, with its strength predominantly due to the mineral phase, and its flexibility and resistance to shattering or brittle fracture due to the collagen fibres.

At the macroscopic level, bone can be described according to its density and architecture. Bone can be classified as either compact (cortical) bone, or cancellous (trabecular) bone. Cancellous bone has a relative density (density of the structure divided by density of the material that the structure is made from, otherwise referred to as solid volume fraction) of between 0.05 and 0.7, and any bone with a relative density greater than 0.7 is classified as compact bone (Gibson and Ashby, 1997). Cancellous bone can be found in cuboidal bones, flat bones and the ends of long bones, it is highly porous and has a porosity of 75%-95% (Martin, Burr and Sharkey, 1998). In long bones, such as the femur, a cortex or shell of compact bone surrounds cancellous bone. Cancellous bone is formed from struts or plates of bone material called trabeculae, giving it a sponge-like appearance, hence it is sometimes referred to as spongy bone. These trabeculae do not contain any blood vessels and therefore receive their nutrients from blood vessels which run adjacent to the individual trabeculae.

Cancellous bone can be found in areas of the bone which have lower stress loadings, and in areas where the bone is stressed in a number of directions. The individual trabeculae will align themselves to support the various directions in which stress is received and are approximately 200 μm thick (Martin, Burr and Sharkey, 1998). Like all other non-mineralised spaces within bone, the pores and spaces within trabeculae are filled with bone marrow consisting of blood vessels, nerves and other cell types. Cancellous bone is metabolically more active; it has a greater rate of turnover due to its surface area, and is therefore more susceptible to losses caused by increased bone turnover.

In long bones, such as that shown in Figure 1.1, the diaphysis is almost entirely made up of compact bone in a thick cortex surrounding the marrow cavity. Compact bone is essentially a solid material with the only spaces in it representing bone cells, blood vessels and erosion cavities. In contrast, cancellous bone has large spaces within it and this difference between the two is visible to the naked eye. Elsewhere in the bone structure, compact bone can also be identified where it forms a cortex or shell around areas of cancellous bone. In some instances of growing bones, compact bone has to be formed in a region where cancellous bone already exists. In these circumstances, instead of replacing this existing bone, new bone forms around the trabeculae producing a random structure with no definitive grain. This formation is called compact coarse – cancellous bone (Currey, 2002). Compact bone has a much lower porosity than cancellous bone, between 5% and 10%; it also has a more regular structure. Compact bone is predominantly found in the shafts of long bones and the posterior elements of the vertebrae where it accounts for approximately 50% of the density of the spine.

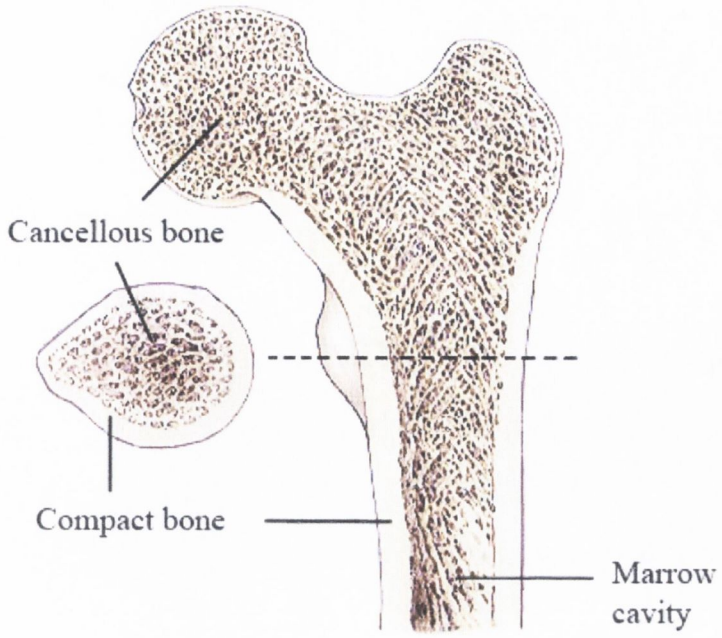

Fig. 1.1 Section through a human femoral head (http://www.familydoctor.co.uk, November, 2005)

1.2 A microscopic view of bone

Thus far, bone has been described according to its appearance as viewed by the naked eye. If bone is now considered at the microscopic level, it can be described according to one of two arrangements. Woven bone is a quickly formed immature bone tissue where the pattern of collagen fibres and mineral crystals are randomly arranged (Martin, Burr and Sharkey, 1998). Woven bone is usually laid down very quickly at a rate of 4 μm per day, and often considerably faster, most noticeably in the foetus and in the callus that is produced during fracture repair (Currey, 2002). Although highly mineralised, woven bone remains quite porous at the micron level. In woven bone the mineralisation process involves approximately spherical centres, impregnating both the collagen and ground substance at the same time, in which the crystals seem to be randomly arranged (Currey, 2002). As a bone matures, the woven bone may often be replaced by lamellar bone and once fully matured, some bone will be remodelled to form Haversian systems. Most woven bone will have completely disappeared by adolescence.

Lamellar bone has an orderly arrangement and is laid down more slowly than woven bone, at a rate of less than 1 μm a day (Boyde, 1980). In lamellar bone there is a highly organised arrangement of the collagen fibres and mineral crystals. The structure of lamellar bone is made up of a number of sheets or lamellae, as a lamella develops layers of collagen are built up in one direction. As one proceeds to a subsequent lamella, the orientation of the collagen fibres will change direction by 90° at the lamellar interface (Martin, Burr and Sharkey, 1998). This division between one lamella and the next appears quite distinctive under a light microscope, particularly when using polarized light. The lamellae are generally arranged tangentially to the bone surface and, together with woven bone, they will develop into a serial stacking of thick layers of bone material.

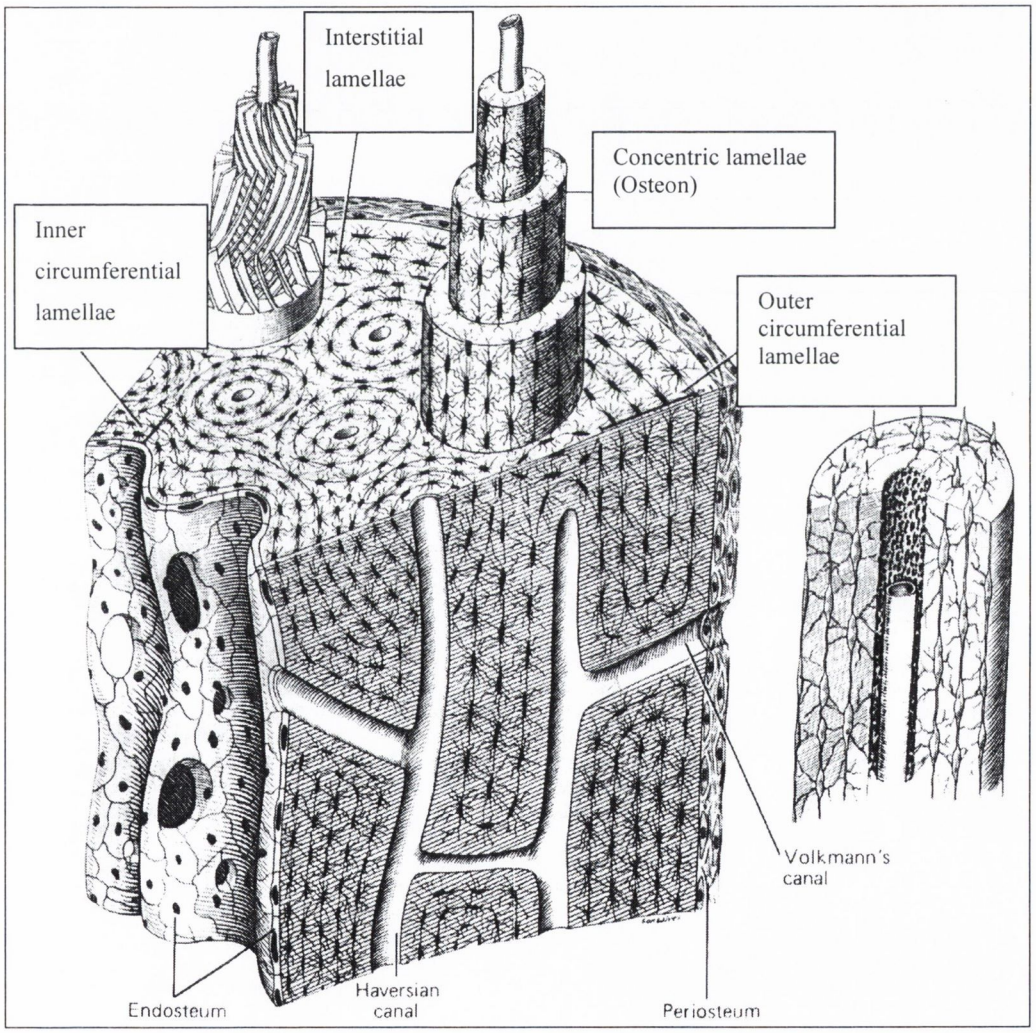

Fig. 1.2 Schematic representation of the wall of a long bone diaphysis (from Junqueira et al., 1992)

Concentric lamellar bone occurs where the lamellae build up in concentric layers around a central canal or blood vessel, approximately 50 μm in diameter (Martin, Burr and Sharkey, 1998). This arrangement of lamellae wrapped around a central Haversian canal is known as an osteon (Figure 1.2). Osteons are generally found to be aligned with the long axis of the bone. Volkmann's canals are similar structures to Haversian canals, however these structures are approximately perpendicular to the bone's surface.

In lamellar bone, the interface between lamellae contains an arrangement of cavities called lacunae, the lacunae house cells known as osteocytes. Although diffusion cannot occur through the hard matrix, osteocytes communicate with the blood vessels and one another by means of slender cytoplasmic extensions, which pass through a network of passageways known as canaliculi.

Since lamellar bone cannot be laid down as fast as woven bone, if a bone needs to grow in diameter faster than lamellar bone can be deposited, woven bone must be laid down instead. Woven bone is mechanically inferior to lamellar bone (Currey, 2002) and a solution to this problem is the development of fibrolamellar or plexiform bone. A lattice of woven bone is formed which is later in filled with lamellar bone. The final result being a network of blood vessels surrounded by layers of lamellar bone, beyond which is the woven bone scaffold. There are, in effect, alternating layers of woven bone and lamellar bone tissue that can extend for many millimetres.

Figure 1.3 (taken from Currey, 2002) shows the formation of fibrolamellar bone. The images shown in Figure 1.3 represent cross sections of the outer surface of a growing piece of bone. In each image the arrowheads show the position of the original surface and blood vessels are shown as black spots. In section (A), the original situation is described before the start of further growth. In section (B), woven bone shown by wavy lines advances rapidly to form scaffolding in advance of the original surface. In section (C), lamellar bone starts to develop and begins to fill in the cavities. As more lamellar bone is deposited (D), additional woven bone is also laid down advancing the bone surface even further. Eventually the original cavities are completely filled in with lamellar bone (E), forming primary osteons, however the surface of the bone has advanced considerably from its original position (Currey, 2002).

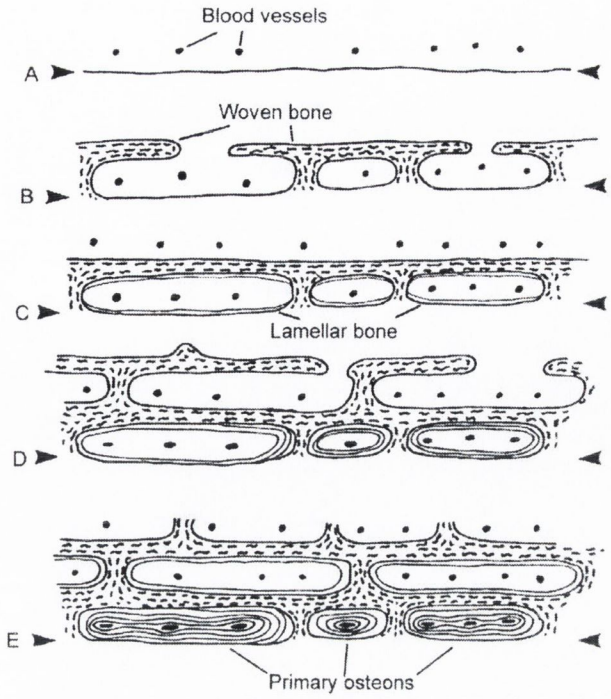

Fig. 1.3 The formation of fibrolamellar bone (from Currey, 2002)

An example of fibrolamellar or plexiform bone is shown in Figure 1.4

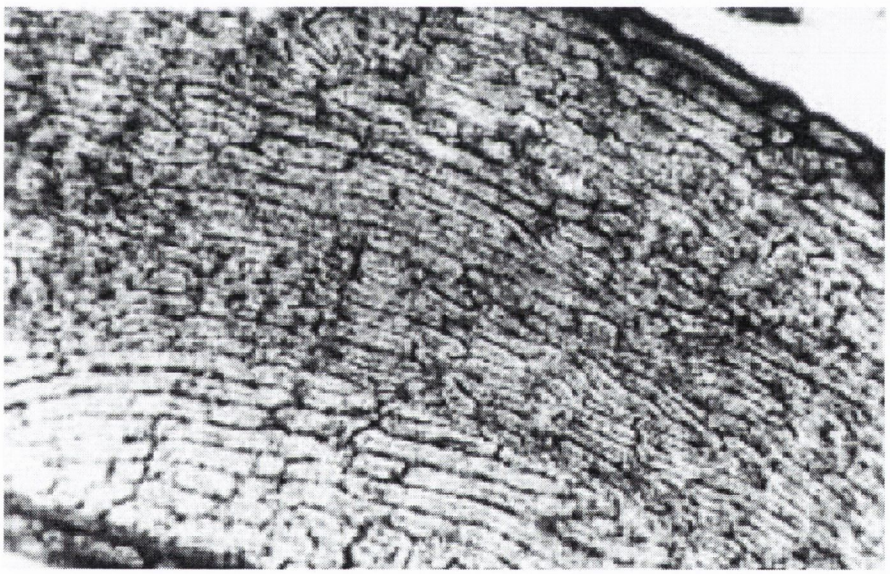

Fig. 1.4 Fibrolamellar bone of a sheep femur at 40 x magnification (from Mulhern and Ubelaker, 2001)

The hierarchical structure of bone is summarised in Table 1.1.

Table 1.1 Summary of bone structure (Adapted from Currey, 2002)

<table>
<tr><td colspan="2">Compact bone</td><td colspan="2">Cancellous bone</td></tr>
<tr><td colspan="2">Solid, only porosity is for canaliculi, osteocyte lacunae, blood channels and erosion cavities</td><td colspan="2">Porosity easily visible to the naked eye. Rods and plates of bone, multiply connected, never forming closed cells.</td></tr>
<tr><td colspan="2">Primary bone</td><td colspan="2">Secondary bone</td></tr>
<tr><td colspan="2">Original new bone tissue laid down on existing bone surfaces</td><td colspan="2">Replacement bone tissue resulting from the resorption of existing bone tissue and replacement with new</td></tr>
<tr><td>Woven bone</td><td>Fibrolamellar bone</td><td>Lamellar bone</td><td>Secondary Osteons (Haversian systems)</td></tr>
<tr><td>Found in large lumps in young animals and in fracture callus Primary</td><td>Alternating sheets of lamellar and woven bone / parallel-fibered bone, with 2D nets of blood vessels. 200 μm between blood vessel nets. Primary</td><td>Often found in large lumps in reptiles. Found as circumferential lamellae in mammals and birds. Primary and secondary</td><td>Cylinders of lamellar bone, solid except for a tube in the middle for blood vessels. 200 μm in diameter. Rarely observed in trabecular bone because will not usually fit inside an individual trabecula Secondary</td></tr>
</table>

1.3 Bone at the cellular level

Bone cells represent only a small percentage of the total bone volume, they are however a critical component, being responsible for the formation and maintenance of the bone matrix. At the cellular level, bone can be seen to consist of a limited number of cell types, associated with either bone formation or bone resorption.

1.3.1 Bone Resorbing Cells

Osteoclasts are the cells that carry out bone resorption; they are multinucleate cells originating from the haemopoietic stem cells of the bone marrow and are closely related to macrophages, cells that migrate through the body to remove debris and pathologic material. Resorption occurs along a specialised surface known as the ruffled border of the cell. The ruffled border is sealed to the bone surface by a clear membrane, which adheres tightly to the bone and seals a resorption space inside which bone resorption takes place. Osteoclasts erode their way through bone at a rate of tens of micrometers

per day by demineralising the bone with acids and then dissolving its collagen with enzymes. The resultant debris is packed into little vesicles and passes through the cell body of the osteoclast and is subsequently dumped into the space above (Nesbitt and Horton, 1997; Salo et al., 1997). Once they have performed their function, osteoclasts will subsequently disappear.

1.3.2 Bone Forming Cells

In contrast to osteoclasts, osteoblasts are bone-forming cells which act in a co-ordinated fashion to produce bone matrix. Osteoblasts secrete the organic matrix of collagen and other proteins (osteoid), which proceed to mineralise extracellularly. Osteoblasts are differentiated from cells known as mesenchymal stem cells and, depending on where the bone formation occurs, these mesenchymal cells come from the deep or cambial layer of the periosteal membrane, or from the stromal tissue of bone marrow. As the bone matrix begins to mineralise, some osteoblasts may become embedded in lacunae and are termed osteocytes. They use cell processes running through canaliculae to communicate with other osteocytes and osteoblasts. The actual connection is by gap junctions permitting the passage of small molecules. Since osteocytes cover all areas of the skeleton and have such a large surface area, the estimated total skeletal surface area of canaliculi in an adult male skeletal is $1200m^2$ compared to $3.2m^2$ for Haversian and Volkmann's canals (Johnson, 1966), they have been considered to act as mechanosensors, sensing and responding to mechanical stresses and strains (Cowin, Weinbaum and Zeng, 1995).

Some osteoblasts do not get trapped in the newly formed bone; instead these osteoblasts remain on the bone surface when bone formation ceases. These cells become quiescent and flattened on the bone surface. Such cells are referred to as bone lining cells.

1.4 Primary & Secondary Bone

It is often desirable to describe compact bone according to the timing and method by which it was formed. This is particularly true in histological studies. For this reason bone may be described as either primary or secondary.

Primary bone is the tissue deposited on a surface during bone growth, consisting of either circumferential lamellar bone or areas of plexiform (fibrolamellar) bone. Primary osteons develop where a blood vessel is enclosed in the mineralising matrix and concentric bone lamellae are laid down centripetally from the canal. These structures are termed primary osteons, as no resorption of existing bone is required for their creation.

Over time, primary bone is replaced by secondary bone by the process of bone remodelling. In compact bone, this manifests itself in the appearance of cylindrical structures known as secondary osteons, or Haversian systems. In contrast to primary bone formation, in secondary bone development resorption of existing bone is initiated, and concentric lamellae are then deposited centripetally. Secondary osteons are approximately 200 μm in diameter and consist of about 16 cylindrical lamellae surrounding the central Haversian canal (Martin, Burr and Sharkey, 1998). A boundary forms around the osteon separating it from the surrounding bone; this boundary is known as the cement line. Cement lines are only found around Haversian systems, primary osteons do not have a cement sheath and this feature is often used as a method to distinguish between a primary osteon and a secondary osteon. By the time the human body reaches adulthood, most compact bone is entirely composed of secondary bone, including whole osteons and the remnants of older osteons that have been partially resorbed. These partially resorbed areas are known as interstitial lamellae (Figure 1.2).

1.5 Bone modelling & remodelling

As the long bones of the body develop, longitudinal growth is determined by the process of endochondral ossification in the cartilaginous growth plate; a region of nonmineralised growth located towards both ends of the bone. Their diameter increases by periosteal intramembraneous ossification, where mesenchymal precursor cells directly differentiate into bone-forming osteoblasts. However, as bones develop they must also be shaped, this is achieved by removing bone in some areas, and depositing it in other areas. This process of sculpting the shape of the bone, through bone resorption in some locations and bone formation in others, is referred to as modelling.

Over time, damage will accumulate within a bone due to the loading experienced. This damage must be repaired in order to maintain structural integrity. In a similar manner, a bone's internal architecture must be adjusted to varying load conditions, both while the bone is developing, and throughout its life. This repair or modification process involves the removal and replacement of bone in particular places, by the coupled actions of osteoclasts and osteoblasts working at the same site. This replacement process is known as remodelling. It can be considered that modelling serves to comply with current mechanical usage from a structural point of view, whereas remodelling serves to match usage from a material properties aspect.

Essentially, modelling involves the independent actions of osteoclasts and osteoblasts (activation & resorption (A-R), or activation & formation (A-F)), whereas remodelling involves the sequential, 'coupled' actions of osteoclasts and osteoblasts (Frost, 1973).

The agent responsible for remodelling is the basic multicellular unit or BMU, which acts over a period of approximately three months (Frost, 1985); it consists of osteoclasts and osteoblasts working together in an ordered manner. There are three principal stages in a BMU's lifetime: activation, resorption, and formation (A-R-F). Activation occurs when a chemical or mechanical signal causes osteoclasts to remove bone somewhere on or in the skeleton. The osteoclasts form a cutting cone, which resorbs a volume of bone in the form of a trough on the bone surface, or a tunnel in compact bone. These cavities tend to be about 200 μm in diameter and progress through the bone at a rate of 40-50

μm/day (Martin, Burr and Sharkey, 1998). During formation, osteoblasts are differentiated from mesenchymal cells; they arrange themselves around the edge of the tunnel dug by the osteoclast and begin to replace the resorbed tissue. Formation is much slower than resorption; the osteoblasts lay down new bone in concentric lamellae, which gradually move towards the centre of the structure. At the tail of the BMU, the osteoblasts and osteoid line the surfaces of new bone. The head of the BMU contains a capillary bud, supplying nutrients and possibly progenitor cells for osteoclasts and osteoblasts. Since osteonal BMUs are located deep within the bone cortex, a vascular supply must be maintained. It is for this reason that the tunnel cannot be entirely refilled, and each BMU leaves behind a new central Haversian canal in the bone.

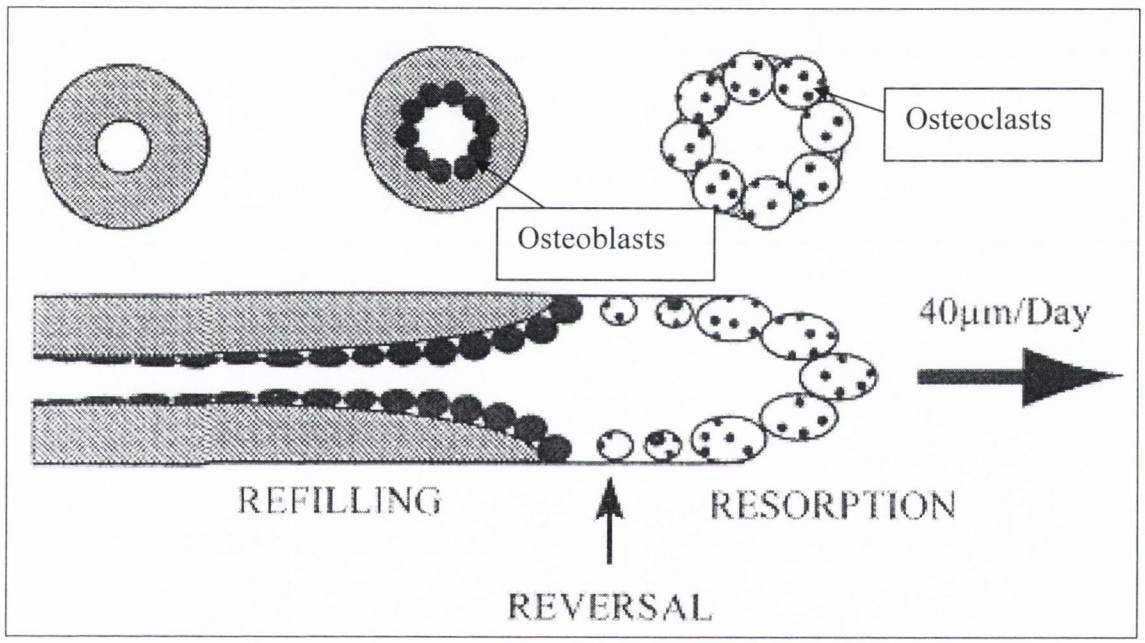

Fig. 1.5 Schematic Diagram of the Basic Multicellular Unit (from Martin, Burr and Sharkey, 1998)

1.6 Microdamage and Remodelling

Various theories exist regarding the mechanisms responsible for initiating remodelling (Lanyon, 1991; Cowin, Weinbaum and Zeng, 1995). However, there is a general consensus that remodelling increases both when mechanical loading is excessively low, for example during a disuse state, and when it is excessively high causing microdamage associated with mechanisms such as creep and fatigue. Creep can be described as the progressive deformation and eventual failure of a material at a constant stress (Dieter, 1986), fatigue is the gradual deterioration and premature failure of a component resulting from repeated stress cycles. Unlike metals, in the post yield region, bone experiences damage in the form of microcracking, which at first is too small to be dangerous. Microcracking or microdamage is a natural phenomenon which exists in healthy humans, it can occur as a result of overloading or during the repetitive loadings of normal activities. The fatigue damage observed within bone is associated with the initiation and growth of microcracks and is considered to be a function of the applied load, the number of cycles and the temperature (Lee et al., 2000b).

Since the early work of Tschantz and Rutishauser (1967), much experimental evidence and many theoretical models have described the association between fatigue microdamage and bone remodelling (Carter and Hayes, 1977b; Martin and Burr, 1982; Currey, 1984; Burr et al., 1985; Burr and Martin, 1993; Mori and Burr, 1993; Prendergast and Taylor, 1994; Prendergast and Huiskes, 1996; Bentolila, 1998; Lee et al., 1999; Muir et al., 1999; Martin, 2000; Verborgt et al., 2000). An important observation made by Carter and Caler (1985) was that the stress-strain curves obtained from their fatigue tests showed a progressive loss of stiffness and increase in hysteresis over time, therefore supporting the hypothesis that microdamage accumulates over time. This also supports the argument that remodelling occurs *in vivo*, since a repair mechanism must be occurring to prevent the eventual failure of bones due to normal activities.

A study by Burr (2000) suggests that as much as 30% of bone remodelling is targeted, inferring that damaged bone is preferentially selected for replacement. This would

suggest that when cracks form, some type of signalling mechanism must trigger such targeted remodelling. However, the nature of any such signal remains unclear.

Microdamage has been observed in both human and animal studies, during normal activities as well as *in vivo* and *in vitro* testing. Frost (1960) was one of the first to observe naturally occurring microdamage in human ribs, suggesting that microcracks formed as a result of the fatigue loading experienced during breathing. Since then, microdamage has also been recorded in human cortical bone showing an exponential increase in microdamage with age, with the greatest increase being observed in women (Schaffler et al., 1995; Mori et al., 1997). Microdamage can occur in a variety of manners and has been observed as diffuse damage, individual microcracks, regions of crazing or crosshatched cracks and complete fractures (see Figures 1.6 through 1.9 for examples). In a flexural fatigue study by Boyce et al. (1998), it was observed that isolated microcracks were primarily found in areas under compression, near the neutral axis finer 'wispy' cracks were identified, and areas of diffuse damage were located in tensile regions of bone.

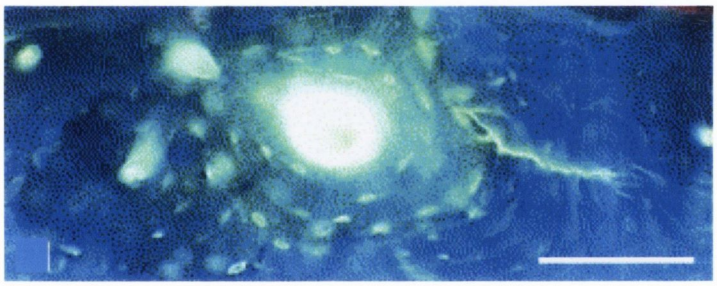

Fig. 1.6 Example of an individual microcrack located bovine bone, it can be observed that the microcrack meets a secondary osteon, microcrack stained with calcein dye and examined under UV epifluorescence microscopy, bar=100μm (taken from O'Brien et al., 2003).

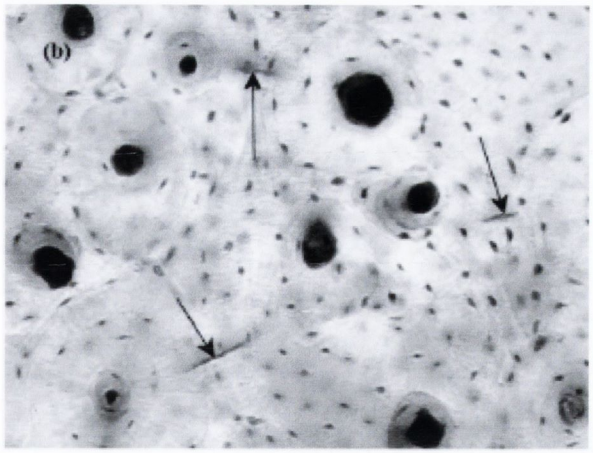

Fig. 1.7 Example of individual microcracks (arrows). From micrographs of canine bone (x 200 magnification) (taken from Frank et al., 2002)

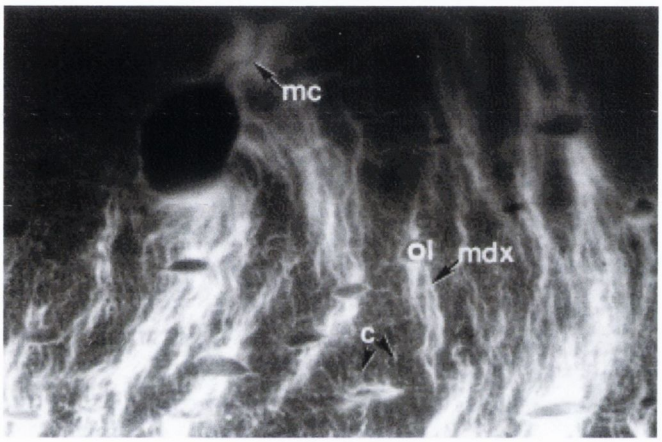

Fig. 1.8 Confocal micrograph of the tensile surface of a beam specimen of bovine tibia, the specimen has been stained with flourescein (similar to calcein). The image shows microdamage (mdx), osteocyte lacunae (ol), canaliculus (c). The image depicts dense array of microdamage associated with osteocyte lacunae and a blood vessel. A macrocrack can also be identified (mc) surrounded by diffuse damage (arrays of tiny microcracks) (from Reilly, 2000)

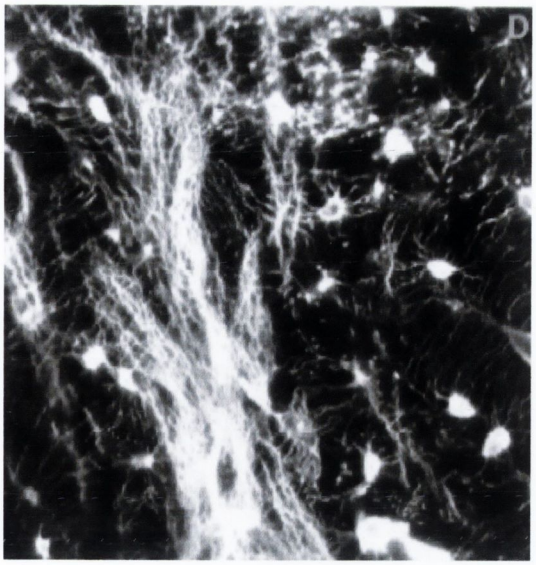

Fig. 1.9 Confocal micrographs of basic fuchsin stained rat bone. Image shows osteocytes in a diffusely damaged region of 'acutely fatigued bone' (from Bentolila et al., 1998)

One of the most compelling arguments for targeted remodelling and repair of microdamage was put forward by Mori and Burr (1993). In their study the left limb of dogs was loaded in fatigue for an hour and a half in such a manner as to produce microdamage. The left limb was then left for eight days and the right limb was loaded in the same manner. The specimens were then sacrificed immediately after testing the right limb. It was surmised that during the period of eight days resorption would start in the left limb. In their study they quantified the number and area of resorption cavities, the total number of cracks and the proportion of those cracks associated with a resorption cavity. In both the left and right groups the number of microcracks was approximately the same, however, leaving the bone to recover for eight days resulted in an almost doubling in the number and total area of resorption cavities. Comparison of the number of resorption cavities in the left leg associated with cracks to those in the right leg, which had not had the opportunity to start repair, showed a high statistically significant increase. This provides clear evidence for the repair of microdamage by bone remodelling, further supported by Lee et al. (2002).

In an attempt to gain further insight regarding the degree to which microdamage governs remodelling, a recent study by Martin (2002) presented a mathematical analysis based on the hypothesis that "all cortical bone remodelling" in a normal, healthy

skeleton is initiated by, and is in close proximity to, microcracks. Martin's findings suggest that such a hypothesis would be valid, but the author does stress that this does not imply that the only role of remodelling in cortical bone is fatigue damage removal.

The mechanisms by which mechanical damage stimulates remodelling remain poorly understood and the study of fatigue damage accumulation in devitalised bone, whilst posing certain limitations, nevertheless represents an important first step in understanding the effects of mechanical fatigue loading on living bone, particularly in the areas of remodelling, fatigue fractures and damage accumulation.

1.7 Mechanical Properties of Bone (Bone Strength)

Bone, like any other material, is dependent upon its material properties and geometry in order to determine its strength. However, traditional material properties such as tensile strength do not give any idea of the toughness of a material or its resistance to crack propagation. Fracture mechanics is widely used to describe a material's toughness, but unfortunately it provides very little information about how bone behaves in compression, and is susceptible to variation between specimens with different histology, or between bones from individuals of different ages. Therefore, due to the wide variety of modes of loading experienced by bone, a number of measures are required to fully describe bone's behaviour under various conditions. Table 1.2 describes a variety of material properties for bone.

In the load bearing bones of the body, regions of compact bone will be subjected to a range of loading magnitudes and directions. In localised areas, bone can experience both tensile and compressive loading (Biewener, 1991). Living bone can experience tensile strains as high as 2500-3000 με and compressive strains as high as 4500 με (Nunamaker et al., 1990; Biewener, 1991).

Bone is an anisotropic material and thus its mechanical properties are dependent on the direction of the applied loading (Hayes and Bouxsein, 1997). When bone is loaded in tension, it is observed to be stronger and to have a higher strain to failure when loaded longitudinally rather than circumferentially. Liu et al. (2000) found that osteonal bone

of baboons was four times stronger when loaded along the long axis of the bone than when loaded normal to this direction (289 MPa vs. 71 MPa). They also found a corresponding 3.75 difference in the strain to failure. As described by Currey (2002), this implies an approximately 16-fold difference in the work necessary to fracture a specimen. In compression, this anisotropy of bone strength is less marked, however it should be noted that the ultimate strain is greater in the circumferential direction than in the longitudinal direction, the opposite of tension.

Bone does not undergo plastic deformation like metals, and the final amount of strain that the bone will withstand before failure will vary depending upon the amount of mineralisation. If bone is loaded and unloaded cyclically, it will, however, exhibit some viscoelastic characteristics, with limited strain recovery upon unloading. The result of this is that bone becomes more compliant each time it is loaded into the yield region.

Something which should also be recognised is that the material properties of bone change with age. Human bone will have fully matured by the age of 30-35 years and from then on deterioration is observed. Over time, a reduced integrity, a fall off in mechanical properties and an impaired response to mechanical stimuli for new bone formation can all be observed. Zioupos and Currey (1998) noted a 2.3% reduction in stiffness for every ten years of later life from bone's original value at 35 years, this was accompanied by a 3.7% reduction in flexural strength and a 4.1% reduction in the critical stress intensity factor, K_c. This would suggest that crack formation in the elderly requires less damage to initiate and, once formed, requires less energy to propagate through the bone, resulting in earlier failure.

Table 1.2 Typical mechanical properties for cortical bone. Reproduced from Martin, Burr and Sharkey (1998)

Property	Human	Bovine
Elastic Modulus (Young's Modulus), Gpa		
Longitudinal	17.4	20.4
Transverse	9.6	11.7
Bending	14.8[a]	19.9[b]
Shear Modulus, GPa	3.51	4.14
Poisson's Ratio	0.39	0.36
Tensile Yield Strength, MPa		
Longitudinal	115	141
Transverse	-	-
Compressive Yield Strength, MPa		
Longitudinal	182	196
Transverse	121	150
Shear yield stress, MPa	54	57
Tensile ultimate stress, MPa		
Longitudinal	133	156
Transverse	51	50
Compressive ultimate stress		
Longitudinal	195	237
Transverse	133	178
Shear ultimate stress, MPa	69	73
Bending ultimate stress, MPa	208.6[a]	223.8[b]
Tensile ultimate strain		
Longitudinal	0.0293	0.0072
Transverse	0.0324	0.0067
Compressive ultimate strain		
Longitudinal	0.0220	0.0253
Transverse	0.0462	0.0517
Shear ultimate strain	0.33	0.39
Bending ultimate strain	-	0.0178[b]

Human data are for adult femur and tibia; bovine data are for femur

Data compiled from Cowin (1989), pp. 102, 103, 111 – 113, except as indicated

[a]*From Currey and Butler (1975); adult femur, three-point bending.*

[b]*From Martin and Boardman (1993); tibia, three-point bending*

1.8 Bone as a composite

A structure will fail in a number of ways depending upon its material properties. A brittle material will fail catastrophically from some existing flaw with relatively little advance warning of failure. In contrast, a ductile material loaded in tension will deform plastically as dislocations occur throughout the material, this results in *necking* where a small region of the specimen becomes increasingly narrower as the material deforms, bearing an ever-increasing stress until failure occurs.

Composite materials consist of at least two different phases. The elastic properties reflect a mixture of the two phases, however, the strength may be quite different from either material. What is clear about composites is their success in controlling crack progression, forcing it to change direction, or to pass into voids thereby blunting the crack's progress. When cracks appear, the phases can often separate themselves and thus retard crack growth. Bone has a well-defined hierarchical structure with many phase and directional changes. For this reason it is often considered as a natural composite material when analysing its failure behaviour, this can of course be applied to various levels within bone structure. With the exception of woven bone, bone has a definitive grain structure at its lowest level; this is produced by the co-orientated cementing together of collagen fibrils and their minerals. This results in bone having a microstructure equivalent to that of a fibrous composite with a very high volume fraction of fibres.

It is important when considering bone to remember that it is a living material that is constantly changing over time. Previous studies have shown that remodelling of compact bone reduces its flexural fatigue strength and resistance in tension (Carter and Spengler, 1978). Compression, shear and bending strengths are also reduced. The effect of bone remodelling will alter the mechanical properties of bone in a number of ways; highly mineralised bone matrix is replaced with less calcified material, the porosity of the bone is increased and any change in the orientation of the collagen fibres will obviously have an effect. The introduction of the cement line interface with its very different mechanical properties will also impact on the properties of bone.

It is generally considered that a reduction in the strength of a material increases the potential for crack initiation but will, at the same time, increase the resistance to crack growth. Osteonal cement lines are beneficial in halting crack growth, as their distribution throughout a more heavily mineralised bone matrix should result in significant stiffness variations (Burr et al., 1988). These less mineralised bands of material are more compliant and as a result, as a crack approaches a more ductile region, it should at first accelerate and then decelerate, finally coming to rest when it reaches another stiff region (Kendall, 1975). Furthermore, Haversian bone is thought to stop the transverse growth of cracks, diverting them along the bone axis and allowing them to expend energy without seriously reducing the structural integrity of the bone (Martin, Burr and Sharkey, 1998). Similarly, the blood channel networks within lamellar bone also possess a relatively weak interface and, as a result, these features may also cause cracks to be stopped, diverted, or made to split up, thus requiring more energy to keep growing.

This approach can also be considered at a higher magnification, where the interlamellar regions appear to have more ground substance and less collagen, thus also giving them a relatively weak interface. The lamellar structure of bone means that the critical stress intensity factor, K_c, will be lower in the longitudinal direction than in the transverse direction and, since cracks will only propagate when the stress concentration at the crack tip exceeds the critical value, then cracks will naturally find it more difficult to travel across the axis of a long bone.

The architecture of bone is such that, at some point, the crack will encounter one of the numerous voids and cavities, and it will not have to travel very far before reaching either osteocyte lacunae or blood channels running through the bone. As the crack encounters such features it will be transformed from what may be considered to be a sharp tipped crack into a crack with a relatively rounded end. The stress concentrations may be high around these discontinuities within the bone, but they will be considerably less than at the end of the crack. This reduces the probability that the crack will grow on the other side of the feature.

Due to the histological structure of bone, a crack cannot build up to any considerable size in the radial direction without encountering many lacunae. Though less abundant

in their number, blood vessels are much larger than lacunae and will therefore be very effective at halting crack growth, particularly in longer cracks.

Although bone may be considered a relatively weak material when compared to steels, what is important to consider is that it has evolved to suit its function, minimising the effects of damage at physiological strains and strain rates.

1.9 Fatigue behaviour of compact bone

Structures can gradually fail due to deterioration in their structural integrity as a result of fatigue, creep or a combination of the two. Mechanically induced fatigue loading provides the most direct comparison to the periodic stresses and strains of varying intensity and type that are observed *in vivo*. Normal activities such as walking, running and breathing involve the application of muscle forces to the skeleton. The nature of these activities and the application of muscle contraction and relaxation mean that bone experiences fatigue loading. In fatigue loading, a gradual deterioration is observed when the material is subjected to a periodic or cyclic stress lower than its ultimate stress. Over time, damage develops in the form of microcracks, which can multiply under sustained cyclic loading and grow into macrocracks. This may ultimately result in the bone's failure. The fatigue life of any material can therefore be described as a function of crack accumulation and crack growth (Agarwal and Broutman, 1980; Mori and Burr, 1993).

It is evident that fatigue is one of the key mechanisms responsible for bone remodelling (Martin and Burr, 1982; Burr et al., 1985; Burr and Martin, 1993; Mori and Burr, 1993; Prendergast and Taylor, 1994; Lee et al., 1999; 2000b; Martin, 2000). O'Brien et al. (2003) described the accumulation of microdamage over time at a stress level above that experienced *in vivo*, however this must be expanded upon in order to understand how microdamage develops in bone during normal activities.

If the assumption can be made that a constant cyclic amplitude is applied to bone, then the number of fatigue cycles required for failure would be a function of the applied stress range. The number of cycles to failure (N_f) can be described by an inverse power

law of the form shown in Equation 1.1, where A and α are constants and α represents the slope of the logarithmic stress life curve.

1.1

$$N_f = A/(\Delta\sigma)^{\alpha}$$

Carter et al. (1976) determined the fatigue life of bovine cortical bone subjected to load-controlled rotating bending as a function of temperature, loading level, apparent bone density, and microstructure.

1.2

$$Log\ (2Nf) = -7.8 \log\sigma - 0.02T + 4.5\rho + 12.0$$

Where σ = *stress (in MPa)*
T = *temperature (in degrees Celsius)*
ρ = *apparent density in* (gm/cm^3)
Nf = *number of cycles to fracture*

Compressive fatigue damage in bone consists of extensive networks of shear lines, suggesting buckling of the collagen fibres (Carter et al., 1976; Chamey, 1970). Tensile damage was shown to differ from compressive damage in flexural fatigue specimens. Oblique cracking and longitudinal splitting was observed on the compressive surface, and debonding was observed at the tensile surface (Carter, 1976). Prior to final fracture, Currey observed diffuse microcracking surrounding bone yielded in tension, and microbuckling and shearing in compression (Currey and Brear, 1974).

Caler and Carter determined the fatigue life for tensile, compressive and fully reversed axial specimens tested wet and under load control at body temperature (Caler, 1988; Caler and Carter, 1989). They determined power laws to express the time to fracture in terms of the applied stress range, $\Delta\sigma$, and the initial elastic modulus, E^*.

1.3

For tensile fatigue : $\log(t_f) = -14.89(\log(\Delta\sigma/E^*)) - 33.07,\ r^2 = 0.94\ n=14$
For compressive fatigue : $\log(t_f) = -11.88\ (\log(\Delta\sigma/E^*)) - 24.32,\ r^2 = 0.97\ n=16$
For fully reversed fatigue : $\log(t_f) = -6.30\ (\log(\Delta\sigma/E^*)) - 11.78,\ r^2 = 0.84\ n=9$
Where $\Delta\sigma$ = *stress range MPa*
E^* = *initial elastic modulus, GPa*
Tf = *time to failure to fracture, s*

This work showed that the time to fracture was dependent on the applied effective strain range, independent of frequency of loading, for tests conducted at 2 Hz and 0.02Hz.

1.9.1 Fatigue in composites

Bone can be considered as a fibrous lamellar composite material and the long-term fatigue behaviour of such materials can be described by the onset and accumulation of damage. Figure 1.10 describes the development of damage in composite laminates under fatigue loading as reported by Reifsnider et al. (1983) for a variety of composites. The initial stage of damage formation consists of primary matrix cracking. This occurs along fibres in off-axis plies, where the fibre axis is not aligned with the principal stress direction. In bone this compares to damage forming in interstitial bone, perpendicular to the loading axis. These homogenous cracks do not interact with one another and are restricted to individual plies where cracks form at discontinuities, or sites of stress concentration. Such cracks will then grow until they reach an adjacent ply where their growth is halted. The numerical density of cracks increases with loading cycles, at a rate determined by the applied stress, and eventually the number of cracks will reach a saturation state, whereby the cracks in each ply will have attained equilibrium spacing. This steady state is referred to as the characteristic damage state, or CDS.

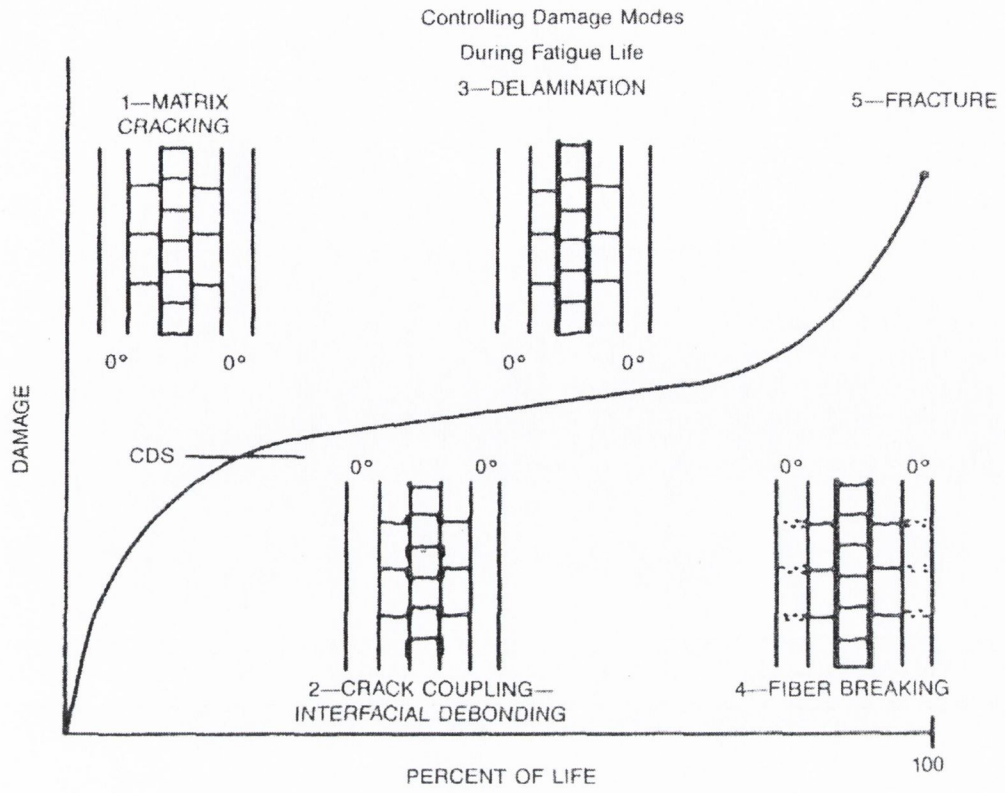

Fig. 1.10 Development of fatigue damage in composite laminates (from Reifsnider et al., 1983)

These microcracks may initiate fibre failure in adjacent plies where stress concentrations have been created by their presence. Secondary cracks form in adjacent plies at the interface with the ply containing the primary microcrack and will grow along the interface in a direction perpendicular to the primary crack. It could be said that cracking is taking a path of least resistance, which involves separation at a relatively weak interface and this normally occurs as a result of tensile stresses acting along the axis of the crack. The next stage that occurs in the progressive failure of composites is delamination or interlamellar debonding. Stresses build up in areas where primary and secondary cracks cross one another causing the growth of interlaminar cracks in tension (Reifsnider and Jaminson, 1982). In compressive fatigue a different mechanism applies; where the out-of-plane displacement of plies will affect the spread of delamination (Shultz and Reifsnider, 1984).

Towards the end of a composite material's life, a rapid increase in all damage modes will be observed and further lamellar debonding occurs combined with a degeneration of the matrix. This will cause stresses to rise in fibres or lamellae acting along the

loading axis, causing fracture of the individual fibres. Consequently, this will increase the stress in any intact fibres causing a cascade effect resulting in ultimate failure of the composite. In bone, any damage may become localised and a single dominant macrocrack may form which will quickly drive through the structure. This final stage is very rapid, accounting for only 10% of the material's life. It is important to realise that each damage mode does not occupy distinct regions, rather that they are the dominant effect at that point in time; fibre failures may occur throughout the life of the material. However, their effect will not be the significant mechanism until it is very close to failure.

1.9.2 Test conditions and data comparisons

Considerable experimental data are available concerning the fatigue behaviour of bone, however differences and inconsistencies in the methods used for testing make comparisons between studies very difficult. Taylor (1998a) analysed several studies where the number of cycles to failure was in the region of 10^5-10^6 cycles, and had been described as a function of the applied stress ($\Delta\sigma$) or strain ($\Delta\varepsilon$) range.

Using a statistical method which took specimen size into account, Taylor (1998a) described the probability (P_f) that the fatigue strength of a given specimen would be less than or equal to a predetermined value. This method is shown in Equation 1.4, where $\Delta\sigma_o$ is the fatigue strength and m and $\Delta\sigma_o^*$ are constants.

1.4

$$P_f = 1 - \exp(-\Delta\sigma_o/\Delta\sigma_o^*)^m$$

Through analysing the scatter in two large sets of fatigue data, Taylor was able to calculate the fatigue strength for any specimen volume, provided the fatigue strength for some other volume was known. Taylor further demonstrated that at 10^5 cycles, approximately one month of normal activity in living bone, fatigue limits could be predicted provided that the stressed volume was accounted for. When examined using this technique, previous published work demonstrated "consistent and separable effects of frequency, bone type and loading type" (Taylor et al., 1999), enabling multiplication factors to be developed for each of these factors on the fatigue strength of bone. These

were subsequently incorporated into the model in order to relate various studies. The effect of temperature previously established by Carter and Hayes (1976) was also incorporated into the model and Table 1.3 describes these multiplying factors, which Taylor applies to different effects when predicting the fatigue strength under various conditions.

Table 1.3 Summary of the effects of various parameters on the fatigue strength of compact bone at 10^5 cycles to failure (Taylor et al., 1999)

Parameter Change	Multiplying Factor (Effect on fatigue strength)
Frequency	
From physiological frequency to high frequency	1.33
Bone type	
From old human bone to bovine bone	1.44
Temperature	
From physiological temperature to room temperature	1.16
Loading type	
From zero tension to zero compression (human bone)	1.08
From zero tension to tension-compression (human bone)	1.12
From zero compression to tension-compression (human bone)	1.04

1.9.3 The effect of fatigue on the mechanical properties of bone

Fatigue damage can be quantitatively defined in a variety of ways and a number of changes in microstructure and mechanical response occur during the course of a specimen's fatigue life. These changes include the formation and propagation of microcracks, the loss of specimen stiffness and ultimate strength and also the consumption of energy by the development of microdamage within the material.

Mechanical property degradation is believed to be a manifestation of damage accumulation within a fatigued sample and studies have shown that microdamage accumulation results in a loss of stiffness (Carter and Hayes, 1976; 1977a; Schaffler et al., 1989; Keaveny et al., 1994a; 1994b; Zioupos et al., 1996). Distributions of crack length, orientation and microcrack density have been studied in composite materials and correlated with property degradation (Wang and Chim, 1983; Wang et al.,1987) Carter and Hayes (1977b) demonstrated that both the modulus and tensile strength of bone

decreased linearly over time for bovine specimens tested in rotating bending. Schaffler et al. (1989) also showed an early stiffness loss accompanied by the development of microdamage in strain controlled tensile fatigue tests, and after this initial loss, specimen modulus was observed to stabilise. In a later study, Pattin et al. (1996) described the differences in property degradation behaviour between tensile and compressive fatigue. In tension, Pattin et al. observed a noticeable change in the stress-strain response of specimens during the first quarter of their fatigue life. However, in compression, no noticeable change was observed by half way through the fatigue life.

Figure 1.11 shows the property degradation curves describing how secant modulus (stress range/strain range) reduction and cyclic energy dissipation increase over the course of fatigue life for (A), a tensile fatigue specimen tested at 3547 με, and (B), a specimen tested in compressive fatigue at 4573 με.

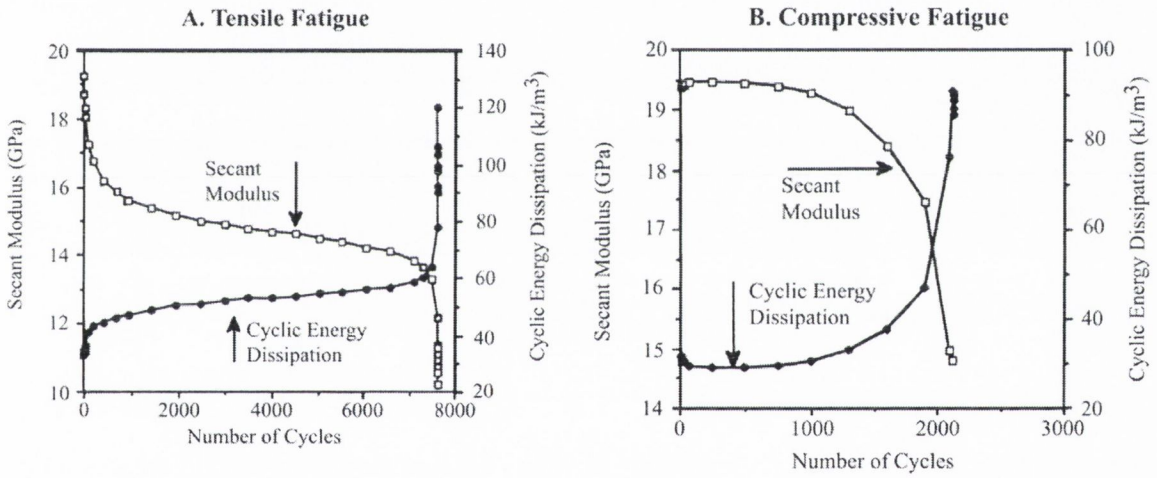

Fig. 1.11 Property degradation curves showing secant modulus reduction and cyclic energy dissipation increase over the course of fatigue life for (A) tensile fatigue and (B) compressive fatigue (Pattin et al., 1996)

In tensile fatigue (see Figure 1.11A), it can be seen that significant initial property degradation occurs, followed by a steady state region, until ultimately there is a rapid degradation of the properties just prior to failure. This is also consistent with findings by Zioupos and colleagues (Zioupos, Currey and Sedman, 1994; Zioupos et al., 1996) who found that the increase in damage in a fatigue test followed a similar pattern. Damage was seen to increase slowly for the majority of the test with a subsequent rapid increase in damage just prior to failure. In the specimen tested in compressive fatigue (see Figure 1.11B), significant property degradation only occurred over the latter half of

the specimen's life, although higher effective strain ranges demonstrated increased modulus degradation at a given life fraction. In both tests, a decrease in secant modulus was mirrored by an increase in cyclic energy dissipation and this was characteristic of all of their tests (Pattin et al., 1996). In their study they predicted an approximate modulus threshold of 2500 με in tensile fatigue and 4000 με in compressive fatigue, with sharp transitions in the fatigue energy dissipation behaviour at these points. Modulus degradation at a given life fraction in compressive fatigue was shown to be proportional to the applied effective strain range above approximately 4000 με. It was shown that bone dissipates more cyclic energy above thresholds of 2500 με in tensile fatigue and 4000με in compressive fatigue. Below these loading levels, cyclic energy dissipation was proportional to the effective strain range raised to the power 2.1. Above these thresholds, cyclic energy dissipation was proportional to the 6.0 power of applied effective strain range in tension, and to the 4.8 power in compression.

It was noted that although cyclic energy dissipation was greater in tensile fatigue at a given effective strain range, this increased energy dissipation took place over a shorter fatigue lifetime. This resulted in comparable total energy dissipation over comparable fatigue lives (Pattin et al., 1996). The energy required to fracture bovine bone in tension is 10^6 Jm^{-3} (Wright, 1976) and Pattin et al. suggest that, as this is close to the energy to fracture predicted by their data, then bone may fail when a critical amount of energy is dissipated at a given fatigue life, independent of the fatigue damage mechanisms and property degradation behaviour in tensile and compressive fatigue.

It therefore remains important to examine how microdamage develops at strain ranges above and below these modulus threshold values which have been indicated, as a similar pattern may be observed for microdamage.

1.9.4 Microdamage, mechanical properties and thresholds in bone

Zioupos, Currey and Sedman (1994) demonstrated that the development of fatigue microdamage in bone is not observed prior to specimen yield, but once microdamage has formed, this will lead to stiffness and strength losses (Burr et al., 1985; Mori and Burr, 1993; Bentolila et al., 1998; Verbogt et al., 2000). Nevertheless, up to a 15-30% modulus reduction may occur before significant microdamage accumulation is observed in cortical bone (Burr et al., 1998). In an examination of whole canine femora tested in bending fatigue, Burr et al. (1998) found an approximately quadratic relationship between crack density and stiffness loss and a linear relationship between damaged area and stiffness loss in the mid-shaft of the bone.

In a series of interrelated studies by Moore and Gibson (Moore and Gibson, 2003a; 2003b; 2003c), the fatigue behaviour of bovine trabecular bone was examined from both the point of view of accumulation of microdamage and the effect that fatigue has on bone's mechanical properties over time. Like the study by Pattin et al. (1996), Moore and Gibson identified the significance of a damage threshold for bone. A threshold number of cycles was identified for fractures to form at any maximum strain tested, independent of normalised stress and below which no trabecular fractures were identified. This threshold was seen to reduce with increasing maximum strain.

Microdamage was not observed at maximum compressive strains below approximately 0.5% and a minimum strain of approximately 0.5% was necessary before changes in modulus or residual strain were observed (Moore and Gibson, 2003b). Moore and Gibson argue that their observations support the hypothesis that an endurance limit, a stress level below which no fatigue damage occurs, exists at about $\Delta\sigma/Eo = 0.0035$ (3500με) for bovine trabecular bone tested in compression (Moore and Gibson, 2003c). This is similar to the 4000 με described by Pattin et al. (1996) for compact bone in compressive fatigue. Moore and Gibson found that below this limit no mechanical property change and no microdamage accumulation could be observed. Moore and Gibson employed a cut-off of 3000 cycles to differentiate between high and low cycle fatigue where different damage mechanisms were responsible for the low and high cycle regimes. Furthermore, at normalised stresses above their threshold strain, fatigue

loading of bovine trabecular bone produced changes such as a decreased normalised modulus, and an increased plastic strain accumulation throughout the test.

There is partial evidence to suggest that thresholds exist for the accumulation of microdamage in cortical bone (Burr et al., 1985). Repetitive loading of a dog's forelimb in three point bending at 1500 microstrains for 10,000 cycles produced significant bone microdamage, however lower strain magnitudes, or fewer number of cycles did not. Tests groups of 625 microstrains for 100 cycles, 625 microstrains for 1000 cycles, 625 microstrains for 10000 cycles and 1500 microstrains for 10000 cycles were examined. Statistically significant differences were found between loaded and unloaded limbs in the 1500 microstrain group, whereas no significant differences were found between loaded an unloaded limbs of the 625 microstrain groups. Significantly more microdamage was also found in the 1500 microstrain group (0.024 cracks / mm^2) when compared with the 625 microstrain groups loaded to either 1000 or 10,000 cycles. In a subsequent study, comparisons of external control limbs with canine forelimbs loaded in three point bending at 2500 microstrains (Mori and Burr, 1993) demonstrated almost five times more microdamage in the limbs of loaded animals than controls as anticipated by mechanically induced loading, with a crack density of 0.055 microcracks / mm^2 and crack length of 49.8 μm after 10,000 fatigue cycles. Schaffler et al. (1989) measured damage accumulation in tensile fatigue at physiological strain ranges of 0 – 1200 microstrains. The measured density of new cracks formed during the test was 1.51 cracks / mm^2 after 10^6 cycles.

In vivo microdamage in compact bone specimens taken from cadavers has identified the presence of microdamage and has also identified an increase in microdamage with age. Cadaveric specimens from the tibia and proximal femur identified mean crack densities of 0.171± 0.127 crack microcracks / mm^2 for the tibia and 0.207± microcracks / mm^2 for the proximal femur Brown et al.,(1996). Wenzel, Schaffler ad Fyhrie (1994) studied in vivo trabecular microcracks in human vertebral bone and found crack densities in the range 0.8 – 23.1 microcracks / mm^2, with a mean of 7.6 microcracks / mm^2. Schaffler et al. (1995) examined the incidence and localisation of microcracks in the mid diaphysis of human femoral compact bone for specimens in the age range 50 to 75 years. Microdamage density of females was reported ranging between 2 and 6 microcracks / mm^2 and for males was between 0.75 and 2 microcracks / mm^2. In a

study of cortical bone from the femoral neck Schaffler et al. (1995b) demonstrated microcrack densities ranging from approximately zero to 2 microcracks / mm^2 with an average density of 0.5 microcracks / mm^2.

With various studies identifying the accumulation of microdamage in bone and others indicating the modulus threshold behaviour of bone's response to fatigue loading, it is therefore important to identify whether an endurance limit for damage accumulation in compact exists.

1.9.5 Damage Accumulation during Fatigue

An earlier study by O'Brien et al. (2003) examined microcrack accumulation at different intervals during fatigue testing of compact bone. This employed a technique which allows microcrack growth to be monitored during the course of a fatigue test, by the application of a series of fluorescent agents (O'Brien et al., 2002). Specimens of bovine compact bone were fatigue tested in cyclic compression at a stress range of 80 MPa, approximately 4000 με with a mean number of cycles to failure of 88,380, where failure was defined as a 10% reduction in modulus (Taylor et al., 1999). The results of this study are shown in Figure 1.12.

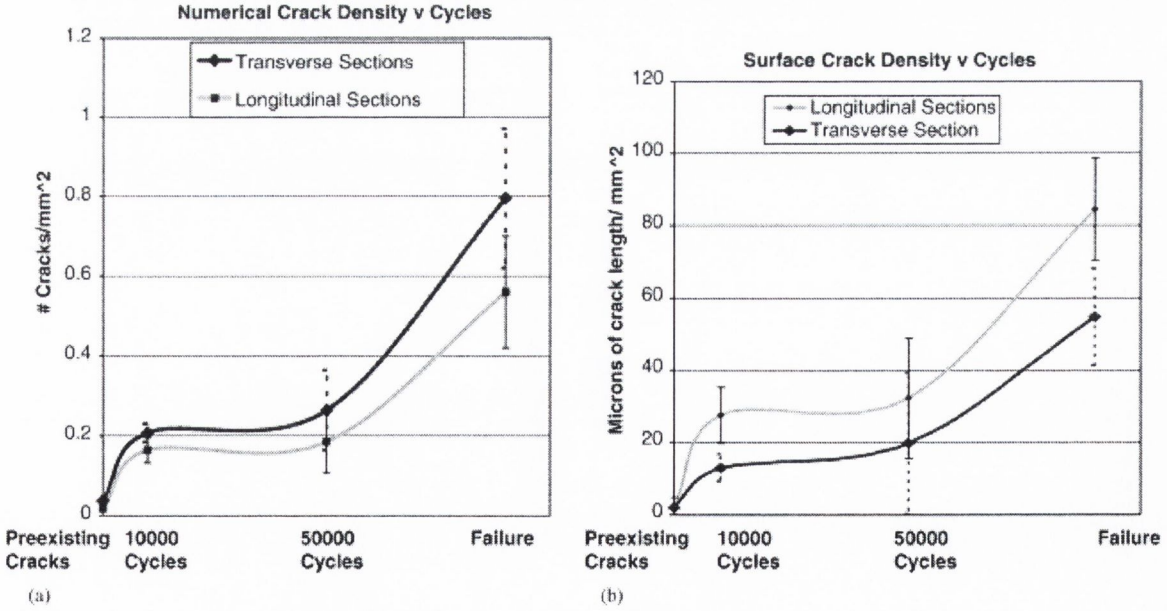

Fig. 1.12 Microcrack accumulation during the course of testing (a) Cr.Dn versus time (b) Cr.S.Dn versus time (O'Brien et al., 2003)

Figure 1.12 shows the variation in microcrack densities, 'Numerical Crack Density' (number of cracks occurring per mm^2) and 'Surface Crack Density' (μm of crack length

occurring per mm^2) as a function of the number of cycles. As can be seen from Figure 1.12, O'Brien et al. demonstrated that microcracks developed rapidly in the first 10,000 cycles, but microcrack density did not increase significantly again until after 50,000 cycles, with the development of new cracks almost suppressed during the intervening period. This is consistent with the pattern observed in composites as described in Section 1.9.1. Microcracks seen on transverse sections were more numerous than microcracks seen on longitudinal sections by a factor of two on average, however, despite being less numerous, cracks in the longitudinal direction were found to be longer than those in the transverse direction by a factor of 2.25 (O'Brien et al., 2003), with crack lengths and densities consistent with other sources (Schaffler et al., 1989; Burr and Martin, 1993; Burr and Stafford, 1990; Lee et al., 1998). Very few cracks were observed to propagate during testing, with only 8% of cracks labelled with two or more agents at different times, demonstrating that they were in fact growing during this time. These growing cracks were found to be longer than any other type of crack observed in their study.

The study by O'Brien et al. (2003) was the first to provide data of this kind, and whilst providing valuable information regarding damage accumulation and crack growth in compact bone, the study is limited to one fatigue stress, higher than that experienced during normal activities. Given the indications of a change in the fatigue behaviour of bone loaded in compression at around 4000με, it is therefore necessary to investigate damage accumulation at stress levels below that examined by O'Brien et al. as a change in the damage accumulation curves may be observed.

In light of these earlier studies, further testing at lower stresses is required to confirm the existence of a possible endurance limit for bone and to better describe the low-strain, high-cycle fatigue loading of bone, characteristic of physiological conditions.

1.9.6 Microcrack barrier concept

Osteonal bone can be compared to a composite material, where discontinuities within the material may cause stress concentration sites for crack initiation, but they also serve as barriers to crack growth which may slow down or even halt crack propagation. The concept of microstructural barriers has been discussed by a number of authors (Martin and Burr, 1989; Taylor and Prendergast, 1997; Taylor, 1998b; Akkus and Rimnac, 2001), whereby the critical stage in the fatigue process is not the initiation of cracks, but their propagation beyond microstructural sizes. Features of the bone matrix ultrastructure are essential in minimising the formation of larger detrimental cracks, whilst at the same time encouraging the formation of smaller cracks which are less likely to cause failure (Schaffler et al., 1994b). Microcracks form in interstitial bone and have been shown to halt at osteon boundaries (Boyce et al., 1998). Schaffler et al. (1994b) found that 80-90% of all microcracks were located in interstitial bone and O'Brien et al. (2004) observed that 80% of all microcracks were interstitial and did not penetrate secondary osteons.

In a study by Forwood and Parker (1989), rat tibiae were loaded in torsion at different strain levels, and numerous microcracks were observed crossing the bone cortex and were then arrested by osteons. However, at the highest level of loading, the deformation applied was sufficient to drive the cracks through the full thickness of the bone cortex. In the study by O'Brien et al. (2003), the majority of microcracks were found in interstitial bone and did not enter secondary osteons; microcracks were only found to enter osteons in the later, pre-failure region. Some cracks were also observed to encounter cement lines surrounding osteons but were deflected and then continued to grow.

This concept of a microstructural barrier to microcrack growth is also supported by the work of Corondan and Haworth (1986). Their work examined the morphology of fractured surfaces of bone and compared these with the morphology of sections adjacent to the fracture plane. Their work showed that bone tends to break where there are fewer osteons, similar evidence was also found by Evans and Riolo (1970), who showed that the more osteons present in bone, the greater its fatigue life.

In an examination of the micromechanics of osteonal cortical bone fracture, Guo et al. (1998) indicated that osteons in cortical bone can either promote or retard crack propagation in interstitial bone tissue, depending upon the ratio of the modulus of the osteon to that of the interstitial bone. A newly formed osteon will contain less mature mineral and thus is less stiff than the surrounding interstitial bone. Fracture mechanics suggests that these less stiff osteons will promote the growth of interstitial cracks toward the osteon increasing the likelihood of delamination at the cement line (Guo et al., 1998). This is because a crack oriented obliquely towards a soft material should be attracted in the direction of the interface (He and Hutchinson, 1989).

In the elderly, reduced bone remodelling activity results in an increased number of older, more highly mineralised osteons (Parfitt, 1993). Over time these osteons will lose their ability to promote, and may even retard crack propagation towards them when their stiffness exceeds that of the surrounding bone matrix. Even though the analysis indicates that a stiff osteon will reduce the stress intensity factor of the interstitial crack (Guo et al., 1998), it does not necessarily imply that a crack will be arrested by a stiff osteon. Instead the crack may be deflected from the interface if it is orientated obliquely towards the stiff material (He and Hutchinson, 1989), and thus cement line debonding is less likely to happen as only softer osteons are going to promote cracks towards the weaker interface.

Theoretical models suggest that in cortical bone, as microcracks increase in length, the crack growth rate decreases as they encounter barriers within the microstructure (Taylor and Prendergast, 1997; Taylor, 1998b). Microcracks in cortical bone have been observed to arrest at a crack length of 150 μm (Akkus and Rimnac, 2001), reasonably close to that suggested for the spacing between microstructural barriers of 100 μm (Taylor and Prendergast, 1995; 1997). This is the point where the crack growth rate is at a minimum and if growth continues, then the crack becomes larger and its growth will be determined by the average resistance of the material. Taylor (1997; 1998b) used a microstructural barrier spacing of 100 μm and the prediction from Taylor's model shown in Figure 1.13 demonstrates how crack growth rate decreases rapidly as crack length increases in the range 0 to 100 μm. Nevertheless, further increases in crack length result in a significant and potentially catastrophic increase in crack growth rate.

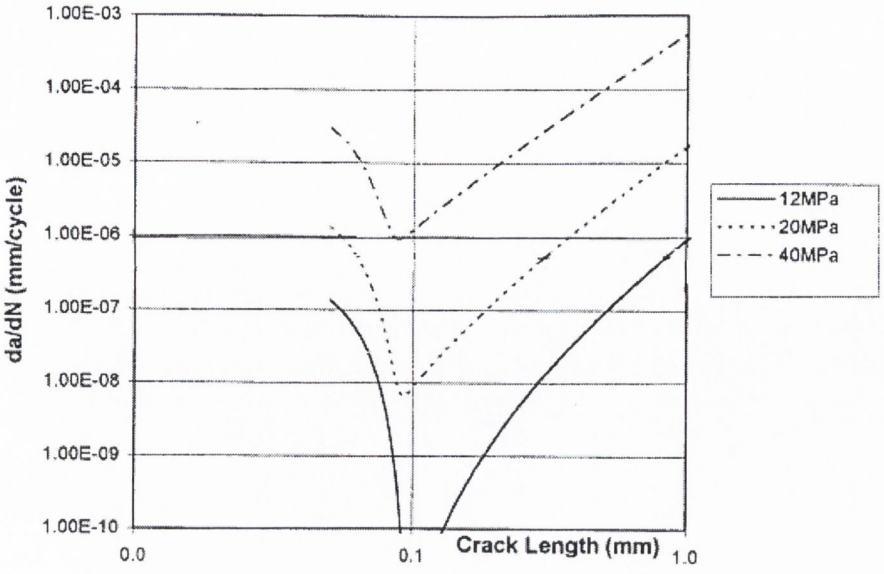

Fig. 1.13 Predicted variation of growth rate, da/dN with crack length for different stress ranges in compact bone (Taylor, 1997).

The foregoing would suggest bone is ideally suited to physiological strains, with its barriers to crack propagation and what appears be a threshold below which damage is limited. In addition, an effective remodelling process should repair the vast number of cracks that initiate in bone at low stresses. Damage accumulates when bone cannot repair this otherwise harmless damage, or when the rate of damage accumulation is faster than that which can be removed.

1.10 Creep behaviour of compact bone

Creep is referred to as the progressive deformation of a material at constant stress (Dieter, 1986). In materials undergoing creep, microdamage is observed to develop over time. In most engineering materials this is in the form of cavities, which accumulate within the structure of the material. These internal cavities first appear towards the end of the test and increase rapidly until failure. In addition to the formation of cavities, microcracks will also develop at grain boundaries where separation occurs. In a similar manner to cyclically loaded materials, the creep life of a material is also a function of load, time and temperature (Ashby and Jones, 1996).

Bone behaves as a viscoelastic material (Fondrk et al., 1988; Deligianni et al., 1994) due to its collagen matrix (Bowman et al., 1999) and, at low stress levels, the fatigue behaviour of bone is such that strains are completely recoverable. However, at higher stresses permanent strains develop and a constant creep rate is observed. The creep behaviour of bone is temperature-dependent with increases in temperature producing faster damage accumulation according to an Arrhenius relationship (Bowman et al., 1999). Experimental work has also indicated that a stress threshold exists (Fondrk et al., 1988). Tensile creep tests by Fondrk et al. (1988) showed that the total strain observed could be broken down into either elastic, linear viscoelastic, creep and permanent plastic components. The experimental work by Fondrk et al. identified a stress threshold; at stress levels below this threshold primarily linear viscoelastic behaviour is observed with time-dependent effects playing only a secondary role. At stress levels above this threshold, time-dependent effects dominate the material's response with the development of a steady state creep rate being observed. Two distinct creep regimes were identified; at lower stresses strains were completely recoverable and approached a limit for a given constant load. At higher stresses, permanent strains developed in the specimens with a constant creep rate for a given constant load.

Tensile creep tests conducted on cortical bone have suggested that a major portion of the inelastic strain is always recovered on unloading, however some does remain with the accumulation of creep strain increasing the material's compliance on subsequent loadings below the creep threshold (Fondrk et al., 1988). Fondrk's work suggests that a damage mechanism is responsible for this non-linear behaviour (Fondrk et al., 1988).

As found in other materials, the effects of creep in bone manifest themselves in the development of microdamage. The microstructural damage mechanisms proposed for cortical bone include cumulative damage within individual lamellae and shear damage between lamellae. This shear damage between lamellae can be found within osteons or between osteons and the surrounding interstitial bone (Lakes and Saha, 1979; Carter and Caler, 1983; Park and Lakes, 1986; Caler and Carter, 1989; Rimnac et al., 1991; 1993). This later mechanism can be represented by osteon pullout in tensile creep tests or cement line slippage in torsional creep tests. Torsional creep tests by Park and Lakes (1986) indicated that any slippage at osteon cement lines could not account for a large

portion of those creep strains which were observed experimentally, suggesting that an additional ultrastructural mechanism must also contribute to creep in bone.

The creep strain versus time curve for both trabecular and compact bone has been shown to present the three distinct regimes found in engineering materials (Smith and Walmsley, 1959; Sedlin, 1965; Knets and Vilks, 1975; Fondrk et al., 1988; Caler and Carter, 1989; Rimnac et al., 1993; Bowman et al., 1994). An example of this characteristic creep curve is shown in Figure 1.14.

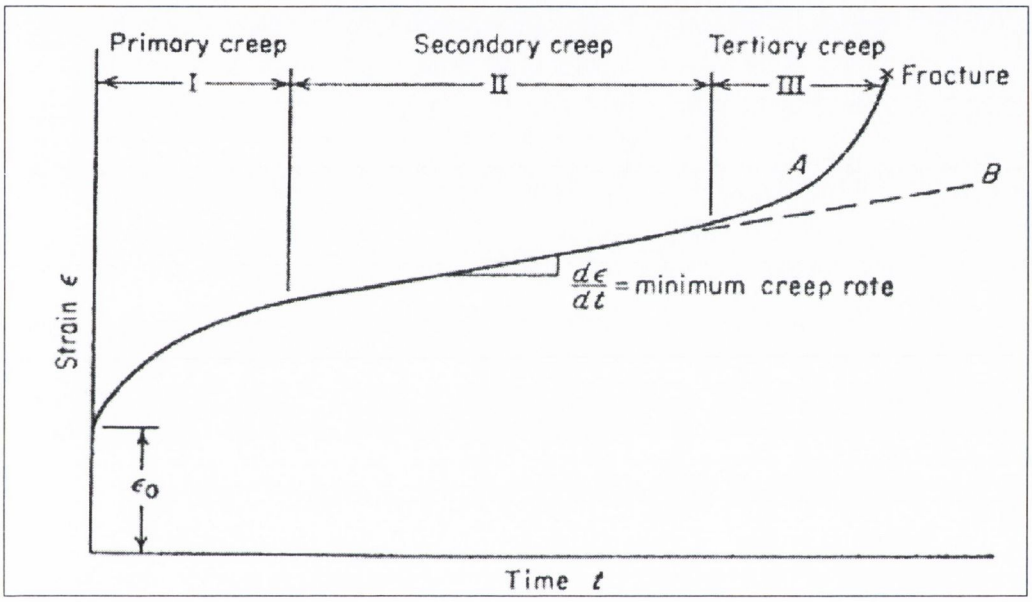

Fig. 1.14 Characteristic creep curve showing the three stages of creep (Dieter, 1986)

The creep process described by the above figure can be broken up into three constituent phases:

- Primary creep: following an initial, rapid elongation of the specimen, ε_0, the strain increases at a decreasing rate for a relatively short period of time.

- Secondary creep: the specimen essentially reaches a steady state, where an approximately constant creep rate can be observed. This lasts for a prolonged period of time.

- Tertiary creep: finally the strain rate increases rapidly until failure occurs. This region of the creep curve is normally characterised by a reduction in cross-sectional area either as a result of specimen necking or the development of void formation in standard materials

Early work by Andrade (1914) considered that the constant-stress creep curve represents the superposition of two separate creep processes, which occur after the sudden strain experienced from first application of the load. The first of these is a transient creep process with decreasing creep rate over time and to this is added a constant-rate viscous component. The result of these two effects is the characteristic creep curve as shown in Figure 1.14. On loading of a specimen an immediate strain (ε_o) is observed, however, despite the application of an applied stress below the yield stress of a material, not all of the initial instantaneous strain (ε_o) will be recoverable upon unloading, a small component of this strain is non-recoverable and therefore plastic by nature (Dieter, 1986).

Numerous power law relationships have also been established between the applied stress, time to failure and steady state creep rate (term given to the slope of the creep strain versus time curve in the secondary creep phase). The exception to this was work conducted by Rimnac and co-workers (Rimnac et al., 1993), who found no correlation between the stress and time to failure at any test temperature.

Many of the relationships described for bone are similar to those for conventional engineering materials such as metals (tensile creep) and ceramics (compressive creep)

(Garofalo, 1965; Cannon and Langdon, 1983; Dieter, 1986; Bowman et al., 1999). This permits bone behaviour to be described mathematically using standard engineering equations.

The general equation for time to failure as a function of the applied stress is shown Equation 1.5.

1.5

$$t_f = A\sigma^{-B}$$

where t_f is the time to failure, A is the creep coefficient and B is the creep exponent.

Experimental work by Bowman et al. (1994) showed a significant linear correlation between steady state creep rate, time to failure and normalised stress (σ / E_0, where E_0 represents the elastic modulus of the material). Most authors when measuring creep properties have adopted this technique of normalising the applied stress since it takes account of inter-specimen variations in density and microstructure, thus allowing comparisons between different studies on bone of different architectures.

The modified equation for time to failure using normalised stress is shown in Equation 1.6.

1.6

$$t_f = A\left(\frac{\sigma}{E_0}\right)^{-B}$$

There have been various arguments put forward for the cause of bone's creep behaviour, (Fondrk et al., 1988; Rimnac et al., 1993; Bowman et al., 1999) and work has shown that the creep rate of bone is significantly affected by the microstructure of the specimen (Rimnac et al., 1993). Rimnac suggests that permanent deformation during creep in bone is primarily due to damage mechanisms in the hydroxyapatite. In contrast, both Fondrk et al. (1988) and Bowman et al. (1999) suggest that collagen is responsible for the creep behaviour of bone. Bowman's analysis suggests that, because bone mineral has a crystalline structure, it will only creep when its homologous temperature (T/T_{melt}) is greater than 0.5 (Rimnac et al., 1993). Given that

hydroxyapatite melts at approximately 1600°C (Holden et al., 1995), it is therefore unlikely that hydroxyapatite will be responsible for creep at body temperature. Both Rimnac et al. (1993) and Fondrk et al. (1988) suggest that creep damage occurs beneath the level of osteons because of the uniformity of creep results from bones with different histological structures such as plexiform and laminar.

1.10.1 The influence of creep during fatigue

Various tensile fatigue studies have reported a 'strain drift' (Pattin et al., 1996), 'plastic strain' (Taylor, M. et al., 1999), and 'creep' (Carter and Caler, 1983; Zioupos et al., 1996) during cyclic loading. These remarks concern observations involving specimens of cortical bone which did not fully return to their original length after removal of the applied fatigue load. The magnitude of such unrecoverable strain is observed to increase throughout the test until failure occurs. Carter and Caler (1983) and Caler and Carter (1989) also established that creep contributes to fatigue failure and Cotton et al. (2003) examined whether the observed permanent strain in tensile fatigue tests was in fact the result of creep. Cotton et al. (2003) showed that the permanent strain observed in such studies fitted the functional form of creep from constant load tests, as observed by Fondrk et al. (1988). Plastic strain characteristics, similar to those observed in creep, were also noted in an examination of torsional fatigue of compact bone, where a plastic strain drift was observed with continued cycling (O'Reilly, 2002). Fleck and Eifler (2003) also showed that differences in the deformation behaviour and strength of specimens of equine bone tested under tensile and compressive loading resulted in cyclic creep deformation. However, the effects of plastic ratcheting may have been present in this study.

Carter and Caler (1983) modelled damage development accounting for both time-dependent and cycle-dependent damage accumulation. They showed that low-cycle fatigue is dominated by time-dependent creep damage, while high cycle fatigue is dominated by cycle-dependent fatigue damage. Their model predicts that in tension-compression fatigue tests, no creep damage will be observed and in zero-tension fatigue tests, creep will be the dominant damage mechanism. They later extended this model to zero-compression tests and suggested that under these conditions fatigue depends only

upon cyclic damage rather than creep damage. Fleck and Eifler (2003) also showed that, in tension compression fatigue tests with a zero mean stress, non–symmetrical deformation between the tensile and compressive parts of the loading cycle, coupled with differences in tensile and compressive strengths, resulted in cyclic creep effects. As in Carter and Caler's study (1983), Fleck and Eifler (2003) showed that compressive mean stresses inhibit cyclic creep effects, whereas tensile mean stresses lead to an increase in cyclic creep effects.

Studies of cortical and trabecular bone have also indicated a strain drift during fatigue (Carter and Caler, 1983; Pattin et al., 1996; Bowman et al., 1998; Moore and Gibson, 2003b). These studies identified that the stress-strain loops observed in fatigue progressively displaced along the strain axis, indicating that creep was also involved in the fatigue process. Moore et al. (2004) revisited this subject, comparing the measured translation of the stress-strain hysteresis loops with the creep strains that would be anticipated. Moore et al. (2004) measured the residual strain in fatigue tests on bovine trabecular bone and compared this with an upper bound estimate of the creep strain in each test. Their results indicated that the contribution of creep to the translation of the stress-strain loops was negligible in bovine trabecular bone. They also suggest that any strain drift in the stress-strain loops along the strain axis may be the result of microdamage formation.

Some unanswered questions regarding the creep behaviour of bone remain, in particular, its importance to the loading experienced *in vivo*. It is well established that both creep and fatigue can be responsible for the development of microdamage within bone, however the question as to which is the dominant factor at *in vivo* stress levels remains unclear and furthermore the interaction between the two mechanisms is not fully understood.

1.11 The influence of temperature on the creep and fatigue behaviour of bone

The effect of temperature on the mechanical properties of cortical bone over the range from room temperature to body temperature was studied by Bonfield and Li (1968) and Carter and Hayes (1976). The elastic modulus of bone has been shown to degrade approximately 0.5% per degree from freezing to body temperature. The viscoeleastic properties of bone have been shown to change dramatically over the upper portion of this range from room temperature to body temperature. Smith and Walmsley (1959) showed a linear relationship between bone bending modulus and temperature. In quasi-static tests of compact bone specimens at temperatures in the range 4.4 to 43.3°C, higher temperatures resulted in lower bending moduli. The effects of the difference between room temperature and body temperature are expected to be greater when considering fatigue or viscoelastic properties than when testing elastic or ultimate mechanical properties.

In a high temperature fatigue study, where specimens were tested as rotating cantilevers, it has been shown that a linear relationship exists between the log of the number of reversals to failure and temperature (Carter and Hayes, 1976). This was shown to occur across the physiological range of temperatures, where higher temperatures resulted in a decreased fatigue life. A temperature reduction of 24°C was shown to increase the fatigue life by a factor of three (Carter and Hayes, 1976). To date the study by Carter and Hayes represents the most in depth study of the effects of temperature on the fatigue behaviour of compact bone, but does not consider the formation of microdamage.

Based on the results of Carter and Hayes, Taylor (1998a; 1999) incorporated a factor for temperature in his stressed volume model for the fatigue strength of bone. Taylor showed that, at 10^5 cycles to failure, a reduction in the operating temperature from physiological temperature to room temperature had a multiplying factor of 1.16 on the fatigue strength of compact bone (Taylor, 1999).

In light of such effects, if a similar pattern exists *in vivo*, then maintaining reduced local temperatures in bone cyclically stressed during prolonged exercise may be essential in preventing fatigue fractures. Deep tissue and bone temperature in the limbs is known to be affected by environmental conditions such as footwear and clothing design and also type of exercise (Newburgh, 1949). Thermal gradients exist along the length of the limbs, and temperatures in the hands and feet may vary over a large range (Bazett, 1949). Foot skin temperatures of up to 43°C have also been recorded in subjects walking briskly in a warm environment (Robinson, 1949). Temperature gradients from the surface to the bone and deep tissues of the hands and feet however are small (Bazett, 1949). Therefore large surface temperatures will be reflected at the deep tissue level. When needle thermocouples were used to measure thermal gradients in hands with skin surface temperatures near 18°C, Bazett et al. (1948) found maximum deep tissue temperatures within 2°C of the surface temperature, indicating that environmental conditions will affect bone temperature and potentially impact its fatigue strength *in vivo*.

In a series of creep studies by Bowman and co-workers (Bowman et al., 1996b; 1999), creep tests conducted on specimens of demineralised bone showed similar creep activation energies and creep exponents to cortical and trabecular bone, providing quantitative evidence that collagen (demineralised bone) is the phase responsible for the creep behaviour of both cortical and trabecular bone. This supports qualitative evidence of the similarities between cortical bone and demineralised bone which both exhibit the three stages of creep prior to specimen failure. Further evidence of a collagen based creep mechanism has been demonstrated through the creep behaviours of various collagenous tissues, like tendon (Morcio and Ciferi, 1969; Cohen et al., 1976), skin (Vogel, 1997) and articular cartilage (Mow et al, 1980; Simon et al., 1984; Schmidt et al., 1990). Both cortical and trabecular bone contain type I collagen, and there are other type I collagenous tissues that have been shown to present the three characteristic stages of creep.

The hydrothermal shrinkage of collagen fibres and tissue is recognized as a characteristic of collagen, the principal constituent of connective tissue (Gustavson, 1956). Mammalian type I collagen fibre, demonstrated in the form of skin or tendon,

has been shown to contract sharply by about one third to one quarter of its original length at a given temperature within the range 60° to 70°C (Gustavson, 1956). This occurrence is due to denaturation of collagen molecules that are covalently cross-linked within the fibre network.

Figure 1.15 shows the shrinkage curves of tendon specimens immersed in water of different temperatures. The highest temperature shown is 62°C, a few degrees below the temperature of instantaneous shrinkage. The figure shows the considerable effect of a few degrees variation in the temperature; a two-degree rise in the temperature reduces the time required for shrinkage by half. The curves indicate that the process of shrinkage is a rate-dependent process and that a true shrinkage temperature does exist from the thermodynamic perspective. Pelt with an instantaneous shrinkage temperature of 65°C has been shown to observe slight shrinkage if kept for a few hours in water at 55°C. This slowly occurring contraction and collagen denaturation is described as 'incipient shrinkage' (Pankhurst, 1947).

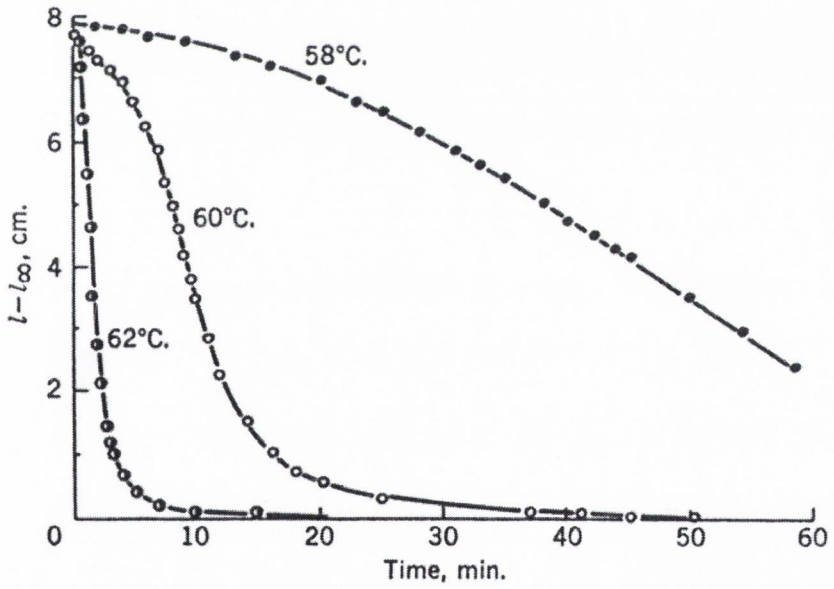

Fig. 1.15 The effect of temperature over time on the shrinkage of tendon collagen (Weir, 1949)

The effects of temperature on collagen can also be observed in the mechanical properties of the material. Yoshini (2000) demonstrated during experiments on demineralised cortical bone that, at circa 60°C, a reduction in both Young's modulus

and critical stress intensity factor (K_c) can be observed. It was hypothesized that the observed reductions were a direct result of collagen denaturation, since circa 60°C the collagen's triple helix structure would shrink to a coil-like configuration where the strengthening 'cross-link' structure brakes and the collagen becomes weaker. At temperatures between 20° and 60°C there were almost no differences in the K_c figures. However, K_c decreased as the temperature reached 70°C where a significant difference could be observed. Yoshino's work showed that temperature had a significant effect on the Young's modulus of demineralised bone at all temperatures, however Young's modulus dropped significantly circa 60°C.

The denaturisation behaviour of bone has been described as occurring at temperatures in the region of 55°C (53-55°C, Bonar and Glimcher, 1970; 52-55°C, Glimcher and Katz, 1965). Bowman et al. (1999) demonstrated that bovine cortical bone denatured at approximately 56°C (mean = 55.7°C, SD = 1.2°C), this was indicated by the onset of axial shrinkage. The maximum amount of shrinkage was approximately 24% (mean = 23.5%, SD = 2.5%).

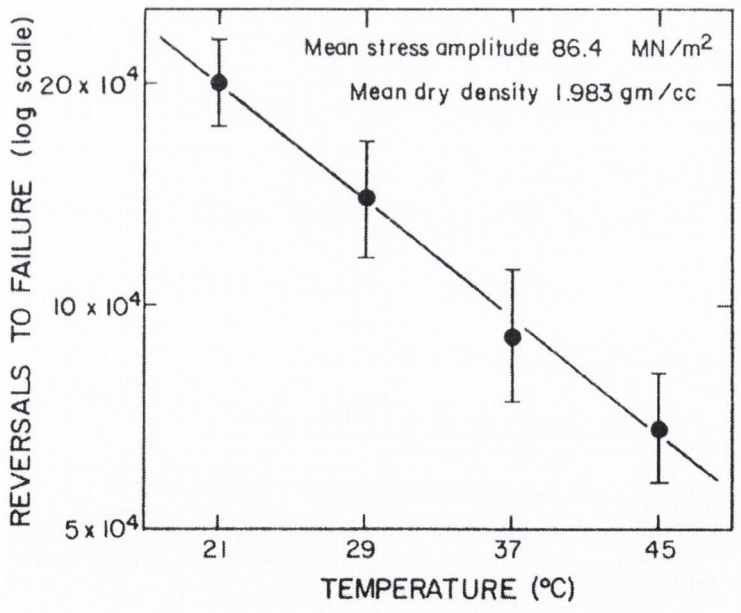

Fig. 1.16 The effect of temperature on the fatigue life of compact bone (Carter & Hayes, 1976)

Studies of mechanical properties of bone at room temperature have been and continue to be performed, due to the difficulties surrounding testing bone at body temperature.

However in order to truly understand the in vivo fatigue behaviour of bone, further testing at elevated temperatures is required to quantify the effects of temperature on microdamage formation, something not previously examined by the literature. Any such testing does need to pay close attention to the effects of temperature on bone's collagen structure and avoid the potential for bone denaturisation.

1.12 Clinical Relevance

The fatigue properties of bone are clinically relevant as bone is subjected to a range of time varying loads throughout life. During normal activities, human bone is subjected to a range of different loading regimes. These loads are responsible for generating fatigue microdamage, which is proportional to the load, number of cycles and temperature. Section 1.6 discussed how bone remodelling repairs such damage in normal healthy bone, however, should such damage be allowed to accumulate, then the strength of bone will be reduced, ultimately resulting in failure (Kaplan et al., 1994).

The accumulation of bone microdamage can be considered to be a result of one of two possible mechanisms (Lee et al., 2000b).

- The development of microdamage at a rate greater than that which bone remodelling can remove it.
- A normal rate of damage production combined with an inadequate or defective repair process.

The clinical manifestations of these damage accumulation mechanisms are stress fractures and fragility fractures respectively.

Orthopaedic surgeons refer to what appears to be fatigue fractures as 'stress fractures'. These fractures generally result from stresses imposed by the muscular system during locomotion. Muscles tend to adapt more quickly than bones in response to increased loading; this discrepancy between the strength of muscles and bone will cause deformation, microdamage and eventual fracture of the bone. These are commonly

found in new military recruits and athletes, due to the high levels of loading experienced by these groups. The clinical symptom of fatigue fracture is pain developing in a bone, when activity has been increased above normal. Living bone has the ability to repair fractures, and so the normal treatment for stress fractures is usually cessation of the activity, which allows time for the bone to heal.

Fragility fractures are fractures that occur as a result of minor traumas that occur during normal activities that would not normally cause failure in a healthy young adult. They are indicative of poor bone quality and quantity. Microdamage accumulation will lead to a reduced bone quality and coupled with a potential reduction in bone quantity, this can result in failure from what might normally be minor incidents. The cost of fragility fractures in real terms is significant, in the United States 280,000 hip fractures (American Association of Orthopaedic Surgeons, 1993) with a mortality rate of 10 – 20% (Riggs and Melton, 1995) occur each year, with a fiscal cost associated with all fracture types of $10 billion. It is estimated that one in two women and one in four men over age 50 will have an osteoporosis-related fracture in her/his remaining lifetime (National Osteoporosis Foundation,2004).

It has been shown that microdamage accumulation increases with age, (Schaffler et al., 1994a; 1995) demonstrating that the repair process in the elderly is inadequate, making the elderly more susceptible to fragility fractures (Carter and Hayes, 1977b; Keaveny et al., 1994a). With an aging population, hip fractures are predicted to increase from an estimated 1.7 million in 1990 to 6.3 million in 2050 (Melton, 1996).

The development of metabolic bone diseases may be the result of alterations to the organic matrix, the mineral phrase, the cellular processes of remodelling, the endocrine system, and nutritional and other factors which affect skeletal and mineral homeostasis (Mellors, 1999). Such disorders can be the result of hereditary or acquired conditions and will generally affect the entire skeleton. Acquired metabolic bone diseases are more common and these include: osteoporosis, osteomalacia, the skeletal effects of hyperparathyroidism and chronic renal failure (renal osteodystrophy), and osteitis deformans (Paget's disease of the skeleton) (Mellors, 1999). Osteopenia is a descriptive term for a loss of bone density observed radiologically, and this may be local or generalised. There are many causes of generalised osteopenia, these include:

osteoporosis that is unrelated to other diseases, endocrinopathies (hypercortisolism, hypogonadism, hyperparathyroidism, hyperthyroidism), deficiency states (rickets/osteomalacia, scurvy, malnutrition) neoplastic diseases (multiple myeloma, metastatic carcinoma, leukaemia), chronic renal failure, drugs (glucocorticoids, heparin, alcohol), and hereditary diseases (osteogenesis imperfacta, homocystinuria). Some of the more relevant diseases are discussed in greater detail in the following sections.

1.12.1 Osteoporosis

Osteoporosis is a condition found in patients that is responsible for a reduction in bone mass sufficient to compromise normal function. The rate of bone formation in most osteoporotic subjects is at the normal adult level although the bone resorption rate is often high. Osteoporosis is characteristic of thinning of bone trabeculae, eventually these trabeculae will disappear completely leading to decreased bone strength. The bone that remains, although diminished in amount, is normally mineralised and lacks the wide osteoid seams, which are typical of osteomalacia and other disorders of bone mineralisation. In osteoporosis there is a loss of bone structure. The bones become brittle and break with minimal trauma. The distinction between normal osteopenia of aging and osteoporosis is a matter of degree and the World Health Organisation (WHO) defines osteoporosis as a bone mineral density more than 2.5 standard deviations below the mean peak value in young adults (WHO study group, 1994). Osteopenia is a bone density that is less than normal, but not as much as 2.5 standard deviations below normal bone density. Osteoporosis is most prevalent in postmenopausal and aging white females, less common in white males, and rarely found in black males or females. It is currently estimated that 29% of women between the ages of 45 and 79 can be considered osteoporotic, where the increase in incidence after menopause has been linked to a decrease in the production of oestrogens. In men of the same age the incidence of osteoporosis is estimated at 18%.

Bone replacement in the form of remodelling occurs throughout a person's life through the coordinated actions of bone formation and resorption through the actions of osteoclasts and osteoblasts. During human growth the total bone mass increases as bone formation exceeds bone resorption, once the body has reached skeletal maturity

bone mass remains constant for several years when bone resorption and formations are approximately equal. After the age of 40 to 50, bone mass starts to decline as bone resorption exceeds formation. The rate of decline is found to be greater in women than in men.

With continued reduction in bone mass the point is reached where the now fragile skeleton no longer meets the mechanical demands imposed upon it, the consequences of this are bone pain and microdamage. Ultimately the resultant decrease in bone mass leads to an increased susceptibility to fracture (Lane et al., 1996), with subsequent healing also impaired. However, researchers have suggested that bone mass is not the sole agent responsible for fractures (Ross et al., 1993) and various studies that have contrasted bone mass density in patients with and without fragility fractures have found an overlap between both groups (Melton et al., 1989; Kimmel et al., 1991). In light of such findings, the importance of bone quality in osteoporosis has been underlined (Lee, 1997).

A common treatment for osteoporosis is the inhibition of osteoclast activity by drugs called bisphosphanates. Their use has been shown to cause a significant increase in bone mineral density at all skeletal sites and a 48% reduction in vertebral fractures when compared to controls (Liberman et al., 1995). These drugs work by inhibiting osteoclast activity, thereby suppressing the resorption phase of remodelling. This will clearly prevent the loss of bone mass and will reduce the risk of fragility fractures. However, as described in Section 1.5, one of the functions of bone remodelling is to remove microdamage. Therefore the use of such drugs could lead to the accumulation of microdamage and reduction of bone quality despite maintaining bone mass. This could lead to additional fractures in the long term. Mashiba and colleagues (Mashiba et al., 2000) demonstrated this possibility when administering the bisphosphanates risedronate and alendronate. In their study two groups of healthy dogs were administered high doses of the drugs during the course of a year. This drug regime was found to suppress intracortical remodelling in both groups and significantly increased microdamage accumulation.

1.12.2 Rickets and Osteomalacia

Bone diseases, such as rickets in children and osteomalacia in adult life, are the result of a vitamin D deficiency. The effects of such deficiencies are insufficient bone mineralisation, resulting in a deficient amount of the mineral phase of bone and an excess of unmineralised osteoid (Mellors, 1999). This is the result of an inadequate mineralisation process unable to keep up with the new development of osteoid during bone formation and remodelling. In infants, such an inadequate mineralisation process affects not only bone but also epiphysial cartilage in areas of endochrondal ossification. This can result in growth disturbances, skeletal deformities and a risk of fractures (Mellors, 1999).

1.12.3 Hyperparathyroidism

Hyperparathyroidism most commonly arises from a tumour of the parathyroid gland. This disorder results in abnormally high serum calcium levels and calcium salts in the skeleton become mobilised and bones weakened. Over-production of parathormone results in resorptive losses and fibrous replacement of bone due to excessive osteoclastic activity compared with osteoblastic activity.

1.12.4 Paget's Disease of Bone

Paget's disease is a chronic skeletal condition, which may result in one or more regions of the skeleton with deformed or enlarged bones. Paget's disease of bone is a localized disorder of bone remodelling. Increased numbers of enlarged osteoclasts initiate the process at affected skeletal sites and the increase in bone resorption is followed by an increase in new bone formation, altering bone architecture (Siris, 1998). Evidence of a genetic risk for Paget's disease with a specific gene on chromosome 18q has been identified (Fraser et al., 1997; Siris, 1998). This condition results in bone being broken down more quickly and when replaced, the bone that replaces it is softer than normal. The clinical effects of this condition are pain in the affected area, bone deformity and increased risk of fracture. Bones affected by Paget's disease can also become shorter as

these softer bones can bend under mechanical load. If the skull is affected patients may complain of headaches and hearing loss.

The study of damage accumulation during normal activities is therefore vitally important to the assessment and treatment of a variety of bone conditions.

1.13 Microdamage Detection

Various techniques have been used to detect microdamage in bone. Morris and Blickenstaff (1967) detected microdamage using radiological techniques, Carter and Hayes (1977b) and Schaffler et al. (1989) used reflected light photomicrography and Chamay and Tschantz (1972) examined overloaded ulnae using scanning electron microscopy. Schaffler et al. (1994b) also experimented with the technique of using heavy metals and back-scattered electron microscopy. In addition, laser scanning confocal microscopy (LSCM) has been used to study microdamage in compact bone (Zioupos and Currey, 1994), trabecular bone (Fazzalari et al., 1998) and also dense arrays of ultra-microcracks in human tibiae (Boyce et al., 1998). Zioupus et al. (1994) also used acoustic emission to detect microdamage, and Akkus et al. (2000) more recently related the types of acoustic emission to particular types of microcrack damage. Using the energy of such emission events microcracking was quantified such that the highest energy was associated with the growth of a major crack.

However, the most widely used method of microcrack detection has been the use of transmitted light microscopy, following staining of specimens in basic fuchsin (Frost, 1960; Burr and Stafford, 1990; Burr and Hooser, 1995). Burr et al. (1985) confirmed the fuchsin staining of microcracks using both transmitted white light and scanning electron microscopy. Lee et al. (1998) also showed that fuchsin stained microcracks prepared using the bulk-staining technique can also be viewed using fluorescence microscopy. This was found to simplify microcrack identification by screening out unstained or partially stained microcracks. This is consistent with other work suggesting that fluorescence against a dark field background aids the identification of microcracks (Zioupos and Currey, 1994; Zioupos, Currey and Sedman, 1994; Zioupos et al., 1996).

All methods of microcrack detection record the presence of microdamage at a particular point in time. In order to differentiate between pre-existing and test-induced damage and subsequently label microcrack growth, a series of site-specific stains are required. As previously described, bone is made up of collagen and hydroxyapatite crystals, thus microdamage in bone can be described as breaks in the hydroxyapatite matrix, which expose new surfaces and in doing so leave charged ions on the surface. As 55% of these ions are calcium ions (Landis, 1995), the development of microcracks will inevitably lead to calcium ions becoming exposed on the walls of these cracks. Chelating agents bind to exposed calcium ions and have been used as markers of mineralising bone seams *in vivo* (Rahn, 1977; Lanyon et al., 1982) and *in vitro* (Aaron et al., 1984). Stover et al. (1993) provided the first study of these agents being used to label microcracks. Lee (1997) further demonstrated the use of fluorochrome dyes as specific markers of microdamage. Lee showed that they are site-specific; since they bind to the surfaces of microcracks and their fluorescent properties give improved methods of crack detection. These agents bind to the exposed surfaces of the bone matrix where they form ionic interactions with vacant sites within the lattice, including sites of microcracking (Parkesh, 2003). Using a series of different coloured agents, Lee et al. (2000a) demonstrated that they could be used to distinguish between artefactual and test-induced damage during fatigue testing of trabecular bone. The presence of microcracks labelled with two or more dyes also indicated that cracks were growing during testing, although substitution of one dye for another made measurement imprecise.

Fluorescent dyes or fluorochromes can be viewed using microscopy techniques because such dyes will emit light of a known wavelength when they are excited by light of a different wavelength, with the emitted wavelength being longer than the excitation wavelength. Epifluorescence microscopy utilises this property by transmitting light at the fluorochrome's excitation maximum, this strikes the fluorochrome causing it to emit a fluorescence emission at its emission maximum. A barrier filter blocks the excitation wavelength from the eyepiece, thus maximising the fluorescence emission that can be observed.

O'Brien et al. (2002) recently improved upon the method of crack detection developed by Lee et al. (2000a) and applied a series of fluorochrome agents to cortical bone. The

aim of their study was to determine the optimal sequence of application and the optimal concentrations, which allowed the different agents to fluoresce equally brightly using UV epifluorescence. Following chemical analysis using ion chromatography and subsequent validation tests on bone samples, an optimum concentration and series of application was developed as shown in Table 1.4. Table 1.4 also details the colour of each agent when viewed under UV epifluorescence microscopy along with the excitation and emission wavelength of each fluorochrome.

Table 1.4 Dye sequence, concentration and wavelengths

Fluorochrome	Concentration	Excitation wavelength (nm)	Emission wavelength (nm)	Colour
Alizarin Complexone	0.0005M	580	625	Red
Xylenol Orange	0.0005M	377	615	Orange
Calcein	0.0005M	495	540	Green
Calcein Blue	0.0001M	375	435	Blue

The work by O'Brien and colleagues developed a sequential labelling technique, which enables the study of microcrack propagation during fatigue testing of bone without the problems associated with agents substituting one another.

1.14 Objectives

This study aims to describe the processes by which damage accumulates during creep and fatigue, the interaction between these two modes of loading and the effect of temperature upon them.

1.14.1 Principal Objectives

- To study microcrack accumulation as a function of the number of fatigue cycles in compressive fatigue at *in vivo* stresses. From these fatigue studies, the interaction between microdamage and bone histology will be investigated, examining the way in which microcracks initiate during fatigue and how they propagate through bone. By carrying out these fatigue tests it is hoped that, based on histological data, it will be possible to model microdamage accumulation at physiological stress levels. It is hypothesized that damage

accumulation at an *in vivo* stress levels will not follow the same pattern identified at higher stress levels, with a change in behaviour identified by a threshold stress range and a potential endurance limit for bone.

- To examine the effects of creep and quantify damage accumulation during a series of creep tests. The damage mechanisms associated with creep will be examined and compared with those observed during fatigue. From these tests it will be determined whether the process of creep is significant compared to fatigue in compact bone and which is the dominant failure mechanism at *in vivo* stress levels. Whilst it might be hypothesized that fatigue loading produces more damage than creep, the nature of creep damage and its contribution during fatigue loading needs further clarification, and this will be examined in this study.

- Having examined the effects of creep and fatigue at room temperature, the effects of temperature on damage accumulation during creep and fatigue will be examined. The effects of temperature on fatigue and creep life will be investigated and the influence of creep at elevated temperatures during compressive fatigue tests will be examined. With increased temperature it would be anticipated that an increased level of damage would be observed, increased temperature may also have an effect upon the relative contributions of creep and fatigue during loading and this will be considered.

2 Materials & Methods

In order to develop a repeatable and comparable testing method, a standardised test protocol was developed, based largely upon a procedure established by O'Brien (2000). This involved manufacturing identical bone specimens in such a way as to minimise machining, thus reducing the development of artefactual damage which could give inaccurate results.

In line with Keaveny et al. (1994a) and O'Brien (2000), cylindrical specimens were manufactured with a waisted central region of smaller diameter. This narrower region will experience higher stresses and will be weaker than the remainder of the specimen and is therefore where the majority of any induced damage should accumulate.

2.1 Manufacture of Specimens

More than 73 blocks of cortical bone were sectioned from the mid-diaphyses of bovine tibiae, using a band saw. These blocks of cortical bone were labelled according to the region of the bone from which they were harvested (i.e. medial, lateral, anterior, posterior). They were then placed in small steel boxes (50x25x25mm) and plaster of paris (Lennox Ltd.) was poured over them. The plaster was then allowed to harden and specimens were subsequently frozen. The bone sections were then cored using a special coring tool (Perenko Ltd.). This high-speed steel cutting tool permitted heat to be conducted away from the cutting surface, along the length of the tool. Specimens were chilled prior to coring to further reduce the effects of heat generation at the cutting surface.

The coring tool permits the repeated manufacture of cylindrical bone specimens, to a diameter of 7 mm. The steel boxes were gripped in a purpose designed vice grip. The vice grip was fixed to the lathe table of an NU Tool (NTL 400P, NU-TOOL, South Yorkshire, UK) centre lathe. Coring was carried out using this centre lathe at a speed of 400 rpm. The tool was slowly lowered into the bone section producing a specimen in excess of 35mm long. Coolant (Industrial cutting fluid, Perenco Ltd., Dublin) was applied to the specimen throughout the coring process in order to prevent the bone specimens from dehydrating, with all coolant being collected in the vice.

A CNC lathe (Denford Novaturn, Denford, UK) was then employed to waist the central section of the bone specimens. Each specimen in turn was placed in the lathe, and a computer numerical control program was performed to manufacture the waisted portion of the specimen, according to the dimensions outlined in the original drawing (Figure 2.1).

The CNC program turned the central section of the specimen to a gauge diameter of 5.25 mm, over a length of 7 mm, with an end radius of 5.56 mm. Once again, during all machining the specimens were kept hydrated and coolant was applied to all work piece and tool surfaces.

The techniques employed in manufacturing these specimens ensured that repeatable specimens were produced, with a good surface finish. After machining, all specimens were visually inspected to ensure that they were suitable for testing. Specimens were visually inspected for signs of any machine-induced damage and dimensional accuracy was verified using a vernier calliper. Cylindricity was also confirmed by slowly rolling the specimen along a level surface at eye level. Any specimen which did not meet these requirements was rejected at this stage, and did not proceed to testing. After machining, the specimens were stored in a freezer at -20°C until required.

Specimens were allocated to the appropriate test protocol so as to prevent two or more specimens from the same animal being tested under the same conditions. A total of 30 specimens were used in the room temperature fatigue work, all from different bovine tibiae. A total of 23 specimens from 13 different animals were allocated to the room temperature creep investigations and a further 20 specimens taken from a different sample of tibiae made up the high temperature creep and fatigue tests.

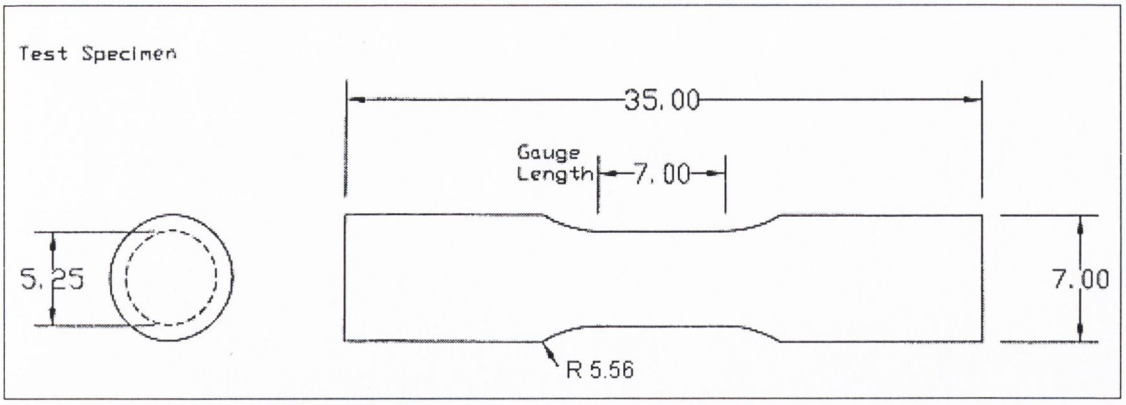

Fig. 2.1 Specimen drawing (dimensions in mm)

2.2 Mechanical Testing

2.2.1 Fatigue

Compressive fatigue tests were conducted at room temperature on an Instron servo-hydraulic testing machine, at one of three applied stress ranges. All tests were carried out at a frequency of 3 Hz, with a nominal stress range of 50, 60 or 70 MPa experienced at the narrower central region of the specimen. The ratio of minimum to maximum stress was set at 0.1 for all experiments at all stress levels. During testing, the Instron was operated in load control, where the applied cyclic load was maintained throughout, suitable trip limits were defined both for position and load in order to prevent excessive damage to the specimen after failure, and so as to remove the possibility of unintentionally loading the specimen outside of the chosen cyclic pattern. When the machine is operating in load control, any necessary adjustment in the position of the machine actuators is automatically carried out without any need for operator intervention. For those specimens tested at 50 and 60 MPa, an Instron model 8501 was employed and for those specimens tested at 70 MPa, an Instron model 8801 was used. This difference was due to machine availability and scheduling requirements.

Testing was conducted according to the layout shown in Figure 2.2. Brass end caps were attached to the specimens before testing, to facilitate loading without damage to the bone specimen (Keaveny et al., 1994a). These brass end caps were then located in aluminium end plates; providing a contact surface to the machine actuators.

All specimens were tested at one of the three fixed stress ranges, which were maintained throughout the test. After calibrating the Instron to a 'zero' load, the assembled test apparatus was slowly loaded to the desired mean load or set-point under position control prior to the start of testing; this ensured that the specimen was fully seated in the jig before switching to load control and the start of cyclic testing.

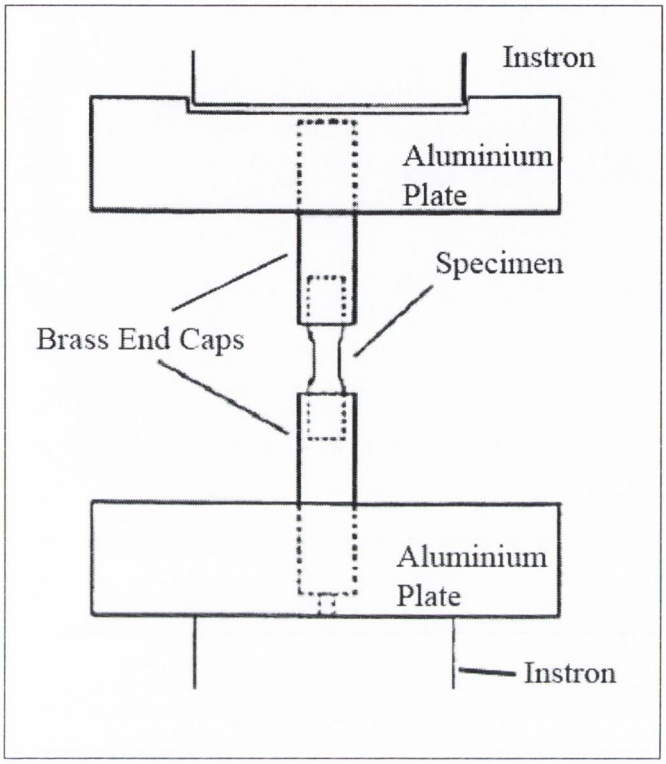

Fig. 2.2 Schematic of test rig used in experiments

2.2.2 Definition of failure in fatigue

Specimen failure can be described in a number of ways, it can be taken as complete specimen failure, a given specimen stiffness loss, or the appearance of cracks of a determined length. In an earlier study of compressive fatigue in compact bone (O'Brien, 2000), it was noted that 60% of specimens failed outright prior to the 10% loss in stiffness that had been established as representing failure of the specimen (Taylor et al., 1999). Consequently, in this study, it was decided that a more consistent and definitive measure of failure would be complete failure of the specimen rather than a measured loss of stiffness. This simplifies control of the Instron and removes the potential of artificial limit trips in the feedback control. Furthermore, only limited benefit would be obtained from attempting to maintain an intact specimen after testing, as previous studies have indicated many specimens would fail before reaching the 10% modulus reduction

2.2.3 Creep

Compressive creep tests were conducted at room temperature on an Instron (model 8501, Instron, Bucks, UK) servo-hydraulic testing machine operated in load control, at four different applied stresses.

Testing was conducted according to the layout described in the fatigue study (Figure 2.2). All specimens were tested at one of four fixed nominal stresses (120, 130, 140 and 150 MPa), maintained throughout the test. Using Equation. 1.5 and values for the creep coefficient and creep exponent as described by Caler and Carter (1989), it was predicted that, at a compressive stress level of 120 MPa, failure would occur within a time period of approximately 30 minutes. Based on this prediction, 120 MPa was chosen as the stress level from which to start creep testing as this also represented a stress level approximately twice that experienced *in vivo*. After completion of the creep tests within the range of stresses 120 to 150 MPa, a supplementary specimen was also tested at 88 MPa, as this represented the maximum stress experienced during a previous fatigue study (O'Brien et al., 2003). In each experiment, a 5kN pre-load was applied to the assembled test apparatus prior to application of the creep load, ensuring that the specimen was fully seated in the jig.

2.2.4 Definition of 'time to failure' in creep

The creep life or 'Time to failure' was determined for creep specimens as the time from the moment of first loading, until either catastrophic failure of the specimen, or until the test was interrupted by the user.

2.2.5 High Temperature

Compressive creep and fatigue tests were conducted at a controlled temperature of 50°C on an Instron (model 8801, Instron, Buckinghamshire, UK) servo-hydraulic testing machine. Fatigue testing was carried out at a stress range of 80 MPa and stress ratio of 0.1. Compressive creep tests were carried out at one of two fixed stresses. The stress levels chosen for these creep tests were 120 and 130 MPa and the applied stress was maintained throughout the test. These stress levels correspond to the lowest stress levels investigated at room temperature. Higher stress levels may demonstrate

instantaneous failure making comparisons between room and high temperature studies difficult.

The methods of mechanically loading the specimens for all high temperature tests were the same as described in Sections 2.2.1 and 2.2.3 in the two room temperature studies.

2.3 Data Analysis

Data from the Instron machine was fed directly to a personal computer fitted with an input/output data acquisition card (Amplicon PC30AT, Liveline Ltd.). This card acquired the output voltage from the Instron, which was then recorded using Labview 5.1 software (National Instruments Corp., Texas, USA). Having previously calibrated the output voltage, this could then be directly converted to an actual displacement in millimetres. The Labview software enables real time viewing of the acquired data, in addition to the output of data to a text file. This permitted the examination of output displacement in order to check for any anomalies that may have affected the results.

Throughout each creep test, different sample rates were used when recording data from the Instron machine. In the early stages of each test (elastic deformation and primary creep), a very high sample rate was used to record the rapid changes in displacement. However, within a relatively short period of time the specimen entered a steady state domain, where any change in displacement was slow and at a fixed rate. Hence once it had been established that the sample had entered this steady state domain, the sample rate was reduced to reflect the need for fewer data points.

The elastic modulus (E) for bovine compact bone (20.4 GPa), as quoted by Martin, Burr and Sharkey (1998), was used to normalise the applied nominal stress level during testing. This enables comparison with other material types loaded in a similar manner. Values of engineering strain were calculated for creep specimens from the movement of the Instron's actuator. Previous studies have shown this to be a reliable technique (Zioupos et al., 1996; Cotton et al., 2003) and it also avoids the problems associated with using a contact extensometer on a wet specimen, where slippage can often give erroneous results.

Creep strain versus time curves were plotted on linear-linear graphs for creep tested specimens. Based on the general shape of these curves, the steady state creep rate ($d\varepsilon / dt$) was defined as the slope of the creep strain versus time curve in the secondary creep phase, which was determined by a least-squares, best fit linear regression of the data in the most linear part of this region.

2.4 Histological Analysis

All specimens were initially labelled with a fluorochrome prior to testing in order to label pre-existing damage. A procedure was adopted whereby the specimen was first allowed to thaw and was then placed overnight in a vial of 0.0005 M Alizarin Complexone, in a vacuum desiccator held at a vacuum in excess of 50 mm Hg overnight. This procedure ensured adequate penetration of stain throughout the specimen. During each test, different coloured agents were applied to the specimen to label damage that accumulated during the course of the test; the pH of these dyes was optimised at physiological levels (pH 7.2-7.4). Adequate staining was achieved by surrounding the specimen in a small bath arrangement that was filled with the required dye. The established sequence for these dyes is: Alizarin Complexone (0.0005M) – Xylenol Orange (0.0005M) – Calcein (0.0005M) – Calcein Blue (0.0001M) (O'Brien et al., 2002) and each dye (all supplied by Sigma-Aldrich Ireland) was applied at different stages throughout the test. As the experiment progressed and dye changes were required, the previous dye was removed from the bath, and the bath and the specimen were rinsed with distilled water prior to refilling the bath with the subsequent dye in the sequence.

To confirm the ability of these agents to identify damage formed at different stages of testing, a simple scratch test was performed on discarded pieces of bone. A line approximately 5mm in length was made to the surface of the bone and stained with the first agent in the sequence for a period of time equal to 100,000 fatigue cycles. It was then removed from the solution and rinsed in distilled water. A second scratch of similar dimensions was then made alongside the first scratch; the sample was then placed in the second solution for another period of time also equal to 100,000 fatigue cycles. This procedure was repeated until all agents had been applied to the sample. This examination was repeated periodically due to the shelf life of these agents and also

prior to using a new batch of agent. These samples were then examined using UV epifluorescence microscopy, this simple test confirmed the ability of each agent to penetrate bone and identified that for the full dye sequence substitution of one dye for another should not be a problem.

2.4.1 Fatigue

Table 2.1 details the timing of dye application throughout all room temperature tests across all stress ranges considered.

At 50 and 60 MPa testing was halted with no sign of failure at 300,000 cycles. At 70 MPa five specimens were tested with the aim of halting the test at 300,000 cycles, thus enabling direct comparisons to be made with those samples tested at the lower stress ranges, however one specimen failed early after approximately 120,000 cycles. A further five experiments were conducted with the aim of cycling until complete failure of the specimen was observed. However, three specimens did not show signs of failure after approximately 2 million cycles and were consequently interrupted at this point. In these last five experiments specimens were not stained with calcein blue during loading, but were instead stained with calcein blue after testing for a period of time corresponding to 100,000 cycles. This procedure was adopted to prevent over-staining of the specimen with the final dye, during this intervening period between 300,000 cycles and failure the bath was filled with brine solution. The use of brine solution, pH balanced to physiological levels (pH 7.2-7.4), prevented bleeding of existing dyes from the bone whilst at the same time keeping the bone hydrated. Brine maintains a high ionic strength of the medium in which organic dyes are not soluble, therefore preventing them from leaching out of the bone specimen. This is further assisted by the crystalline layer formed by the brine solution around the bone hydroxyapatite. Table 2.1 details the timing of dye application throughout all tests for all stress ranges.

Table 2.1 Timing and application of fluorochromes – room temperature fatigue tests

Stress Range	Number of specimens	Alizarin Complexone	Xylenol Orange	Calcein	Calcein Blue
50 MPa	10	Prior to testing	0 – 100,000 cycles	100,000 – 200,000 cycles	200,000 – 300,000 cycles
60 MPa	10	Prior to testing	0 – 100,000 cycles	100,000 – 200,000 cycles	200,000 – 300,000 cycles
70 MPa	5 [(a)]	Prior to testing	0 – 100,000 cycles	100,000 – 200,000 cycles	200,000 – 300,000 cycles
70 MPa	5[(b)]	Prior to testing	0 – 100,000 cycles	100,000 – 200,000 cycles	200,000 - Failure

(a) 1 specimen failed after approximately 120,000 cycles

(b) 1 specimen failed after approximately 450,000 cycles, 1 specimen failed after approximately 1 million cycles, 3 specimens were halted after approximately 2 million cycles. For these specimens Calcein Blue was applied post testing.

Immediately following testing, all specimens were washed in de-ionised water and then stored at -20°C prior to sectioning and mounting.

All specimens were then examined for the presence of microdamage. A number of sections were taken from the gauge length of each specimen and slides were prepared according to the following protocol (Table 2.2).

Table 2.2 Preparation of ground sections of compact bone, hand grinding adapted from Frost (1958)

1. Specimen was placed in a small clamp and approximately 250 μm was cut using a diamond saw (Struers Miniton, Copenhagen, Denmark).

2. A sheet of No. 1200 silicon carbide paper was placed on a flat surface under running de-ionised water and the section was placed upon it. Another piece of paper was wrapped around a glass slide and the section was manually ground between the two pieces of paper. Grinding was performed in a circular fashion using light pressure.

3. This grinding was continued and periodically the thickness was checked using a micrometer until the required thickness (100-150 μm) had been obtained.

4. Specimens were agitated in 0.01% washing up liquid, placed in a Coors porcelain funnel with fixed perforated plate and washed in de-ionised water to remove debris.

5. Specimens were then air-dried and mounted using a mounting medium (DPX, Fluka Chemie, GmbH) under a glass cover slip.

(The use of de-ionised water throughout this procedure prevents displacement of fluorescent agents from individual microcracks and exposed bone surfaces)

Ground sections were then examined under epifluorescence microscopy using a Nikon Eclipse E800 microscope (Nikon, Tokyo, Japan) equipped with a Nikon DXM1200 digital video camera and connected directly to a Dell Dimension 4100 PIII personal computer (Dell Corporation, Ireland). Images of each whole section were captured using a 0.5x objective under transmitted white light. Cross sectional areas of these images were measured using Lucia Measurement 4.71 Build 74 software (Laboratory Imaging, Czech Republic). This software was used to acquire the images directly and came pre-calibrated to all lenses attached to the microscope. The default calibration was verified using a standard graticule prior to first use.

The ground sections were then examined and sections that were deemed of poor quality due to processing were discarded. Three sections were chosen at random from those remaining and were examined for microcracks, based on the criteria developed by Lee et al. (1998, 2000a).

Table 2.3 Criteria for identifying microcracks in bone (Lee et al, 1998, 2000a)

1. Fluorescence microscopy – green incident light (G – 2A filter block, λ=546 nm), x125 magnification: Candidate crack should be intermediate in size, being larger than canaliculi but smaller than vascular canals.

2. Fluorescence microscopy – green incident light (G – 2A filter block, λ=546 nm), x125 magnification: Candidate crack should have a sharp border, with fluorescence of fluorochrome agent being evident within the crack borders.

3. Fluorescence microscopy – UV incident light (λ=365 nm), x125 magnification: Candidate crack should be stained through the depth of the section.

Images of microcracks were captured and archived on the personal computer using Nikon's Act One software (Nikon, Tokyo, Japan). Images were then analysed and crack measurements were made using Lucia Measurement. The software works by recognising which microscope lens was used when taking the image and applying a calibration factor which enables the user to directly measure dimensional features using conventional units. For crack measurements the user traces over the crack of interest on the computer screen using the mouse pointer, the software programme then outputs the actual length in the selected units. In doing so, Lucia Measurement scales the number of pixels that have been traced through by the appropriate factor according to which microscope lens had been used to acquire the image.

In all specimens, one observer identified microcracks; removing the possibility for inter-operator variability, a lower limit for reliable crack detection was found to be in the region of 10-15 μm. The crack numerical density (number of cracks occurring per mm^2) and the crack surface density (total crack length per mm^2) were then calculated

for each specimen over time and tabulated accordingly. Microcrack surface density is particularly useful when damage is diffuse, as it is difficult to determine where one crack starts and another begins. Under these circumstances microcrack density may not give an accurate representation of the level of damage. Propagating or growing microcracks, i.e. cracks labelled with two or more dyes, were recorded separately to all other microcracks. Crack numbers and lengths were also recorded for each section, along with the period during which each crack was formed.

When the three specimens which were tested to around two million cycles at a stress range of 70 MPa were examined under epifluorescence microscopy, a very high intensity of background staining by calcein blue was observed. This made microcracks almost indistinguishable under the normal UV and green incident light filters. However, by switching to an FITC green filter with an excitation wavelength in the range of 465-495 nm, microcracks were distinguishable due to the increased contrast offered by this filter, which is designed for high signal to noise ratios. Unfortunately, because all cracks appear the same colour under the FITC filter, it was not possible to identify which stain had labelled individual microcracks. For this reason, microcrack density and length could only be measured at the end of the test in the three experiments concerned.

In specimens tested at 50 and 60 MPa, the location of each microcrack was examined and defined according to the following criteria. Those cracks that were solely in the interstitial matrix were termed 'interstitial'. Cracks that were located in the interstitial matrix and touched the cement line were classified as 'interstitial touching cement line'. Those that were interstitial but managed to penetrate the cement line were termed 'penetrating' and those that were entirely located within an osteon were termed 'osteonal'.

In any specimens where complete failure occurred, the main fracture crack and any microcracks directly associated with its propagation were discounted. Any microcracks in the vicinity of the main failure crack would form as a result of its rapid propagation through the specimen rather than as a result of damage accumulation from prolonged fatigue loading.

When compact bone is examined under UV epifluorescence microscopy, it appears light blue in colour. Newly formed secondary osteons appear much darker in colour than interstitial bone or primary osteons. For this reason, when examined using UV light, secondary osteons can be clearly identified. For each specimen examined at 50 and 60 MPa the number of osteons appearing in any given section was recorded and osteon density for each specimen was calculated in a similar manner to microcrack density.

2.4.2 Creep

Initially the aim was to apply a range of different coloured agents throughout the test as described previously, thus labelling the development of microdamage at various intervals. However, the inherent variability in the time to failure for creep specimens meant that applying a complete series of agents at regular intervals was not achievable. Only a limited number of specimens were stained with more than two dyes. Therefore while damage caused during testing can clearly be identified, only limited knowledge could be gained regarding its development over time. Without completing the full dye sequence, certain combinations of dyes have limited contrast; hampering differentiation between the stains. This was not identified in the simple scratch test.

Immediately following testing, all specimens were rinsed with de-ionised water and stored at -20°C prior to sectioning and mounting. A stress level of 130 MPa was chosen for histological studies, because of a relatively large range of values for time to failure and because all specimens tested at this stress level had been stained with at least two dyes (Alizarin Complexone and Xylenol Orange). A total of six sections were taken from each specimen, all specimens were divided in two and three sections were then taken from each half of the specimen. Slides were subsequently prepared according to the same protocol developed by Frost (1958), as used in the earlier fatigue tests.

Ground sections were then examined under epifluorescence microscopy using an Optiphot microscope with fluorescence attachment (Nikon, Tokyo, Japan.). Images of each whole section were captured at x10 magnification using transmitted white light and transferred to a HP PII Vectra personal computer (Hewlett Packard, Grenoble, France), using a CCD colour video camera (Optronics Engineering, Goleta, Ca). Cross

sectional areas of these images were measured using Scion Image^{TM} software (Scion Corporation, Frederick, Maryland, USA), previously calibrated by transferring an image of a graticule containing a 1 mm scale bar from the CCD camera to the PC.

The ground sections were then examined for microcracks, which were identified using the same criteria developed by Lee et al. (1998, 2000a), as used in the earlier fatigue tests.

Images of microcracks were captured, transferred to the PC and archived. After enhancing the image quality, each section was characterized by the crack numerical density (number of cracks occurring per mm^2) and the crack surface density (crack length per mm^2). Crack numbers and lengths were also recorded for each section. The location of each microcrack was defined as either osteonal or as interstitial, according to the criteria developed by Schiller (1994), (Table 2.4).

Table 2.4 Definitions of microcrack location in bone according to Schiller (1994)

Osteonal: Microcrack located completely within an osteon or crossing the cement line or concentric lamellae of an osteon.

Interstitial: Microcrack located in interstitial lamellar bone between osteons or located completely or partially on the cement line, but not actually crossing it.

2.4.3 High Temperature Creep & fatigue (histological analysis and temperature control)

Elevated temperature creep and fatigue tests differed from the room temperature protocols, by replacing the small bath receptacle with a temperature-controlled tank. The complete tank arrangement is described in Figures 2.3 and 2.4.

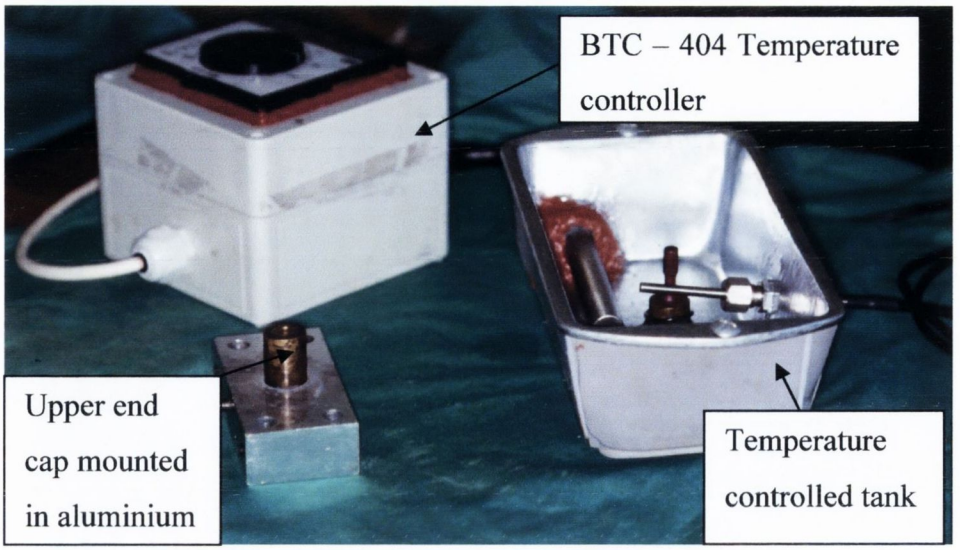

Fig. 2.3 Temperature controlled tank assembly

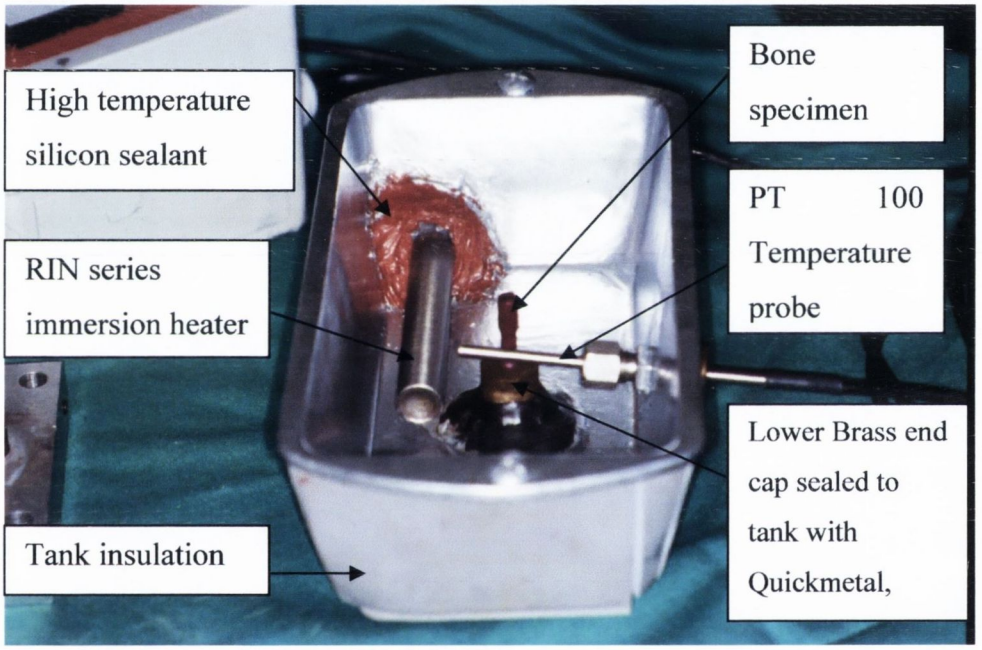

Fig. 2.4 Temperature controlled tank

The tank slides over the brass end caps previously illustrated in Figure 2.2 and the two are sealed using 'QuickMetal™' (Loctite® Hyso® 3463, Metal Magic Steel™ Stick, Henkel Loctite European Group, Munich, Germany) as shown in Figure 2.4. Once filled with the required agent, the solution was heated by the immersion heater, a RIN 250 screw plug immersion heater, (Omega Engineering Ltd, Manchester, UK). Control of the heater was provided by a BTC-404 temperature controller and feedback was provided by a PT 100 temperature probe (Rototherm Ltd, Dublin, Ireland). Correct location of the temperature probe is essential in controlling temperature immediately in

the vicinity of the bone specimen. Since measurement was made at the tip of the PT 100 probe, the probe's tip was located as close as possible to the bone specimen. Accuracy of the temperature controller enabled temperature control to within +/-1% of the full scale reading, this was done by switching the heating element on and off as required. The body of the tank was insulated on all sides with synthetic padding to prevent heat loss, a removable perspex lid was also fitted to the top of the tank in order to minimise the loss of dye due to evaporation.

The temperature controller was set to 50°C and throughout all high temperature testing the dye was maintained at this level for both high temperature creep and fatigue testing. Previous tests had been conducted at room temperature, approximately 22°C. Human body temperature is 37°C in a healthy individual; therefore if a noticeable difference exists between microdamage formation at room temperature and at body temperature, then increasing the ambient temperature even further should heighten the effects of temperature. In light of published studies (Glimcher and Katz, 1965; Bonar and Glimcher, 1970; Bowman et al., 1999) where it was shown that bovine cortical bone denatured at approximately 55°C, a maximum operating temperature of 50°C was chosen, where denaturisation of the specimens should not occur. This would enhance any development of microdamage whilst minimising the possibility of denaturation.

All high temperature fatigue specimens were stained with the complete dye sequence described in Table 2.1 (Alizarin Complexone, Xylenol Orange, Calcein, Calcein Blue). The timing of each dye application was selected to correspond with the sequence applied by O'Brien et al. (2003) in their room temperature fatigue study, also conducted at 80 MPa. All specimens were initially stained with Alizarin Complexone prior to testing in order to highlight any pre-existing damage. For the first 10,000 cycles specimens were fatigue tested in a Xylenol Orange solution, after 10,000 cycles the Xylenol Orange was removed from the temperature bath, the bath cleaned and the dye replaced with Calcein which had been pre-heated to 50°C. On reaching 50,000 cycles the Calcein dye was replaced with Calcein Blue until failure.

After completing five fatigue tests, the timing of dye application was adjusted to Xylenol Orange for the first 5,000 cycles, followed by Calcein until 10,000 cycles and

then Calcein Blue from 10,000 cycles until failure of the specimen. A further five fatigue tests were completed using this dye sequence.

Following the experience gained from the room temperature creep tests, the high temperature creep samples were stained with only two fluorochromes. In order to give the greatest contrast between pre-existing and text induced damage, creep samples were stained with Alizarin Complexone overnight in a vacuum dessicator prior to testing. They were subsequently stained with Calcein during the creep tests. The Calcein solution was maintained at 50°C throughout testing.

Immediately after testing, all specimens were rinsed with de-ionised water and stored at -20°C prior to performing any histological examination. To provide a direct comparison with the earlier creep experiments conducted at room temperature, histological analysis was performed on those high temperature creep specimens tested at 130 MPa. All high temperature fatigue specimens were examined for the presence of microdamage. For both creep and fatigue specimens, a number of sections were taken from the gauge length of each specimen and slides were prepared according to Frost's protocol (1958), as described in Table 2.2.

Ground sections were then examined under epifluorescence microscopy using a Nikon Eclipse E800 microscope (Nikon, Tokyo, Japan) equipped with a Nikon DXM1200 digital video camera and connected directly to a Dell Dimension 4100 PIII personal computer (Dell Corporation, Ireland). Images of each whole section were then captured using a 0.5x objective under transmitted white light. Cross sectional areas of these images were measured using Lucia Measurement 4.71 Build 74 software (Laboratory Imaging, Czech Republic).

These ground sections were then examined with any poor quality sections discarded prior to quantifying any microdamage present. From those sections that remained three sections were selected at random and examined for the presence of microcracks. This was carried out according to the criteria developed by Lee et al. (1998, 2000) in Table 2.3.

Images of microcracks were captured and archived on the personal computer using Nikon's Act One software (Nikon, Tokyo, Japan). Images were analysed and crack measurements were made using Lucia Measurement. The crack numerical density (number of cracks occurring per mm^2) and the surface crack density (total crack length per mm^2) were then calculated for each specimen and subsequently recorded. Crack numbers and lengths were also recorded for each specimen.

In the fatigue studies, where the development of microdamage over time was recorded, any propagating microcracks, i.e. cracks labelled with two or more dyes, were recorded separately from all other microcracks.

2.5 Pre-existing microdamage

Pre-existing microdamage is the term applied to all microdamage formed prior to the start of testing and covers both naturally occurring *in vivo* damage and artefactual damage created as a result of the machining process. In an earlier study, only one out of 54 pre-existing microcracks was found to propagate during testing and the specimen containing this crack did not have a shorter life than the mean, suggesting that *in vivo* or machine-induced microcracks did not affect the fatigue behaviour of the specimens (O'Brien et al., 2003). From their control study it was found that only 25.9% of all pre-existing cracks were *in vivo* microcracks. *In vivo* microcracks were found to have lower crack densities when compared to *in vivo* crack densities found in human bone (Burr and Stafford, 1990; Lee et al., 1998), however this should not be surprising as the samples of bone were taken from young cattle and any damage would be expected to be repaired during the animal's life within a short period of time.

After careful consideration it was deemed unnecessary to quantify any pre-existing damage as it is generally considered stable and the majority of all damage of this type is machine-induced and obviously not directly applicable to the study of fatigue microdamage. Nevertheless, damage of this type was labelled with alizarin, to prevent any such damage from being quantified as formed during testing. However, as O'Brien et al. (2003) demonstrated, the machining process developed less than 5% of all microcracks formed during their study and consequently this eventuality is unlikely.

2.6 Examination of creep fracture surfaces using SEM

A random specimen was taken from each stress levels and using scanning electron microscopy the creep fracture surfaces were examined. The advantage of the scanning electron microscope (SEM) is that it can provide very detailed 3-dimensional images at much higher magnifications than is possible with a light microscope. The principal behind the SEM is that electrons instead of light are used to form an image; electromagnets bend an electron beam which produces the image of the specimens surface. Specimens are placed inside the SEM, a vacuum is created and the specimens are bombarded with a beam of high-energy electrons. The beam of electrons is passed through a series of magnetic lenses, where the electrons can be focused with great accuracy. As the focused beam of electrons strikes the specimen this causes secondary electrons to be released from the specimen's surface. It is these secondary electrons that are used to form the 3-dimensional image of the specimen. By using electromagnets, an observer can have more control in how much magnification is obtained. The electron beam also provides greater clarity in the image produced and enables a far greater depth of field, thus allowing a large amount of the sample to be in focus at any one time. The SEM also produces images of high resolution, which means that closely spaced features can be examined at a high magnification enabling a detailed study of the fracture surface. The magnification employed in this work varied from ×25 to ×2500.

The Electron Microscope Unit in Trinity College Dublin made a Hitachi (model S-3500N) Variable Pressure Scanning Electron Microscope (VPSEM) available for use in this study. A requirement when using an SEM is that the sample's surface is conductive. Traditionally, this is done by coating the surface of the specimen with a very thin layer of a conductive material such as gold, however, since this could prevent further histological examination, this method would not be acceptable in this work. The problem was avoided because the Hitachi machine freezes the sample using a low vacuum and cold stage, thus making the surface of the specimen conductive.

3 Results

3.1 Fatigue

Ten fatigue tests were carried out at both 50 and 60 MPa stress ranges until a total of 300,000 cycles was achieved. All tests at 50 MPa were successful and no sign of failure was observed during the course of the tests. At 60 MPa, nine out of the ten tests were successful with technical difficulties preventing analysis of one specimen. Once again, all of these specimens were cycled until a total of 300,000 cycles was reached with no indications of failure during this time.

At 70 MPa five tests were conducted with the aim of achieving 300,000 cycles, thus making them directly comparable with those at 50 and 60 MPa. Four specimens were interrupted at 300,000 cycles with no indication of failure, and one specimen failed after approximately 120,000 cycles and was identified as an outlier due to the nature of damage accumulation. An additional five specimens were conducted at 70 MPa with the objective of continuing to failure to obtain a definitive cycles to failure at this stress range, in a manner similar to that achieved by previous studies. One specimen failed at approximately 450,000 cycles and one specimen failed at just over a million cycles. A further three specimens were interrupted at approximately 2 million cycles with no indications of failure.

In those specimens where failure was observed the main fracture plane occurred in the gauge length of the specimen at an approximate angle of 45° to specimen axis. When the specimens were sectioned and examined using epifluorescence microscopy, no evidence of substitution by one fluorochrome for another was found to occur.

In those specimens where testing was interrupted with no indication of failure, microdamage was generally concentrated towards the perimeter of the specimen, however the three specimens tested to approximately two million cycles demonstrated more widespread damage throughout the specimen.

The following images show examples of microcracks stained with different fluorescent agents.

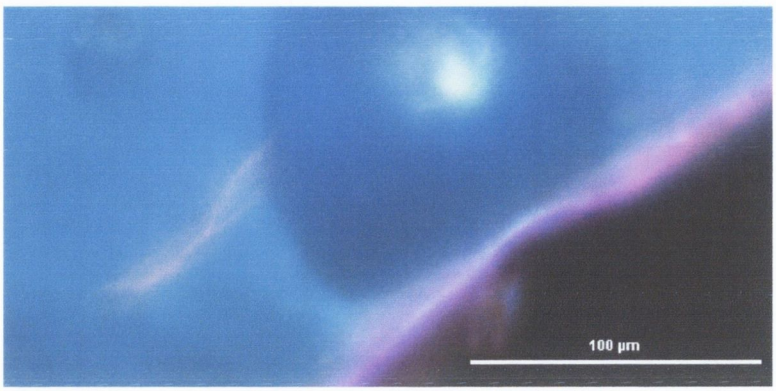

Fig. 3.1 Microcrack stained with xylenol orange, stopped at osteon cement line

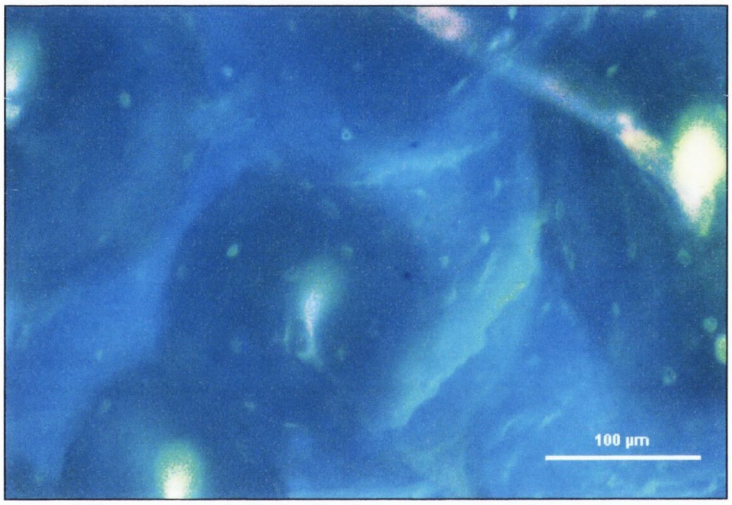

Fig. 3.2 Calcein stained microcrack in interstitial bone, arrested at cement line interface

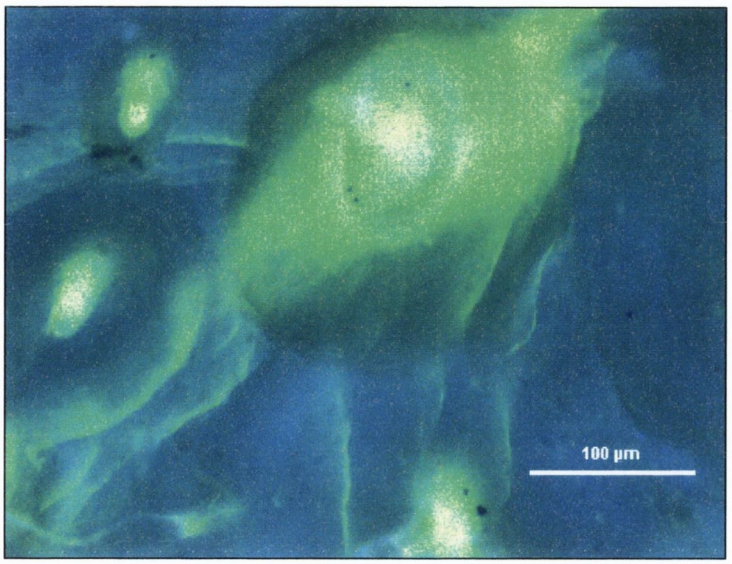

Fig. 3.3 Number of calcein stained microcracks

3.1.1 Microcrack densities

Figures 3.4 through 3.7 highlight the accumulation of microdamage over time for all experiments conducted at the stress ranges of 50 and 60 MPa. This information is presented in the form of numerical crack density (number of cracks occurring per mm^2) and surface crack density (µm of crack length occurring/mm^2), two standard measures used to describe the development and accumulation of microcracks. All figures start at 100,000 cycles since pre-existing damage was not quantified in this study. A total of 120 microcracks were measured at 50 MPa, 663 microcracks at 60 MPa and 667 (up to 300,000 cycles) microcracks at 70 MPa. Despite the number of individual microcracks measured at 60 and 70 MPa being of the same order, the number of microcracks per unit area was greater at 70 than 60 MPa, and this is demonstrated by the differences in numerical and surface crack density.

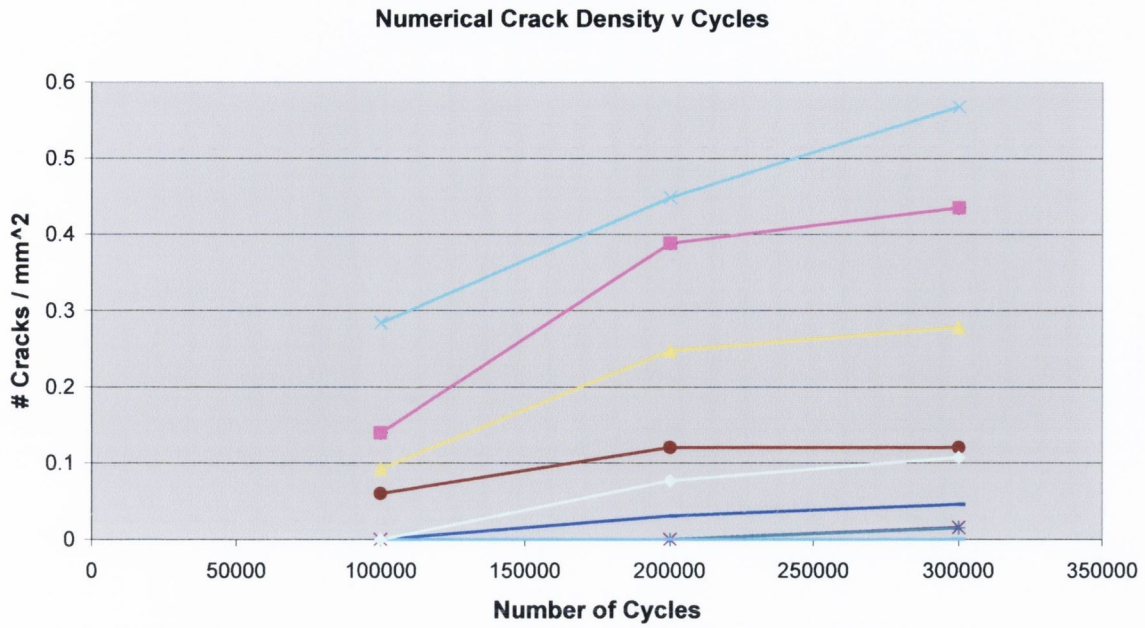

Fig. 3.4 Numerical crack density versus number of cycles - 50MPa

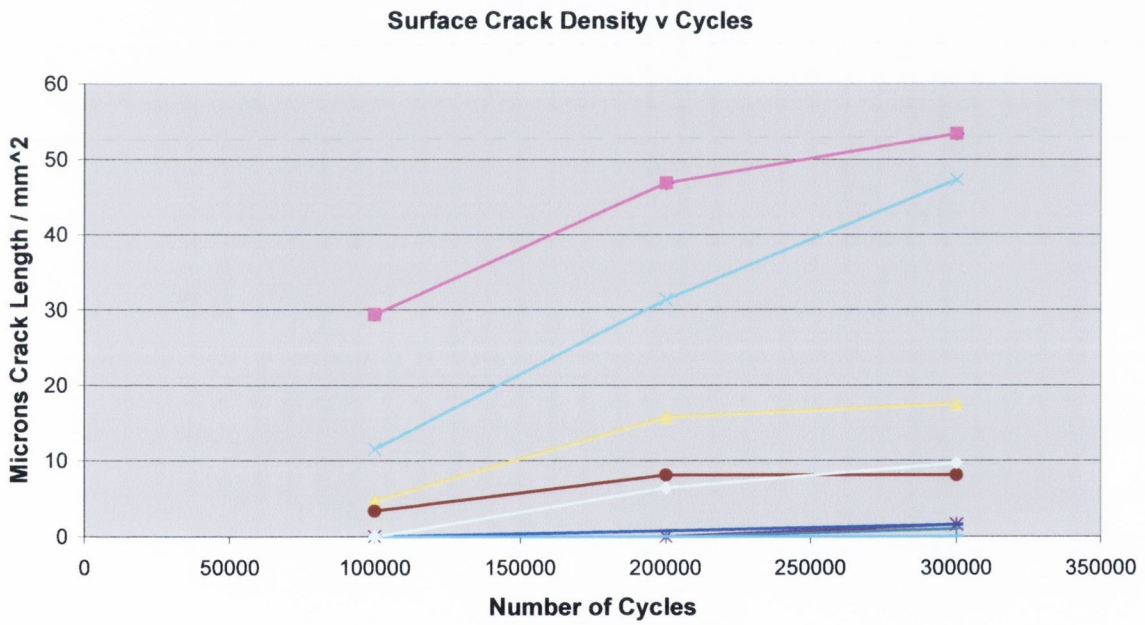

Fig. 3.5 Surface crack density versus number of cycles - 50 MPa

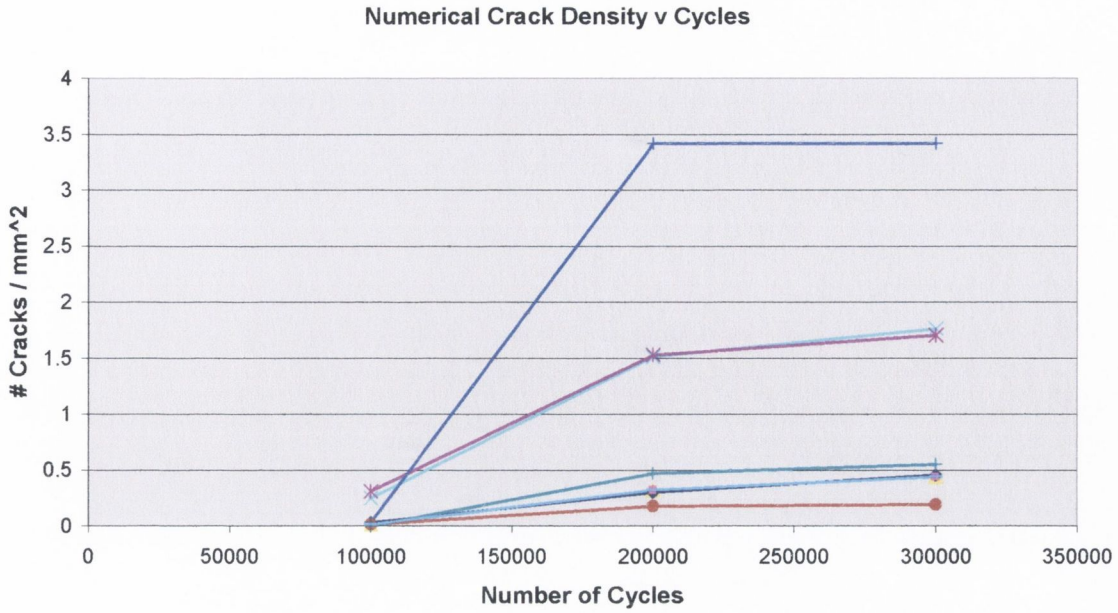

Fig. 3.6 Numerical crack density versus number of cycles - 60MPa

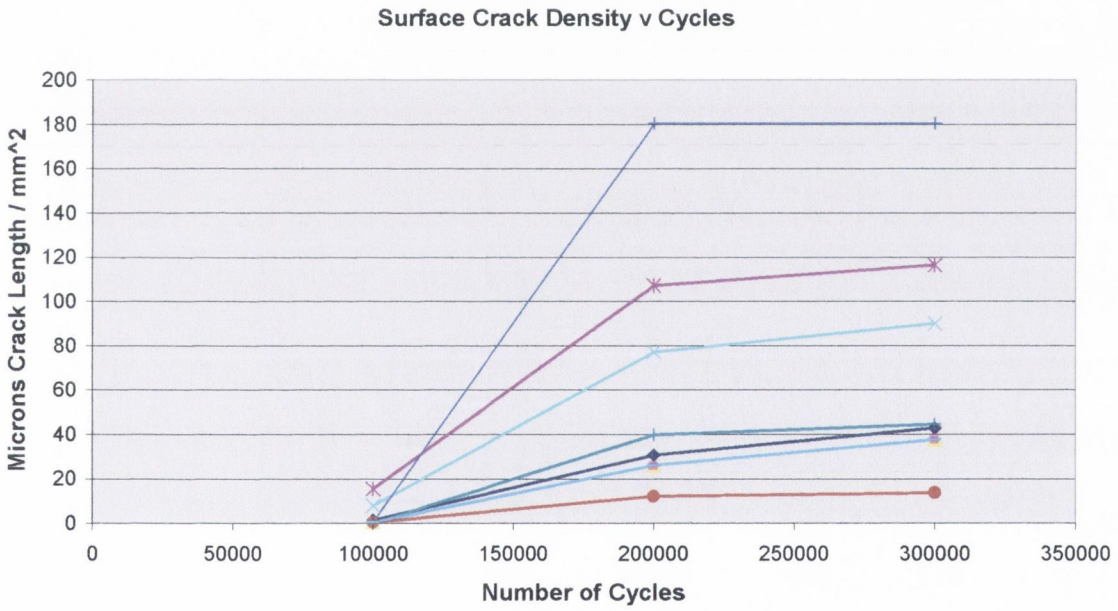

Fig. 3.7 Surface crack density versus number of cycles - 60 MPa

Figures 3.4 through 3.7 show that at the stress levels considered here, very few cracks form during the early part of the test up to 100,000 cycles, with the majority of cracks developing during the second stage of the test between 100,000 and 200,000 cycles. During the final third of the investigations very little further increase in damage is observed, with the curves all tending to level off as they approach what appears to be a steady state regime. Analysis showed that numerical crack density (2-tailed t-test; t=-

2.490, $p<0.05$) and surface crack density (2-tailed t-test; $t=-2.686$, $p<0.05$) were significantly greater at 60 MPa than at 50 MPa.

Figures 3.8 to 3.11 demonstrate the accumulation of microdamage over time for all experiments conducted at the stress range of 70 MPa, those curves marked with the letter 'F' identify failed specimens. This information is once again presented in the form of numerical crack density and surface crack density. Figures 3.9 and 3.11 present the same information as Figures 3.8 and 3.10, however they are rescaled to highlight damage accumulation during the first 1,000,000 cycles.

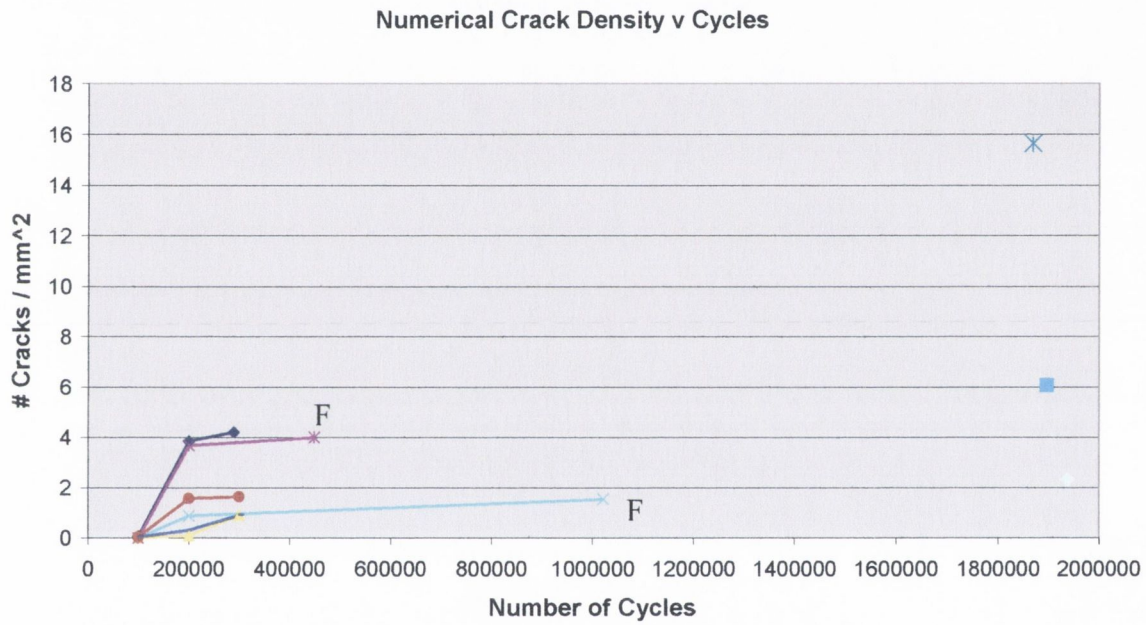

Fig. 3.8 Numerical crack density versus number of cycles - 70MPa

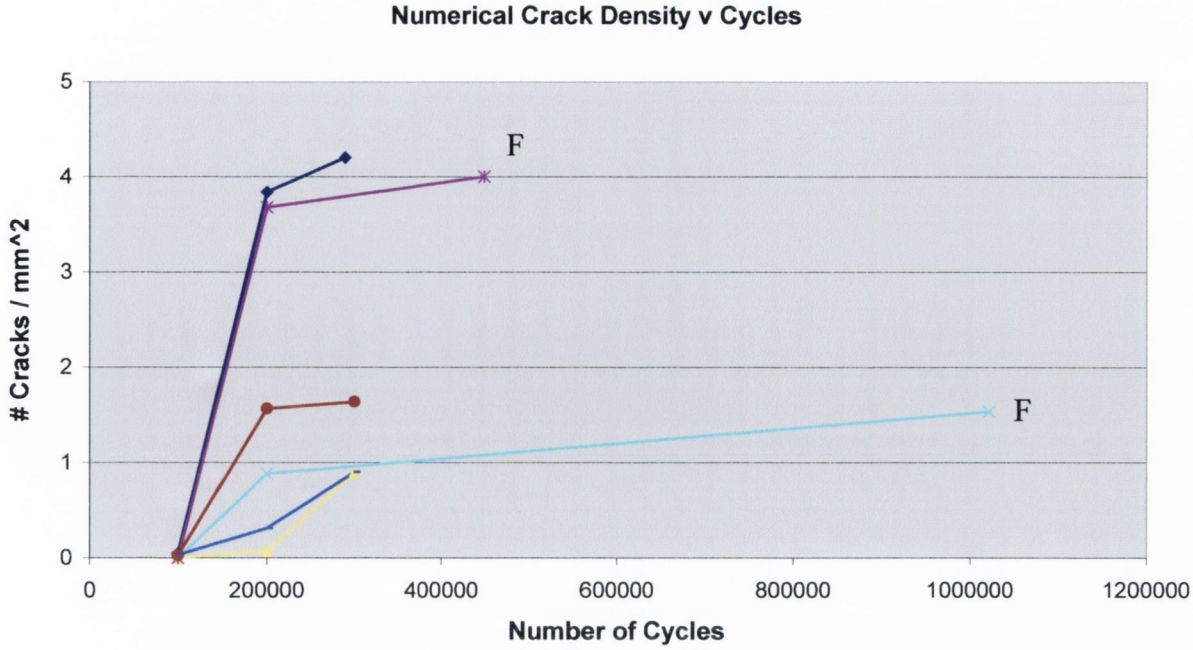

Fig. 3.9 Numerical crack density versus number of cycles - 70MPa (0-1,000,000 cycles)

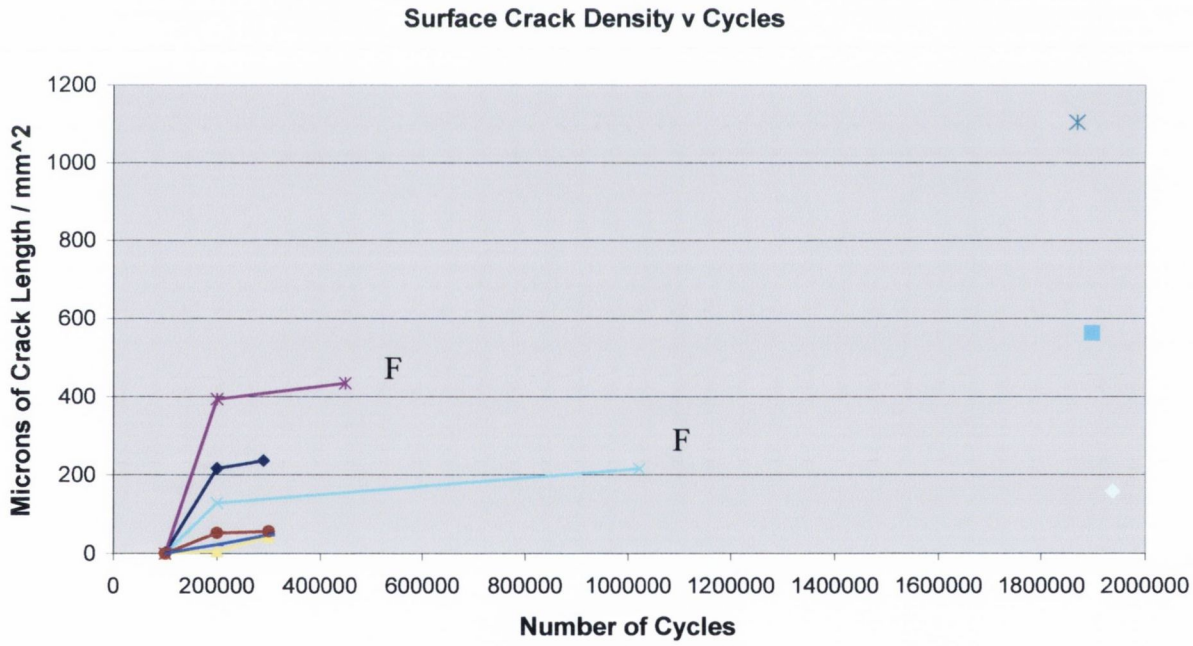

Fig. 3.10 Surface crack density versus number of cycles - 70 MPa

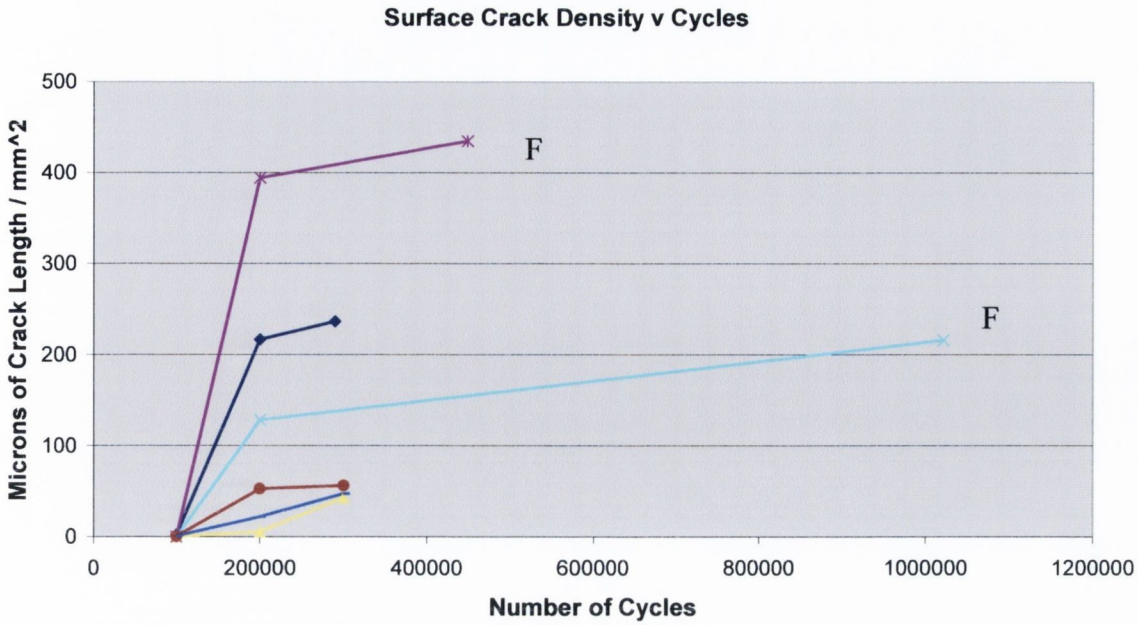

Fig. 3.11 Surface crack density versus number of cycles - 70 MPa (0-1,000,000 cycles)

Figures 3.8 to 3.11 once again show that initially very little damage formation is observed with the majority of damage initiating between 100,000 and 200,000 cycles, after which the rate that damage accumulates reduces considerably with limited increase in crack density after this time. On the right hand side of the graphs are the three individual points marked for those tests that were interrupted at approximately two million cycles, where the crack densities are only available at this point in time for those specific tests. Experimental data from specimens tested at a fatigue stress range of 70 MPa indicated that one specimen behaved erratically. After 100,000 cycles minimal microdamage was present in the specimen, however failure occurred very shortly afterwards with considerable microdamage occurring during the intervening period. In light of this unusual behaviour this specimen was considered to be an outlier and as such not included in any analysis.

Tables 3.1 and 3.2 show the mean cumulative microcrack densities during the course of the fatigue tests at stress ranges of 50 and 60 MPa.

Table 3.1 Crack Data - 50 MPa

Stage of crack formation	0 – 100,000	100,000 – 200,000	200,000 – 300,000
Num. Density (No./mm^2)	0.065	0.151	0.183
Standard Deviation	0.091	0.165	0.195
Surface Density (μm/mm^2)	5.74	12.96	16.54
Standard Deviation	9.26	15.87	19.61

Table 3.2 Crack Data - 60MPa

Stage of crack formation	0 – 100,000	100,000 – 200,000	200,000 – 300,000
Num. Density (No./mm^2)	0.079	0.943	1.066
Standard Deviation	0.116	1.063	1.047
Surface Density (μm/mm^2)	3.45	59.04	66.77
Standard Deviation	5.24	54.36	52.92

From the tests at 70 MPa mean crack densities can be calculated for 100,000, 200,000 and 300,000 cycles based on the five specimens tested to 300,000 cycles (omitting the identified outlier) and using linear interpolation to estimate crack densities at 300,000 cycles for the specimens which failed at 450,000 cycles and 1 million cycles. These two specimens were clearly in the steady state region of damage accumulation at this point and therefore reasonable estimates of damage accumulated during this period can be made. A total of six data points made up the calculation of mean crack density at each of the three stages.

Table 3.3 Crack Data - 70 MPa

Crack Stage	0 – 100,000	100,000 – 200,000	200,000 – 300,000
Num. Density (No./mm^2)	0.0173	1.725	2.068
Standard Deviation	0.020	1.659	1.397
Surface Density (μm/mm^2)	0.67	136.65	155.67
Standard Deviation	0.92	148.34	155.25

Table 3.4 describes the proportion of microcracks formed during each stage of testing and also those microcracks that were observed to propagate during the course of a fatigue test.

Table 3.4 Number and percentage of microcracks formed during each stage of testing

Stage of crack formation	0 – 100,000	100,000 – 200,000	200,000 – 300,000	Propagating
50 MPa	38, *31 %*	56, *47 %*	21, *18 %*	5, *4 %*
60 MPa	58, *4 %*	512, *81 %*	73, *12 %*	20, *3 %*
70 MPa	7, *1 %*	525, *79 %*	133, *20 %*	2, *< 0.3 %*

At 70 MPa, in all specimens where crack growth could be monitored (all specimens except the three tested to 2 million cycles), only two microcracks were identified as propagating or growing cracks, representing less than 0.3% of all cracks identified.

Figures 3.12 and 3.13 show the mean numerical crack densities and surface crack densities plotted as a function of time for 50, 60 and 70 MPa up to and including a total of 300,000 cycles. In both graphs the three curves show minimal damage accumulation during the first 100,000 cycles followed by an increase in damage accumulation between 200,000 and 300,000 cycles. The rate of damage accumulation during this

time is seen to increase as a function of the applied stress. After 200,000 cycles the rate of damage accumulation is seen to fall rapidly with a levelling off in the crack density curves.

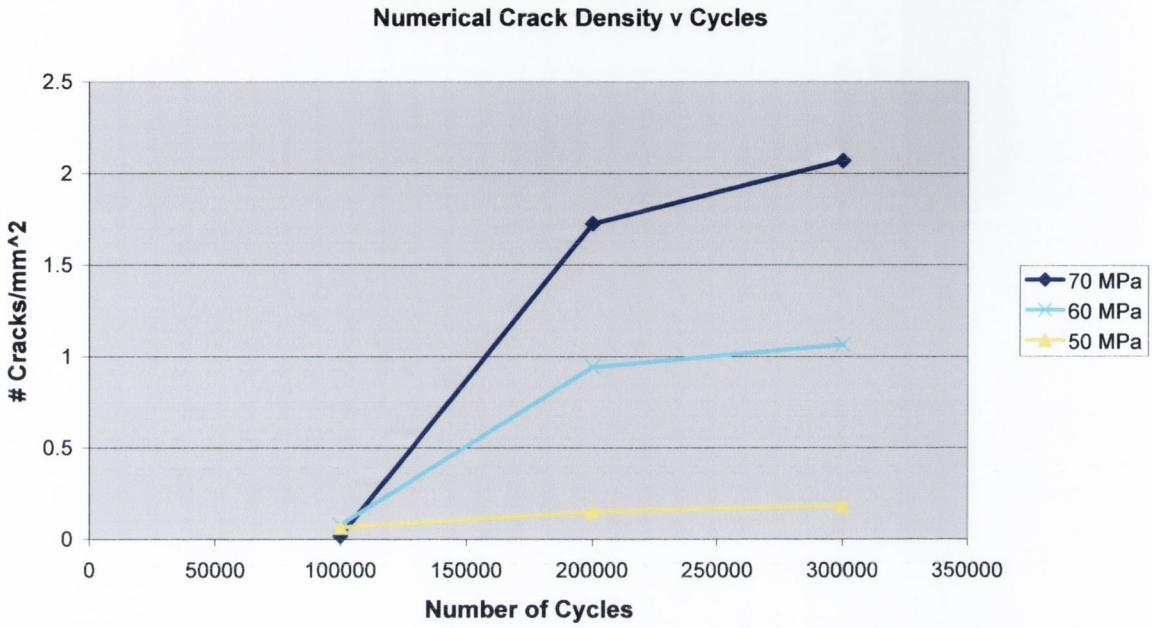

Fig. 3.12 Mean numerical crack density versus cycles at 50,60 & 70 MPa, 0-100,000 cycles

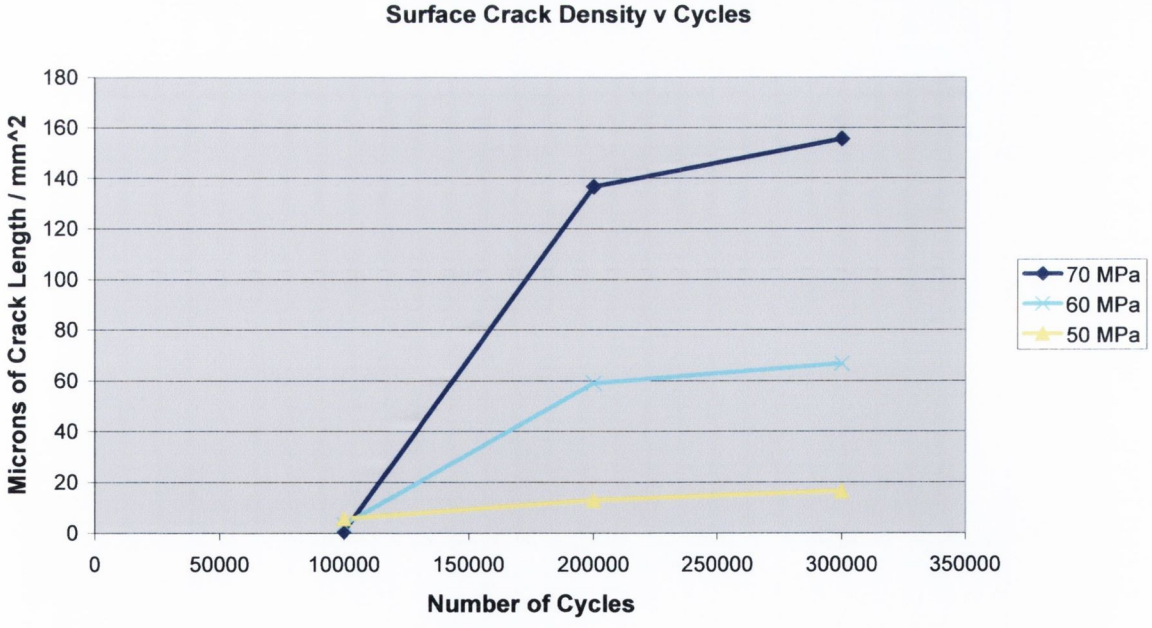

Fig. 3.13 Mean surface crack density versus cycles at 50, 60 & 70 MPa, 0-300,000 cycles

3.1.2 Microcrack Length

In addition to microcrack density, microcrack length was monitored throughout each test by measuring each crack length and then coordinating the dye that had stained the microcrack with the number of cycles at the point of application. Figure 3.14 shows the variation in mean microcrack length versus number of cycles at each applied stress range.

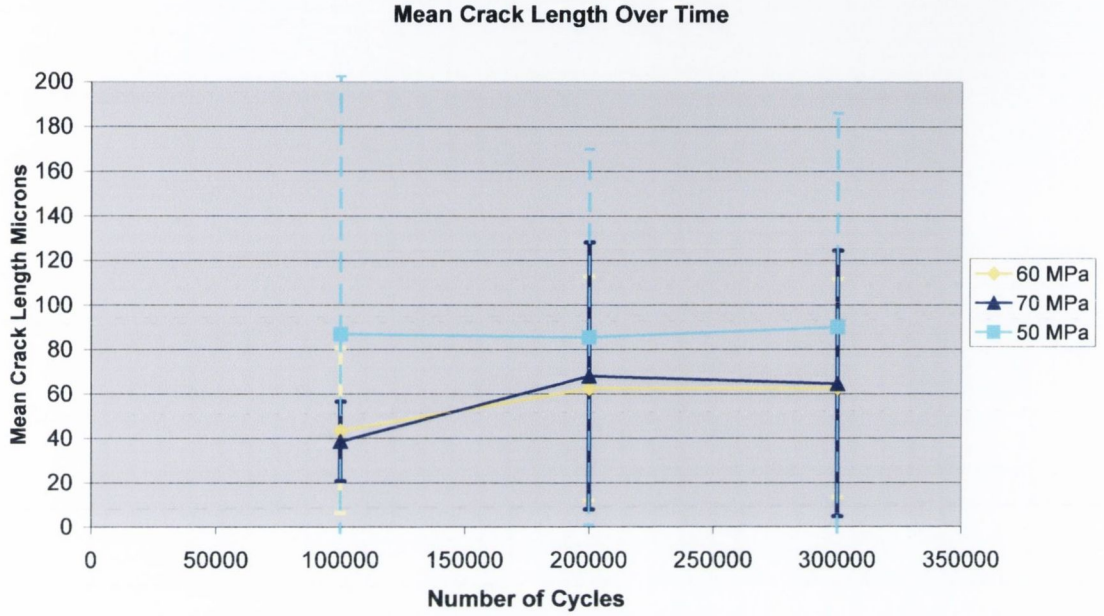

Fig. 3.14 Mean crack length versus number of cycles - 50, 60 & 70 MPa

From Figure 3.14 it can be observed that at 50 MPa the mean crack length varies very little over time during the course of a fatigue test, however at 60 and 70 MPa as the number of cycles increases between 100,000 and 200,000 an increase in mean crack length can be observed with a subsequent stabilising in crack length between 200,000 and 300,000 cycles. After 300,000 cycles the mean crack length is estimated to be 90.12 μm, 62.54 μm and 64.57 μm at the stress ranges of 50 MPa, 60 MPa and 70 MPa respectively, however by two million cycles mean crack length at 70 MPa had increased to 73.03 μm. Figure 3.14 also displays the standard deviations for each stress level after 100,000, 200,000 and 300,000 cycles. Given that the error bars associated with each stress level overlap one another, any difference between mean crack lengths at each stress level is irrelevant.

Figure 3.15 shows a histogram of crack length measurements for those cracks examined at all of the stress levels considered up until 300,000 cycles. The data are clearly skewed towards the smaller microcrack with a low incidence of longer microcracks. The data are well represented by the lognormal distribution as identified by the blue line on the graph.

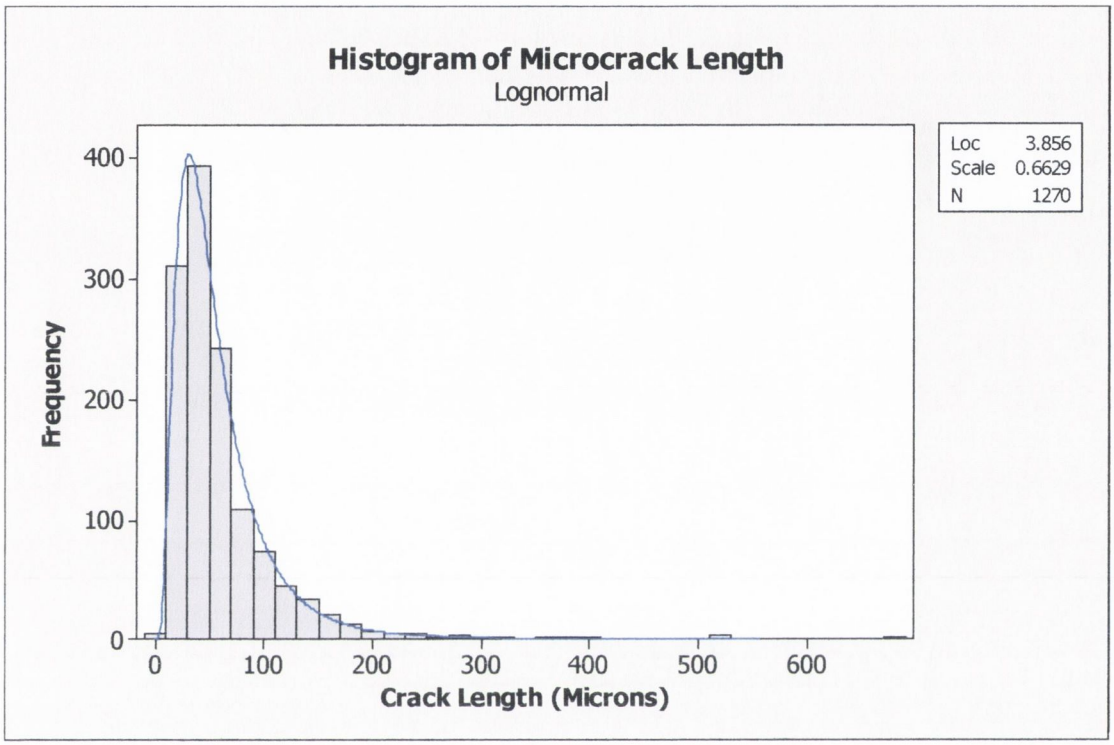

Fig. 3.15 Histogram microcrack length measurements 50, 60 & 70 MPa, 0 – 300,000 cycles

Figures 3.16 and 3.17 demonstrate the probability density function (Equation 3.1) fitted to the data and the associated cumulative density function (Equation 3.2), demonstrating the low probability of obtaining a longer potentially dangerous microcrack. In Figure 3.17 it can be seen that 50% of all microcracks have lengths less than 45 μm.

3.1

$$\frac{1}{\sigma x\sqrt{2\pi}}e^{\left(-\frac{(\ln(x)-\mu)^2}{2\sigma^2}\right)}$$

$$\int_{-\infty}^{x} \frac{1}{\sigma x \sqrt{2\pi}} e^{\left(-\frac{(\ln(x)-\mu)^2}{2\sigma^2}\right)} dt$$

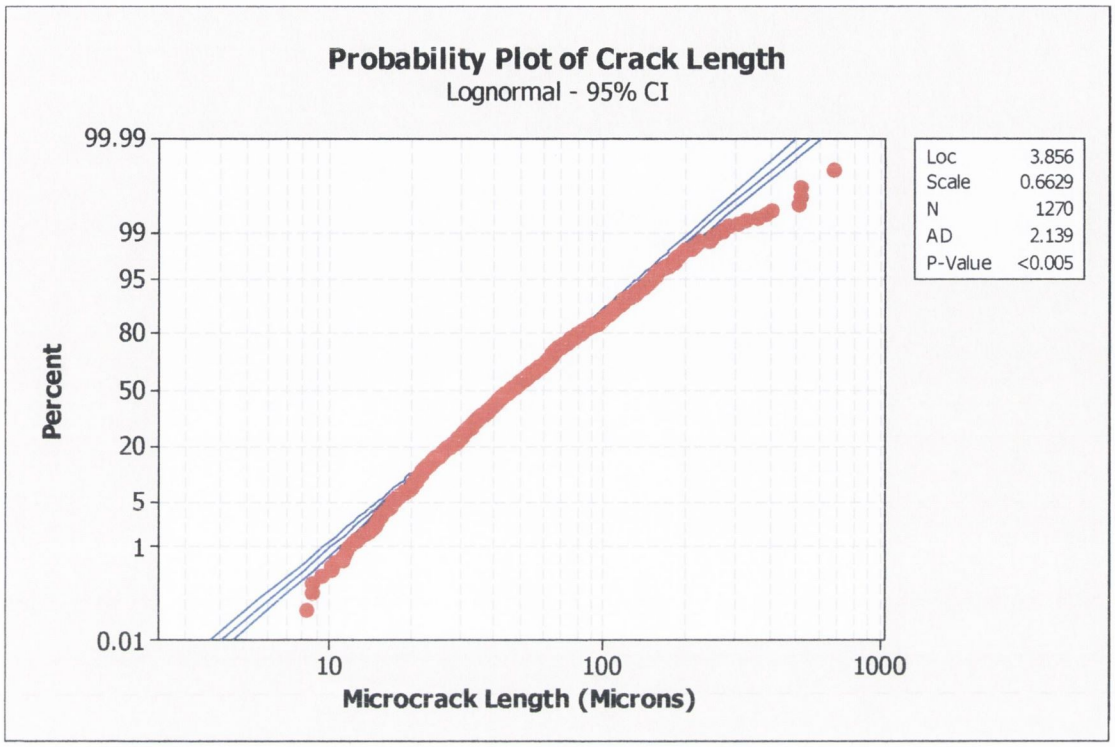

Fig. 3.16 Lognormal probability plot for microcrack length

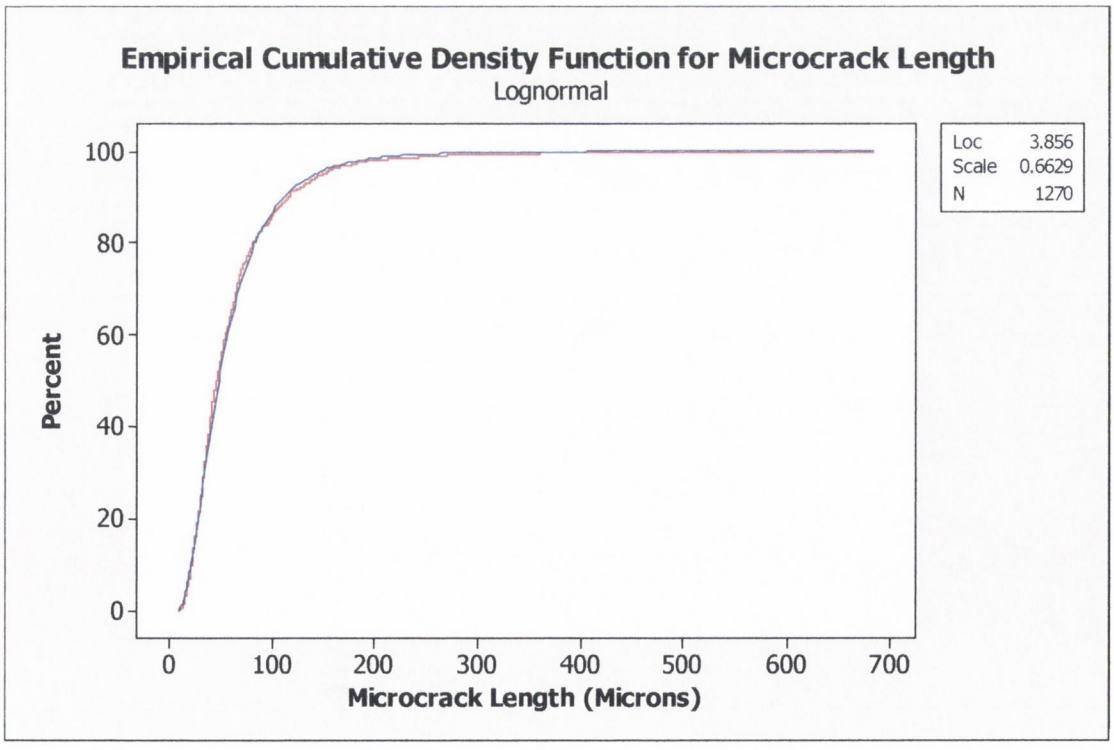

Fig. 3.17 Lognormal cumulative density function for microcrack length

Figure 3.18 considers the variation in mean crack length during each stage of testing for tests conducted at a stress range of 60 MPa. Propagating microcracks (labelled with two agents indicating growth at two different stages during testing) were found to be longer than those formed at individual periods during testing (86 μm; S.D 55μm). Comparison of means using a multiple pair t-test indicate a significant difference in length between propagating microcracks and those formed during the first or second stages of testing (difference in means greater than least significant difference at the 0.05 level). However the Tukey-Kramer adjusted t-test for all pairs, which reduces the possibility of making a type I error does not identify any significant difference between means. The mean crack length at each of the three stages was found to be 49 μm (S.D. 42 μm), 62 μm (S.D. 51 μm) and 63 μm (S.D. 39μm) respectively. Microcracks formed earlier in a specimen's life are smaller than those formed at a later stage, however this difference is not significant by an examination of multiple pair t-tests or an all pairs Tukey – Kramer test, both at the 0.05 level.

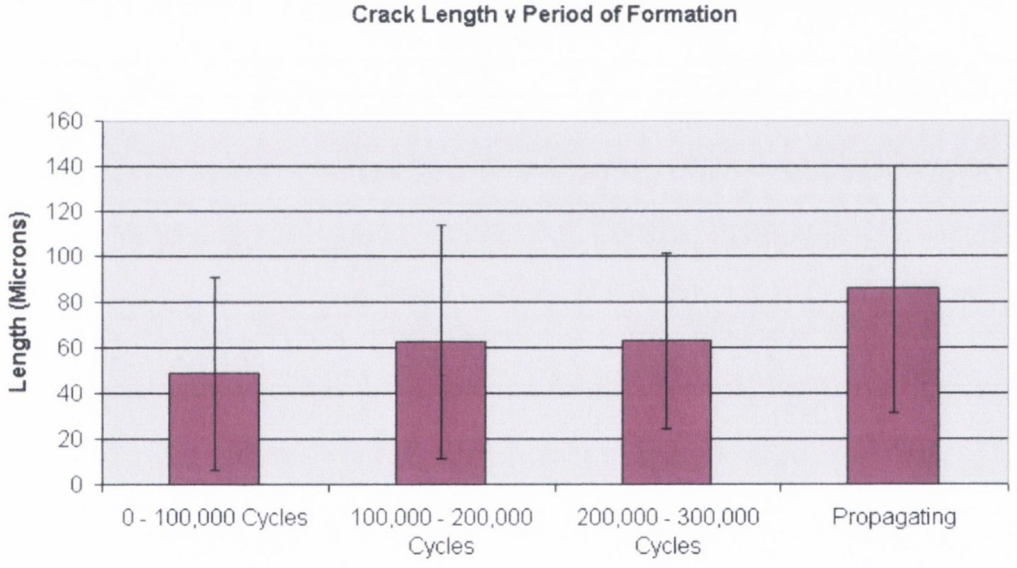

Fig. 3.18 Variation in mean crack length versus period of crack formation – 60 MPa

3.1.3 Microcracks and bone's microstructure – microcrack location

The effect of bone microstructure on the initiation and growth of microcracks was examined in two ways for those specimens conducted at 50 and 60 MPa: firstly by examining the location of microcracks in relation to osteons, and secondly by considering the effect of the number of osteons present on the development of

microcracks. Figures 3.19 and 3.20 show the variation in location of microcracks formed during each phase of the test and, additionally, the variation in location of microcracks which were observed to propagate during testing.

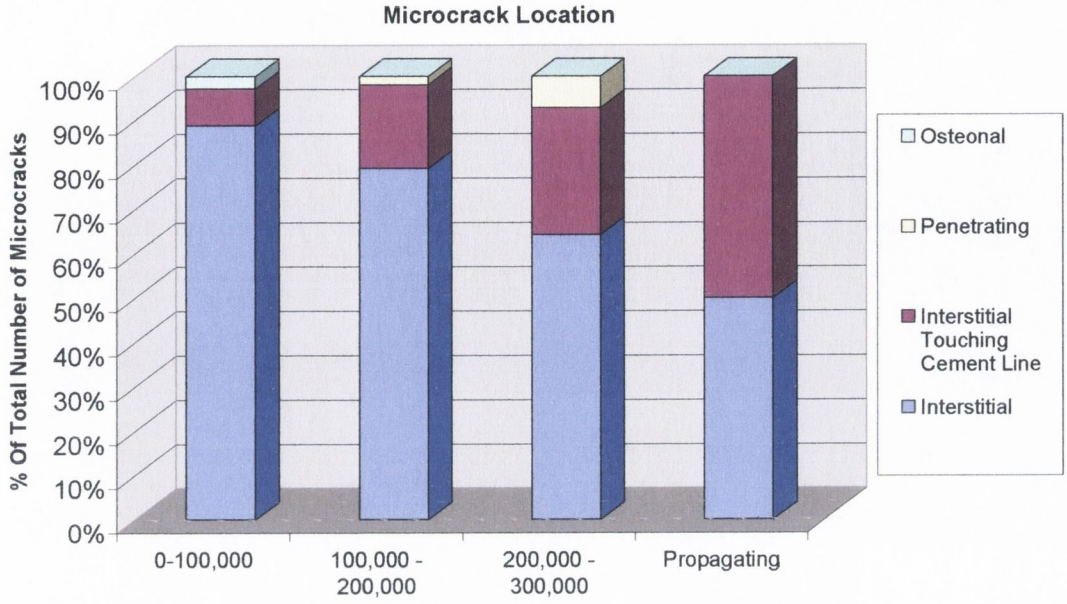

Fig. 3.19 Relationship between microcrack location and the period of crack formation – 50 MPa

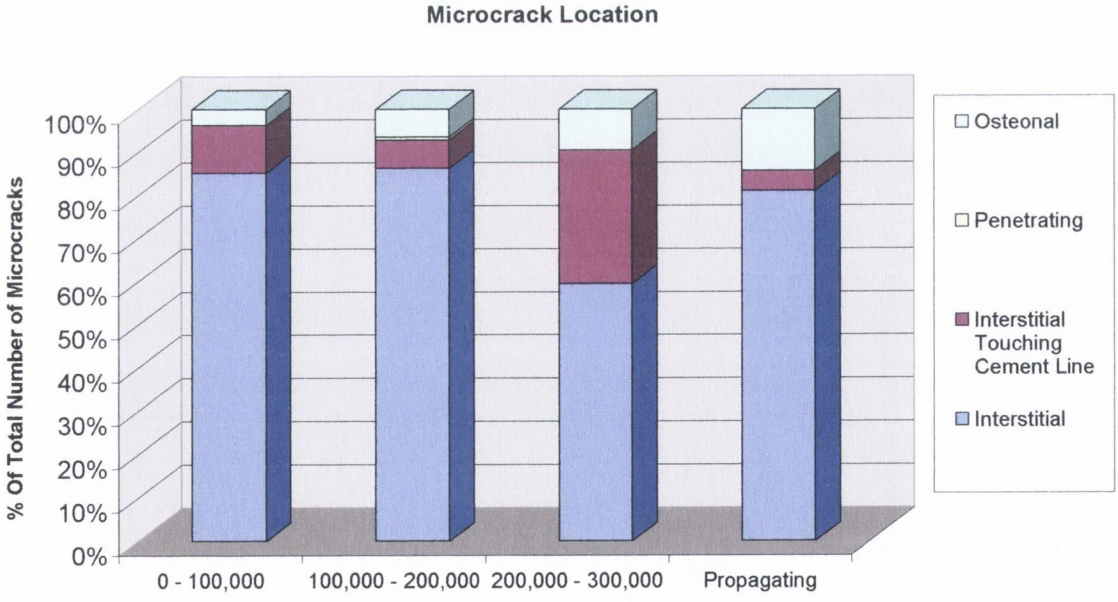

Fig. 3.20 Relationship between microcrack location and the period of crack formation – 60 MPa

It can be noted from Figures 3.19 and 3.20 that over the course of a fatigue test the proportion of microcracks which occur entirely within interstitial bone is observed to reduce and consequently the percentage of microcracks which are observed to touch a cement line or penetrate an osteon are seen to increase. Only a minimal number of microcracks were classified as osteonal microcracks in which cracks were entirely located within a secondary osteon.

As described in Tables 3.1 and 3.2, only a very small percentage of microcracks were described as growing or propagating cracks, 3% of all microcracks formed at 60 MPa and 4% of all microcracks formed at 50 MPa. The limited number of propagating microcracks observed at 50 MPa (a total of 5 microcracks) would advise using caution when considering the potential implications of the distribution of microcrack location for this type of microcrack. However, despite the fact that this type of microcrack represents a slightly smaller percentage of total microcracks at 60 MPa than at 50 MPa, at the higher stress range a greater number of propagating cracks (a total of 20) were observed. At 60 MPa, by far the greatest percentage of propagating microcracks were those located in interstitial bone, with a larger percentage of microcracks managing to penetrate secondary osteons than those formed during an individual stage of testing.

3.1.4 Microcracks and bone's microstructure – the effect of osteon density

In an attempt to better describe the effect that bone microstructure has upon the development of microdamage, this study also examined the relationship between osteon density and the development of microcracks. The effect of variations in osteon density upon microcrack density, microcrack surface density and microcrack length are all considered. Figures 3.21 and 3.22 describe the observed relationship between osteon density and either numerical crack density or surface crack density.

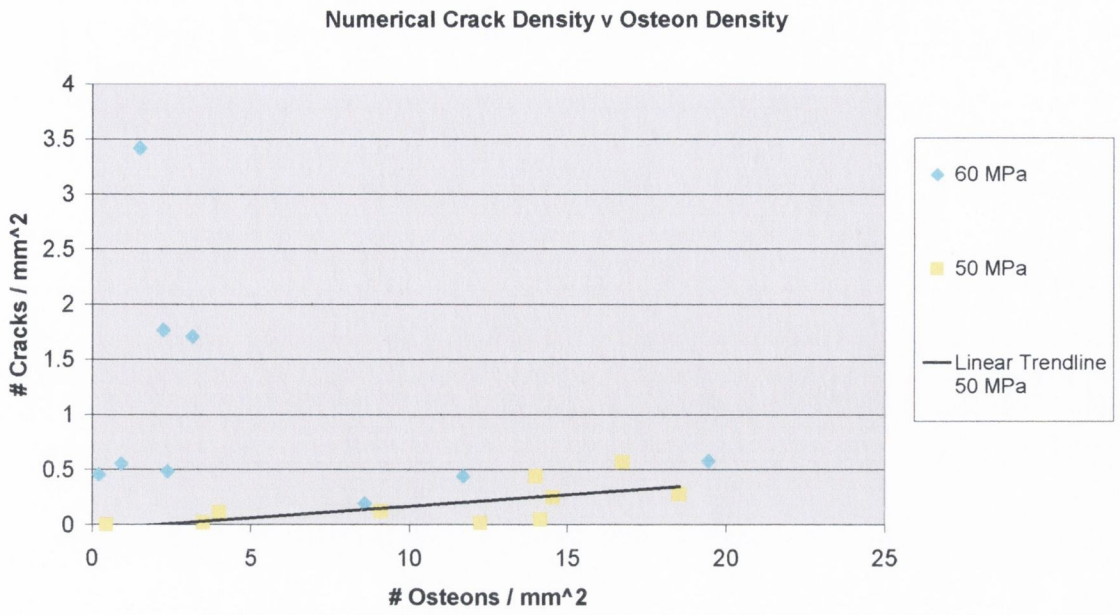

Fig. 3.21 Relationship between numerical crack density and osteon density

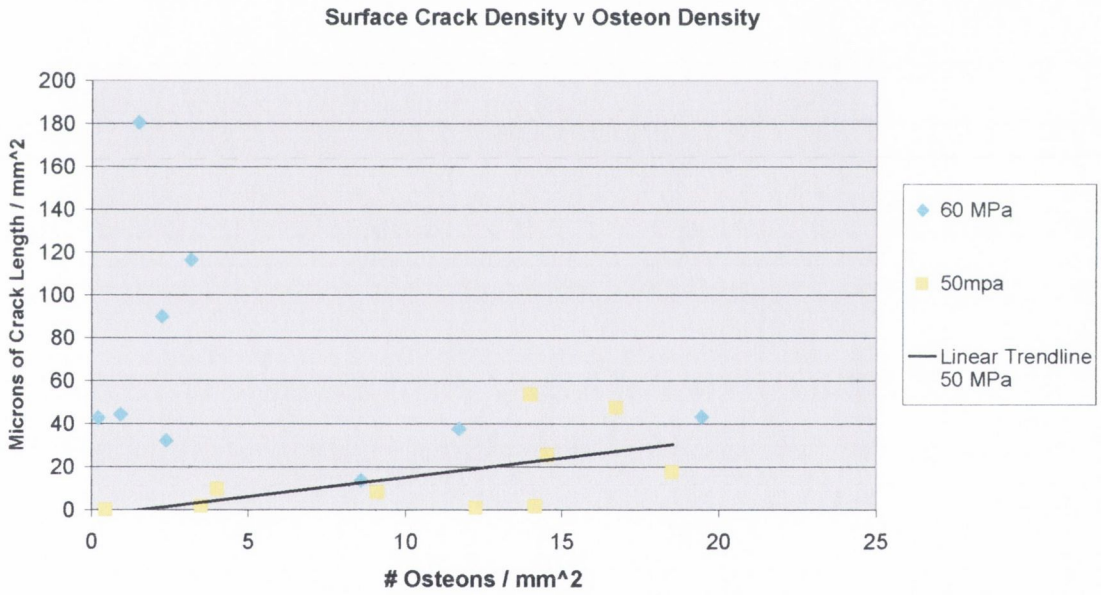

Fig. 3.22 Relationship between surface crack density and osteon density

Figures 3.21 and 3.22 demonstrate that at 50 MPa microcrack density is seen to increase slightly with an increasing osteon density and this is highlighted by the trend lines shown on the two graphs. However at 60 MPa such a pattern is not observed, and three individual specimens with low osteon densities are observed to have above average microcrack densities. Even if the three specimens with the highest crack densities were to be removed from the figures, there would still be no overlying trend between microcrack density and osteon density at the 60 MPa stress range.

At both stress levels considered in this examination, osteon density was observed to be unrelated to microcrack length and this is shown below in Figure 3.23, which depicts the distribution of mean microcrack length with osteon density. It should also be noted that the three specimens with higher microcrack densities, described in the preceding paragraphs, were observed to have the lowest mean crack lengths of all specimens considered at this stress level, two of which are below the mean crack length for all cracks identified at 60 MPa. For convenience these specimens have been circled for the readers attention.

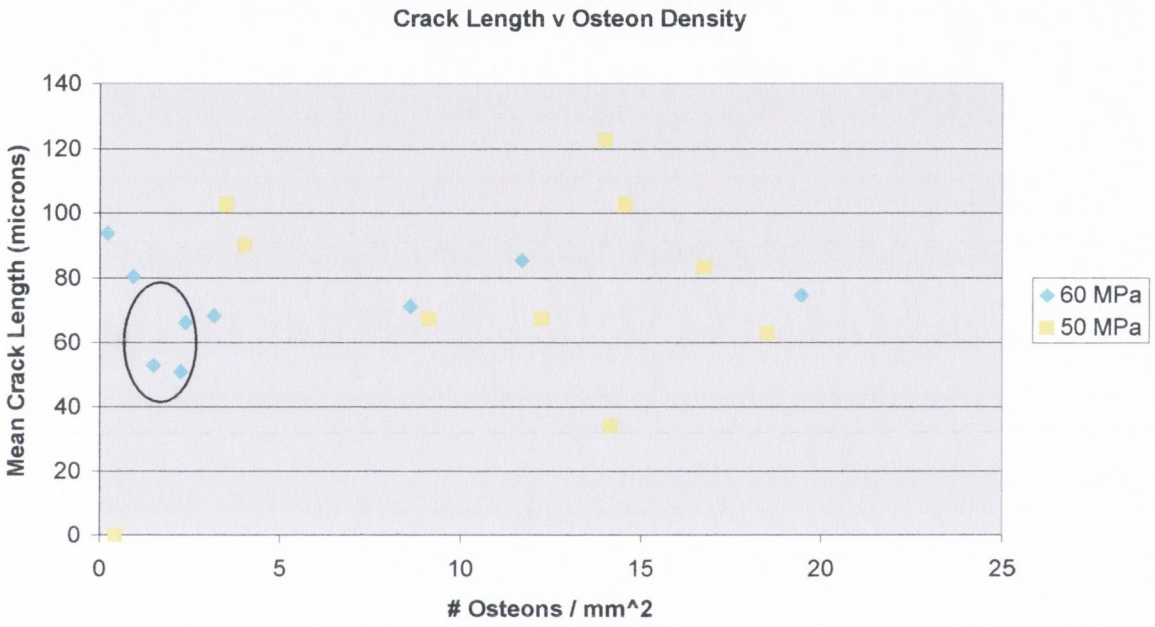

Fig. 3.23 Mean crack length versus osteon density

Figure 3.24 describes the relationship between microcrack location and osteon density when tested at a 60 MPa stress range.

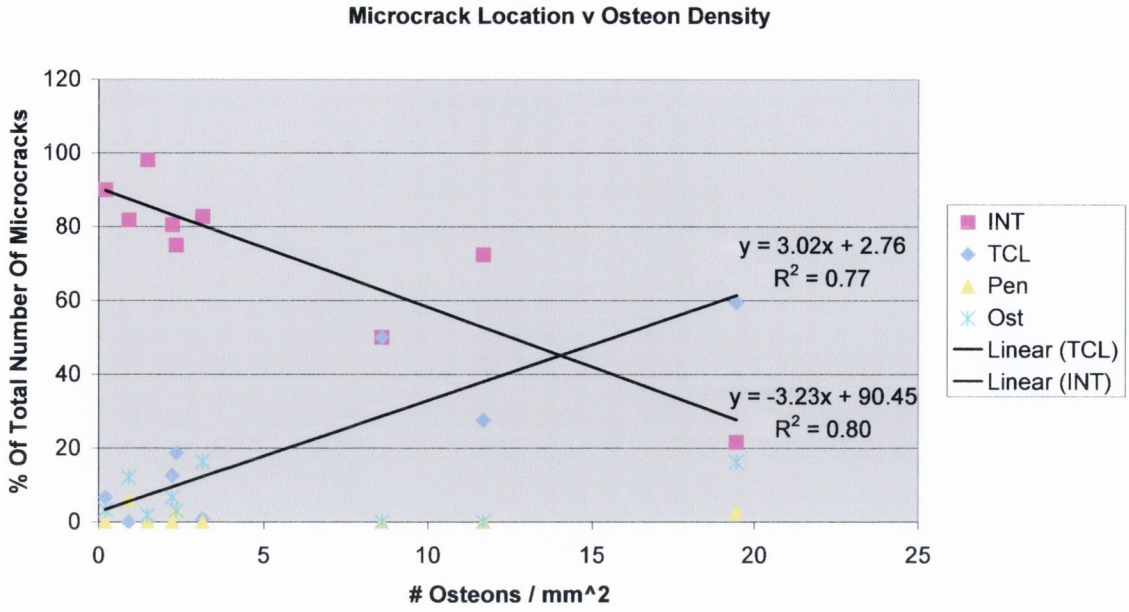

Fig. 3.24 Relationship between microcrack location and osteon density

The graph of microcrack location against osteon density (Figure 3.24) shows that the percentage of microcracks located entirely within interstitial bone is seen to reduce linearly with an increase in osteon density ($p=0.001$). Conversely, the percentage of microcracks which are interstitial but touching a osteon cement line are seen to increase linearly with an increase in osteon density ($p=0.002$).

3.2 Creep

A total of 23 bone specimens were tested, with 16 failing within a time period of 20 hours. A further 6 specimens did not fail during this time. Where complete failure was observed, the main fracture plane was oblique to the specimen axis, with most specimens failing along a plane at an approximate angle of 40 to 60° to the horizontal. Figure 3.25 shows a diagrammatic representation of the fracture plane.

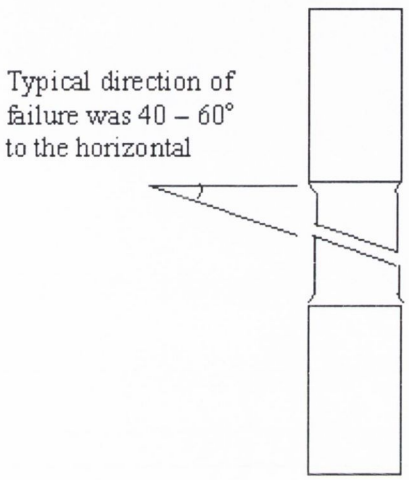

Fig. 3.25 Representation of specimen failure

The number of specimens tested at each of the stress levels is shown in Table 3.5. As can be seen from the table, more specimens were tested at 120 MPa than at any other stress level. This was because 120 MPa was the first stress level at which any testing was carried out, hence this stress level was used to establish the testing protocol.

Table 3.5 Creep tested specimens

Stress Level (MPa)	Number of tested specimens
88	1
120	7
130	5
140	6
150	4

The three characteristic stages of creep exhibited by many materials were also observed in these tests conducted upon bovine compact bone. Strain-time histories for these

failed specimens showed an initial elastic region upon loading followed by a region of primary creep, where the strain increased at a decreasing rate, until an approximately constant strain rate was reached (secondary creep). Eventually, the strain rate increased again, leading to complete failure of the specimen (tertiary creep). The final increase in strain was found to start gradually and then accelerate rapidly over a short period of time, making it difficult to pick a specific point where secondary creep ended and tertiary creep began. In those specimens which did not fail, the elastic, primary creep and secondary creep regions were observed, however the tertiary creep domain was not reached. Figure 3.26 gives an example of the strain time history observed for a failed specimen.

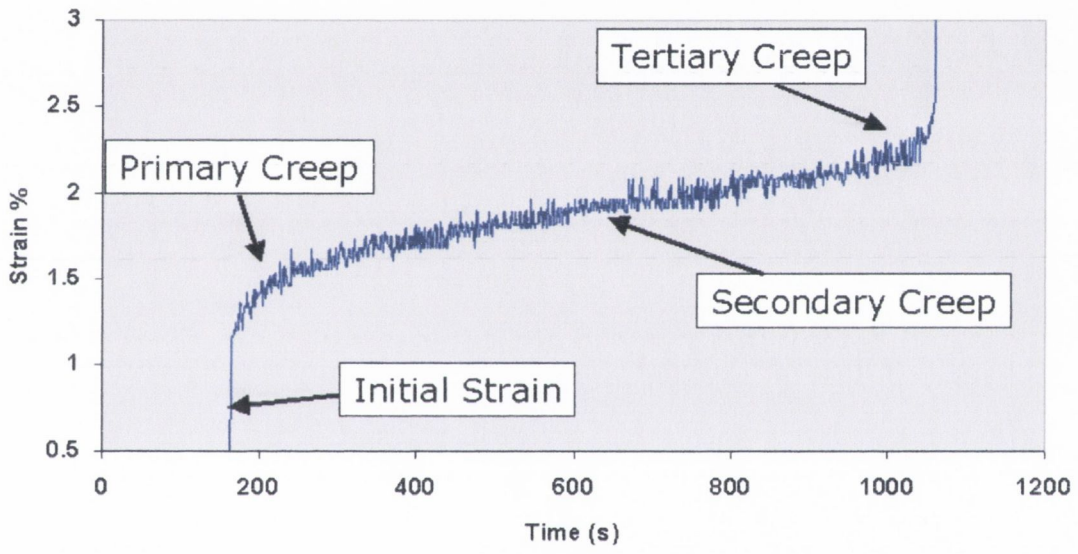

Fig. 3.26 Strain time history for a failed specimen, applied stress = 130 MPa

3.2.1 Time to Failure

Where failure was observed for a given test, the total time to failure consisted of all three creep stages, although the contributions made by primary and tertiary creep can be seen to be negligible. As noted in the Materials and Methods section, the recorded 'time to failure' for unfailed specimens is taken to be the point where the test was interrupted, and therefore only included primary and secondary creep. The maximum test duration recorded for a specimen was 109,377 seconds (30.4 hours), at a stress level of 120 MPa. In this specimen failure was not observed and the user interrupted testing,

the test duration therefore provides a non-finite result. The duration goes beyond the self-imposed time limit of 20 hours, however this was the first test to reach such high duration; all previous experiments had resulted in complete failure of the specimen. After experiencing such a long test duration, it was decided to impose a maximum constraint of 20 hours for practical reasons.

Figures 3.27 and 3.28 show plots of the variation in time to failure for all specimens tested. It can be seen from these graphs that an increase in the compressive stress level or normalised stress has a considerable effect on the time to failure of the specimen. They have an inverse relationship, whereby an increase in stress level reduces the time to failure. Values for time to failure, where complete failure was observed, varied from 18 to 59,355 seconds, whereas recorded values for 'time to failure' for un-failed specimens was observed to be as high as 109,377 seconds.

In Figure 3.28 all specimens are normalised (divided by) with Young's modulus, the data are linear on a log-log plot, which is similar to the power law creep behaviour of other materials when subjected to a constant stress. The Young's modulus used to normalise the data is a typical value for the Young's modulus of bovine compact bone (20.4GPa) and not the exact value for any given specimen. Hence the time to failure can be described by an equation of the form shown in Equation 3.3. Considerable scatter in the time to failure was observed as expected in tests of this nature.

3.3

$$t_f = A(\sigma / E)^{-B}$$

where t_f = time to failure, σ / E = normalised stress, A = creep coefficient and B = creep exponent.

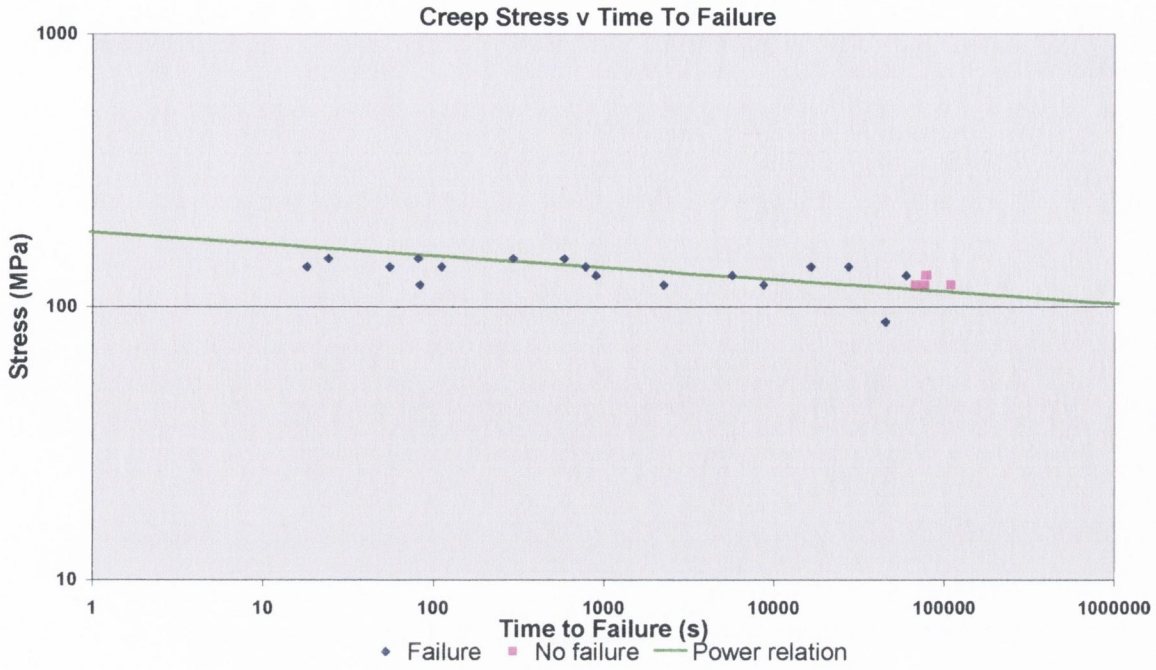

Fig. 3.27 Stress versus time to failure for all creep specimens

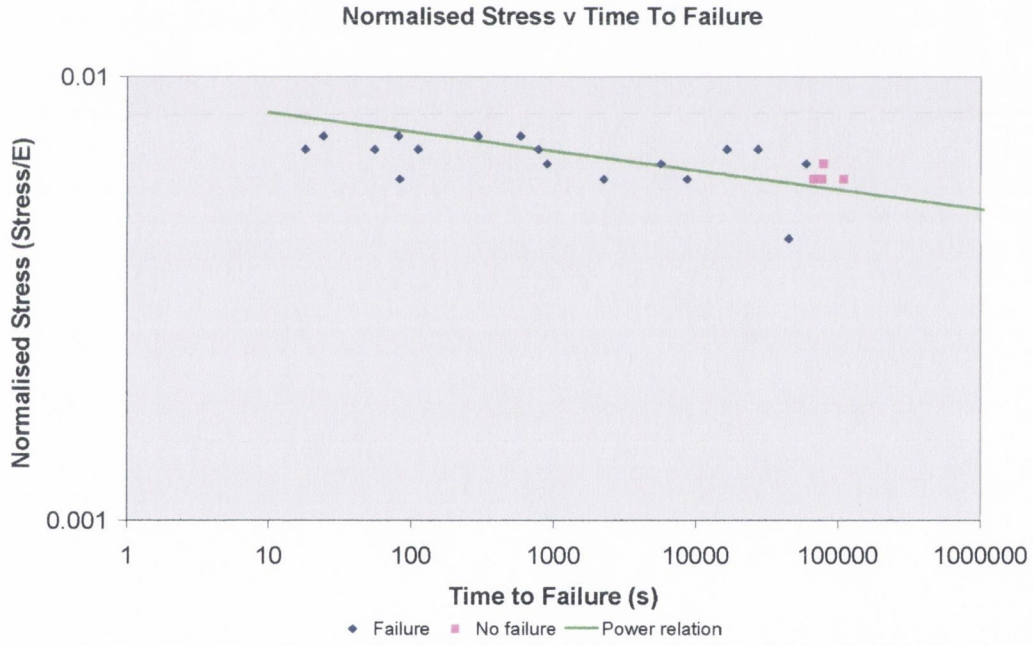

Fig. 3.28 Log-log plot of normalised stress versus time to failure for all specimens

By taking log transformations of the data and then calculating the mean of these values, the data can be plotted so that using linear regression, a power law function for time to failure can be derived. Figure 3.29 demonstrates this relationship and Equation 3.4, is the power law function derived from this plot.

3.4

$$t_f = 2.77 \times 10^{-47} (\sigma / E)^{-22.87}$$

(r^2=0.85, n=4 number of data points, t=3.299, p=0.08) (NB. n has been reduced from 22 to 4 in using mean values, hence explaining the strong (r^2=0.85,) yet marginal (p<0.09) relationship)

t_f = time to failure (seconds), σ / E = normalised stress, A = creep coefficient and B = creep exponent. (Using all 22 values A=6.54×10^{-45}, B=21.77 (r^2=0.36, n=22, t=3.375, p=0.003))

In the above treatment, the r^2 value is the coefficient of determination and essentially is an indicator of how well the model fits the data, the closer to 1 the better the model is at predicting the data. N simply refers to the number of data points or samples, the statistical 't' value and probability 'p' are then used to measure the significance of the model's fit to the data; the 't' statistic is a measure of the ratio of the estimate to its standard error and the 'p' value is the significance level.

One specimen was tested at 88 MPa, however the data for this individual test is not included here in developing an equation for time to failure. When compared to specimens tested at higher stress levels, this test showed a surprisingly low time to failure (45,032 seconds), well below that anticipated. It was therefore judged that this data point was an outlier and, with only one test carried out at 88 MPa, it was deemed that this data point had limited relevance compared to other stress levels, where a number of tests had been carried out. Mean values for time to failure accompanied with minimum and maximum error values calculated from the log transformations are shown in Table 3.6. The error values were calculated according to Equation 3.5.

3.5

Error (Min / Max) = Inverse Logarithm ((mean of log values for time to failure) + / - (standard deviation of the log values))

Table 3.6 Mean time to failure

Stress (MPa)	Mean Time to Failure (s)	Error Min–Max (s)
88	45,032	-
120	13,130	925 - 186,410
130	17,888	2,410 - 132,791
140	581	28 - 12,241
150	135	33 - 554

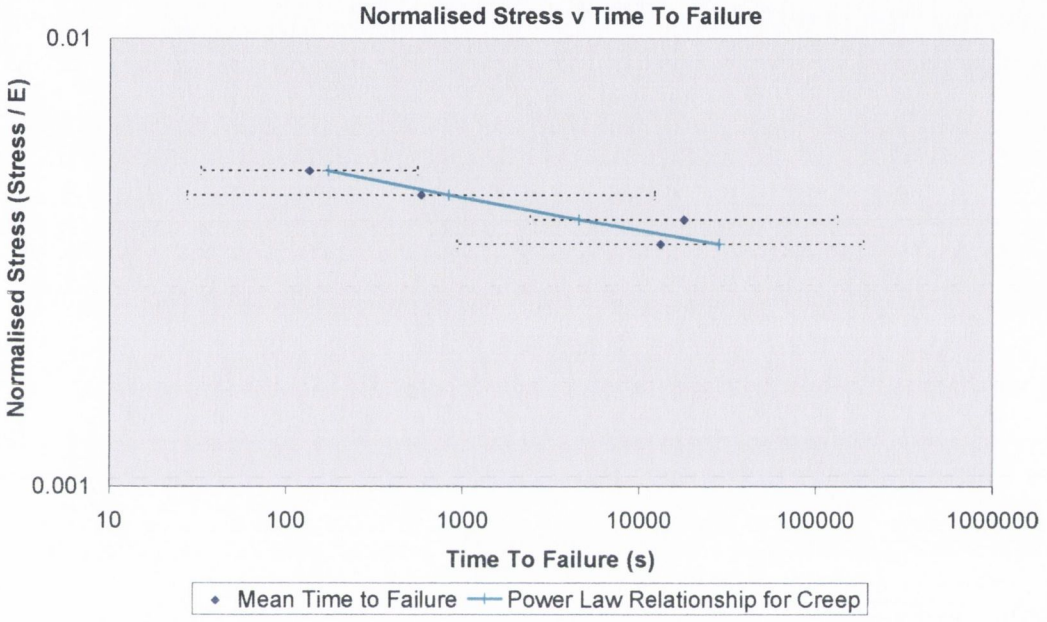

Fig. 3.29 Power law function for time to failure, including minimum and maximum error values

3.2.2 Steady State Creep Rate

Regression analyses indicated that there was a strong and significant power law relationship between steady-state creep rate ($d\varepsilon/dt$) and normalised stress (σ/E). This is shown in Equation 3.6 and Figures 3.30 and 3.31.

3.6

$$d\varepsilon/dt = 5.76 \times 10^{47} (\sigma/E)^{24.48}$$

($r^2 = 0.82$, n=4, p = 0.09), where $d\varepsilon/dt$ is in s^{-1}.

As in Equation 3.4, Equation 3.6 is calculated by taking log transformations of the data and then calculating the mean of these values, with the exception of the individual test

carried out at 88 MPa. Due to technical difficulties with data acquisition, two of the tests carried out at 120 MPa were not included in the analysis of steady state creep rate. Steady state creep rate was found to vary from $9.973\times10^{-8}s^{-1}$ to $1.633\times10^{-4}s^{-1}$ and individual values for all specimens tested can be found in the appendix. Considerable scatter in the steady state creep rate was observed as expected in tests of this nature.

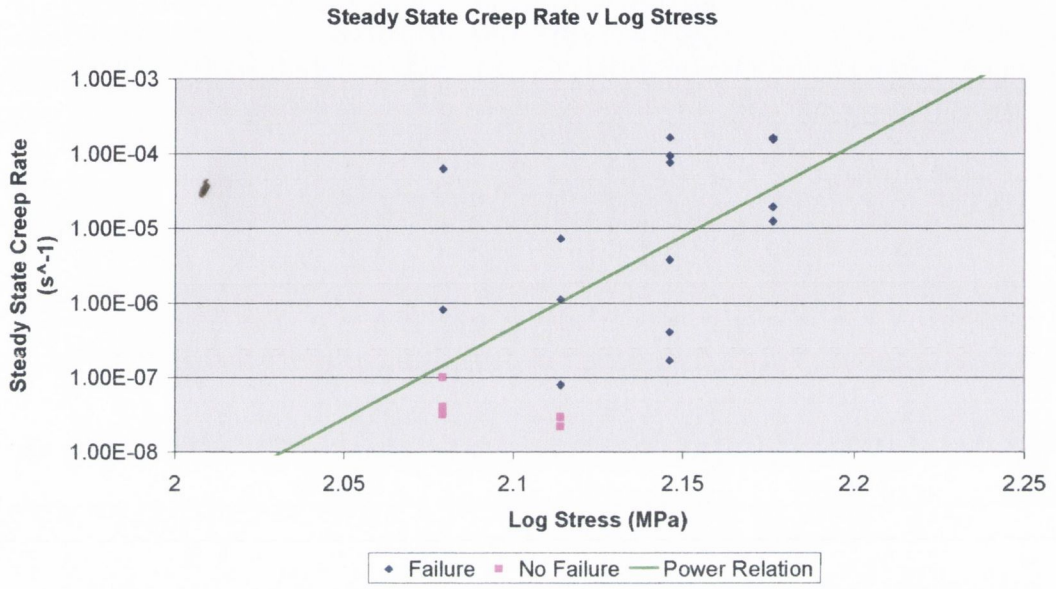

Fig. 3.30 Log - log plot of steady state creep rate ($d\varepsilon/dt$) versus stress (σ)

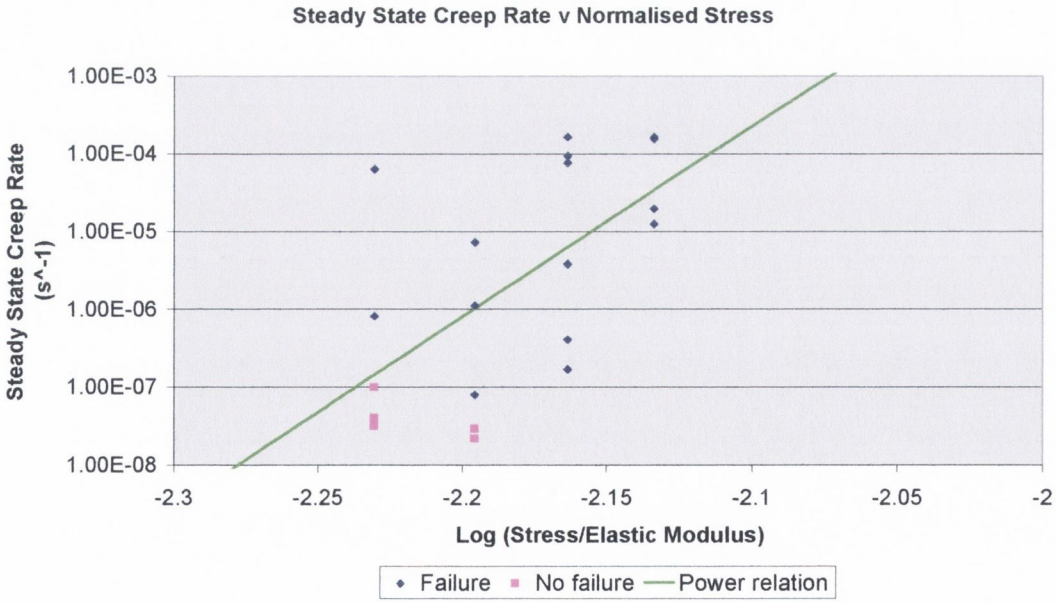

Fig. 3.31 Log - log plot of steady state creep rate ($d\varepsilon/dt$) versus normalised stress (σ/E)

3.2.3 Creep fracture surfaces

Scanning electron micrographs are shown for three creep-fracture specimens in Figures 3.32-3.39. In all fracture surfaces observed, the fracture plane was oblique to the specimen axis and loading direction with a rough appearance to the fracture surface. Figures 3.32 and 3.33 show the surface of a specimen tested in compression at a stress of 130 MPa. Failure occurred after 5,638 seconds. The fracture plane is covered with a series of ridges, with a ridge spacing of between 100 and 200 μm. This is clearly seen at the higher magnification (Figure 3.33), where arrows indicate the ridge pattern. This ridge spacing is consistent with the sizes suggested for the diameter of osteons, thus suggesting that separation at osteon boundaries may be occurring.

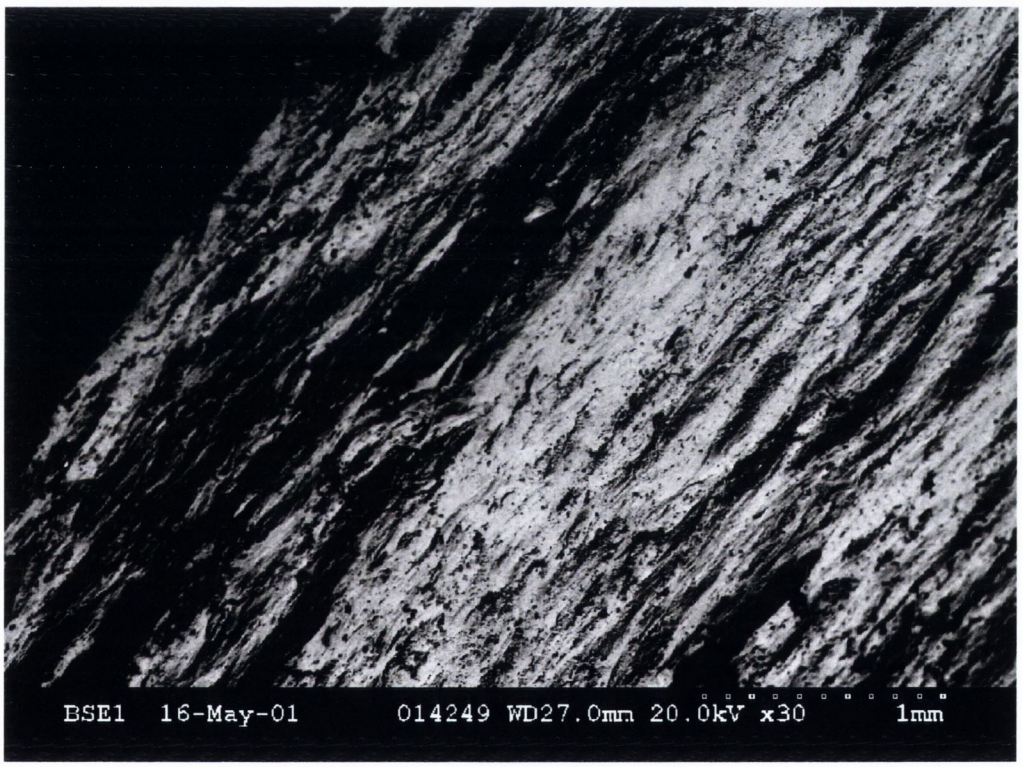

Fig. 3.32 Scanning electron micrograph of the fracture surface of a specimen tested at 130 MPa, x30 magnification (appendix 2.1 specimen 12).

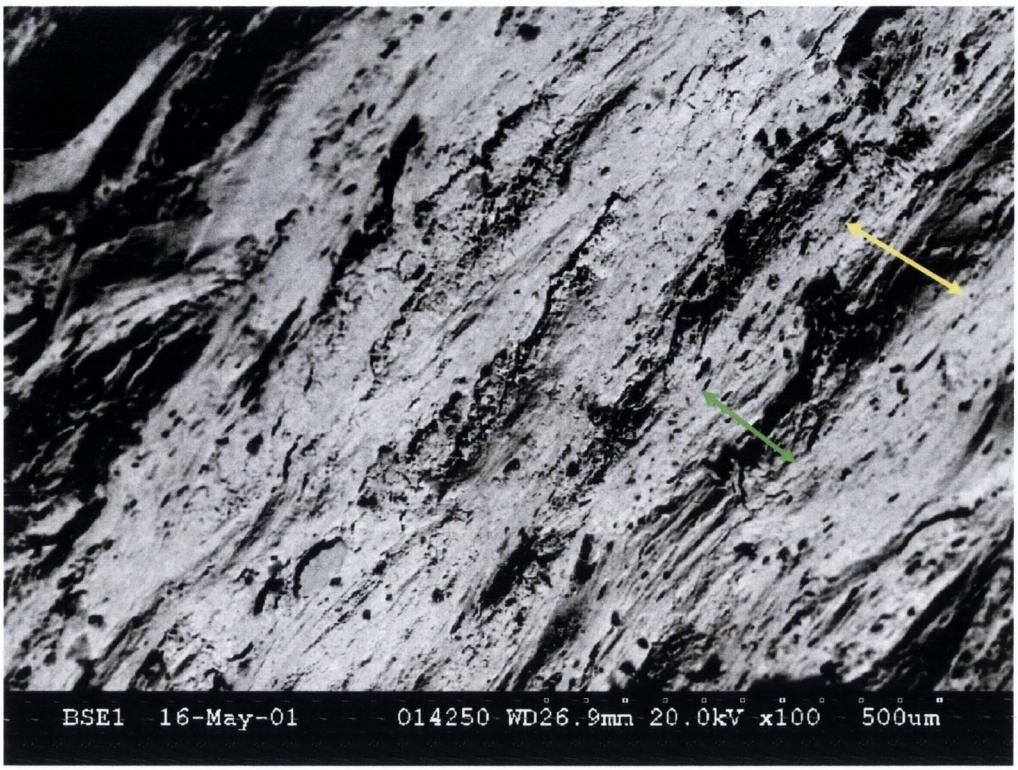

Fig. 3.33 Scanning electron micrograph of the fracture surface of a specimen tested at 130 MPa, x100 magnification. Arrows indicate ridge spacing (appendix 2.1 specimen 12).

Figures 3.34 and 3.35 show the surface of a specimen tested in compression at a stress of 140 MPa, failure was observed to occur after 27,302 seconds. Due to the angle at which this electron micrograph is taken, the ridge spacing is not so clearly visible, however ridge spacing is once again consistent with that observed at 130 MPa. In Figure 3.35 it can clearly be observed that the surface has a step like appearance, with what appears to be sheet-like structures drawn out and folded over (as indicated by arrows). At the higher magnification these structures are observed to be approximately 7 μm thick, thus suggesting that their thickness is consistent with the dimensions quoted for lamellar thickness. This suggests that we are observing the ends of lamellae which are being drawn out and folded over. Interlamellar cleavage is observed over the fracture surface to varying degrees, from limited cleavage, where adjacent lamellae are still connected to one another, to extensive cleavage, where lamellae separate and peel away from the fracture surface as described in Figure 3.35.

Fig. 3.34 Scanning electron micrograph of the fracture surface of a specimen tested at 140 MPa, x30 magnification (appendix 2.1 specimen 17)

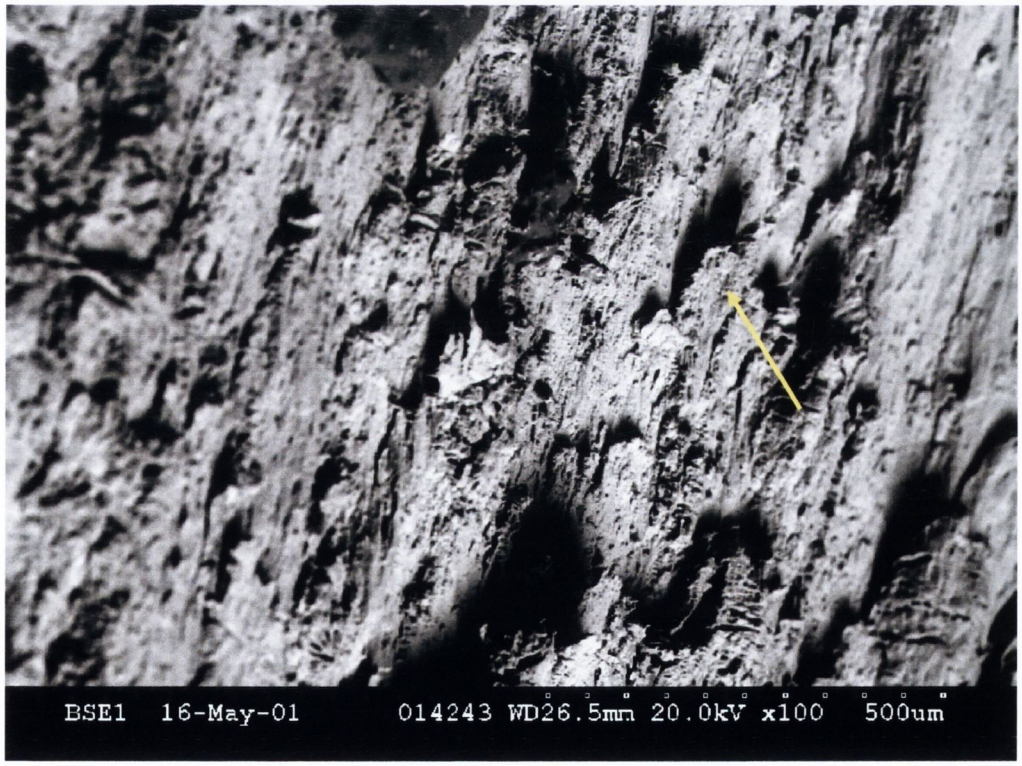

Fig. 3.35 Scanning electron micrograph of the fracture surface of a specimen tested at 140 MPa, x100 magnification. Arrow indicates lamellar cleavage (appendix 2.1 specimen 17)

Figures 3.36 and 3.37 show the surface of a specimen tested at a stress level of 150 MPa, failure occurred after 24 seconds. At this higher compressive stress, the fracture surface appears to be considerably smoother, with less detail to the surface. Once again ridges are seen running diagonally along the surface with a separation of 150 to 200 μm. In Figure 3.36 the fracture plane has travelled through what appears to be osteons, leaving tunnels and grooves that appear to show osteonal pull out from the bone. The failure plane of the osteon is different to that of the main fracture plane of the specimen. The exposed tunnels show separation along the long axis of individual osteons where osteons become separated from the surrounding bone. This is the result of shear failure along the interface or osteonal cement line. In Figures 3.36 and 3.37, surface damage is clearly evident, exposing cracks in the surface of the bone. At higher magnifications, it appears that an osteon has been exposed with cracks surrounding the osteon, in this instance the osteon stands out prominently from the fracture surface.

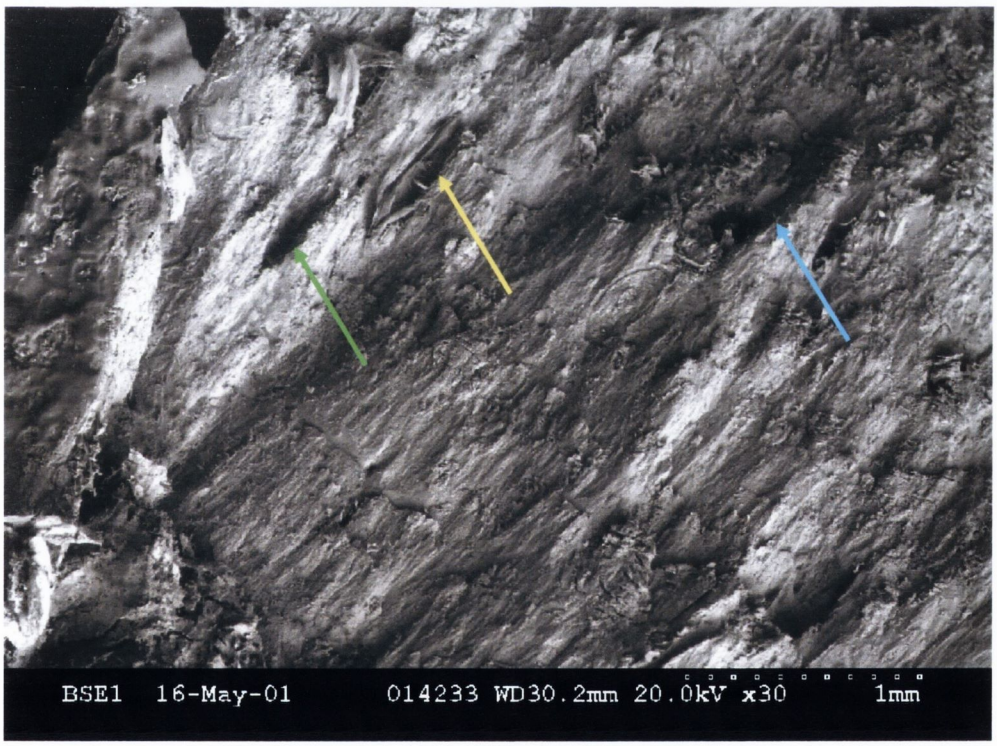

Fig. 3.36 Scanning electron micrograph of the fracture surface of a specimen tested at 150 MPa, x30 magnification. Arrows indicate separation along the long axis of individual osteons (appendix 2.1 specimen 23)

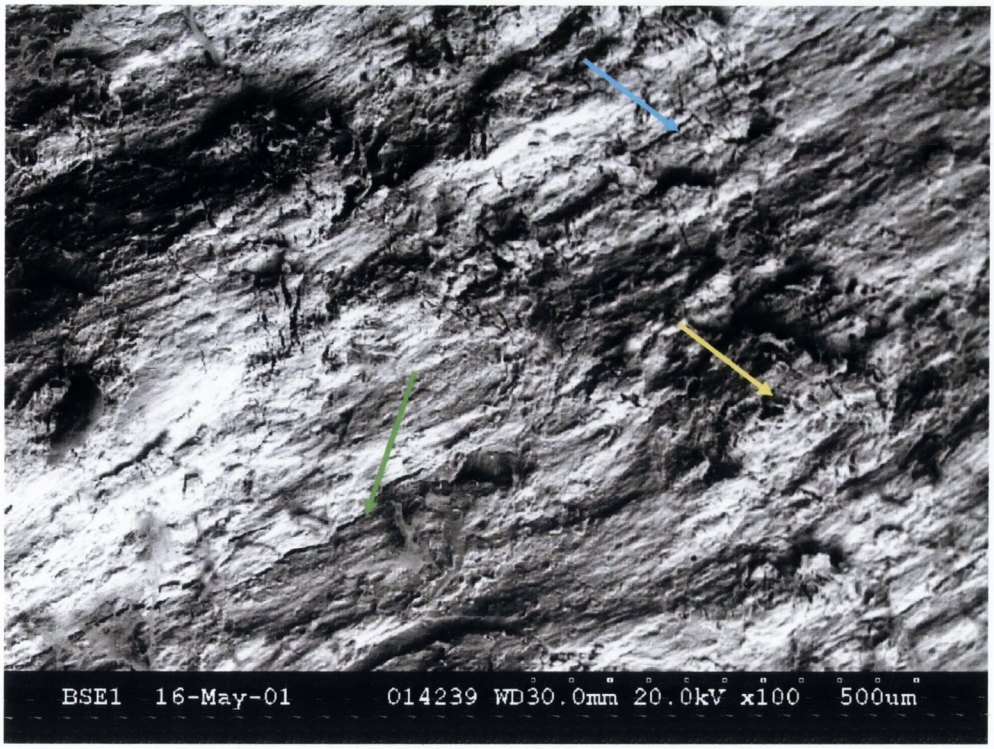

Fig. 3.37 Scanning electron micrograph of the fracture surface of a specimen tested at 150 MPa, x100 magnification (a). Green and blue arrows indicate microdamage on the surface, yellow arrow: osteon prominent in relief (appendix 2.1 specimen 23)

The fracture surface of creep specimens often demonstrated irregular fracture of osteons. This could be identified by the distortion of osteons, to the extent where the normal structure of the osteon could no longer be observed. Some indications were also observed of osteons splitting along their length with exposure of the central canal over a section of their length, this is shown in Figures 3.38 and 3.39. Areas of the bone surface also demonstrated a coordinated fracture pattern where a portion of the fracture surface has broken en masse. Such areas appeared to not be limited by the structural features of the bone.

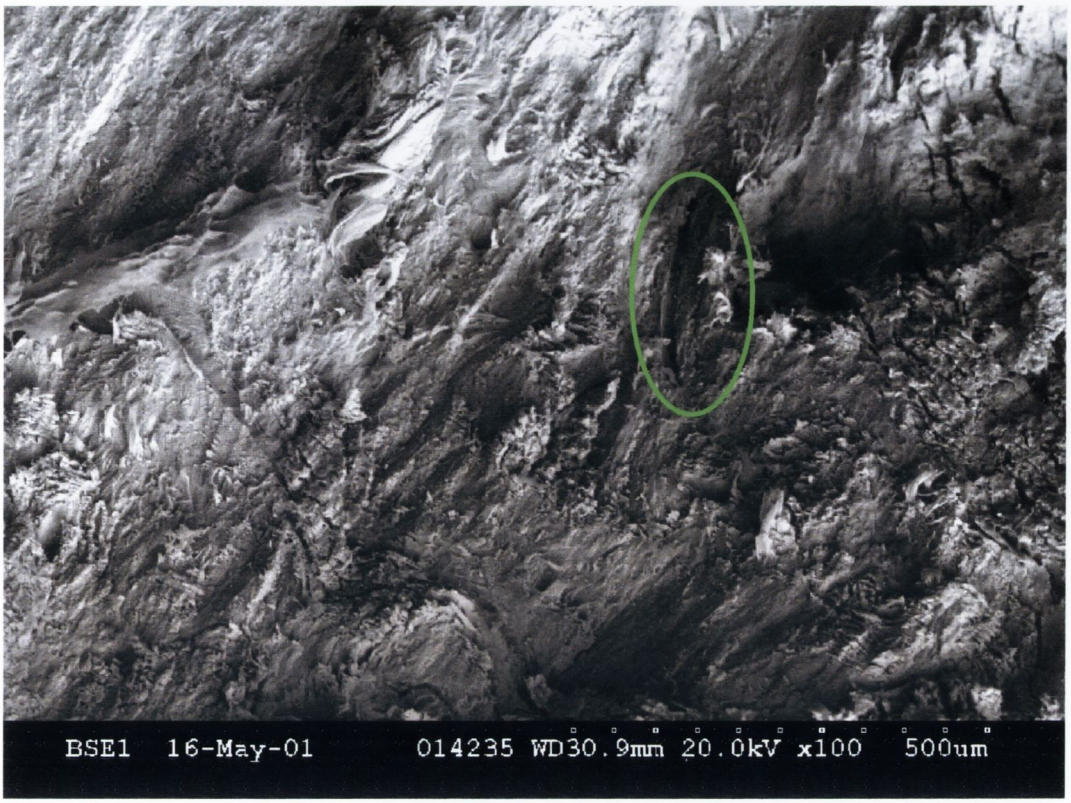

Fig. 3.38 Scanning electron micrograph of the fracture surface of a specimen tested at 150 MPa, x100 magnification (b). Circled area indicates osteons splitting along their length with exposure of the central canal (appendix 2.1 specimen 23)

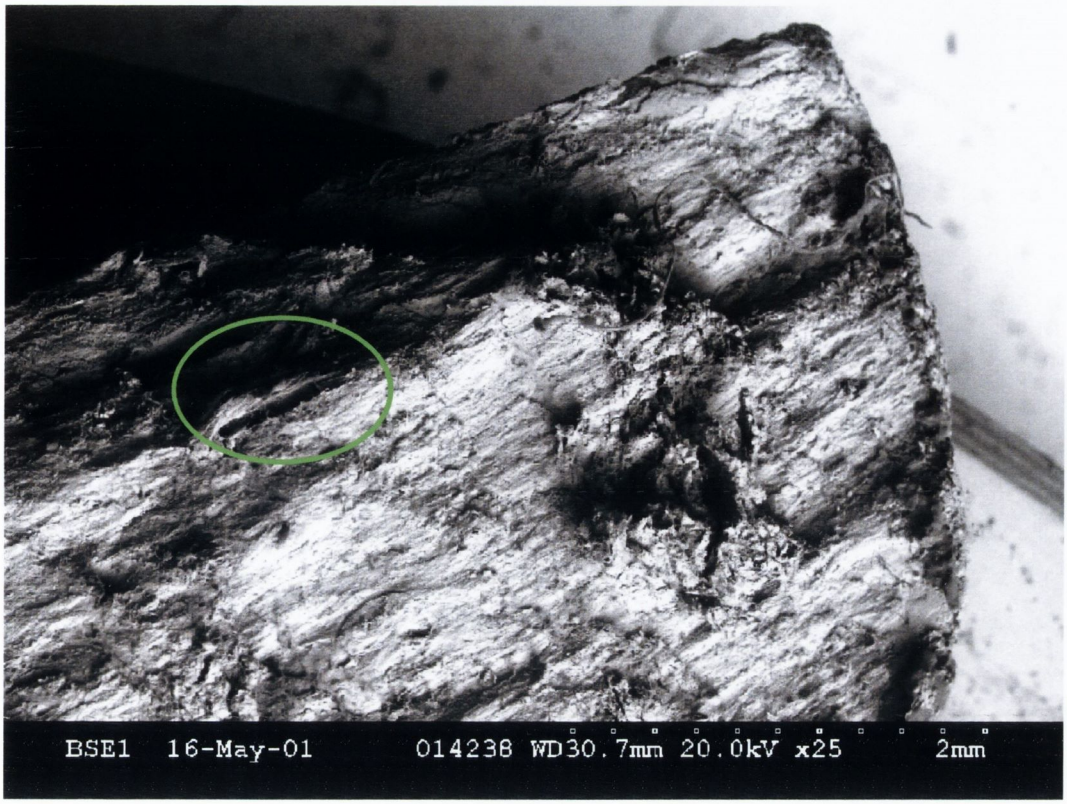

Fig. 3.39 Scanning electron micrograph of the fracture surface of a specimen tested at 150 MPa, x100 magnification (c). Circled area indicates osteons splitting along their length with exposure of the central canal (appendix 2.1 specimen 23)

3.2.4 Histology

Histological examination of microcracks was possible due to the fluorescent properties of the dyes when viewed under green and UV incident light (λ=546 and 365 nm). Unfortunately the application of only Alizarin Complexone and Xylenol Orange in many of the specimens resulted in the two dyes being indistinguishable from one another; therefore no distinction could be made between pre-existing damage and that created during loading. All microdamage measured was either test-induced damage or was present in the specimen prior to testing.

Microcracks were found to occur individually, rather than in groups. However, when a higher incidence of damage was observed, a greater interaction between cracks could be identified. The majority of microcracks were found in interstitial bone, without crossing

the boundaries of primary or secondary osteons. In specimens with a low incidence of microdamage, damage was located around the perimeter of the specimen.

Figures 3.40 and 3.41 show a series of interstitial microcracks when viewed under green and UV incident light.

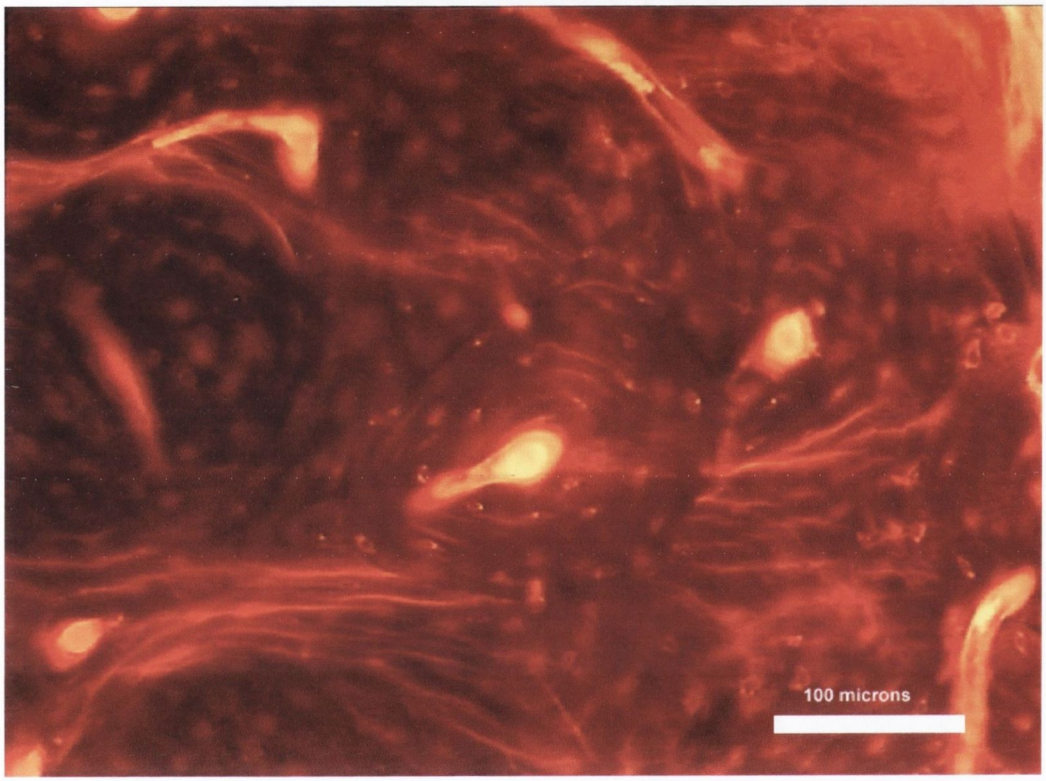

Fig. 3.40 Examples of microcracks labelled with xylenol orange, observed under green light at a magnification of x250. All microcracks were located in interstitial bone, 100 μm scale bar

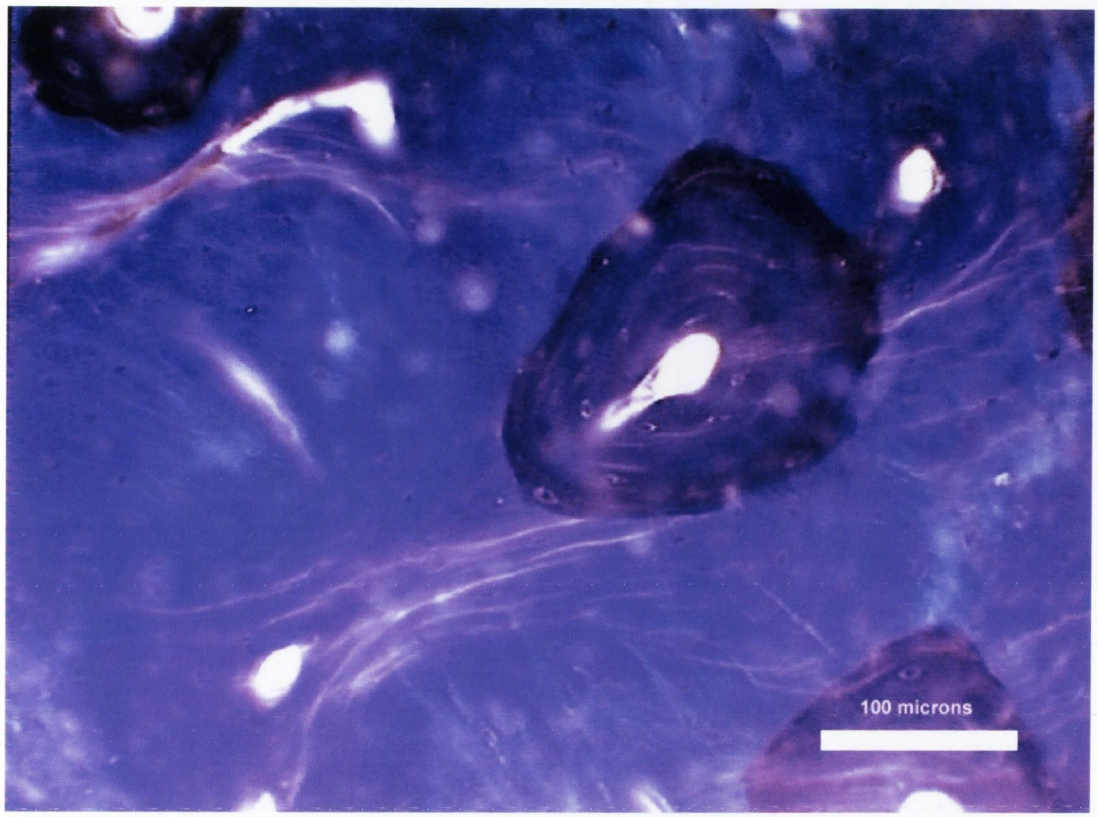

Fig. 3.41 Examples of microcracks labelled with xylenol orange observed under UV epifluorescence at a magnification of x250. All microcracks were located in interstitial bone, 100 μm scale bar

Histological examination of a number of sections identified areas of diffuse microdamage, where microcracks are clustered together in such a way that they cannot be individually identified. Damage of this nature was often directly associated with the main fracture surface, or a macrocrack passing through the specimen. For this reason damage of this type was not quantified. Figure 3.42 shows diffuse microdamage viewed under UV incident light.

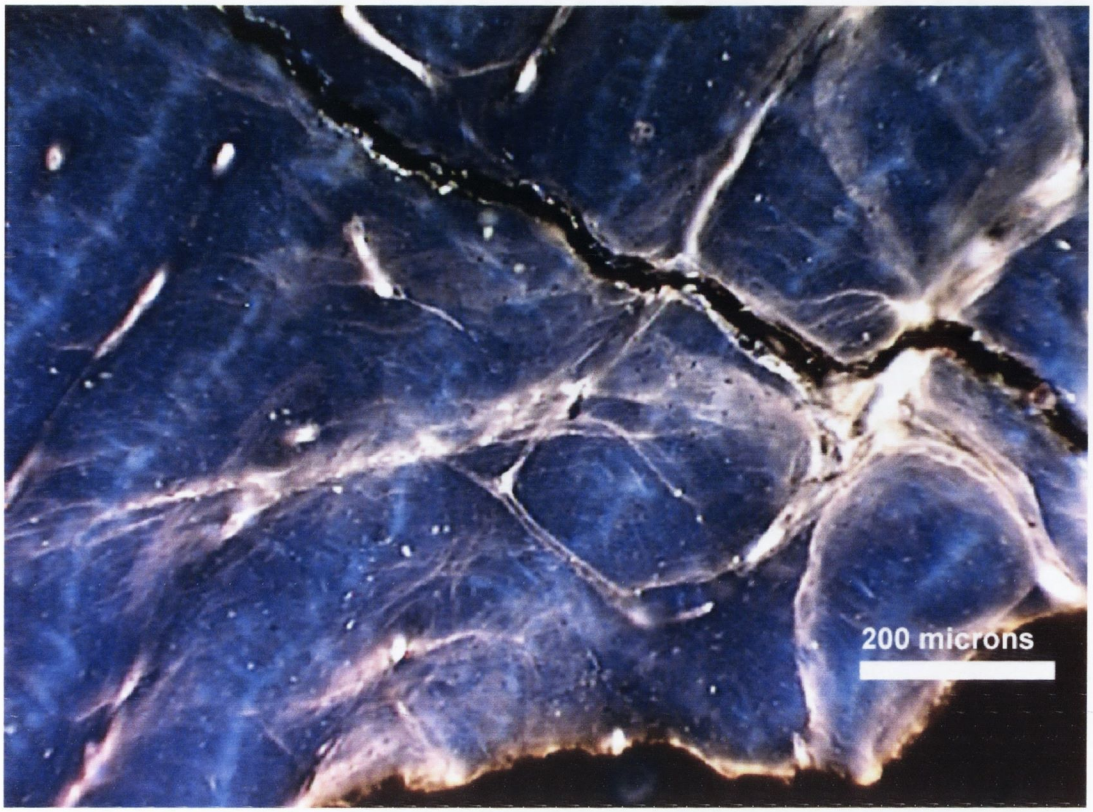

Fig. 3.42 An example of diffuse microdamage labelled with xylenol orange, observed under UV epifluorescence at a magnification of x125. These microcracks were not quantified, because they were directly associated with the main fracture surface. 200 μm scale bar

Histological data gathered from all specimens tested at 130 MPa are presented in Table 3.7. This includes information on crack number, crack length, crack location, as well as numerical crack densities and surface crack densities for each specimen.

Table 3.7 Creep crack data – 130 MPa

Specimen	a	b	c	d	e	Mean
Time to failure (s)	897	5638	59355	77196	79039	17888
Number of cracks	5	36	19	5	9	14.8
Mean Crack Length (μm)	217.20	334.95	203.31	179.74	131.08	257.91
Numerical crack density (no./mm^2)	0.016	0.201	0.104	0.015	0.03	0.073
Surface crack density (μm/mm^2)	3.47	67.34	21.09	2.73	3.87	19.70
Ratio, Interstitial:Osteonal	80:20	72:28	90:10	100:0	89:11	86:14

Considerable variations in crack number and crack length were found, with crack numbers ranging between 5 and 36 and crack lengths between 131 and 335 μm. These large variations are reflected in the measured numerical and surface crack densities, which showed ranges of 0.015 to 0.201 cracks/mm2 and 2.73 to 67.34 $\mu m/mm^2$ respectively.

Table 3.7 also documents the ratio of interstitial to osteonal cracks. This clearly shows that crack location is weighted towards interstitial cracks, with very few osteonal cracks being identified.

Statistical analysis showed that no significant correlation existed between creep life and any of parameters identified in Table 3.7 for two tailed t-tests ($p>0.05$), however at the one-tailed (prior conception that a positive correlation would exist) level a significant positive correlation exists between creep life and the percentage of interstitial microcracks (Pearson's $R=0.873$, $p<0.05$). Likewise, a significant negative correlation exists between time to failure and the percentage of osteonal microcracks (Pearson's $R=-0.873$, $p<0.05$). Under this scenario the null hypothesis would be that longer times to failure are associated with specimens that inhibit the development of osteonal microcracks.

3.3 High Temperature Fatigue

A total of ten specimens of bovine compact bone were fatigue tested at 80 MPa whilst being held at 50°C. Eight of the ten specimens failed outright with the main fracture plane consistent with that observed in room temperature fatigue and creep studies. Two specimens did not fail and testing was interrupted at approximately 280,000 fatigue cycles with no immediate indications of failure; neither specimen observed a noticeable reduction in modulus consistent with the onset of failure (Taylor et al., 1999). However histological examination indicated that in one of these specimens a large macrocrack was present suggesting that failure would have resulted under continued fatigue cycles. Figures 3.43 and 3.44 show examples of microdamage developed during testing.

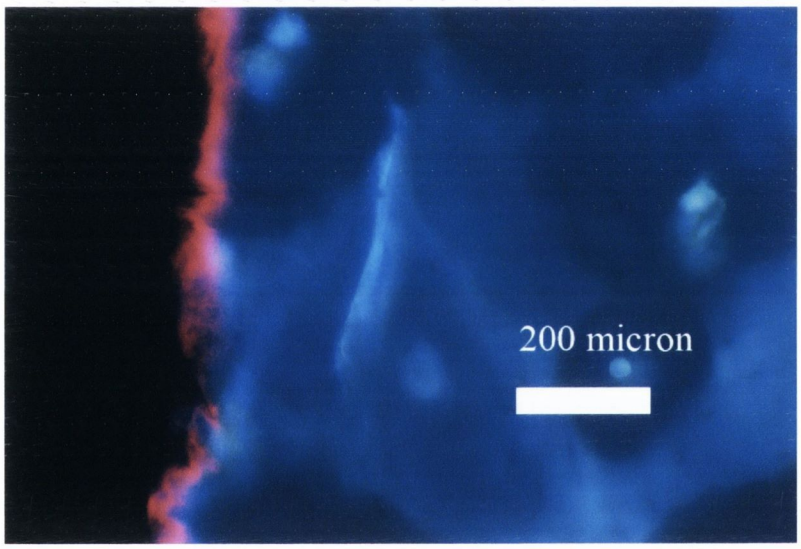

Fig. 3.43 Fatigue microcrack stained with Calcein Blue, microcrack growth is halted by a secondary osteon. 200 μm scale bar

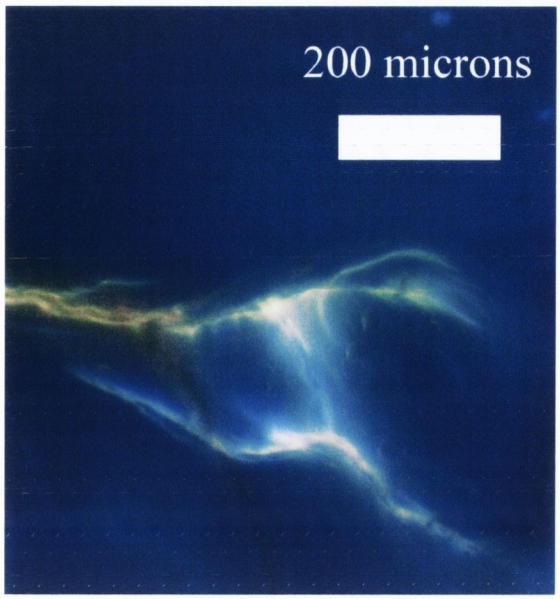

Fig. 3.44 Propagating fatigue microcrack stained with Xylenol Orange and Calcein. 200 μm scale bar

Figure 3.45 is a box plot diagram demonstrating the variation in number of cycles to failure for all high temperature fatigue tests. Figure 3.45 shows that for fatigue tests at 80 MPa with an operating temperature of 50°C, the median number of cycles is 53,113 with lower and upper quartiles of 16,837 and 209,105 cycles. The sample median represents the middle value where 50% of the data are on either side of this value. The boxed in part within each plot surrounds the middle half of the data. The lower edge of the rectangle represents the lower quartile, the higher edge represents the upper quartile, and the line in the middle of the rectangle is the median. The distance between the two edges of the rectangle is called the interquartile range. The lines (whiskers) extending from the boxes represent the tails of the distribution; they extend to the farthest point within 1.5 interquartile ranges from the quartiles. Points farther away are marked individually as outliers. By taking log transformations of the data, the mean number of cycles to failure was calculated to be 57,317 cycles with a corresponding minimum and maximum error of 147,321 and 222,993 cycles calculated according to Equation 3.3.

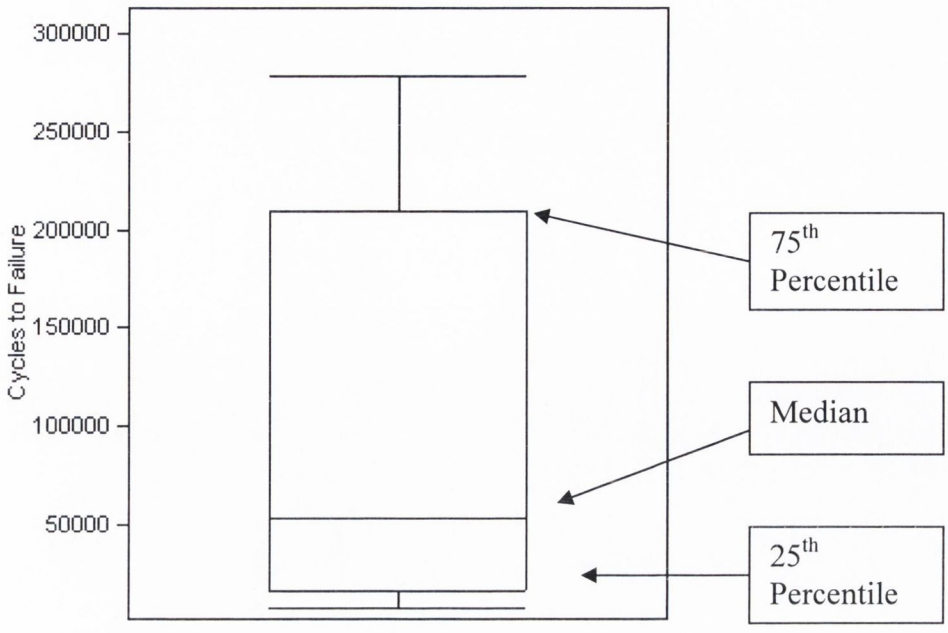

Fig. 3.45 Box plot diagram – Distribution of fatigue cycles to failure for all specimens

3.3.1 Microcrack densities

Figures 3.46 through 3.49 show the accumulation of microdamage over time for all high temperature fatigue tests. This information is presented in the form of numerical crack density (number of cracks occurring per mm^2) and surface crack density (total crack length per mm^2). Figures 3.47 and 3.48 are rescaled representations of Figures 3.46 and 3.48, designed to highlight crack accumulation in greater detail during the first 100,000 cycles of testing. A total of 1275 cracks were measured in all ten specimens.

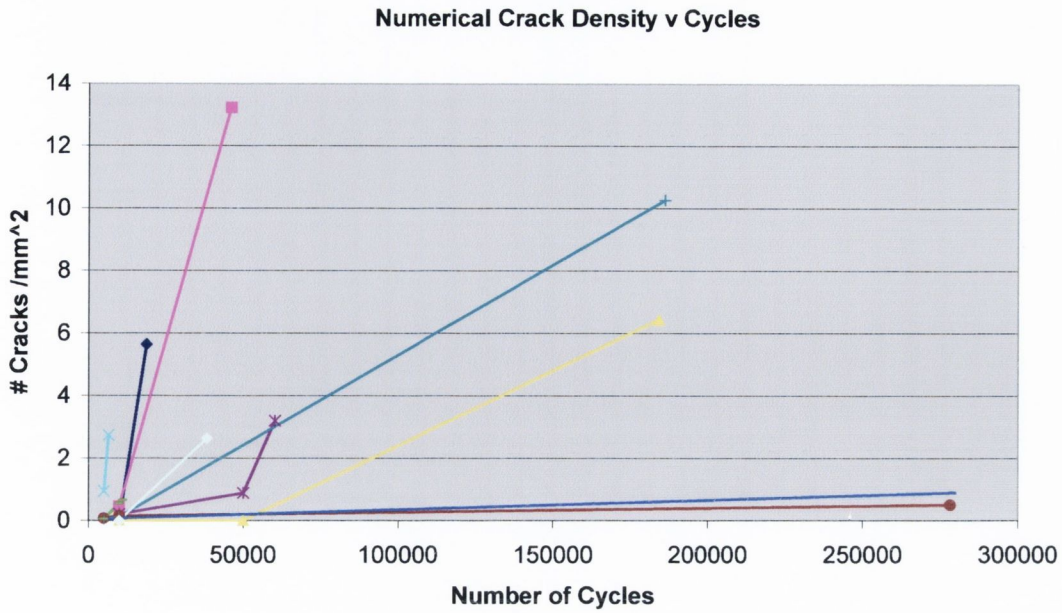

Fig. 3.46 Fatigue numerical crack density versus number of cycles (a)

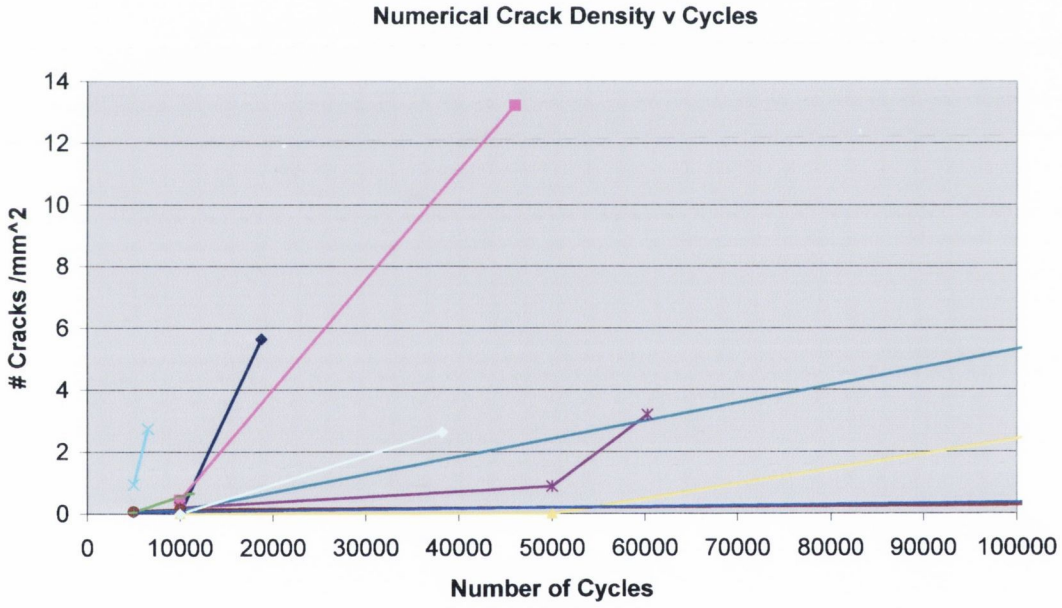

Fig. 3.47 Fatigue numerical crack density versus number of cycles (b)

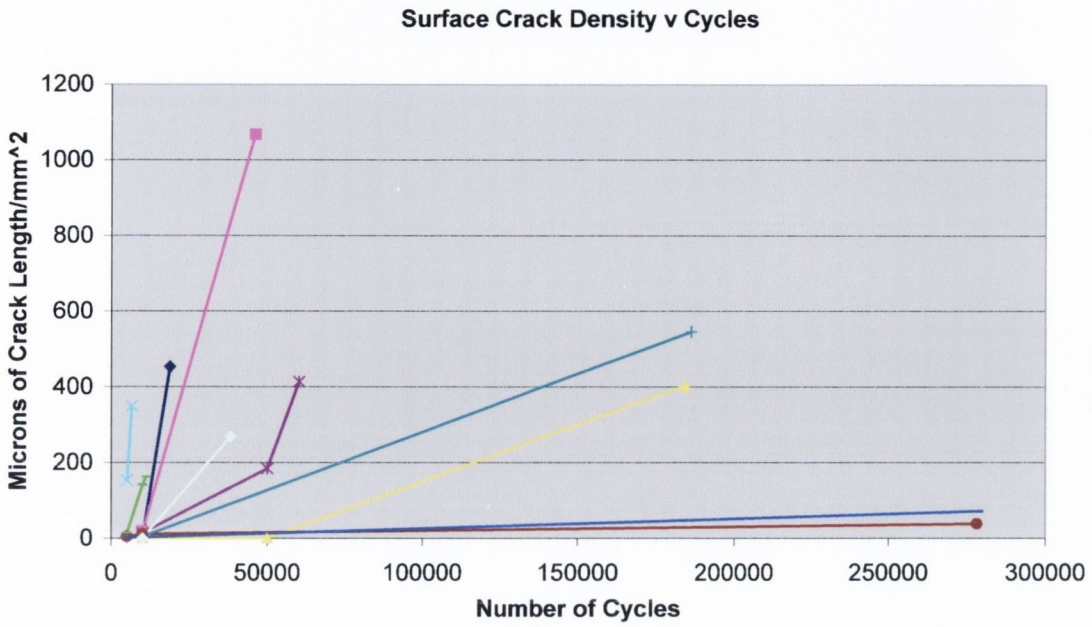

Fig. 3.48 Fatigue surface crack density versus number of cycles (a)

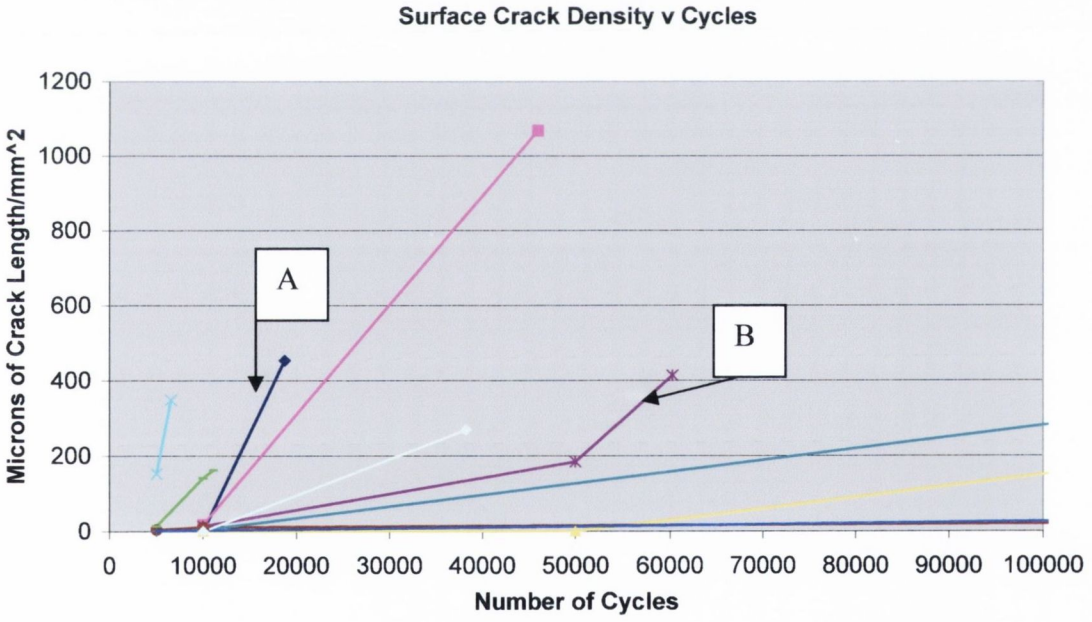

Fig. 3.49 Fatigue surface crack density versus number of cycles (b)

The general patterns observed in Figures 3.46 to 3.49 indicate continuous damage accumulation. However, as can be observed from the data point markers, very few specimens have accurate values of microdamage in the period immediately before failure. Only two out of the ten specimens fatigue tested have accurate values for

microdamage closer to the point of failure, these are highlighted as A and B in Figure 3.49. These two individual tests would suggest that the majority of damage accumulates towards the end of the end of a fatigue test, just prior to failure. Figure 3.50 plots the data for numerical crack density for all failed specimens against the ratio of number of cycles over number of cycles to failure for each individual specimen. This figure also suggests that the majority of damage occurs towards the end of the test where damage is seen to rise rapidly with the onset of failure. Figure 3.50 indicates that damage accumulation was very slow for the first half of a specimen's lifetime.

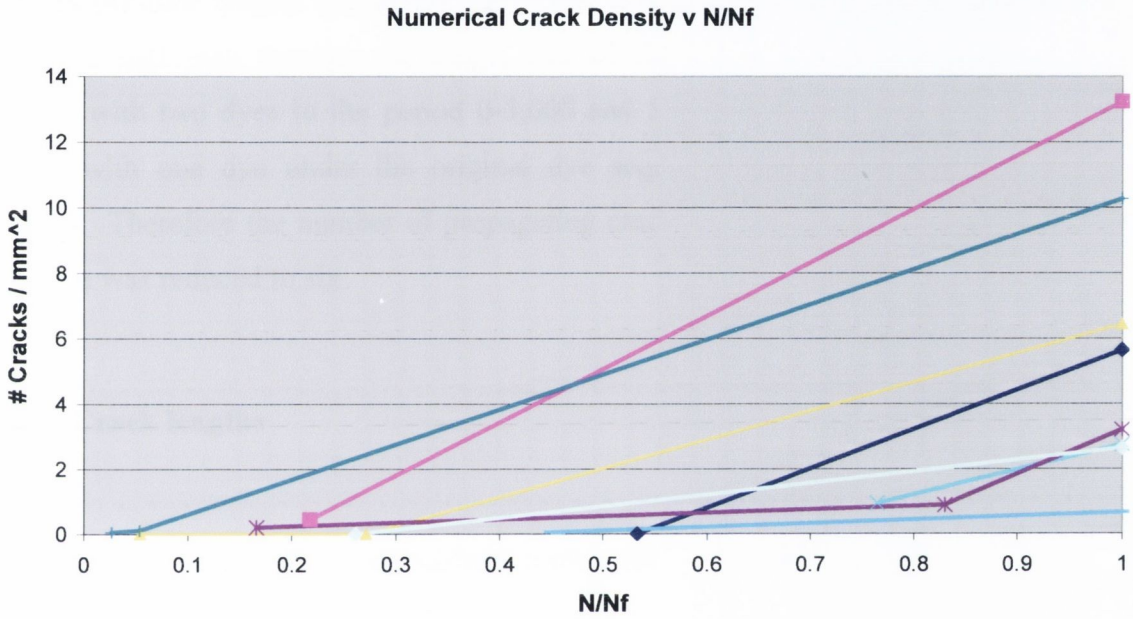

Fig. 3.50 Numerical crack density versus the fraction of fatigue lifetime (N/N_f)

Due to the degree of scatter in the results shown in Figures 3.46 through 3.49, mean values for numerical and surface crack densities do not truly reflect the diversity of results obtained for the greatest part of a high temperature fatigue test. Mean values for numerical and surface crack densities can only be obtained with some confidence towards the start of a fatigue test and these are shown in Table 3.8 for crack densities after 5,000 and 10,000 cycles respectively.

Table 3.8 Microcrack density – Fatigue 80 MPa – 50°C

Number of cycles	0-5,000	5,000-10,000
Num. Density	0.234 (SD: 0.40)	0.246 (SD: 0.25)
Surf. Density	34.796 (SD: 65.94)	39.207 (SD: 64.20)

A total of eight propagating microcracks were observed from histological studies of the high temperature fatigue specimens. However, given the change in the dye sequence employed half way through the study, two of these propagating cracks that were labelled with two dyes in the period 0-5,000 and 5,000-10,000 cycles would only be stained with one dye under the original dye sequence employed for the first five samples. Therefore the number of propagating cracks observed under the original dye sequence was reduced to six.

3.3.2 Crack lengths

Crack length was monitored throughout testing for all fatigue specimens through the timing of different dye applications. The 1,275 microcracks measured in the current study were found to have a mean crack length of 80.77 μm with a standard deviation of 133.47 μm. Figures 3.51 and 3.52 show the variation in mean crack length over time for all high temperature fatigue specimens. In all graphs of crack length, mean crack length is calculated on a cumulative basis. Where a mean value is taken from all crack measurements, for all cracks formed up until that number of cycles.

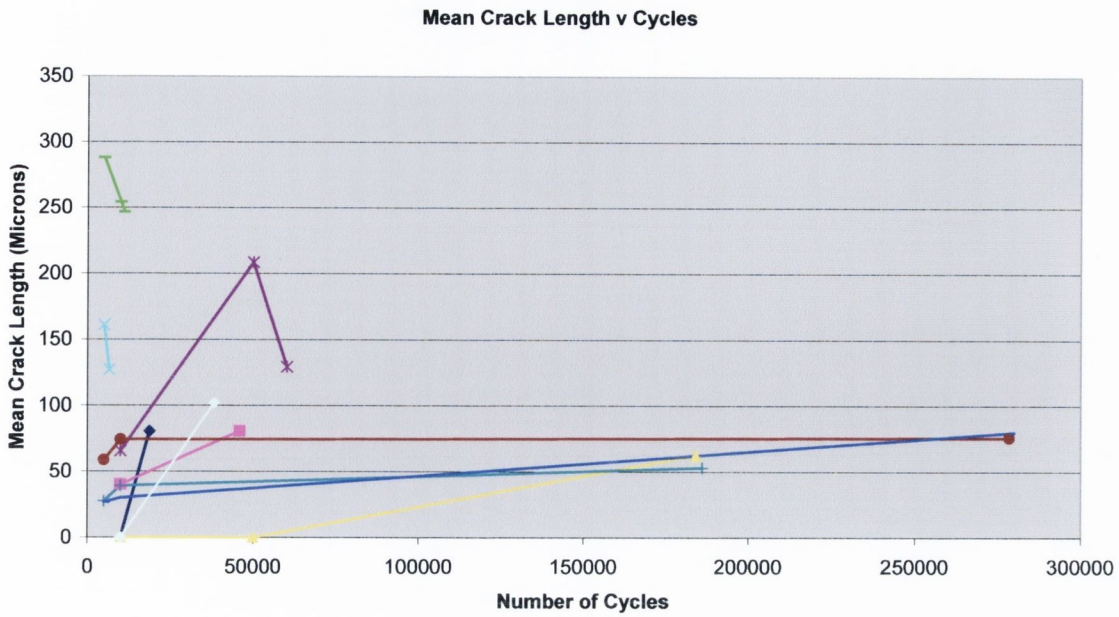

Fig. 3.51 Fatigue mean crack length versus cycles, specimen by specimen (a)

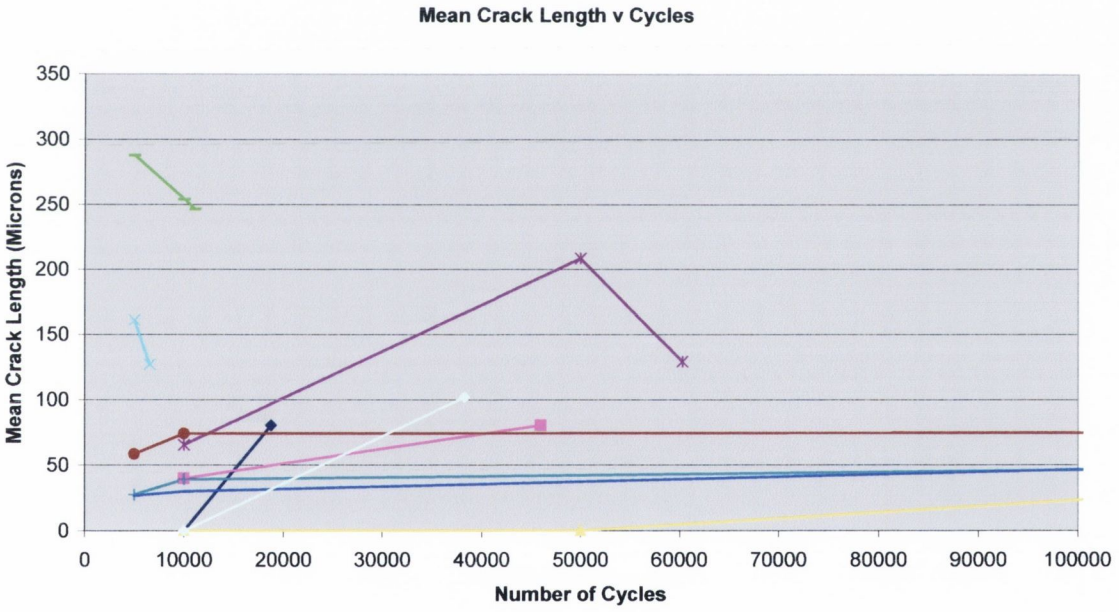

Fig. 3.52 Fatigue mean crack length versus cycles, specimen by specimen (b)

Given the considerable scatter in time to failure and the variations in dye sequence, which attempted to cater for such variations, only limited values for mean crack length as a function of number of cycles can be calculated from the data shown in Figures 3.51 and 3.52; this information is presented in Figure 3.53.

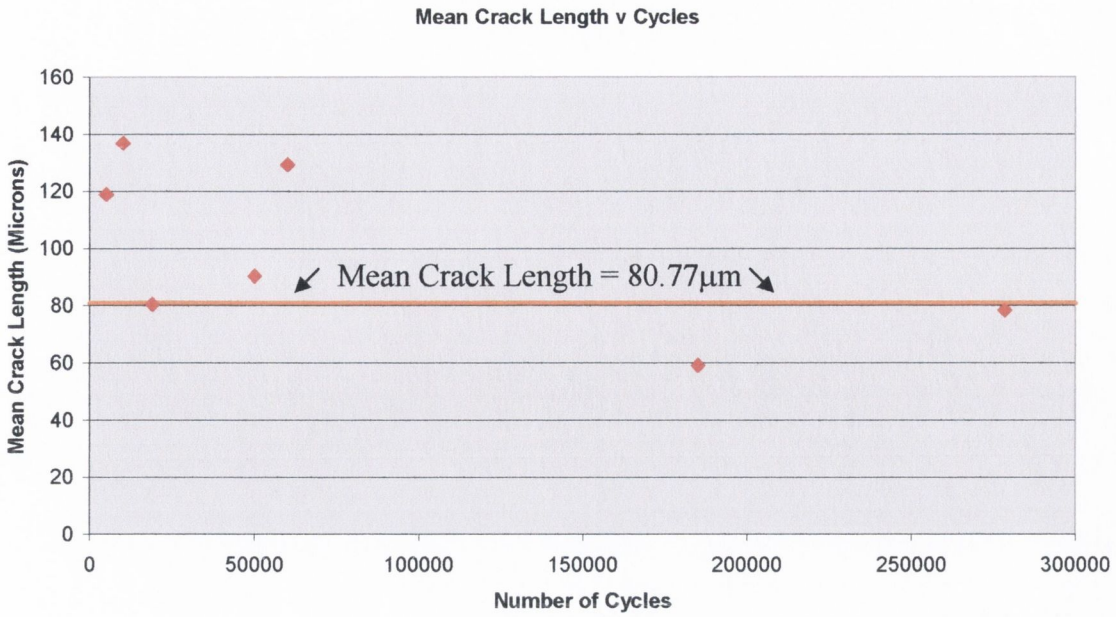

Fig. 3.53 Fatigue mean crack length over time

Figure 3.53 represents the mean crack length at a given number of cycles from all available data from the high temperature fatigue tests. Due to the degree of scatter observed in the number of cycles to failure, as the number of cycles in Figure 3.53 increases, a reduced number of data points are available to calculate the mean crack length after that number of cycles. Figure 3.53 also shows the overall mean crack length of 80.77 µm across all 1275 microcracks from all ten specimens. Table 3.9 shows the mean crack length for each value of number of cycles shown in Figure 3.53 along with the number of cracks measured for the given number of cycles and the number of samples from which crack measurements were taken in calculating these values.

Table 3.9 Fatigue mean crack length over time

Number of Cycles	Mean Crack Length (μm)	Number of cracks measured	Number of samples with cracks measured for this number of cycles
5,000	118.84	31	5
10,000	136.83	53	9
19,000	80.42	232	1
50,000	90.29	280	3
60,000	129.23	76	1
185,000	59.00	487	2
278,000	78.35	96	2

3.4 High Temperature Creep

A total of ten bovine compact bone specimens were creep tested at an operating temperature of 50°C. Five specimens were tested with an applied creep stress of 120 MPa and a further five specimens were tested at a creep stress of 130 MPa. All specimens were observed to fail outright within a maximum time period of 58,331 seconds (16.2 hours). The maximum time to failure recorded at 130 MPa was 18,268 seconds (5.1 hours). Consistent with the earlier room temperature tests, complete failure of the specimen resulted in a principal fracture plane oblique to the specimen axis, at an approximate angle of 40° to 60° to the horizontal.

The three characteristic stages of creep failure identified as primary, secondary and tertiary creep were all observed in these high temperature creep studies. Strain-time histories were generally consistent with that described in Figure 3.26. However, some specimens showed a discontinuity part way through the secondary creep regime where a step like pattern can be observed. Following the discontinuity, creep continues in a similar manner to that observed prior to the discontinuity, until the onset of tertiary

creep is observed. An example of this behaviour is shown in Figure 3.54 and is believed to represent internal failure within the specimen, or formation of a macrocrack.

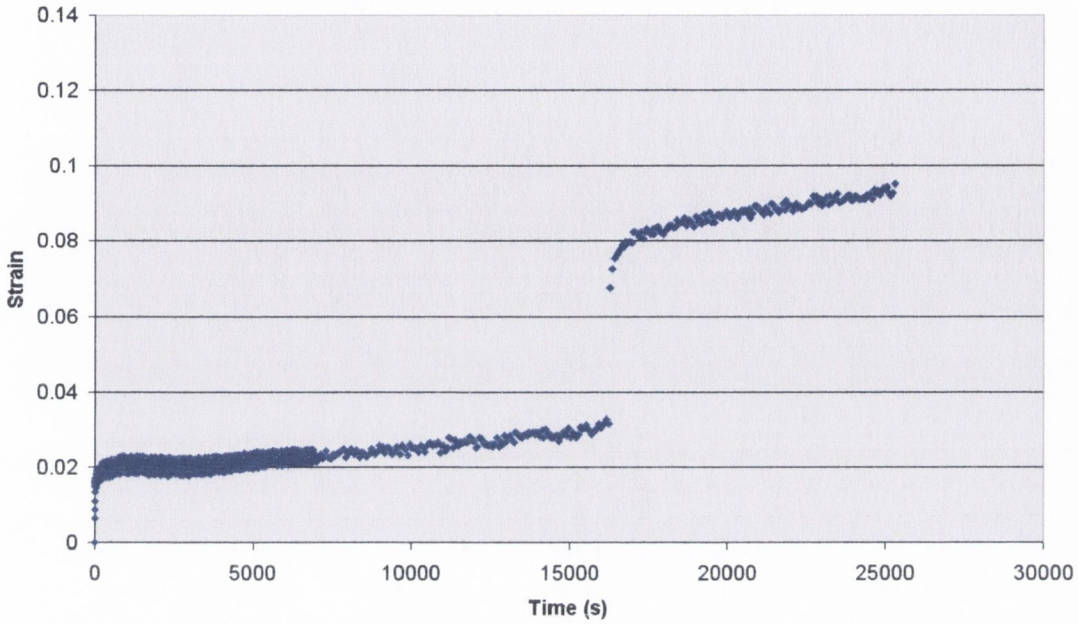

Fig. 3.54 Creep strain history demonstrating step discontinuity during secondary creep

3.4.1 Time to Failure

At both stress levels, all specimens showed complete failure within a reasonable period of time, the maximum time to failure recorded for all high temperature creep tests was 58,331 seconds (16.2 hours) at a stress level of 120 MPa. The maximum time to failure recorded at 130 MPa was 18,268 seconds (5.1 hours). Minimum times to failure recorded at 120 and 130 MPa were 2,358 seconds and 243 seconds respectively. Figures 3.55 and 3.56 show the variation in time to failure for all specimens using two different methods, Figure 3.55 is a box plot diagram describing creep life for all specimens at 120 and 130 MPa, and Figure 3.56 is a log-log scatter plot showing all time to failure data points across the two stress levels.

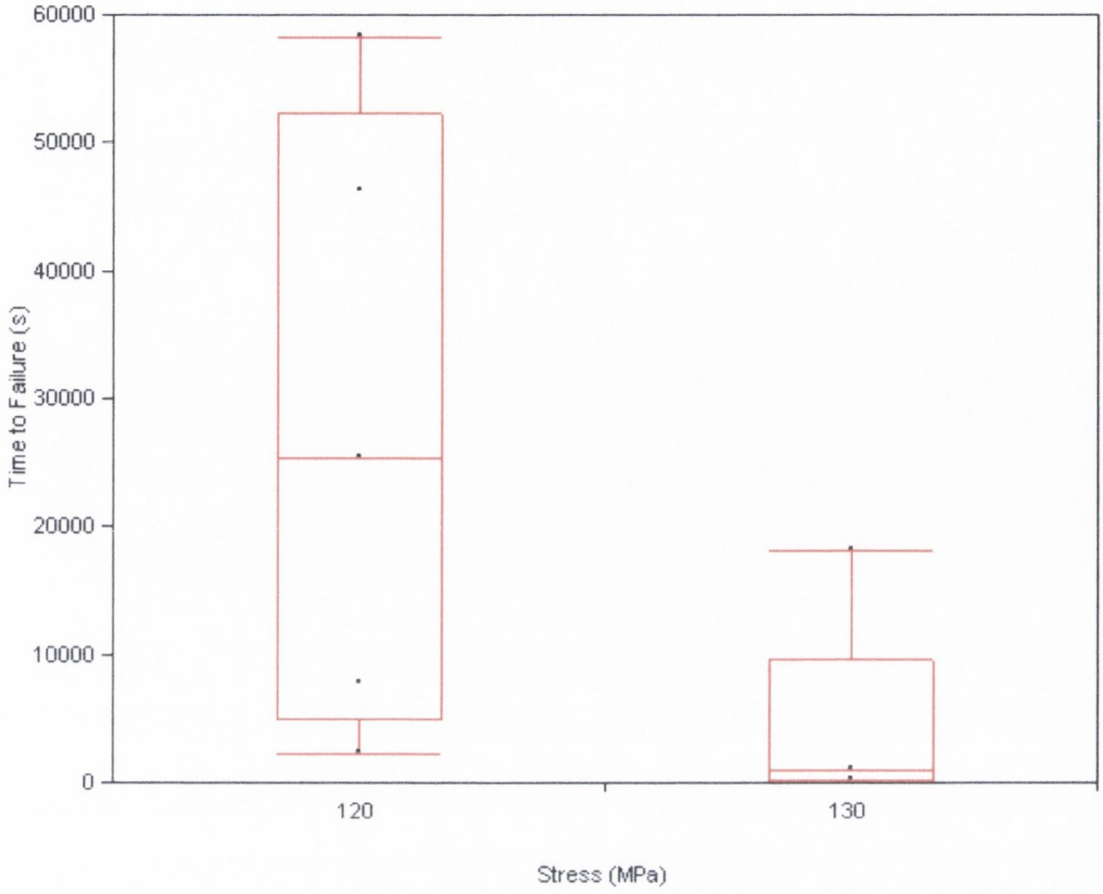

Fig. 3.55 Box plot diagram – time to failure for high temperature creep specimens

Table 3.10 Median and quantiles – time to failure high temperature creep

Quantiles

Level	Minimum	10%	25%	Median	75%	90%	Maximum
120	2358	2358	5100	25365	52319	58331	58331
130	243	243	276	997	9674	18268	18268

Figure 3.55 shows the variation in time to failure for the two stress levels. There is far greater spread in the data at 120 MPa than at 130 MPa. Table 3.10 shows the various quantiles used to make up the box plot. Using a Mann-Whitney U test, a nonparametric test for two independent samples, (nonparametric or distribution-free tests, making no assumptions about the underlying distribution of the data) a statistically significant difference exists between the observed times to failure at 120 and 130 MPa ($p<0.05$). The data show a 25-fold increase in the median time to failure between the two stress levels.

Fig. 3.56 Log-log plot of stress versus time to failure for all high temperature creep specimens

Figure 3.56 shows the variation in time to failure for all specimens tested at 50°C. It can be seen from the graph that an increase in the compressive stress level has the effect of reducing the time to failure as expected. By taking log transformations of these data points and then calculating the mean of these values, mean values for time to failure along with minimum and maximum error values can be calculated in the same way as described previously. Mean values for time to failure along with the corresponding minimum and maximum error values are shown in Table 3.11. The data show a 15-fold increase in the mean time to failure between the two stress levels.

Table 3.11 Mean time to failure – high temperature creep tests

Stress (MPa)	Mean time to Failure (s)	Error Min-Max (s)
120	16,616	4351 – 63462
130	1,081	194 – 6021

Through log transformations of the data and subsequent regression analyses, a power law function for time to failure as a function of the normalised stress (applied stress normalised by a Young's Modulus of 20.4 GPa) was developed for these high temperature creep studies. These data are presented in Figure 3.57 along with the function derived from the transformed data, the data shown in Figure 3.57 are linear on

a log-log plot, similar to the power law creep behaviour of other materials. Equation 3.7 describes the power law function derived from the data.

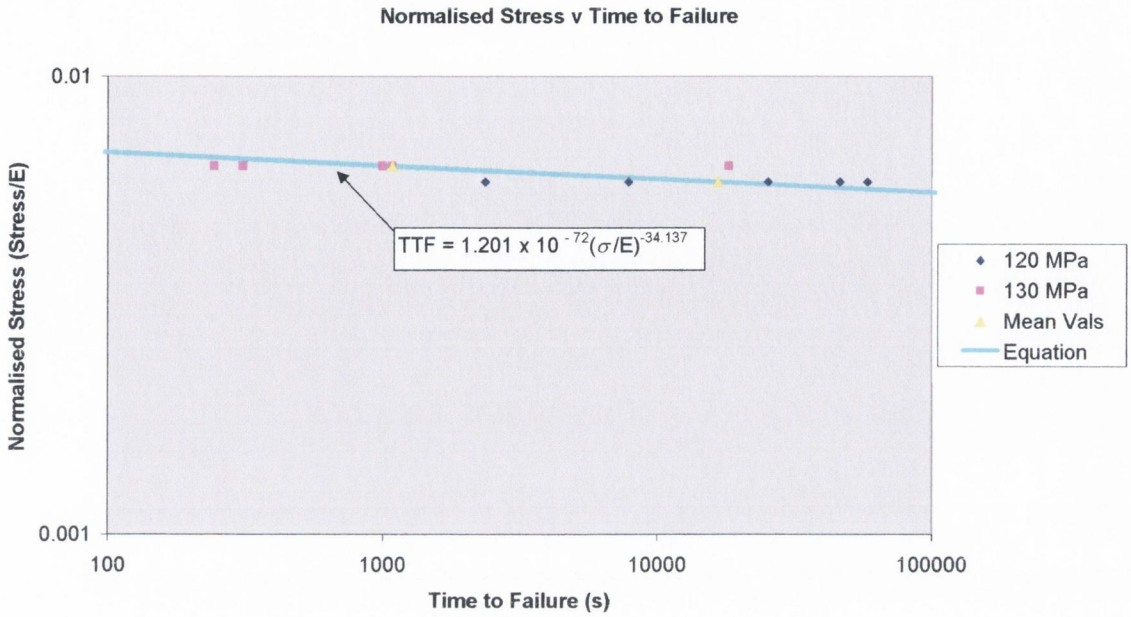

Fig. 3.57 High temperature creep – normalised stress versus time to failure (s)

3.7

$$t_f = 1.201\times10^{-72}\left(\frac{\sigma}{E}\right)^{-34.137}, r^2 = 0.50, n = 10, p = 0.023$$

Whilst indicating the expected fall in time to failure with increasing stress the inherent scatter in the data result in a relatively poor fit r^2=0.5

3.4.2 Steady State Creep Rate

Regression analyses indicated that, like the room temperature tests, a strong and significant power law relationship exists between steady state creep rate ($d\varepsilon/dt$) and normalised stress (σ/E) at these elevated temperatures.

3.8

$$d\varepsilon / dt = 4.176\times10^{48}(\sigma / E)^{24.60} r^2 = 0.37, n = 10, p = 0.06$$

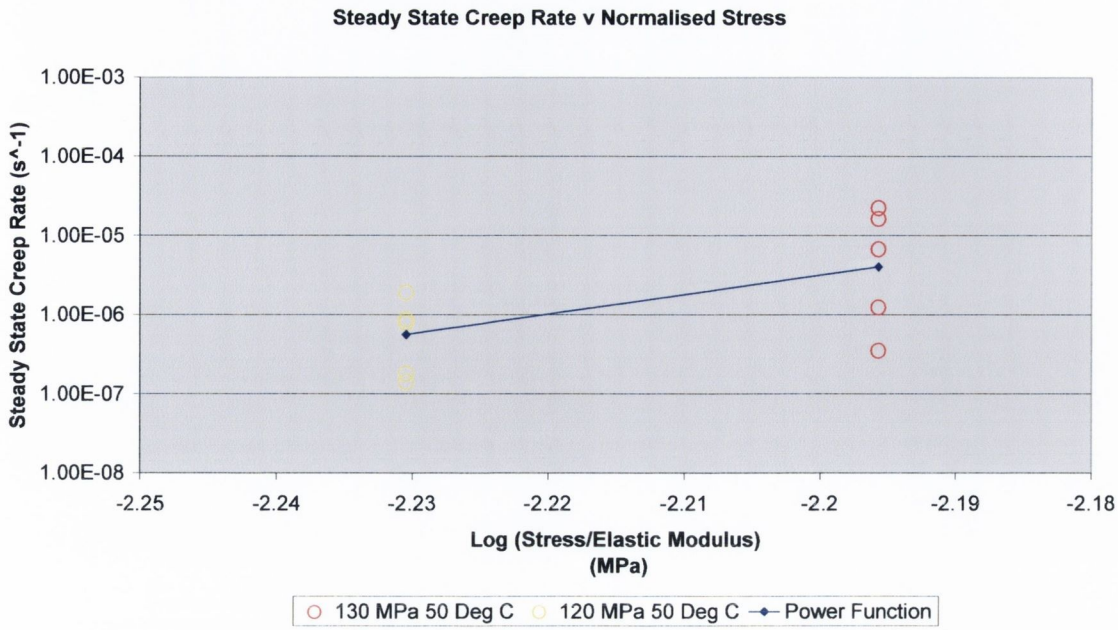

Fig. 3.58 Steady state creep rate ($d\varepsilon/dt$) versus log normalised stress

Steady state creep rate was found to vary from $1.786 \times 10^{-7}\ s^{-1}$ to $2.227 \times 10^{-5}\ s^{-1}$ and individual values for all specimens can be found in the appendix.

3.4.3 Histology

All specimens creep tested at 130 MPa were examined for the presence of microcracks using the techniques described. Any pre-existing damage was stained with Alizarin Complexone and Calcein stained any test-induced damage fluorescent green. An example of a Calcein stained creep microcrack is shown in Figure 3.59.

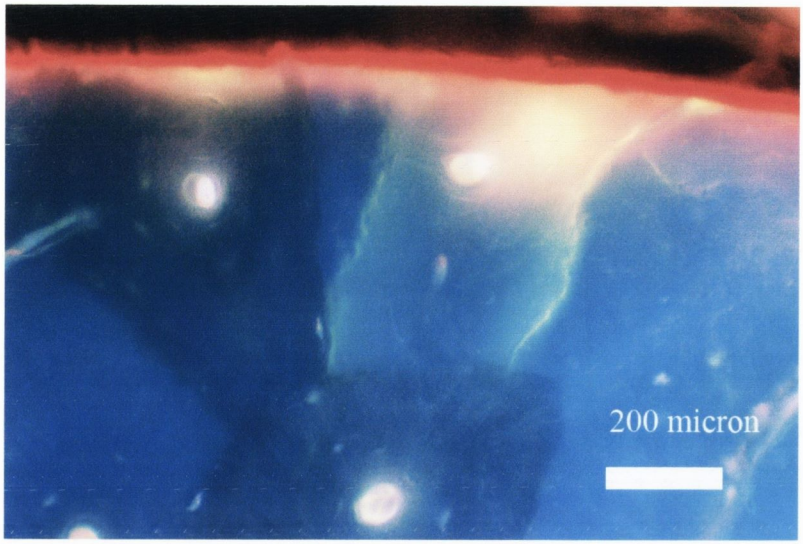

Fig. 3.59 Microcrack stained with Calcein during creep tests at 130 MPa with an operating temperature of 50°C. 200 μm scale bar

Although individual in nature, in areas of considerable microcrack accumulation, interaction between individual microcracks could be observed. This was particularly noted in areas close to the fracture surface of the specimen or in close proximity to a macrocrack passing through the specimen. Any microdamage directly associated with the fracture surface of the specimen was not counted for the purpose of this study. In all specimens examined, significant microdamage could be observed throughout the sections. In areas of considerable staining, the microscope's green FITC filter (excitation wavelength 465-495 nm) was employed to give increased contrast with its improved signal to noise ratio. The vast majority of microcracks observed were located in interstitial bone without crossing osteon boundaries. Histological data gathered from all high temperature creep specimens tested at 130MPa are shown in Table 3.12.

Table 3.12 Histological creep data 50°C

Specimen	a	b	c	d	e	Mean
Time to failure (s)	243	18268	309	997	1080	1081
Number of cracks	116	114	117	60	203	14.8
Crack Length (μm)	130.19	126.60	116.26	116.50	137.81	128.04
Numerical crack density (no./mm^2)	3.82	7.50	3.26	2.72	7.21	4.90
Surface crack density (μm/mm^2)	497	950	379	317	994	627
Ratio, Interstitial:Osteonal	90:10	90:10	93:7	97:3	95:5	93:7

The histological analysis indicates that microcrack location is considerably weighted towards interstitial microcracks with very few osteonal microcracks found in the specimens. Statistical analysis showed that no significant correlations existed between time to failure and any of the parameters identified in Table 3.12.

4 Discussion

The majority of the results presented in Chapter 3 depend upon the measurement of microdamage in one form or another and it was found that the fluorochromes used were effective markers of microdamage for all tests conducted. Successful labelling of microcracks formed at different stages of a specimen's life was achieved and microcrack growth was monitored successfully when cracks were labelled with two dyes at different stages of testing. Microcracks were easily identified through successful penetration of fluorescent agents deep into the bone matrix providing a reliable and effective marker of microdamage formation. The majority of microcracks were stained with only one dye and were therefore formed during a specific stage of testing without exhibiting continued growth over time. In the room temperature fatigue study 4% of microcracks at 50 MPa, 3% of microcracks at 60 MPa and less than 1% of microcracks at 70 MPa were shown to propagate during testing, similarly in the high temperature fatigue tests 0.5% of microcracks showed continued crack growth over time. These figures may however be underestimated given the techniques employed in section preparation (O'Brien et al., 2003). Furthermore, no cracks were labelled with three fluorochromes and no microcracks were labelled with the same agent in different regions of the crack length.

4.1 Fatigue

4.1.1 Microcrack accumulation in room temperature fatigue

The results presented in Section 3.1 show that for all tests the accumulation of microdamage appears as a stepwise function with some form of switching mechanism at around 100,000 cycles. The stepwise pattern observed in these results is different to those studies which measured damage accumulation as a reduction in modulus or stiffness (Zioupos et al., 1996 (Figure 4.6); Carter and Hayes, 1977b), where a continuous accumulation of damage over time was observed in fatigue tests on bone. Schaffler et al. (1990) showed an immediate loss of stiffness followed by a tendency to stabilise at low strain levels in tensile fatigue (Figure 4.1). These studies quantified damage by a damage parameter related to a change in material stiffness and did not quantify any visible physical damage in bone.

This difference is not surprising however given the two different methods used to describe damage. Damage will develop at all levels within bone's microstructure including those beyond the resolution of microscopy techniques. In composite materials an area of ultrastructural damage defined by increased molecular permeability, called the damage process zone (Schaffler et al., 1994b) can be identified outside of a primary crack (Fyhrie and Schaffler, 1994). Schaffler et al. (1996) support this idea of the development of damage at a level below which individual cracks can be identified when they studied stiffness losses of 18 – 30 % in fatigue specimens. The accumulation of dye-penetrated individual microcracks was not identified until 30% modulus degradation had been achieved, whereas the area fraction occupied by areas of diffusely stained bone matrix increased in direct proportion to the degree of modulus degradation. It can therefore be inferred that at some point in time this damage will become visible using microscopy techniques and will appear as a population of microcracks develops within the specimens.

The pattern observed in Figure 3.12 would certainly suggest that only after a certain point in time will uniform cracks start to form and then continue to grow; cracks will first form in weaker areas increasing in number until a saturation point is reached. In compressive loading crack initiation is more difficult than under tensile loading (Martin, Burr and Sharkey, 1998), supporting the observation that limited damage is observed early in the specimen's life, and only after the tissues resistance has been broken down will cracks start to form. Therefore the pattern observed in these tests could be anticipated given the method of loading and the level of detection associated with the techniques used to identify damage in this study. The simple scratch tests described in Section 2, demonstrate that the low incidence of microdamage identified early in testing is unlikely to be attributable to substitution of one dye for another dye. Whilst the simple scratch test cannot confirm penetration deep into the centre of the specimen and indeed some fatigue specimens did identify a concentration of damage toward the outer surface, damage stained with the first dye was not limited to the perimeter of the specimen. Therefore whilst not being totally conclusive, the low incidence of microdamage specifically identified early in testing is unlikely to be attributable to limited penetration of the first dye in the sequence.

Although a reduction in modulus was not recorded in the current study, it does reinforce the idea proposed by Burr et al. (1998), that bone can undergo significant modulus degradation before microcracks appear. This implies that the mechanical properties of bone can be significantly compromised before substantial crack accumulation is observed. Burr et al. (1998) propose a threshold-related non-linear damage accumulation for bone, observing that significant microdamage accumulation was not detected until bone had lost 15 % of its elastic modulus in a study of whole bones tested in four point bending, clearly a pattern which fits with the current data.

It can be seen from Figure 3.12 that when microdamage does start to accumulate the greater the stress, the faster the rate of damage accumulation. The graph also shows that after an initial accumulation of damage, damage stabilises towards some crack density at which fracture does not occur and at which the specimen is capable of experiencing further fatigue cycles with only a limited increase in microdamage. This stable value of microcrack density, or total microcrack density, that can be sustained without causing rapid failure is also seen to increase with the applied stress. This is in contrast to the ideas proposed by Martin, Burr and Sharkey (1998), where they suggested for bone loaded in compression, if continued loading breaks down the tissue's resistance to crack initiation, then the cracks which form would could continue to grow to failure. In a study by Zioupos et al. (1996) where they monitored modulus reduction in compact bone specimens fatigued in uni-axial tension, the accumulation of damage was observed to increase in a stable manner and only at the very end of a specimen's life was damage seen to increase rapidly (Figure 4.6). They noted that this stable damage level, or target value of damage as they describe, beyond which fracture becomes uncontrollable, was also seen to increase with increasing stress. This target value is identified in Figure 4.6 as D_t. This is in direct agreement with the findings of this work. A final prefailure increase in damage has not been observed, as these tests have not reached imminent failure.

This study indicates that for any given stress level there is an almost natural population of microcracks that will develop in such a way that will not have a detrimental effect on the structure of bone for a given period of time.

In Section 3.1 it was described how at 50 and 60 MPa no sign of failure was observed within 300,000 cycles. At 70 MPa with the exception of the outlier, failure was not observed within 300,000 cycles with some specimens continuing to approximately two million cycles without fracture. These stresses equate to strain ranges of between 2,500 and 3,500 με, below the modulus threshold of 4000 με described by Pattin et al. (1996) as necessary for a reduction in material modulus in specimens tested in compressive fatigue. These strains are also below the maximum compressive strains which have been observed in living bone (Nunamaker et al., 1990; Biewener, 1991). At these lower stress levels failure does not occur within a relevant period of time. Previous studies have previously estimated that the skeleton will experience two million major cycles (running climbing of stairs etc.) per year at a stress level of approximately 40 MPa (Taylor et al., 2002). A study of walking activity of patients with artificial hip joints (Wallbridge & Dowson, 1982) identified the number of gait cycles per year to be between 0.5 and 3 million cycles based on pedometer data.

In an adult animal's musculoskeletal system during high physiological activity peak periosteal strains have been shown to lie in the range 2000 – 3000 με (Rubin and Lanyon, 1982). Experiments have also shown that strains in excess of 3000 με can be generated during jumping (Martin, Burr and Sharkey, 1998). Providing explanation of the high incidence of shin splints in basketball players. Thoroughbred racehorses have been shown to generate strains in the range 5000 – 6000 με on the surface of their metacarpal bone, when running at racing speeds (Martin, Burr and Sharkey, 1998). During running Burr et al. (1996) noted tensile strains of 1200 με and shear strains of 2000 με in the human tibia.

A study by Schaffler et al. (1990) examined the long-term behaviour of compact bone specimens tested in tensile fatigue at low strain magnitudes and rates. Schaffler et al. cyclically loaded specimens in uni-axial tension between 0 and 1200 or 0 and 1500 με for up to 13 – 37 million cycles, these strains are characteristic of *in vivo* tensile strains as reported by a number of investigators during strenuous activities (Rubin and Lanyon 1982; Biewener et al., 1983; Biewener and Taylor, 1986; Burr et al., 1996). This is below the modulus threshold predicted by Pattin et al. (1996), for compact bone in tensile fatigue of 2500 με. In their study, fatigue damage was quantified by calculating

stiffness loss or decrease in specimen modulus over time, where cyclic loading was found not to cause fatigue failure in any specimen within their experimental period. In all specimens they observed an initial stiffness loss over a period of 500,000 cycles or more, after which specimen modulus stabilized and no subsequent change was detectable for the duration of their experiments. Accounting for the delayed observation of microdamage in this study due to the level of detection using fluorescent microscopy, it can be assumed that the pattern observed by Schaffler et al. (1990), below the suggested tensile threshold, is the same as that observed in the current study at strain ranges below the suggested compressive threshold.

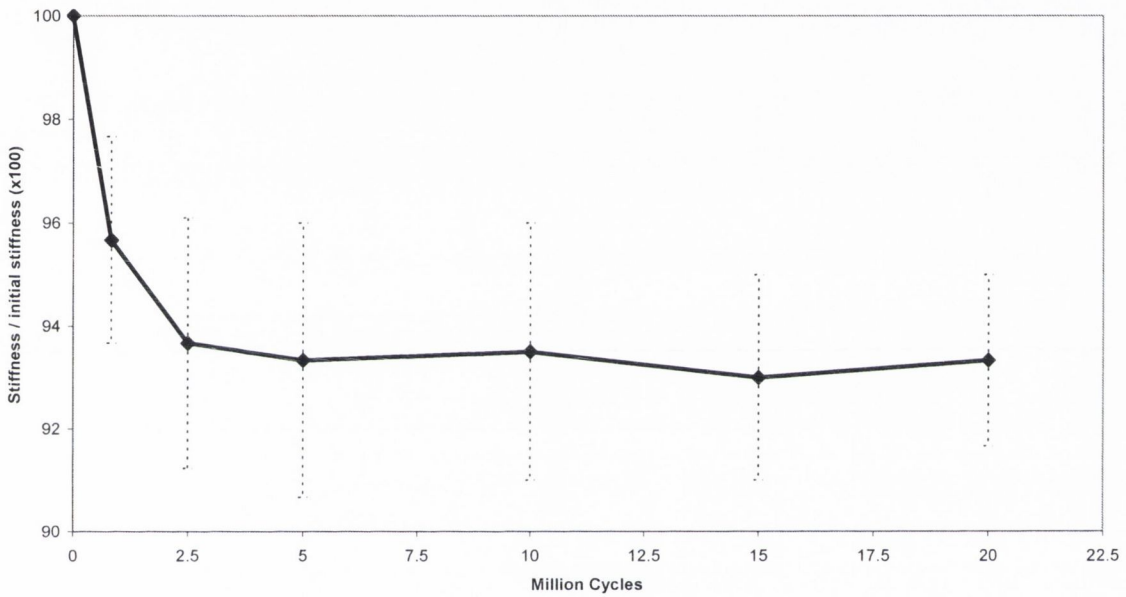

Fig. 4.1 Summary of fatigue induced modulus decreases versus number of loading cycles (after Schaffler et al., 1990)

As described earlier, previous studies (Carter and Hayes, 1976; 1977a; Carter et al., 1981a; b) have characterised fatigue of bone as a progressive increase in damage over time, however the findings of this study when combined with previous studies indicates that at stresses and strains more typical of normal physiological loading in the corresponding mode (i.e. tension or compression) the mechanisms by which lower stresses and strains affect bone may differ to those at higher magnitudes. This observation must be considered when examining any results which measure damage in bone. The mechanisms by which microdamage accumulates in bone at *in vivo* stresses are different to those observed at higher stresses.

The results of these experiments along with the study by Schaffler et al. indicate that *in vitro* fatigue failure of compact bone does not result within a physiologically relevant period of time, consistent with expectations from previous literature. Carter and Caler (1985) predicted that failure would occur in zero tension fatigue loading between 10 and 100 million loading cycles for a 1200 με loading range. Thus bone has an infinite life when subjected to tensile or compressive loading at strains below the suggested threshold values for tensile and compressive loading. Schaffler et al. described how each million cycles equates to 1136 miles of running without the possibility of remodelling or repair. Taylor et al., (2002) developed a theoretical model to simulate microdamage accumulation and repair in compact bone. Figure 4.2 taken from the Taylor et al., 2002 study shows how their model can be used to simulate failure in bone and compares the model with various other work. At physiological stress levels longer lives and increased scatter are observed.

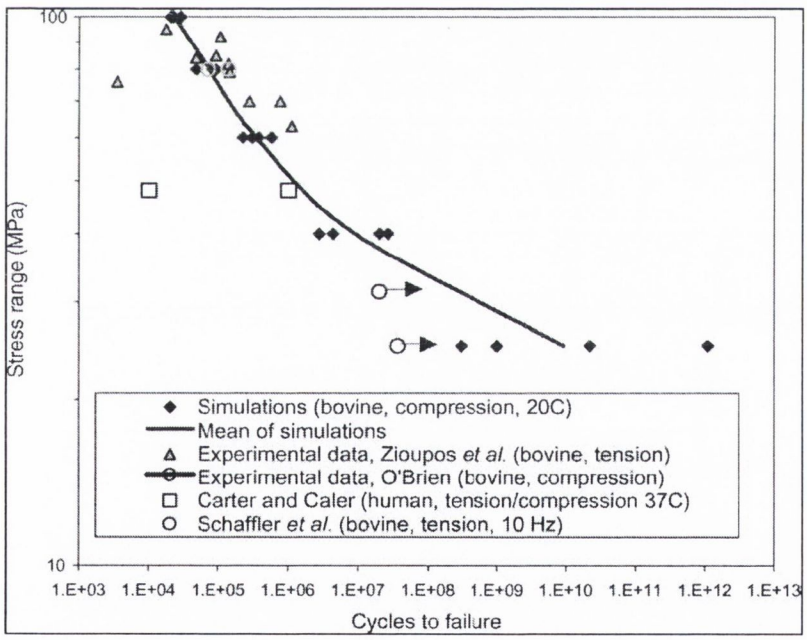

Fig. 4.2 Simulated stress/life curve for bovine bone in axial compression, plus experimental data from various sources (after Taylor et al., 2002)

These results could question the role of bone remodelling in the repair of microdamage, since the results would suggest that microdamage experienced at *in vivo* levels would not compromise the integrity of bone and therefore failure would be unlikely during a

persons lifetime. Nevertheless, in bone with an existing population of microcracks, brief periods of high strain loading, through things such as falls or stumbles could easily enlarge any existing damage, resulting in their propagation leading to failure (Agarwal and Broutman 1980; Reifsnider et al., 1983; Martin and Burr 1989). Therefore bone remodelling must remove any damaged bone in order to prevent the potential for microdamage developed during normal loading from becoming potentially disastrous in the event of some kind of trauma. Taylor (Taylor, 1998a, Taylor D et al., 1999, Taylor et al., 2002) addressed this issue by considering the stressed volume effect of specimens in relation to whole bones. This suggests that large bones will fail more easily than tests specimens for statistical reasons; principally being that there is an increased probability of weak regions being present leading to dangerous failure inducing cracks.

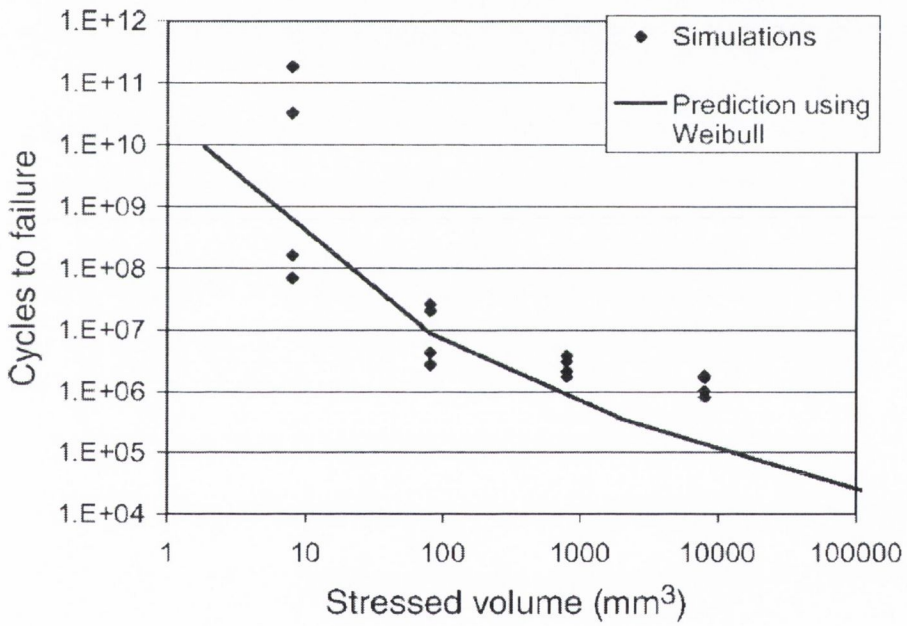

Fig. 4.3 The effect of stressed volume on N_f at 40 MPa (axial compression), (after Taylor et al., 2002)

Figure 4.3 shows the prediction of the stressed volume effect upon Taylor's (Taylor et al., 2002) model of microdamage accumulation. Taylor et al., found that the predicted number of cycles to failure will decrease considerably with increased size, where the life of whole bones being less than specimens by approximately an order of magnitude. Therefore demonstrating the requirement for bone remodelling due to the increased risk of fracture.

Figures 4.4 and 4.5 compare the accumulation of microdamage in the current set of experiments with those carried out in an earlier study by O'Brien et al. (2003) at a fatigue stress above that experienced during every day activities. The results from O'Brien et al.'s work reflect the accumulation of microdamage in compressive fatigue at a stress range of 80 MPa, approximately 4,000 με assuming a Young's Modulus of 20.4 GPa (Martin, Burr and Sharkey, 1998). It can be seen from the graph that in contrast to the current study, O'Brien et al. observe an immediate increase in microdamage from the very start of cyclic loading. The increase in damage accumulation quickly stabilises around 10,000 cycles with limited further increase in damage until just prior to failure at a mean number of cycles to failure of just less than 90,000 cycles.

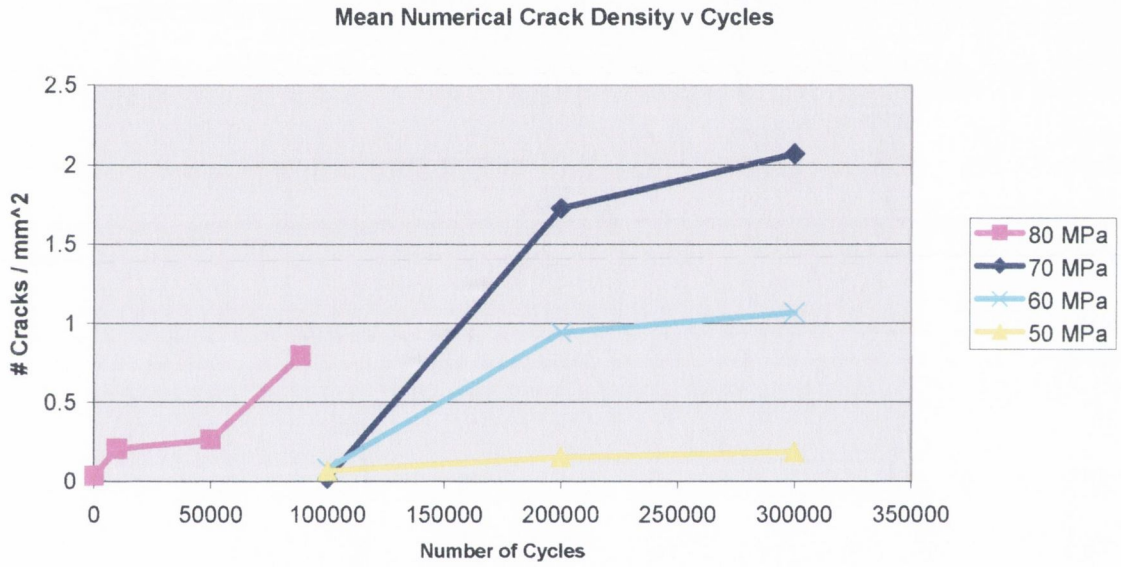

Fig. 4.4 Mean numerical crack density versus number of cycles - 50, 60, 70 (present study) & 80 MPa (O'Brien et al., 2003)

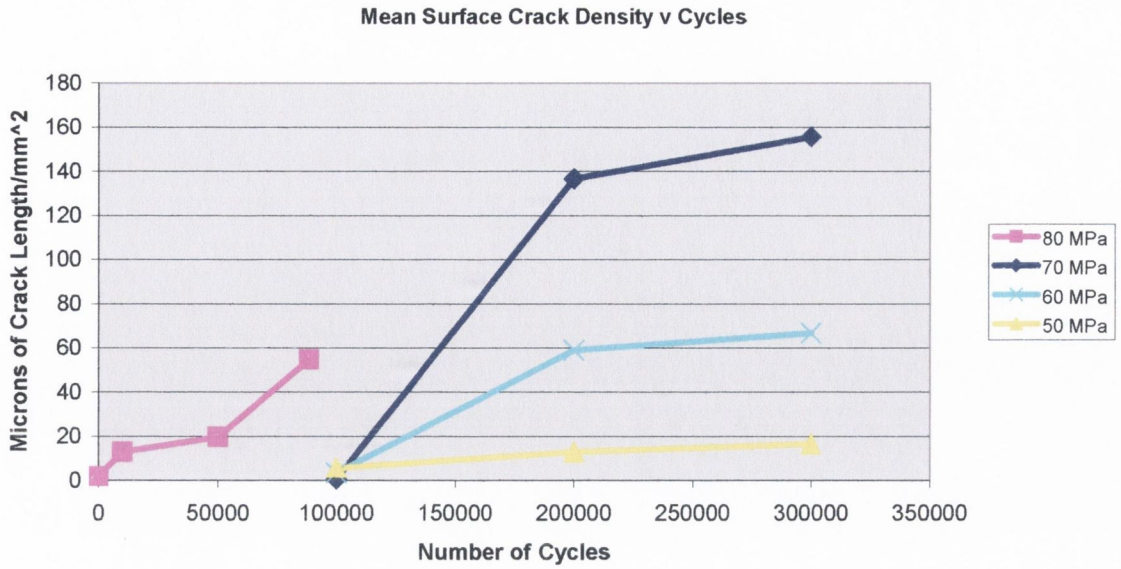

Fig. 4.5 Mean surface crack density versus number of cycles - 50, 60, 70 (present study) & 80 MPa (O'Brien et al., 2003)

Given that O'Brien et al. (2003) observes a continuous accumulation of microdamage from the very start of cyclic loading, this appears to reflect the continuous accumulation of damage observed in those studies that measured damage as a function of modulus reduction. However it was observed by Zioupos et al. (1996), that in fatigue tests conducted below a maximum stress of approximately 90 MPa, the accumulation of damage was very slow for approximately 20-30% of the complete lifetime, whereas above 90 MPa, accumulation of noticeable damage occurs from the very first cycle, suggesting some sort of transition. This is demonstrated in Figure 4.6 where each curve is identified by the stress level examined. It should be noted that Zioupos et al. used a maximum stress, whereas the current experiments and those of O'Brien et al. used a stress range, the maximum stress experienced in O'Brien et al.'s experiments would have been approximately 88MPa.

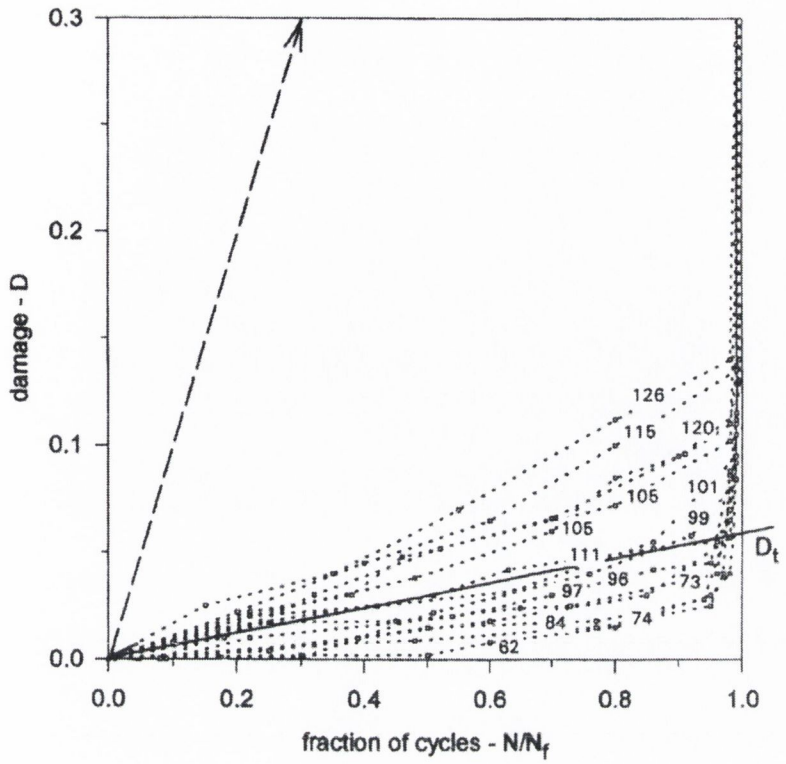

Fig. 4.6 Damage, D, versus the fraction of cycles to failure for different fatigue stresses (stress in MPa) (after Zioupos et al., 1996)

It can be noticed from Figure 4.4 that at 80 MPa failure occurs in a relatively short period of time when compared to those experiments at 50, 60 and 70 MPa, with a lower microcrack density than that observed at some of the lower stress ranges. This suggests that at low stress levels (50 – 70 MPa), larger amounts of damage can build up without failure occurring whereas as the stress range increases beyond 70 MPa (3,500με) crack accumulation develops more rapidly, without reaching the higher microcrack densities observed after prolonged testing. This transition in behaviour from the current experiments to that observed in O'Brien et al.'s study adds further credence to the existence of a fatigue limit or threshold for compact bone as postulated by Pattin et al. (1996), since the difference in behaviour being described would cover the period surrounding Pattin et al.'s suggested threshold for compact bone loaded in compressive fatigue.

Advances in microscopy techniques have been found to reduce the limit of detection for microcrack identification from 30 μm (O'Brien et al., 2003) down to approximately 10

– 15 μm (current work), the influence that this may have upon the difference in damage accumulation patterns is negligible. To confirm that any differences between the two studies were not due to improvements in microscopy techniques and were in fact representative of a change in behaviour, all microcracks less than 30 μm in length were artificially removed from the data sets at 50, 60 & 70 MPa and were once again compared with the results of O'Brien et al. (2003) at 80 MPa. As expected the numerical crack density is reduced at each of the stress levels considered, however the pattern to the data and its relation to the results of O'Brien et al. remains unchanged. This is described in Figure 4.7.

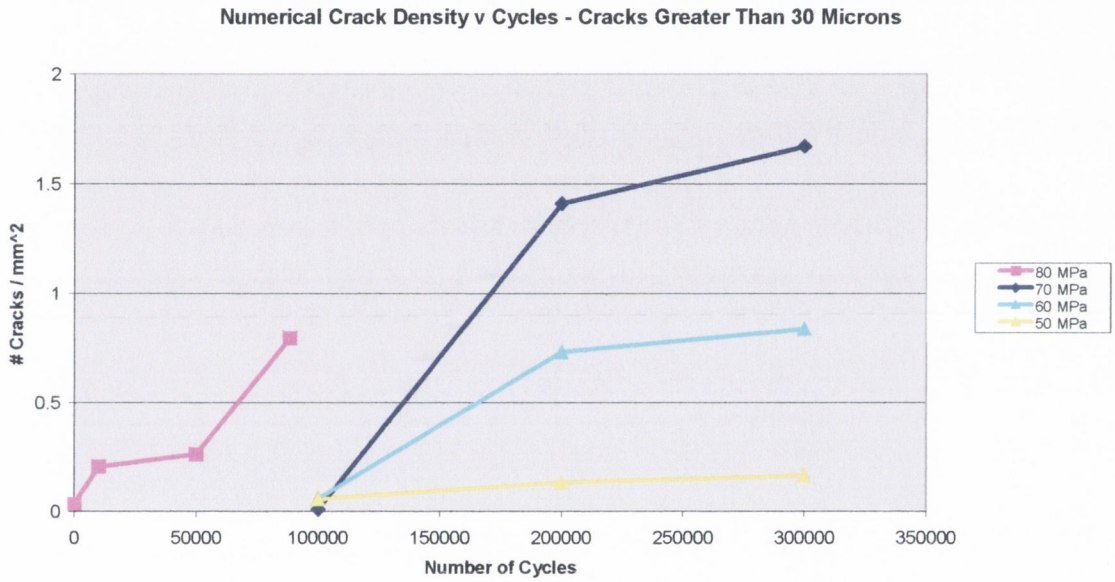

Fig. 4.7 Mean numerical crack density versus number of cycles - 50, 60, 70 (present study, cracks greater than 30 μm) & 80 MPa (O'Brien et al., 2003)

Whilst a fatigue threshold for compact bone may explain some of the differences observed in fatigue damage accumulation observed at 50, 60 and 70 MPa. The considerable change in behaviour between 70 and 80 MPa (Figure 4.4) would need to be confirmed by further testing in the region 70 to 80 MPa.

Previous examination of damage accumulation in canine bone loaded in three point bending at 625με showed no significant difference between unloaded controls and bones loaded to either 100, 1,000,or 100,000 cycles, below the fatigue thresholds for both tensile and compressive fatigue (Bur et al., 1985). Only at higher loading levels,

1500 με (Burr et al., 1985) and 2500 με (Mori & Burr, 1993) did mechanical loading cause significantly more microdamage than control specimens. Animal models loaded at 2,500με showed approximately five times more microdamage (0.055 cracks / mm^2) than unloaded controls. The work of Burr and co-workers and the current study both demonstrate that substantial microdamage can accumulate in bone within physiological loading limits.

Zioupos et al. (1996) developed an equidamage contour plot for the number of cycles required to reach a given damage level at any given stress for their fatigue tests of bone and antler. The damage contour plot for bone is reproduced in Figure 4.8. Their damage levels corresponded to reductions in modulus of 1, 3, 5, 10 and 20% where the 20% contour line also corresponded with the final fracture regression line indicating that bone was not capable of withstanding damage values higher than 20%. It was noted that all contours greater than a damage value of 3% intersected the final fracture regression line at a maximum stress of around 80 MPa, but that the damage contour at 3% converged at around 50 MPa (lowest stress investigated 62 MPa). This has two implications, firstly at low stress levels the damage target level prior to failure cannot be increased by merely increasing the number of cycles and secondly at any given stress level there is a limit as to the maximum achievable target damage which can be accumulated before the onset of failure.

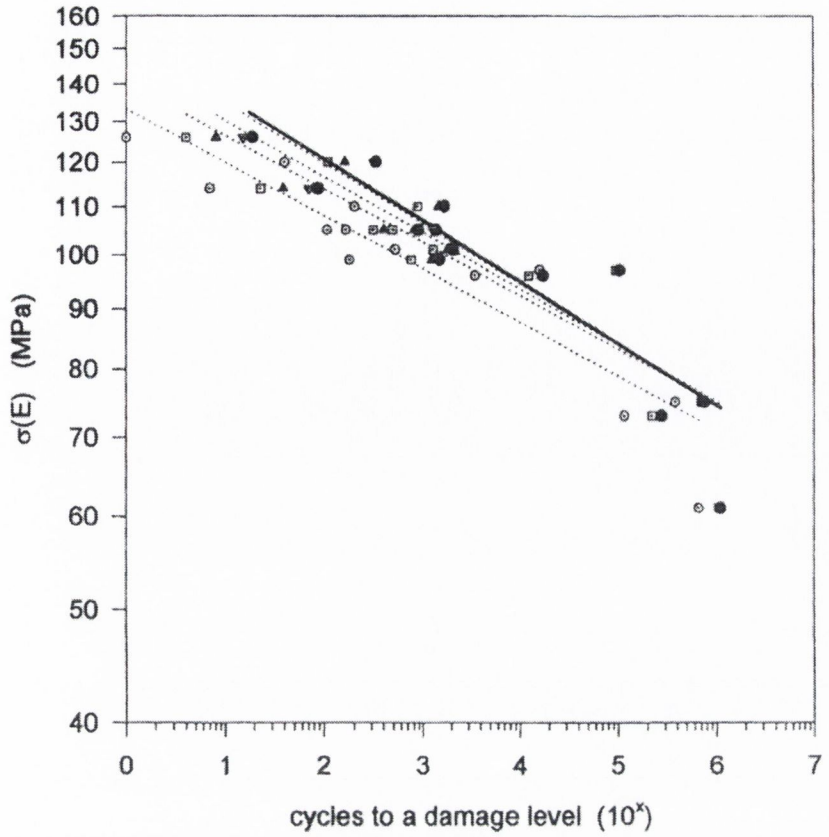

Fig. 4.8 Equidamage plot for bone. The solid line represents a regression line of the σ-N_f data. The equidamage contours are at damage levels (starting from left) of D = 1, 3, 5, 10%, (after Zioupos et al., 1996)

This observation would correspond with the differences observed between the data for microcrack accumulation in experiments between 50 and 70 MPa (3,500με) and those at 80 MPa, where microcrack accumulation was not able to reach the higher densities observed at the lower stresses.

Within the limitations of this research, particularly surrounding the number of measured fatigue cycles, it can be considered that specimens of bone will not fail within a physiologically relevant period of time when subjected to compressive loading strains below a strain threshold of approximately 4,000με. At strains above this threshold an immediate increase in microdamage can be observed from the very start of cyclic loading.

4.1.2 Modelling fatigue crack accumulation

The aim of the current work was to describe the fatigue behaviour of compact bone at *in vivo* stresses from the point of view of microdamage development. The experiments conducted here describe the development of microdamage at three distinct stress levels. The next stage in this analysis would be to try and describe the development of microdamage for all stress levels in this region. Having no definitive information regarding the development of microdamage right up until complete failure at *in vivo* stresses, and also given that failure is unlikely to be observed within a physiologically relevant period of time, it was decided to model the data up until the characteristic damage state. This assumed that for the current data, by 300,000 cycles all tests had reached this level.

All experimental data showed an initial period of minimal damage accumulation up until 100,000 cycles, followed by a period of damage development between 100,000 and 200,000 cycles, after which time the rate of damage development reduced dramatically as a steady state or target value of damage was approached. Given this type of development a non-linear model would obviously be necessary in order to describe the results accurately. A sigmoid response curve was chosen to model the accumulation of damage over time as it demonstrates a similar pattern to that observed in the current work. Figure 4.9 demonstrates a typical sigmoid response curve as it approaches a target value in the y domain with increasing values in the x domain.

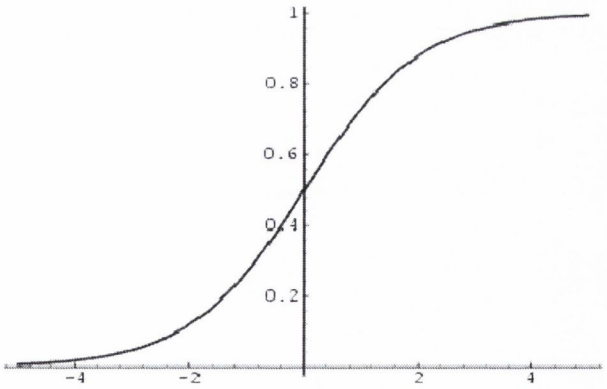

Fig. 4.9 Typical sigmoid response curve

Using Sigmaplot 2002 software (SPSS Science Ltd., Chicago, USA) non-linear regression analyses were applied to damage accumulation curves at the three different stress ranges considered. These generated functions of the form shown in Equation 4.1.

4.1

$$y = \frac{a}{(1 + \exp(-(x - x_o)/b))}$$

In Equation 4.1, a and b vary depending upon the applied stress range and x_o represents the x value corresponding to a y value of half its target value. For the current analysis 'x' represents the number of cycles and 'y' represents numerical crack density. Having generated three different equations of the form shown in Equation 4.1 it was found that by analysing the factors a and b for each stress level they were in fact functions of the applied stress. It was found that over the range of stresses considered by the present study the factors a and b could be accurately described using further regression analyses and these are described in Equation 4.2 and 4.3, x_o was found to vary very slightly over the range of stresses of interest and could be accurately described using linear regression and if fixed then indeed x_o could be replaced with a constant resulting in a minimal reduction in accuracy. Figure 4.10 describes results obtained from this model for stresses ranging between 50 and 70 MPa. The figure also describes the results predicted for damage accumulation at 80 MPa by this model. Dashed lines identify model predictions and marker points identify observations.

4.2

$a = C + D \cdot \Delta\sigma$, where C = -4.53, D = 9.4 × 10-8 and $\Delta\sigma$ is the applied stress range in MPa.

4.3

$b = \frac{E + F \cdot \Delta\sigma}{1 + G \cdot \Delta\sigma}$, where E = 1854, F = -1.57 × 10^{-4}, G = 2.2 × 10^{-8}

4.4

$x_o = H + I \cdot \Delta\sigma$, where H = 26802, I = 2.11 × 10^{-3}

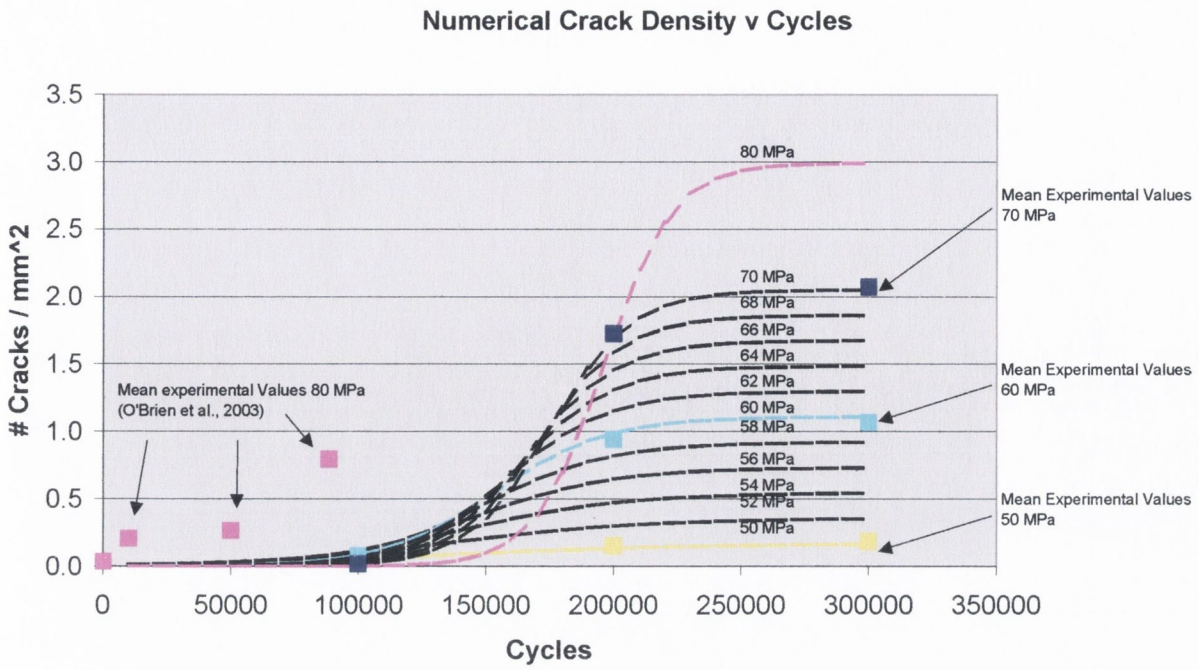

Fig. 4.10 Modelling numerical crack density as a function of the applied stress and the number of cycles (a)

At approximately 48 MPa the model predicts that no damage accumulation will be observed for any given number of cycles. The model accurately predicts the measured microcrack densities over all stresses considered in the current study, however it can only be used reliably within the range of experimental data to which it is fitted. At 80 MPa we can see that the predicted values for microdamage are very different to those observed by O'Brien et al. (2003). Firstly the model predicts limited damage accumulation up until 100,000 cycles followed by a period of damage accumulation until a steady state is reached. This is very different to the pattern observed by O'Brien et al. and clearly some change has occurred between 70 and 80 MPa in the manner in which damage develops. An unusual feature of these predictions is that at low number of cycles the curves appear to cross one another at larger fatigue stresses, suggesting less damage at higher stresses. In practise this is unlikely to occur and is an artefact of this model

Given the limited range of application of the current model it was decided to try and extend the current model to include all stress ranges including those outside range of values considered in the current experiments. It was assumed that given the number of experiments conducted in which a sigmoid response curve was observed, that this

should remain the general form of any chosen model. It was therefore accepted when developing this model that at 80 MPa the damage accumulation curve should be allowed to follow the same type of pattern but predicting what may have happened to microcrack density should failure have not occurred at approximately 90,000 cycles. Damage would accumulate until a target damage value would have been reached appropriate to this stress level. Once again a sigmoid curve was fit to all data sets, and from this non-linear regression was performed to calculate the variables for any given stress range. Equations 4.5 through 4.7 demonstrate the method in which the variables a, b and x_o from Equation 4.1 were re-calculated in this modified model.

4.5

$a = J \cdot \exp(K \cdot \Delta\sigma) + L \cdot \exp(M \cdot \Delta\sigma)$, where J=$9.67\times10^{-8}$, K=$2.37\times10^{-7}$, L=$2.02\times10^{-3}$, M=$8.57\times10^{-8}$ and $\Delta\sigma$ is the applied stress range in MPa.

4.6

$b = N + O \cdot \left|\Delta\sigma - P_o\right|^{Q}$, where N=$1.17\times10^{4}$, O=$2.93\times10^{-6}$, P=$6.65\times10^{7}$, Q=1.40.

4.7

$x_o = R + S \cdot \Delta\sigma$, where R=$-7.94\times10^{3}$, S=$2.73\times10^{-3}$

Figures 4.11 and 4.12 describe the predicted numerical crack density as a function of the applied stress and the number of cycles, Figure 4.12 represents the same data as Figure 4.11, but the crack density axis has been rescaled to provide further clarity at lower stresses enabling the presentation of additional crack density contours for intermediate fatigue stresses. Once again dashed lines identify model predictions and marker points identify observations

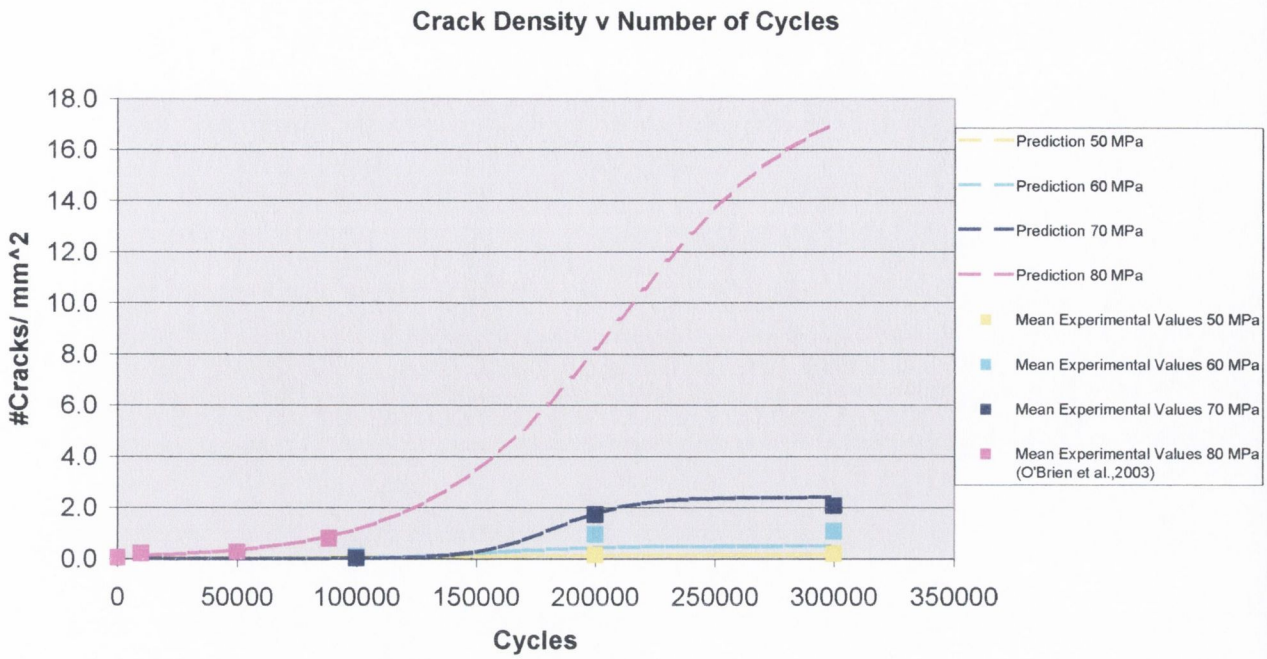

Fig. 4.11 Modelling numerical crack density as a function of the applied stress and the number of cycles (b)

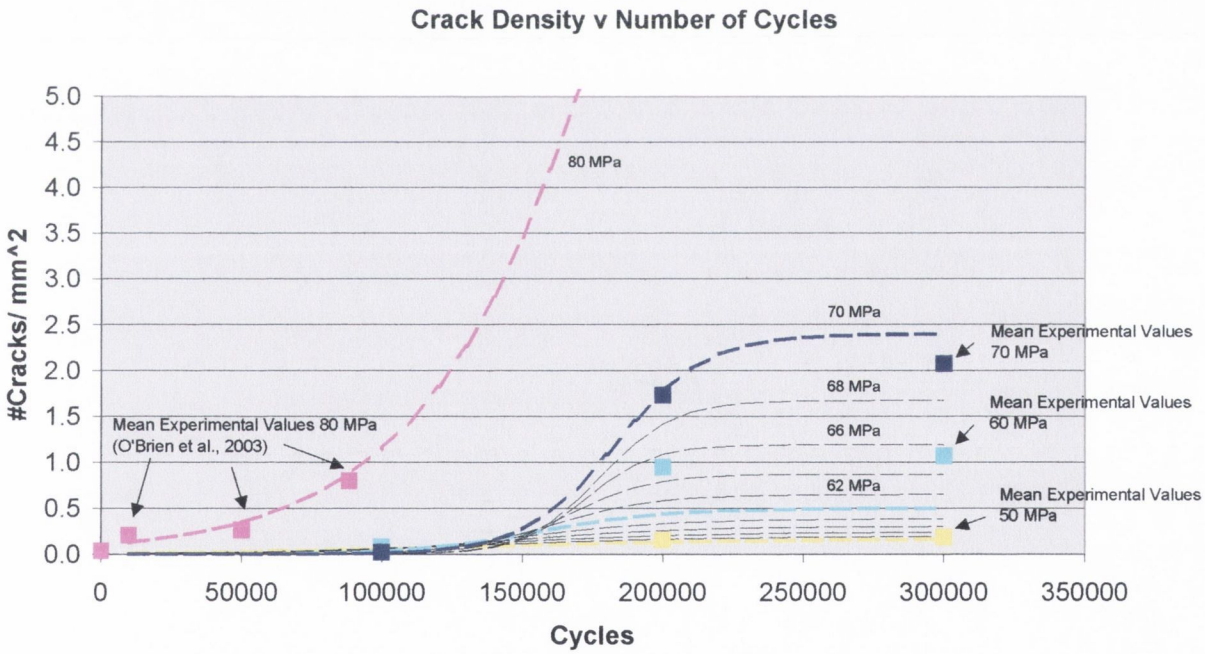

Fig. 4.12 Modelling numerical crack density as a function of the applied stress and the number of cycles (c)

The graphs show that the model does have greater error in predicting the observed microcrack density at all stresses observed in the current experimental work. Nevertheless it does predict the microcrack density with reasonable accuracy at 80 MPa

up until failure. It does however have limitations in the early part of the test where this type of model misses the initial increase in microcrack density observed during the first 10,000 cycles. Although not predicting the point at which failure occurs, numerous models have previously been developed which predict the number of cycles to failure as a function of the applied stress and a standard stress against number of cycles to failure curve could be combined with the current model to provide the final limit. This adapted model predicts that if failure was not observed within a time period sufficient for microdamage in bone tested at 80 MPa to reach its target microcrack density, then microcrack density would increase until it stabilized around a value of 19 cracks / mm^2.

In Equation 4.1 'a' represents the target value of microcrack density predicted for microdamage saturation at any given fatigue stress. It is this value which the sigmoid curve approaches with prolonged cycling, when the curve levels off in the period beyond 200,000 cycles. This target value of microcrack density is a linear function of the applied fatigue stress such that the total microcrack density that can be sustained without causing rapid failure is also seen to increase with the applied stress. This reinforces the observation that for any given stress level there is a natural population of microcracks that will develop without having a detrimental effect on the structure of bone for a given period of time.

4.1.3 Rate of damage accumulation

Figure 4.10 demonstrated that at stress levels consistent with physiological activity only after a certain point in time do microcracks start to form, increasing in number until saturation occurs. Microcrack accumulation occurs in the period 100 – 200, 000 cycles, the model described by Equation 4.1 indicates that the rate of damage accumulation between 100,000 and 200,000 cycles increases with increasing stress. Assuming a linear increase in microdamage between the predicted microcrack density at 100,000 and 200,000 cycles. Figure 4.13 shows the rate of damage accumulation against the applied fatigue stress.

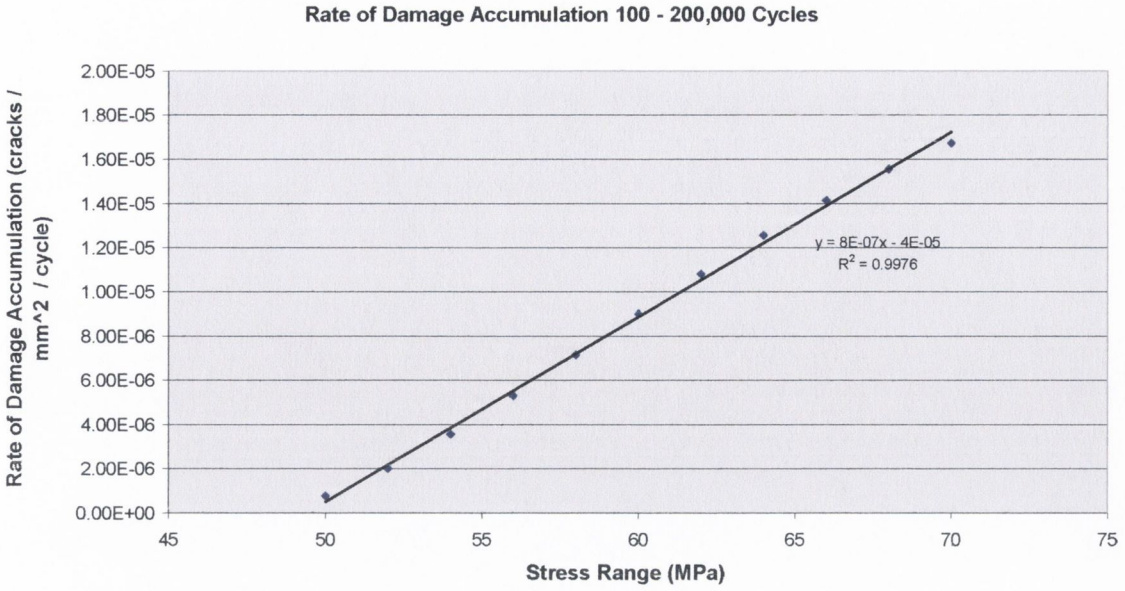

Fig. 4.13 Rate of damage accumulation 100,000 – 200,000 cycles

The rate of damage accumulation clearly increases linearly with increasing fatigue stress. This pattern can be described by a linear model which shows that microcrack density increases at a rate of 8×10^{-13} per unit increase in fatigue stress, in the period 50 – 70 MPa. The rate of damage accumulation is a function of the applied fatigue stress, with increasing fatigue stress increasing the rate of microdamage formation.

4.1.4 Crack Density in High Temperature Fatigue

Figure 4.14 compares numerical crack density in each of the high temperature fatigue tests with the mean crack densities from the room temperature fatigue study of O'Brien et al. (2003) and the room temperature fatigue tests conducted in this investigation at stress ranges of 50, 60 and 70 MPa, up to a maximum of 300,000 cycles. With the exception of the two specimens which did not fail, all high temperature specimens had a dramatic increase in microcrack density ultimately leading to failure of the specimen.

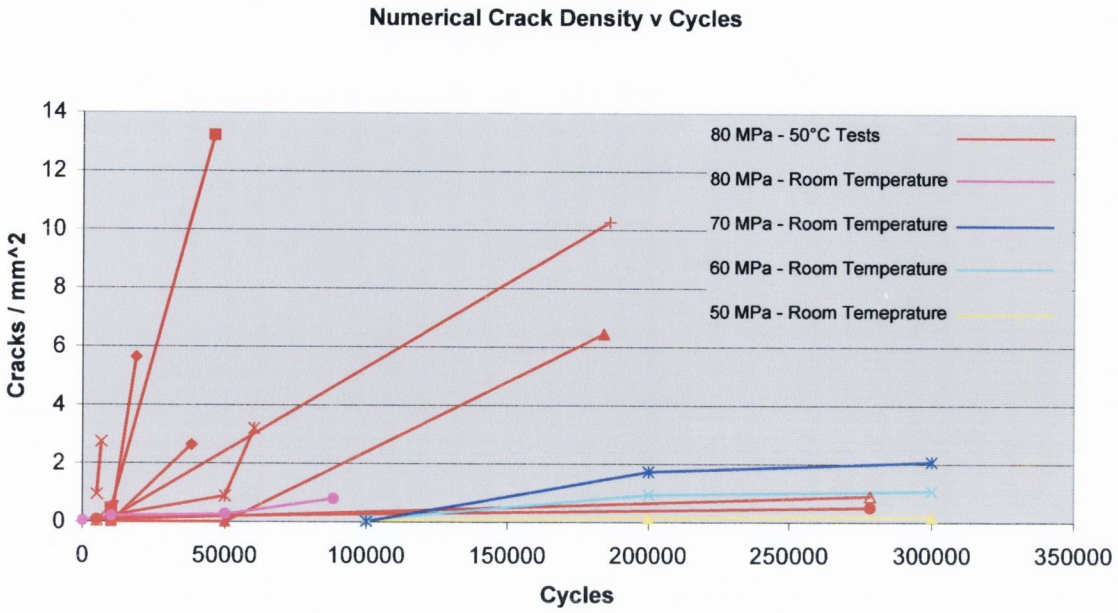

Fig. 4.14 Numerical crack density versus cycles – room temperature versus high temperature fatigue

Due to the degree of scatter in the fatigue life for high temperature specimens, the timing of the dye sequence provides very limited information about the accumulation of microdamage over time. Very few specimens have accurate values for microdamage in the period just prior to failure. Only two of the specimens marked, A and B in Figure 3.49, have accurate values for microdamage closer to the point of failure, or at least further through the fatigue test. These two specimens show a marked increase in damage accumulation later in the life of the specimen. Figure 3.50 shows that for the first half of a specimen's life damage accumulation is very slow with rapid increases in damage towards the end of a specimen's life. This observation is similar to that found by Zioupos et al. (1996), where in fatigue tests conducted below a maximum stress of approximately 90 MPa, the accumulation of damage was very slow for approximately 20-30 % of the complete lifetime, with subsequent rapid increases in damage accumulation immediately prior to failure. Although not readily apparent in Figure 4.14 due to the scale in the crack density axis, this is supported by the pattern observed by O'Brien et al. (2003), where microcrack density increased rapidly eventually resulting in failure, (Figure 1.12 shows the results of O'Brien et al. in further detail).

The vast majority of the high temperature specimens reached microcrack densities greater than those experienced in O'Brien's room temperature study. Notably, the two specimens which did not fail and have considerably lower microcrack densities are approaching the mean crack densities observed by O'Brien et al. towards the end of the test. The majority of all high temperature fatigue specimens reached microcrack densities greater than the mean crack densities in the room temperature fatigue tests conducted at physiological stress ranges. The only fatigue test to reach a crack density greater than all of the high temperature fatigue tests was in one of the room temperature fatigue tests that were tested to approximately two million cycles without failure. This specimen had a final microcrack density of 15.66 microcracks / mm^2.

Figure 4.15 is a box plot diagram comparing numerical crack density at the point of failure between the current high temperature fatigue test and the room temperature fatigue studies of O'Brien and co-workers (O'Brien, 2000; O'Brien et al., 2003). The first box plot describes crack densities for all high temperature fatigue specimens, the second box plot considers only failed specimens and the third box plot describes O'Brien's (2000) room temperature fatigue study at 80 MPa. The diagram shows a considerable difference between numerical crack density at failure in the high temperature and room temperature studies, with a factor of 10.38 between the median numerical crack density of those failed high temperature specimens and the median crack density in O'Brien's (2000) room temperature study. Similarly a factor of 9.05 can be found between the mean numerical crack density in the two studies. Crack densities are greater in the high temperature study. The red and green lines passing through the middle of each box represent the median and mean crack densities at the point of failure. Microcrack density was greater in the high temperature study than the room temperature study; with a significant difference between them, $p=0.016$, $p<0.05$ (80 MPa 50°C, 80 MPa Room Temperature). Table 4.1 gives details of the various quantiles associated with the box plot shown in Figure 4.15.

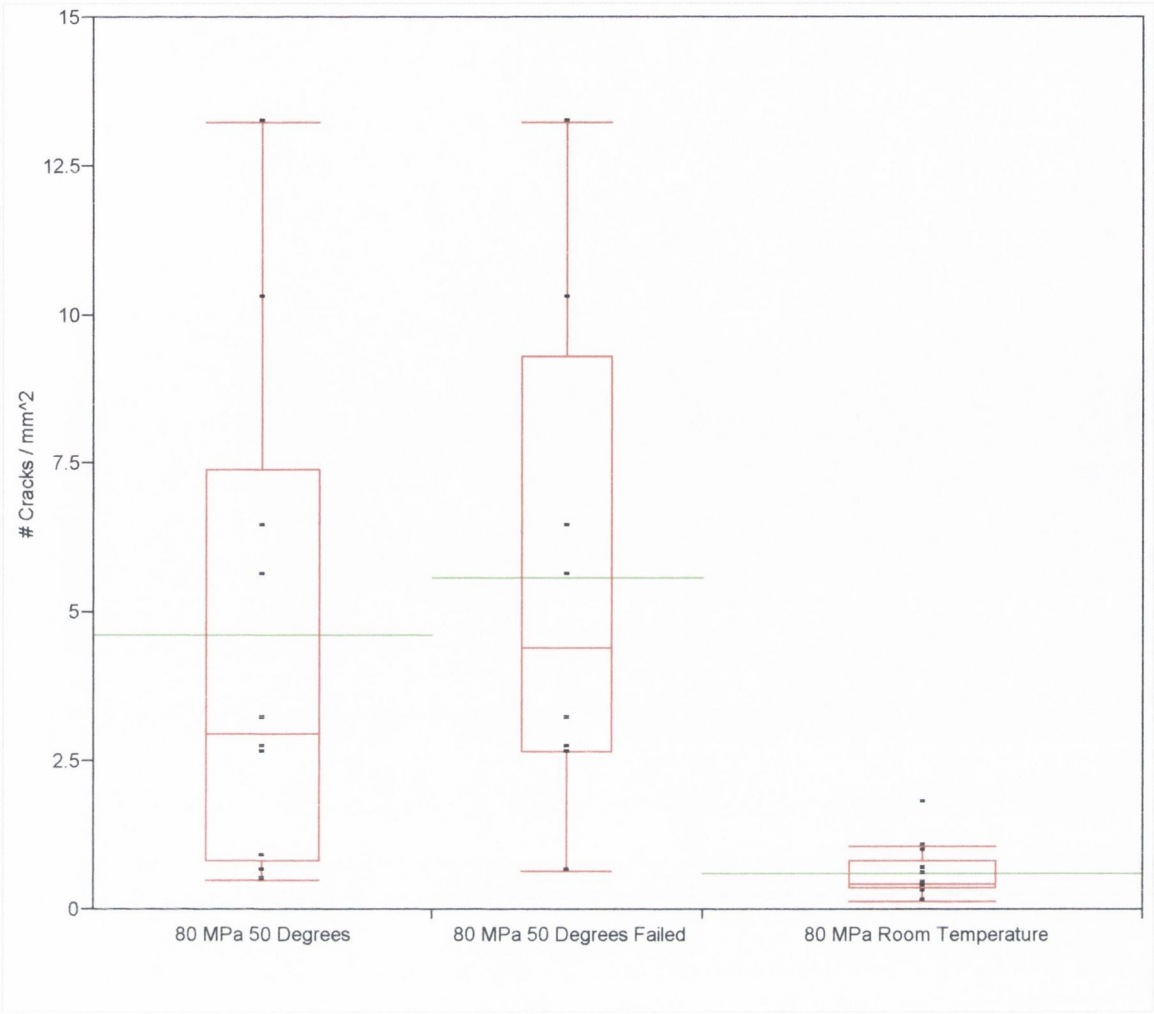

Fig. 4.15 Box plot diagram – fatigue numerical crack density versus operating conditions

Table 4.1 Median and quantiles – numerical crack density versus operating conditions

Quantiles

Level	Minimum	10%	25%	Median	75%	90%	Maximum
80 MPa 50 Degrees	0.503229	0.518532	0.833353	2.973586	7.397773	12.9313	13.22729
80 MPa 50 Degrees Failed	0.656256	0.656256	2.66304	4.421373	9.310825	13.22729	13.22729
80 MPa Room Temperature	0.15	0.202	0.3875	0.426	0.834	1.5168	1.808

In experiments lasting only a short period of time the implications of a temperature less than *in vivo* will be negligible (Evans, 1973). However, for prolonged testing the effects of temperature will be more significant, this was observed in studies on viscoelasticity (Currey, 1965) and fatigue (Carter and Hayes, 1976). Carter and Hayes (1976) demonstrated that between 21°C and 37°C there was a fall of approximately half in the fatigue life. This is the first study to compare fatigue microdamage at different

temperatures and from these results it would be anticipated that at *in vivo* temperatures, fatigue microdamage would be greater than observed at room temperature. Although previous fatigue studies have not quantified fatigue microdamage as a function of the operating temperature, studies have equated an increase in temperature to an equivalent increase in the applied fatigue stress (Carter and Hayes, 1976; Taylor, 1998a; 1999).

In the room temperature fatigue investigation it was observed for a given fatigue stress range a stable incidence of microdamage was attained with continued fatigue cycles. It was also observed that with an increase in stress this stable microcrack density was also seen to increase. A similar pattern was observed by Zioupos et al. (1996), where they monitored modulus reduction in compact bone specimens fatigued in uni-axial tension. The accumulation of damage (modulus reduction) was observed to increase in a stable manner and only at the very end of a specimen's life was damage seen to increase rapidly. It was observed that this stable damage level, or target value of damage beyond which fracture became uncontrollable, was also seen to increase with increasing stress. These findings would indicate that if an increase in temperature can be equated to an increase in stress, then obviously an increase in temperature would correspond to an increase in microdamage.

4.1.5 Microcrack Accumulation as an indicator of failure

Figure 4.16 contains all of the high temperature and room temperature fatigue data from Figure 4.14 along with additional data on microcrack density taken from various literature studies. These include both *in vivo* measurements and fatigue studies.

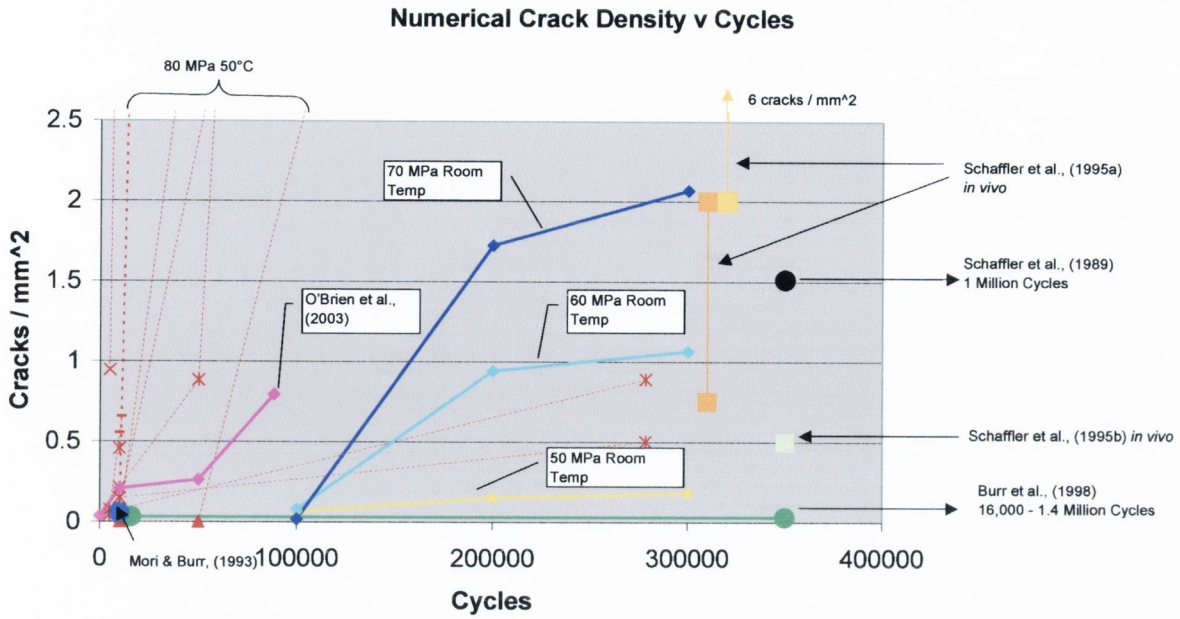

Fig. 4.16 Numerical crack density versus cycles, current data versus literature

Fatigue data is represented by circular markers on the graph and *in vivo* data is represented by square data point markers. Burr et al. (1998) loaded canine femurs in four point bending with an initial strain magnitude of 2700 microstrains (approximately 55 MPa, assuming E = 20.4 GPa) at 37°C. Femurs were loaded to between 1.59×10^4 and 1.41×10^6 cycles. Compressive cortices showed crack densities of 6.42 ±5.76 cracks / cm^2. Mori & Burr (1993) loaded canine radii in three point bending for 10,000 cycles with a peak strain of 2500 microstrains (approximately 50 MPa). Histological examination of tensile surfaces identified crack density of 0.055 cracks / mm^2, almost five times greater than controls. Schaffler et al. (1989) measured damage accumulation in tensile fatigue at physiological strain ranges of 0 – 1200 microstrains (24 MPa) for one million cycles. The measured density of new cracks formed during this time is 1.51 cracks / mm^2. The current set of results, and therefore the models developed here, show reasonable consistency with those studies that examined damage accumulation in fatigue tests loaded in bending (Mori & Burr, 1993, Burr et al., 1998), but they do not represent the tensile data of Schaffler et al. (1989). Burr et al. (1998) concluded from bend tests, that in this respect damage accumulates more rapidly in tensile cortices, but that crack growth is greater in compressive cortices. Comparing the tensile data from Schaffler et al. (1989) with the models developed in Section 4.1.2, suggests that in order to predict a similar level of damage to that observed by Schaffler et al., going from a

compressive to tensile loading regime is equivalent to a factor of approximately 2.7 on the fatigue strength, assuming that the material reaches a stable target damage level.

Figure 4.16 also describes a selection of studies measuring *in vivo* microdamage in bone. Schaffler et al. (1995a) examined the incidence and localisation of microcracks in the mid diaphysis of human femoral compact bone for specimens in the age range 50 – 75 years. Microdamage density of females was reported ranging between 2 and 6 microcracks / mm^2 and for males was between 0.75 and 2 microcracks / mm^2. In a study of cortical bone from the femoral neck, Schaffler et al (1995b) demonstrated microcrack densities ranging from approximately 0 to 2 microcracks / mm^2 with an average density of 0.5 microcracks / mm^2. Elsewhere, Wenzel et al. (1994) studied *in vivo* microcracks in human vertebral bone and found crack densities in the range 0.8 – 23.1 microcracks / mm^2 with a mean of 7.6 microcracks / mm^2.

The room temperature fatigue studies at 50, 60 and 70 MPa are reported up to 300,000 cycles along with the 80 MPa room temperature fatigue work of O'Brien et al. (2003). The data of O'Brien et al. failed relatively early at lower crack densities, the high temperature fatigue work conducted here observed very high crack densities in those failed specimens. Burr et al. (1998) identified relatively low crack densities despite cycling for longer periods and experiencing up to 43% loss of stiffness, with the observation that significant microdamage accumulation was not detected until the bone had lost 15% of its elastic modulus. Whilst it may be clear from the graph that in failed specimens an increase in damage is generally observed prior to failure, there is no clear crack density beyond which failure will occur. This is in contrast to the observations of modulus reduction as identified by Pidaparti et al. (2001). Their investigation identified a failure criterion beyond which failure will occur. They used a stiffness loss of 30% as the failure criterion for whole bones, which produced substantial fatigue damage without catastrophic failure. After a stiffness loss of 30% Pidaparti identified that bone can carry load, similar to the post yield behaviour of other materials, but eventually catastrophic failure will occur.

Schaffler et al. (1996) reported that the accumulation of dye – penetrable microcracks did not increase until a 30% modulus reduction had been observed in tensile fatigue. This observation whilst indicating a consistent effect with the findings of Pidaparti et al.

(2001), it does highlight that at face value combining the findings of all three studies into a feasible measure of damage relating both microdamage and stiffness is not achievable. O'Brien (2000) identified failure as a 10% reduction in stiffness, however many specimens had completely failed prior to achieving this criterion, during which time microcracks had been identified. In this study greater damage was observed without any indication of failure. No indication of failure would on the one hand indicate limited stiffness loss (<10% based on the findings of O'Brien), yet according to other literature microdamage would be indicative of having noticeably reduced the materials stiffness.

Figure 4.17 reproduces results taken from Pidaparti et al. (2001), the graph shows the probability of damage (measured as modulus loss) versus loading cycles for three cumulative probabilities (5%, 50%, 95%) at a strain of 3000 με (60 MPa). The figure shows a continuous loss of stiffness during the period 0 to 100,000 cycles. Unlike the current work, which measured damage as an increase in microcrack density, showing limited damage accumulation during the initial period of loading for the first 100,000 cycles.

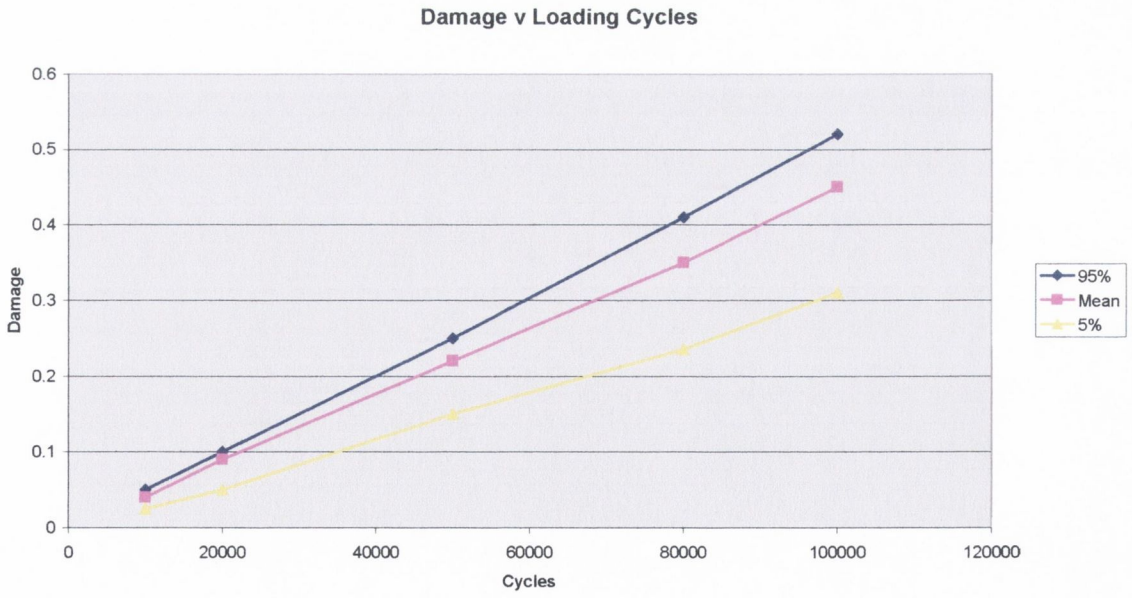

Fig. 4.17 Probability of damage versus loading cycles (after Pidaparti et al., 2001)

Danova et al. (2003) investigated the effect of cyclic fatigue on monotonic structural properties of the rat ulna whilst simultaneously accumulating microdamage. Cyclic end

loading of the ulna was performed at 4Hz, *ex-vivo* at an initial peak strain of – 6000 με to 20% loss of stiffness, or 40% loss of stiffness bilaterally. A 0% loss of stiffness monotonically loaded control group was also included. Histologically Danova et al. demonstrated that microcracking was significantly influenced by fatigue loading. Crack density increased after fatigue loading to 20% and 40% loss of stiffness, when compared to 0% monotonic controls, which did not contain microdamage. However, only small insignificant increases in microcracking were found at 40% loss of stiffness, when compared with less damaging fatigue loading to a 20% loss of stiffness. Despite further stiffness losses increased microdamage formation was minimal as shown in Figure 4.18 which reproduces data taken from Danova et al. (2003). Whilst damage is continuing to develop in the specimen, as identified by continued modulus reduction, microcrack density remains constant and therefore does not identify what damage mechanisms are occurring during this time.

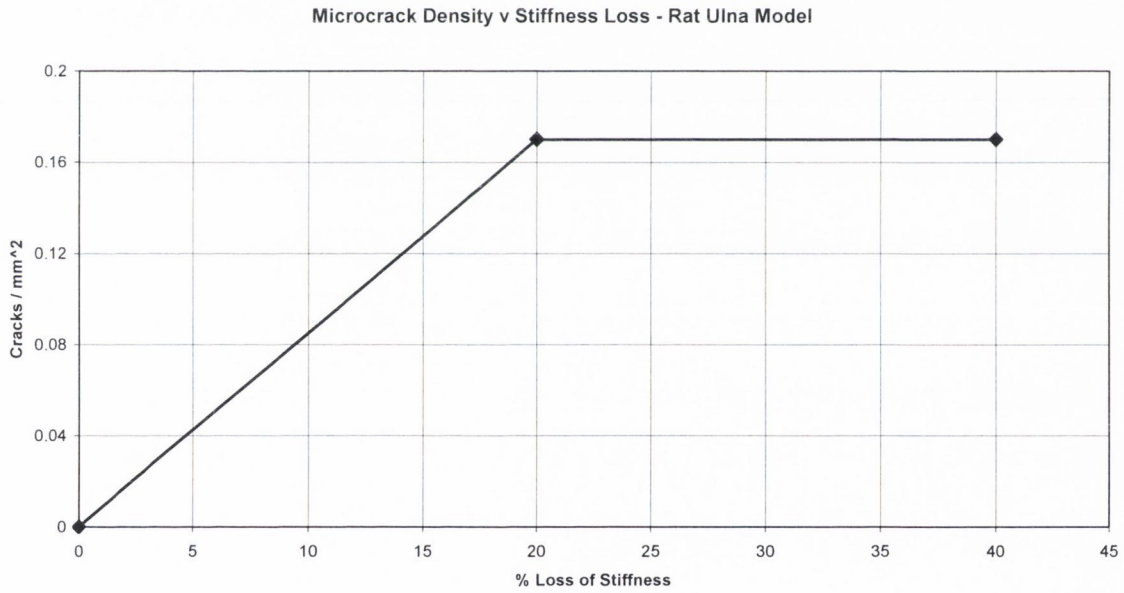

Fig. 4.18 Microcrack density versus stiffness loss (after Danova et al., 2003)

Given that microcrack density is not constant at failure, and in particular not identifying certain periods of damage development, as an indicator of damage it is not predicting failure in compressive fatigue specimens. Further examination is required to better predict the appropriate failure mechanisms.

4.1.6 Microcrack Length

Microcrack lengths observed in the fatigue investigations at physiological stress ranges (90 μm at 50 MPa, 63 μm at 60 MPa and 65 μm at 70 MPa after 300,000 cycles) were found to be consistent with published work, particularly when considerations of loading type and level are made (O'Brien et al., 2003; Schaffler et al., 1989; Burr and Stafford, 1990; Lee et al., 1998; Donahue et al., 2000). In fatigue tests of bovine compact bone tested at 80 MPa in compression, O'Brien et al. (2003) found mean crack length to vary between approximately 100 μm and 120 μm during each stage of testing. In compact bone specimens cyclically loaded in uniaxial tension for one million cycles at a physiological strain range of 0 – 1200 με, Schaffler et al. (1989) found a mean crack length of 80 μm, independent of strain rate. In four point bending tests of canine femurs Burr et al. (1998) found a mean tensile crack length of 66 μm and a mean compressive crack length of 72 μm.

The pattern observed in mean crack length over time (Figure 3.14), is noticeably different at 50 MPa where very low crack densities are observed, when compared with those at 60 and 70 MPa where considerably greater crack densities were noted. Despite mean crack lengths being greater at 50 MPa than at 60 or 70 MPa, the high standard deviation observed at 50 MPa and the lower density of cracks makes any difference in mean inconsequential. As per Reilly and Currey's observations (Reilly and Currey, 1999), these compressive microcracks observed could be very small in the region of 10 – 15 μm, however they could also be considerably longer of the order of several hundred microns. However the histogram of microcrack length (Figure 3.15) shows that the distribution of microcrack length is skewed towards smaller microcracks.

Figure 3.14 shows that mean crack length at 60 and 70 MPa increases between 100,000 and 200,000 cycles, after which time crack length stabilizes. The pattern observed in mean crack length corresponds very well with the accumulation of microcracks described in Figure 3.12. If it is assumed that the development of microcracks increases the compliance of the specimen and, locally reducing the stress as load is shed to other areas of the specimen. Thus increasing the likelihood of further crack formation

elsewhere in the specimen, these results would suggest that new cracks which are formed will be able to grow to a longer length. A positive and significant correlation between mean microcrack density and mean crack length was found for specimens tested at 60 and 70 MPa between 0 and 300,000 cycles (Pearson's R=0.906, p=0.013 two tailed).

Examining Figure 3.18 which considers the variation in mean crack length during each stage of testing for tests conducted at a stress range of 60 MPa, it can be seen that cracks formed earlier in a specimens life are smaller than those formed later in the fatigue life of the specimen. Despite an increase in crack length of cracks formed at later stages of a fatigue test, very few cracks continued to grow over a prolonged period of time and thus categorized as propagating microcracks. At the higher stress level considered by O'Brien et al. (2003), propagating cracks were far longer (231.4 μm) than those identified here (85.6 μm) and thus potentially more dangerous in fatigue. Although relatively few in number, those microcracks identified as propagating microcracks were longer than those that formed solely within an individual period of the test, and therefore potentially more dangerous. It is however probable that some microcracks that were indeed propagating were not detected, as with small crack lengths, the likelihood of not identifying a propagating crack will indeed be greater. This is particularly the case for cracks that have small growth rates. Furthermore due to sectioning effects it is also likely that some propagating cracks will fail to be identified as growing.

For all of the stress levels considered in the current study the majority of microcracks (≥ 96%) were labelled with only one fluorochrome demonstrating that they did not grow between different stages of testing. This would suggest that most microcracks are not dangerous and will never grow to cause failure. This confirms the findings of Akkus and Rimnac (2001) who demonstrated that microcracks form, spread quickly and then slow down and stop. Consequently microcrack development could be described according to a limited period of crack growth following initiation after which time microcracks stop growing and will require considerably greater stress to spread any further. Microcracks will form in weaker areas of bone and will continue to grow until they are stopped by some crack arresting mechanism. The log normal probability

distribution (Figure 3.16) and cumulative density function (Figure 3.17) show that the probability of obtaining a microcrack longer than 100 μm, the length associated with microstructural barrier spacing (Taylor and Prendergast, 1995; 1997), after which crack growth rate accelerates rapidly (Taylor, 1997, 1998b) is only 13%. If this is increased to 150 μm, the length at which cracks have been observed to arrest in compact bone (Akkus and Rimnac, 2001), then the probability of obtaining a crack longer than this length is reduced further to 4%. Indicating a small probability of obtaining a microcrack, which could continue to cause failure during physiological loading.

It is evident that the majority of cracks can be considered not dangerous as they are unlikely to propagate to failure. The most important factor in determining failure is identifying the individual crack or cracks that may continue to grow. Monitoring the mean crack length over time will not identify this as the individual dangerous crack will be masked by the number of dormant microcracks. A key measure of failure is the ability to identify those dangerous microcracks and that can only be achieved by considering the whole population of microcracks through methods such as the cumulative density function. Here identification of those key dangerous cracks will become evident, it is these cracks that bone remodelling would hopefully target and repair in the living skeleton. It is hypothesised, yet not totally substantiated from these results that failure will be dominated by the propagation of a small number of individual microcracks, rather than the behaviour and interaction of a large population of smaller cracks.

4.1.7 Temperature Effects on microcrack length

At elevated temperatures, mean crack length was found to be generally consistent with crack length measurements made on room temperature fatigue studies. Figure 4.19 shows the mean crack length at a given number of cycles based on the number of available fatigue specimens. The graph shows the overall mean crack length calculated from all cracks measured in the high temperature fatigue study. Also illustrated are plots for crack length with increasing number of fatigue cycles for the room temperature fatigue study. In addition to these various studies, crack length data from each stage of testing in the work of O'Brien et al. (2003) are also shown. The work by O'Brien et al. describes crack length measurements, according to a mean crack length for each

individual stage of testing. This is in contrast to the method adopted here, where mean crack length was calculated in a cumulative manner in which each data point represents the mean length for all cracks formed up until that point in time, regardless of the stage at which it was formed. This difference accounts for the step like appearance of the data taken from the study by O'Brien et al.

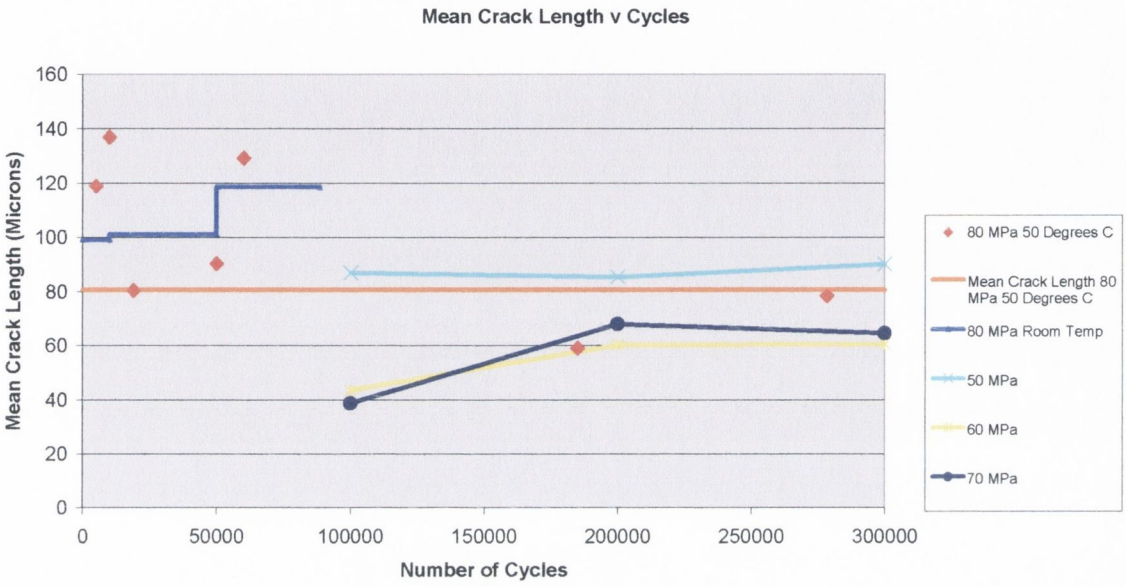

Fig. 4.19 Crack length versus cycles – high temperature and room temperature fatigue

Figure 4.19 suggests that crack length is independent of operating temperature, as the overall mean crack length passes directly between values calculated for 50 and 70 MPa. Crack length measurements for these high temperature specimens agree very well with all available data for both *in vivo* microdamage and microdamage formed during *in-vitro* testing, immaterial of whether the studies were conducted at room temperature or under physiological conditions (Schaffler et al., 1989; Burr et al., 1998; Donahue et al., 2000). The step like pattern of O'Brien's crack length measurements passes directly through the middle of those values calculated from the available data at 50°C.

The high temperature data points representing 185,000 and 278,000 cycles in Figure 4.19 both concur well with measurements taken from the room temperature studies. Re-examining Figure 4.19 demonstrates that, in specimens which failed within a particularly short period of time, mean crack length was greater and microcracks were able to grow to a larger length than would normally occur, potentially becoming more

dangerous and thus resulting in premature failure of the specimen. This would raise the question of whether such specimens are potentially inferior in their structure or architecture.

4.1.8 Microcracks and bone's microstructure – microcrack location

Various studies have examined microcrack interaction with bone microstructure and some authors have described a microstructural barrier concept for bone (Martin and Burr, 1989; Taylor and Prendergast, 1997; Taylor, 1998b; Akkus and Rimnac, 2001). These theories are largely based on the findings that microcracks develop in interstitial bone and then stop at osteonal boundaries. Theoretical models (Taylor and Prendergast, 1997; Taylor, 1998b), predict that the fatigue crack growth rate of a microcrack will reduce following identification eventually leading to crack arrest.

The current study tries to examine how microcracks interact with bone's microstructure at *in vivo* stresses. Microcrack interaction with secondary osteons was first considered by examining microcrack location. For room temperature fatigue at 50 and 60 MPa, microcracks were categorized according to whether they were entirely located in interstitial bone, whether they were interstitial but made contact with an osteon cement line (interstitial touching cement line), whether they penetrated the osteon cement line, or finally where they were located within a secondary osteon.

Most microcracks were located in interstitial bone and a proportion of these microcracks appear to have halted their growth where they met an osteon cement line. During the course of a fatigue test Figures 3.19 and 3.20 demonstrate that cracks formed at a later stage in the test are more likely to meet an osteon cement line than those formed earlier in the test. If we reconsider the fact that cracks formed later in the fatigue test are generally longer, then we can surmise that as cracks increase in length their growth is halted as they meet a secondary osteon or potentially other features. This is confirmed by the fact that of those few cracks which observed continued growth (propagating microcracks), the greatest proportion of these cracks were located in interstitial bone where their growth was not limited by the presence of secondary osteons and were consequently able to grow to a longer length.

The finding that the majority of microcracks were located in interstitial bone is consistent with previous studies; Schaffler et al. (1994b) found that 87 % of microcracks were interstitial or interstitial touching the cement line. This would indicate that microdamage in bone occurs primarily in older areas of bone tissue, which happen to be stiffer and more highly mineralised (Burr et al., 1998; Guo et al., 1998).

4.1.9 Microcracks and bone's microstructure - the effect of osteon density

Published work has shown that smaller and/or more osteons can prevent catastrophic failure as they slow the progress of cracks (Moyle et al., 1978) and the stiffness discrepancy of the osteon cement line is believed to inhibit crack propagation (Evans, 1958; Frost, 1966; Burr et al., 1988). Furthermore, Yeni et al. (1997) showed that the fracture toughness of bone is positively correlated to osteon density where an increase in osteon density increases the bone's resistance to crack growth. O'Brien et al. (2004) also demonstrated that if a microcrack is only 100 μm or less in length when it meets a cement line it will stop.

From Figures 3.21 and 3.22 the relationship between microcrack density and osteon density remains somewhat unclear for *in vitro* microdamage formed at *in vivo* stress levels. A limited positive relationship between microcrack density and osteon density was found at 50 MPa, similar to that found by Brennan (2001) for *in vitro* microdamage formed at stress levels above that experienced *in vivo*. However, at 60 MPa the results would suggest that those specimens with a higher microcrack density tended to have a lower osteon density, nevertheless the result does not infer that a lower osteon density necessarily resulted in a higher microcrack density. These particular specimens were observed to have higher microcrack densities and the three lowest values of mean crack length for any specimens tested at 60 MPa with average crack lengths in the region of 50 – 66 μm. It was noted in this study that at the stress ranges considered, osteon density was observed to be unrelated to microcrack length. Based upon the findings of O'Brien et al. (2004), the vast majority of microcracks observed would be halted when they met an osteon. The introduction of osteons is more likely to reduce the length of potentially longer microcracks, having a lesser effect on the size of microcracks observed in this study.

Other histological features may also have the same effect of limiting crack growth in bone. This is particular true of bovine material, where large areas of the predominantly brick like architecture of plexiform bone may cause a similar effect to that of secondary osteons in limiting crack growth. This is due to the vascular spaces between the brick like sections of lamellar bone. This aspect of microcrack development warrants further investigation in the future as vascular canals have previously been shown to limit crack growth in human cortical bone (Carter and Hayes, 1977b).

Secondary osteons are on average 200 μm in diameter (Martin and Burr, 1989), however if cracks do form in bone the osteon separation will be important in limiting crack growth; micro structural separations of the order of 120 μm (Zioupos and Currey, 1994) for laminar bone and 125 μm (Martin and Burr, 1989) for plexiform bone have been reported. Taylor and Prendergast (1997) modelled the effects of microcracks, where they showed that no improvement in fatigue life was anticipated by reducing crack length below 50 μm, approximately half the size of osteon separation. Taylor and Prendergast consider that it would be uneconomic for bone to repair cracks of this order and that only those cracks with lengths greater than those associated with osteon separation cause a rapid reduction in the fatigue life. They also suggest that any repair process will concentrate on detecting and repairing cracks in this range.

These proposals may explain some of the ambiguity in the analysis of microcrack density in the current set of experiments. Given the mean crack lengths observed at 60 MPa, according to the analysis of Taylor and Prendergast the effect of these cracks on bone's integrity will be limited and thus may provide some explanation for the pattern of microcrack density against osteon density at this stress level. The three specimens with higher crack densities may have had a particularly brittle composition making them more susceptible to crack initiation, this could be a possible explanation given the lower osteon density suggests that these bones may be older and thus more highly mineralised. Clearly further investigations are needed to clarify this situation as it still remains unanswered as to why in bone with low osteon densities, and therefore above average osteon separations, it appears from these observations that microcracks which form in these areas of bone tissue do not continue to cause failure. This might be, as highlighted in the introduction, that less stiff osteons will promote the growth of

interstitial cracks toward the osteon. A crack oriented obliquely towards a soft material should be attracted in the direction of the interface (He and Hutchinson, 1989), and having encountered an osteon boundary cracks would then be directed towards the Haversian canal which acts as a stress concentration.

The effects of increasing osteon density on microcrack location and microcrack interaction with secondary osteons are clear. As the incidence of secondary osteons increases, the percentage of microcracks touching cement lines increases and the percentage of microcracks occurring entirely within interstitial bone decreases, as shown in Figure 3.24. On the assumption that osteons prevent further crack growth by halting a microcracks growth due to the modulus mismatch at osteon boundaries, it can be assumed that by reducing the proportion of potentially dangerous microcracks (those occurring in interstitial bone), and increasing the proportion of microcracks which have been halted by secondary osteons, they do reduce the risk of outright failure.

4.1.10 The Effects of Temperature on Fatigue Life

Fatigue and creep investigations have shown considerable scatter in both fatigue and creep life, (Carter and Caler, 1983; Caler and Carter, 1989; Bowman et al., 1994). It is considered that such variations are attributable to factors such as orientation of the bone lamellae, porosity and the degree of bone mineralisation (Taylor et al., 1999; Lee et al., 2000b). The variation in both time to failure and cycles to failure can be considered to be the result of variations in structural properties within the bone microstructure and also a result of any variation in material properties such as the degree of porosity and mineralisation. However the influence of temperature appears to have increased the degree of scatter when comparing these high temperature fatigue studies with experimentally identical room temperature studies (O'Brien et al., 2003).

Figure 4.20 is a box plot diagram comparing the number of cycles to failure in the current high temperature fatigue study with an earlier room temperature fatigue study by O'Brien et al. (2003). Table 4.2 describes the quantiles for each set of results. The results taken from O'Brien et al. (2003) were also conducted on dumbbell like

specimens of bovine compact bone. They were also tested under comparable operating conditions at a fatigue stress range of 80 MPa in axial compression.

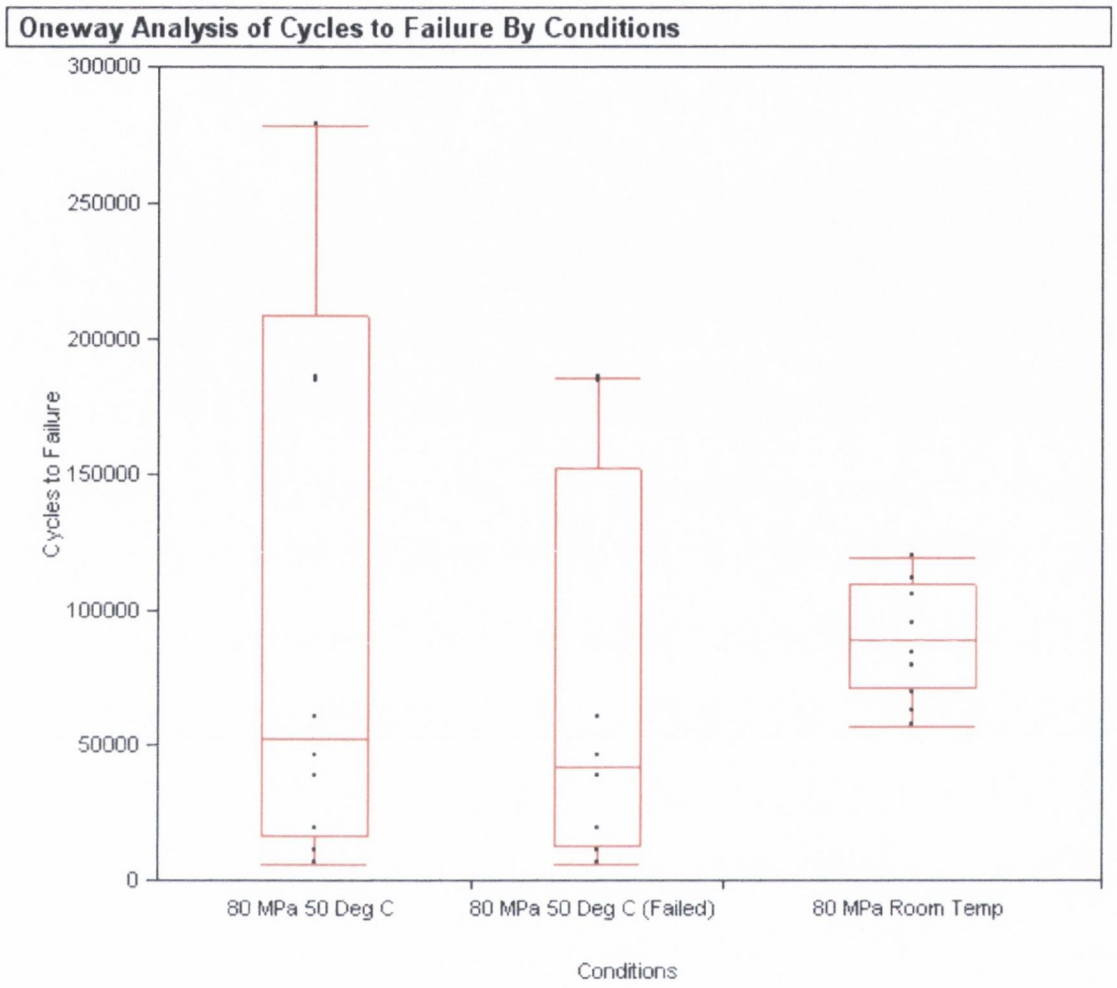

Fig. 4.20 Box plot – fatigue life versus operating temperature

Table 4.2 Median and quantiles – fatigue life high temperature versus room temperature fatigue

Quantiles

Level	Minimum	10%	25%	Median	75%	90%	Maximum
80 MPa 50 Deg C	6541	6997.3	16837	53113	209105.5	278351.2	278355
80 MPa 50 Deg C (Failed)	6541	6541	13015	42106.5	153136	186035	186035
80 MPa Room Temp	57500	58965.2	71675	89670.5	110319.5	117618.2	120002

The first box in Figure 4.20 represents the current high temperature fatigue study for all 10 fatigue samples tested, including the two specimens which did not fail. For the two specimens that did not fail, the number of cycles to failure is taken to be the number of fatigue cycles experienced by the bone samples at the point of interruption. This box has a range of 271,814 cycles, a median number of cycles to failure of 53,113 and an

interquartile range of 192,268 cycles, representing the central 50% of the data. The mean number of cycles to failure using log transformations was 57,317 cycles. Using the technique described in Chapter 3 (Equation 3.5, replacing time to failure with cycles to failure) minimum and maximum error values were calculated as 14,732 cycles and 222,993 cycles. If an outlier contaminates the data, the median will be little affected, but the mean could be greatly influenced, particularly if the outlier is an extreme value.

Two of the data points in this first box represent specimens which did not fail, with no immediate indication of failure when testing was interrupted (one specimen did have a macrocrack present). Histological examination of these two specimens showed very different behaviour from that of all other specimens. Figures 3.46 through 3.49, which describe the accumulation of microdamage in all the high temperature fatigue tests, demonstrate that these two specimens that did not fail (shown in dark blue and brown) show considerably smaller damage accumulation throughout the test than all other specimens. The second box in the diagram shows the number of cycles to failure for the same high temperature fatigue specimens, but with the two un-failed specimens excluded from the analysis. This box has a range of 197,494 cycles, a median number of cycles to failure of 42,106 cycles, and an interquartile range of 140,121 cycles. The mean number of cycles to failure for this adjusted set of values is 38,611 cycles with a minimum and maximum error of 11,433 and 130,394 cycles.

The third box in Figure 4.20 represents the room temperature fatigue study of O'Brien et al (2003) (cycles to failure taken from O'Brien, 2000), it has a range of 62,502 cycles, a median number of cycles to failure 89,670 and an interquartile range of 38,645 cycles, the mean number of cycles observed by O'Brien et al. was 88,380.

The box plots shown in Figure 4.20 highlight the increased variation in time to failure resulting from increased operating temperature. This is demonstrated by the physical size of the two high temperature box plots compared to that of the room temperature box plot. The median values are shown on each box plot by a horizontal bar passing through the middle of each box. The lines extending from the boxes show the tail of each distribution, the points that the data occupy outside the quartiles. These lines or whiskers, extend to the farthest point that is still within 1.5 interquartile ranges from the quartiles. The position of the median line in the two high temperature box plots

demonstrates that the majority points have lower number of cycles to failure, it can be observed from the diagram that more than half of the samples failed at a lower number of cycles to failure than the entire population of tests in the room temperature study of O'Brien et al. (2003).

These results demonstrate that an increase in the operating temperature, from room temperature to 50°C, has reduced the number of fatigue cycles required to cause failure of the specimen by a factor of 2.13 on the median and 2.29 on the mean.

It can also be noted that the effect of increasing the operating temperature has introduced considerable scatter into the fatigue test. This is demonstrated by the size difference between the high temperature boxes and the room temperature box in Figure 4.20. The high temperature box is considerably bigger, overlapping the room temperature fatigue study of O'Brien et al. (2003) both at the upper and lower end of the range of values for time to failure. It would appear that raising the operating temperature has, in fact increased the degree of variation in the fatigue life of compact bone. Although not commented on in the study by Carter and Hayes (1976), in their fatigue study of compact bone, Figure 1.16 taken from this publication indicates a similar pattern of increasing scatter with increased temperature. It has been established that the degree of mineralisation may explain the variation in fatigue life from specimen to specimen, the effects of variations in mineralisation could well be increased as a result of increasing the operating temperature of the fatigue specimen. Since collagen is the phase responsible for creep (a temperature-dependent process) in bone (Bowman et al., 1999), a less mineralised specimen may be more adversely affected by the influence of temperature, reducing the fatigue life even further.

4.2 Creep in Compact Bone

The current study has reaffirmed previous work in respect of the creep behaviour of bone. This investigation has shown that for all specimens tested, bovine compact bone demonstrated the three characteristic creep regimes of primary, secondary and tertiary

creep, consistent with metals, ceramics and previous work on cortical bone (Carter and Caler, 1983; Caler and Carter, 1989; Rimnac et al., 1993).

The results clearly demonstrate that a variation in the applied stress can have a significant impact on the time it takes for a creep specimen to fail. An increase in the applied stress level results in a non-linear reduction in time to failure.

The values of time to failure span a range of several orders of magnitude at each stress level. Work carried out by other authors when examining creep failure in bone have demonstrated similar variations (Carter and Caler, 1983; Caler and Carter, 1989; Bowman et al., 1994; 1999). Carter et al. (1981b) have shown that the Young's modulus can be used to explain the degree of scatter in the fatigue life of a material and it can be surmised that, like fatigue, this may also have an effect on the creep life of a given material. The variation in time to failure can be considered to be the result of variations in structural properties within the microstructure of the bone and also a result of any variation in material properties such as the degree of porosity and mineralization (Taylor et al., 1999; Lee et al., 2000b). Since an assumed value for Young's modulus was used to normalise the applied stress in the current study, any scatter will not have been reduced, as would be the case in studies where the individual modulus of each specimen was measured prior to testing.

Having established a power law relation, as shown in Figure 3.29, it is possible to compare this investigation with other work carried out on human cortical bone and bovine trabecular bone. Bowman and co-workers (1994) carried out work on the creep behaviour of bovine trabecular bone, where they developed a similar function for time to failure (seconds). This is shown in Equation 4.8.

4.8

$$t_f = 9.66 \times 10^{-33} \left(\frac{\sigma}{E} \right)^{-16.18}$$

In Bowman's function, the value of Young's modulus was not arbitrarily assumed, as in this work, but was instead determined by first cyclically loading each specimen with a triangular waveform. This was done under strain control for 10 cycles, at a constant strain rate.

Caler and Carter (1989) investigated creep in human cortical bone. They found a relationship between time to failure (seconds) and normalised stress as shown below.

4.9

$$t_f = 4.07 \times 10^{-37} \left(\frac{\sigma}{E} \right)^{-17.76}$$

The differences between the equations shown here, and those calculated from these investigations, are assumed to stem from the different types of bone employed in these other studies. In addition to the effect that differences in the material properties of bone may have upon the creep behaviour of bone, microstructural finite element analysis has shown that, in compression loading of trabecular bone, both tensile and compressive strains will be observed within individual trabeculae (van Rietbergen et al., 1995). This suggests that the localised mode of loading experienced by trabecular bone will differ from that of compact bone, despite both being loaded in compression.

Figure 4.21 compares this study with that of previous creep and fatigue work. The lines depicted for the study by Bowman et al. (1984) and the creep work by Caler and Carter (1989), are based on the above equations. These are valid, since the lines depicted on the graph are only calculated at stress levels consistent with those used in the relevant studies.

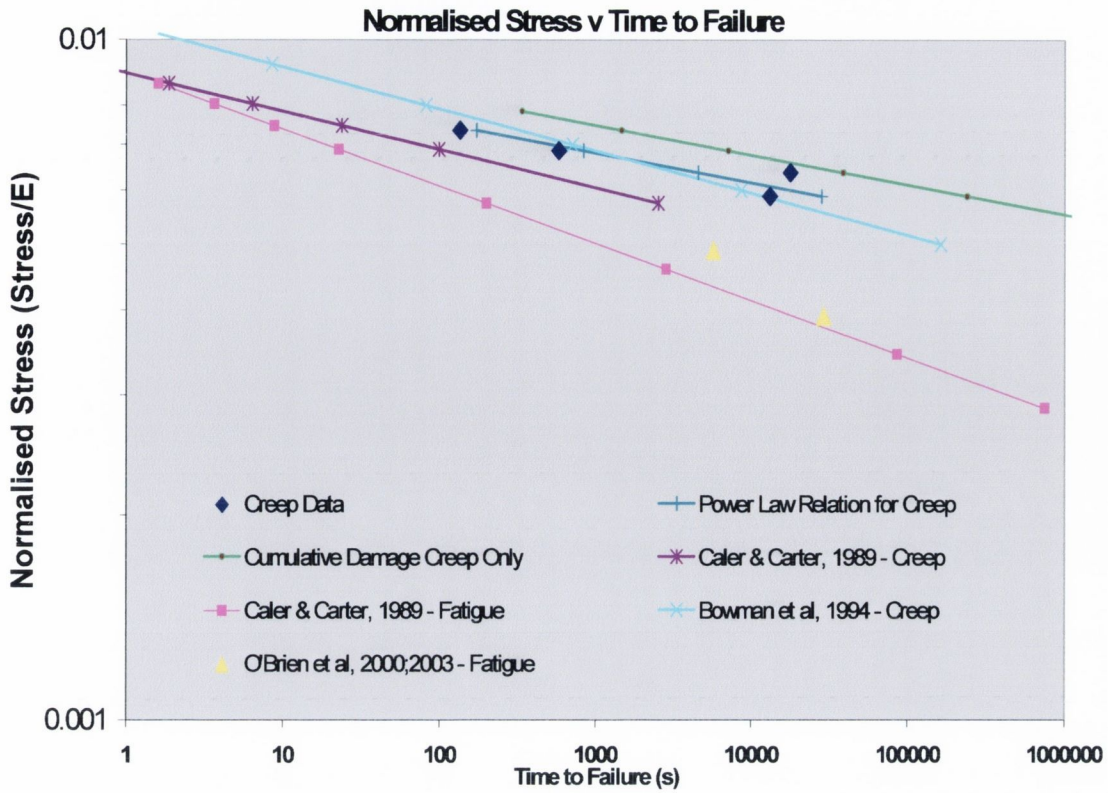

Fig. 4.21 A comparison of time to failure for various creep and fatigue studies

The graph demonstrates that the fatigue work of O'Brien concurs very well with the fatigue function developed by Caler and Carter for human femoral compact bone (Caler and Carter, 1989) as described by Equation 4.10. The fatigue work carried out in this investigation is not included here since, time to failure was not considered for those *in vivo* stress levels.

4.10

$$t_f = 4.79 \times 10^{-25} \left(\frac{\sigma_{max}}{E} \right)^{-11.88}$$

Figure 4.21 would suggest that, in the stress ranges examined, cyclic loading has a far greater effect on bone than time-dependent loading. The cyclic factor is clearly dominant, causing a far shorter time to failure with a significant difference in time to failure between creep and fatigue. This observation is supported by the findings of Caler and Carter (1989).

4.2.1 Cumulative Damage Model

This comparison between creep and fatigue loading can be taken one stage further by considering the damage caused during a fatigue cycle resulting directly from time-dependent effects. This is done using a cumulative damage model. In a specimen undergoing a cyclic loading regime, damage due to generalised stress can be seen to consist of both time-dependent and cycle-dependent contributions. Carter and Caler (1985) also suggest that there may be some interaction between creep and fatigue effects, which either accelerates or inhibits the accumulation of damage. Carter and Caler therefore considered the relation, as described in Equation 4.11.

4.11

$$D_s = D_c + D_f + D_t$$

where D_s is the damage due to generalised stress present in the bone, D_c is the creep damage function, D_f is the fatigue damage function and D_t is the interaction damage fraction between creep and fatigue.

In this creep analysis, the fatigue component will be neglected and only the time-dependent loading component for a given cyclic load will be examined. According to Equation 4.11 the contributions made by D_f and D_t can therefore be ignored.

The creep-fracture characteristics for creep failure can be described by a brittle fracture creep model, similar to that proposed by Kachanov (1958, 1961). This model assumes that the creep process is accompanied by the progressive accumulation of cracks within the material, where the accumulation of cracks can be related to a damage function D_c. The damage function should have a value such that $0 \leq D_c \leq 1$ where D_c will gradually increase until it reaches a value of 1 where complete failure will occur. The applied load results in the accumulation of creep damage, which is dependent on both magnitude and duration of loading. For a constant applied stress (σ), the time to failure (t_f), can be related to the stress by a power function of the form described in Equation 3.3.

If damage is assumed to occur at a constant rate, Equation 4.12 can be used to describe the rate of damage accumulation.

4.12

$$\frac{dD_c}{dt} = \frac{1}{A\left(\frac{\sigma}{E}\right)^{-B}}$$

Assuming an arbitrary time varying stress history is applied to the specimen, the cumulative creep damage is given by Equation 4.13.

4.13

$$D_c(t) = \int_0^t \left(\frac{1}{A\left(\frac{\sigma(t)}{E}\right)^{-B}} \right) dt$$

In neglecting the effects of fatigue and therefore interaction, specimen fractures will be due to the accumulation of creep damage alone, consequently Equation 4.13 can be rearranged and solved for t_f, by setting $D_c(t_f) = 1$.

For a sinusoidal load profile the stress history can be described by Equation 4.14.

4.14

$$\sigma(t) = \sigma_m + \left(\frac{\triangle\sigma}{2}\right)\sin(2\pi\omega t)$$

σ_m is the mean stress; an average of the maximum and minimum cyclic stresses.

Assuming a zero – compression cyclic loading regime, the mean stress will be half of the stress range.

4.15

$$\sigma_m = \frac{\Delta\sigma}{2}$$

Equation 4.13 can therefore be rewritten as shown in Equation 4.16

4.16

$$1 = \left(\frac{1}{A}\right) \cdot \left(\frac{\Delta\sigma}{2E}\right)^{B} \cdot \int_{0}^{t} (1 + \sin(2\omega t))^{B} dt$$

By rearranging the above equation, time to failure in seconds (t_f) can be described according to Equation 4.17.

4.17

$$t_f \omega \cdot \int_{0}^{\overline{\omega}} (1 + \sin(2\pi\omega t))^{B} dt = \left(\frac{\Delta\sigma}{2E}\right)^{-B} \cdot \int_{0}^{\frac{1}{\omega}} (1 + \sin(2\pi\omega t))^{B} dt$$

For sinusoidal loading at physiological frequency, ω can be assumed to be equal to 3Hz, as used experimentally in the fatigue analysis. In order to calculate the time to failure in Equation 4.17, the denominator was integrated using Simpson's rule over 100 subintervals.

Equations 4.12 through 4.17 are all developed from Carter and Caler's work (1983, 1985). In this study, stress has been normalised with the elastic modulus E = 20.4 GPa. Values for the creep coefficient (A) and exponent (B) were taken from the tests conducted in this work ($A = 2.77 \times 10^{-47}$, B = 22.87, t_f in seconds).

The position of this cumulative function also shown in Figure 4.21 demonstrates that, under the stress ranges investigated here, the contribution of creep in a cyclic loading regime is relatively small compared to the damage caused by fatigue. This is demonstrated by the significantly higher times to failure predicted by the cumulative damage function when compared to the measured times to failure for fatigue loading. This is verified by Caler and Carter's observation (1989), that cyclic tensile loading is associated with significant time-dependent damage accumulation, whereas cyclic compressive loading is dominated by cycle-dependent damage.

The cumulative damage model presented here assumes that a damage fraction can be established for both time-dependent and cycle-dependent damage. No attempt has been made to account for damage that was already present in the specimens due to *in vivo*

loading, or created during the manufacture of the specimens, however this can be assumed to be minimal (O'Brien et al., 2003).

The initial cumulative damage model presented by Carter and Caler (1985) predicts a transition from creep to fatigue behaviour in zero-tension cyclic loading. This occurs after approximately 10^6 loading cycles for a tensile strain characteristic of normal activities, such as standing, walking and running which cause strains below 2500 με.

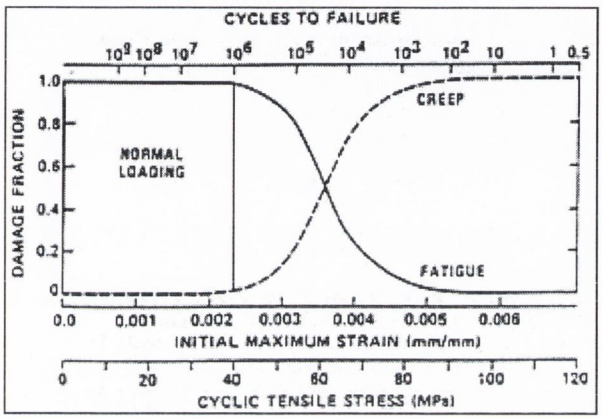

Fig. 4.22 Creep - fatigue transition curve (Carter and Caler, 1985)

In normal activities, it is speculated that creep due to cyclic loading may be relatively insignificant in the cortical bone of the normal adult skeleton. This is due to the low level of strain experienced during normal activities; far less than that required to result in a creep response. Although peak strains of the order of a few thousand microstrains may be experienced *in vivo* (Rubin and Lanyon, 1982; Biewener and Taylor, 1986; Biewener et al., 1986; Burr et al., 1996; Martin, Burr and Sharkey, 1998), for a large proportion of the day most animals are involved in activities associated with far smaller strain magnitudes than vigorous, peak magnitude activities (Fritton et al., 2000). If a creep-fatigue transition exists, then one can speculate on how ageing of bone tissue or bone pathology could influence the transition point, and thus the relative contributions of fatigue and creep damage (Carter and Caler, 1985). The clinical manifestations of certain bone diseases may reflect a shift in the creep-fatigue transition point, so that creep effects begin to dominate during normal activities. It is also probable that the relative contributions of creep and fatigue may change during bone maturation. The high degree of inelastic (plastic) deformation observed in children's bones (Currey and

Butler, 1975) suggests that the creep properties of younger bone may be significantly different to the more mineralised adult bone.

If Figure 4.21 is reconsidered it is unlikely that a transition point as described in Figure 4.22 really exists for compression in normal bone tissue. Examining the data points from the work of O'Brien et al. (2003), the graph suggests that if the pattern observed for fatigue life were continued until it crossed the cumulative damage model this would occur at approximately 170 MPa. It would cross the creep life model at approximately 140 – 150 MPa. Such stress levels are far greater than those associated with *in vivo* fatigue stresses and failure would occur within approximately 100 seconds. This would, in effect, represent almost instantaneous failure with only 300 fatigue cycles.

4.2.2 Time to failure – High Temperature Creep

Increasing the operating temperature for creep testing was observed to have a noticeable effect on the time taken to initiate failure in specimens of compact bone. In all high temperature creep tests, complete failure of the specimen was observed within a reasonable period of time, unlike the room temperature studies where, at stress levels of 120 MPa and 130 MPa, some specimens did not fail within a time period of 20 hours and testing was interrupted. Figure 4.23 compares the time to failure of room temperature and high temperature creep test at 120 and 130 MPa.

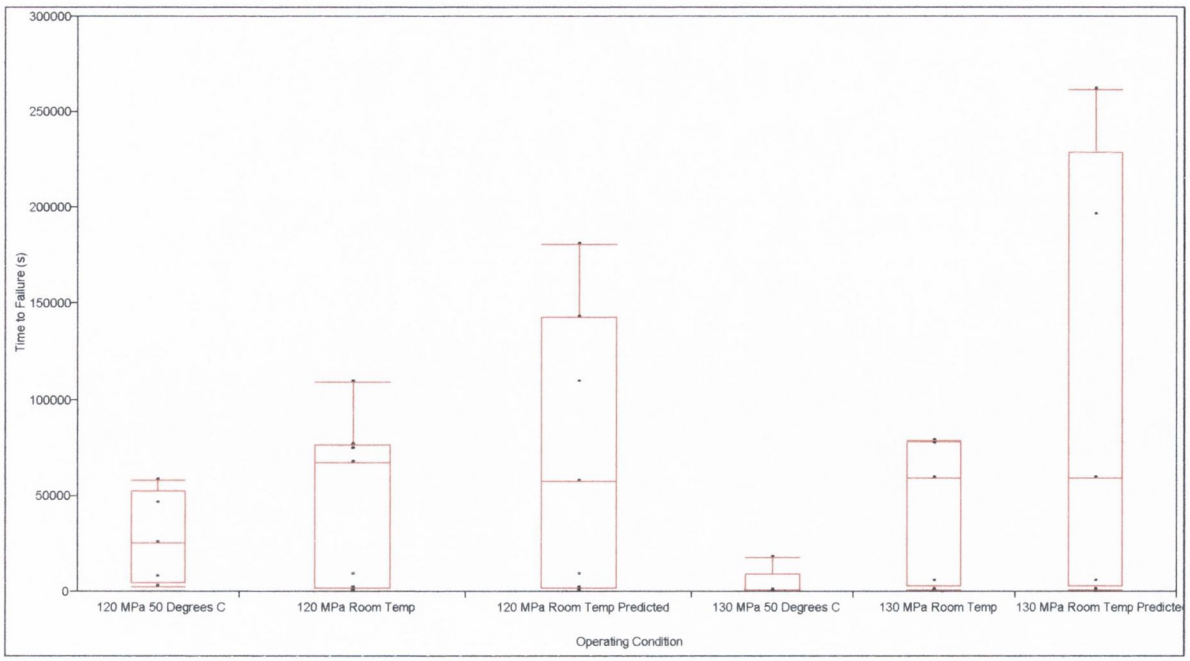

Fig. 4.23 Box plot diagram – creep time to failure (s) versus operating condition

Table 4.3 Median and quantiles – creep time to failure (s) versus operating condition

Quantiles

Level	Minimum	10%	25%	Median	75%	90%	Maximum
120 MPa 50 Degrees C	2358	2358	5100	25365	52319	58331	58331
120 MPa Room Temp	83	83	2235	67296	76615	109377	109377
120 MPa Room Temp Predicted	83	83	2235	57340.7	142840.9	180769.2	180769.2
130 MPa 50 Degrees C	243	243	276	997	9674	18268	18268
130 MPa Room Temp	897	897	3267.5	59355	78117.5	79039	79039
130 MPa Room Temp Predicted	897	897	3267.5	59355	229184.5	261887.2	261887.2

Figure 4.23 is a box plot diagram comparing time to failure across the two studies. For the room temperature tests, two boxes are shown, the first box describes time to failure as the point of specimen failure or the point at which testing was interrupted. The second box describes the time to failure as being the point at which a specimen failed or the predicted time to failure for those specimens which did not fail, where the predicted time to failure was calculated using the relationship between steady state creep rate and time to failure. Although the boxes based on predicted values are much larger, the effect on median time to failure is minimal, demonstrating that the first half of the

sample distribution still occurs within approximately the same time period. Table 4.3 details median and quantile values for the conditions described in Figure 4.23.

There is a considerable difference between the high temperature and room temperature boxes with the high temperature creep specimens failing within a much shorter period of time. Increasing operating temperature has had the effect of reducing the spread of values for time to failure.

4.2.3 Steady state creep rate

The range of values for steady state creep rate was found to span several orders of magnitude in a similar manner to time to failure. This degree of scatter in steady state creep rate is also consistent with published work by Bowman et al. (1994; 1999) and Rimnac et al. (1993). Bowman et al. (1999) showed that steady state creep rates and times to failure spanned several orders of magnitude. As was the case for time to failure, such a high degree of scatter is a result of structural variation within the microstructure of the bone and variation in material properties, porosity and mineralisation. In support of this assertion, Rimnac et al. (1993) developed an empirical model, which suggests that steady state creep rate is in fact a function of the bone microstructure.

The strong and significant power law relationships developed for steady-state creep rate and time to failure as a function of the applied stress (Equation 3.4 and Equation 3.6) suggested that steady state creep rate would also be highly correlated to time to failure. Using least squares linear regression further analysis showed a significant relationship for steady state creep rate as a function of the time to failure in the room temperature creep tests.

4.18

$$\frac{d\varepsilon}{dt} = 0.0048\,(t_f)^{-0.97} \quad (r^2 = 0.98, n = 16, p < 0.001)$$

Figure 4.24 demonstrates this relation between time to failure and steady state creep rate and compares it with previous work by Bowman et al. (1994) for bovine trabecular bone tested in compression.

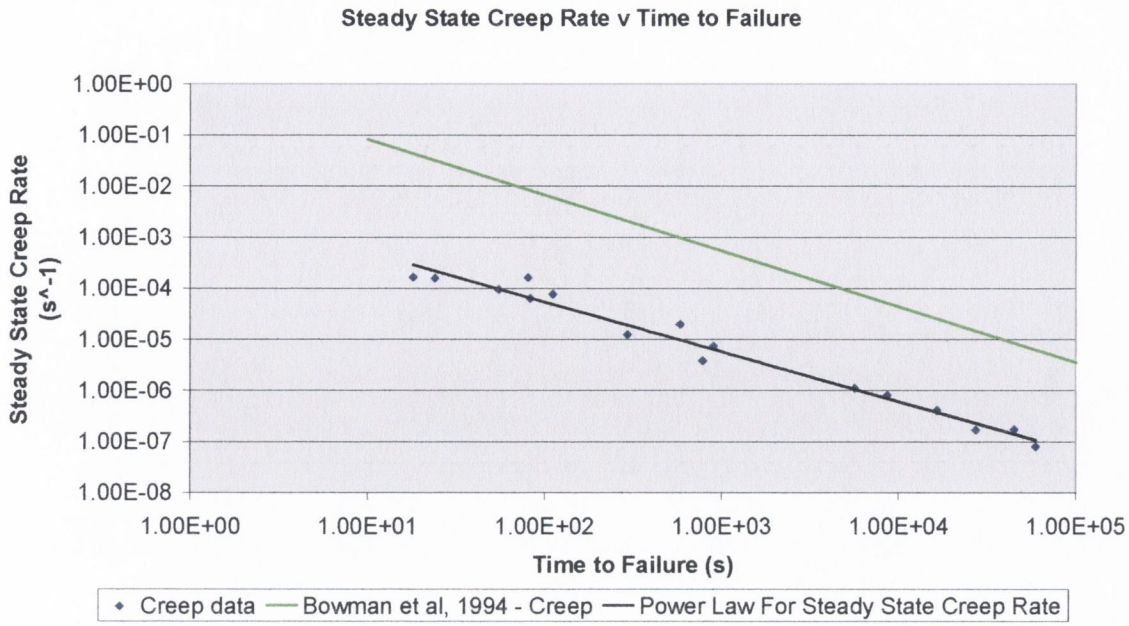

Fig. 4.24 Steady state creep rate as a function of the time to failure

Both Equation 4.18 and Figure 4.24 are based on data from failed specimens in the room temperature creep investigations. By considering only the failed specimens it is then possible to predict the true time to failure for those specimens that did not fail. Table 4.4 shows modified average failure times for all stress levels. In this table, individual values for specimens which did not fail have been replaced with a predicted time to failure according to Equation 4.18, where time to failure is calculated as function of the steady state creep rate. As per the values in Table 3.6, values in Table 4.4 have been calculated from log transformations of the data.

Table 4.4 Revised values for time to failure

Stress (MPa)	Mean Time to Failure (s)	Error Min – Max (s)
88	45,032	-
120	*15,928*	*944 – 268,927*
130	*27,401*	*2,394 – 313,576*
140	581	28 – 12,241
150	135	33 - 554

Figure 4.25 depicts both the calculated and predicted mean time to failure for each stress level. As can be seen in the graph, only the values for 120 and 130 MPa differ in any way because these were the only two stress levels at which catastrophic failure was not observed for every specimen.

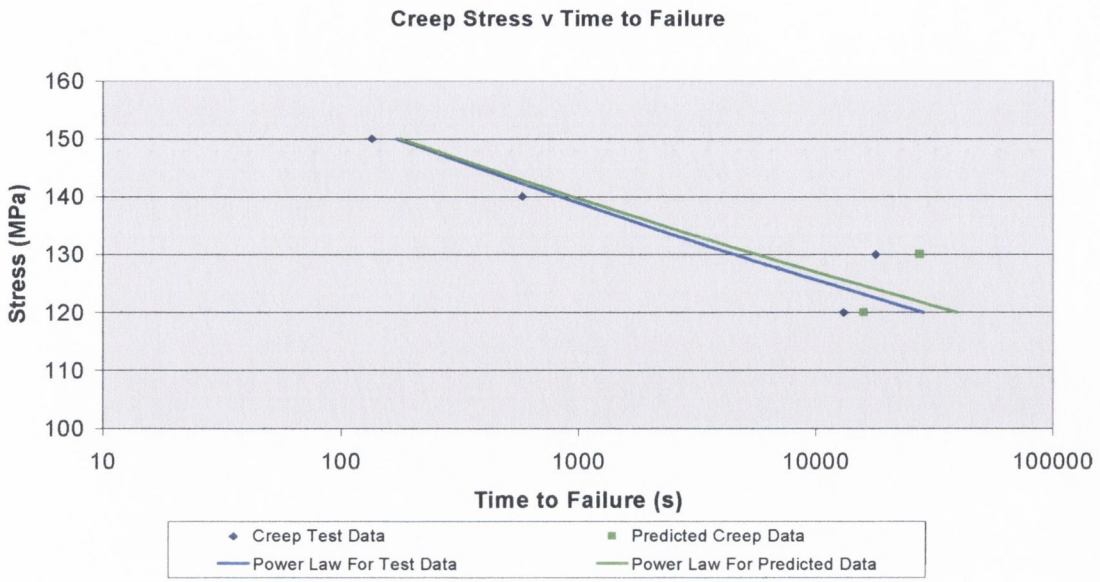

Fig. 4.25 Time to failure as a function of the applied stress, experimental and predicted data

Having predicted alternative times to failure for those specimens that did not fail, the function developed by this work can be adjusted to reflect these alterations. This altered model is shown in Equation 4.19, which can be used to predict the creep life from the applied stress.

4.19

$$t_f(predicted) = 4.14 \times 10^{-50}\left(\frac{\sigma}{E}\right)^{-24.20} \quad (r^2 = 0.82, n = 4, p < 0.1)$$

The consequence of this is a slight increase in time to failure at the lower end of the stress levels investigated.

4.2.4 Steady State Creep Rate – High Temperature Creep

In the room temperature investigations, strong and significant power law relationships for steady state creep rate and time to failure as a function of the applied stress led to the development of a relationship between steady state creep rate and time to failure as described in Equation 4.18 and Figure 4.24. Figure 4.26 shows the same graph, but with the addition of all specimens from the series of high temperature creep tests conducted at an operating temperature of 50°C.

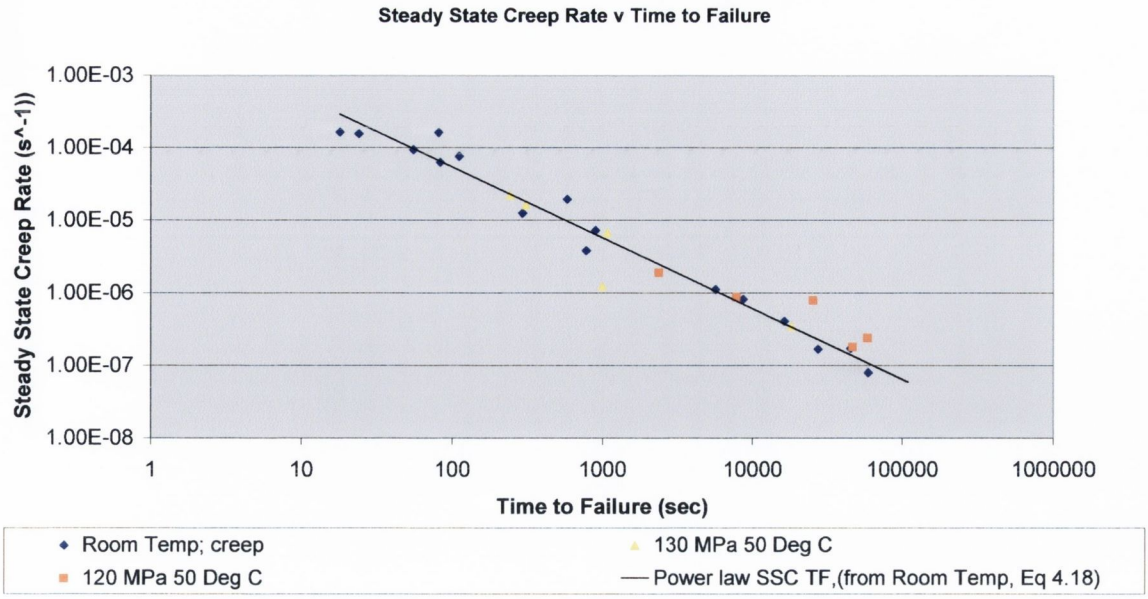

Fig. 4.26 Steady state creep rate as a function of time to failure

The high temperature creep data correspond very well with Equation 4.18 developed from the room temperature tests. This confirms that, whilst time to failure is highly correlated with steady state creep rate ($d\varepsilon/dt$), the relationship between them is independent of temperature. Previous studies (Bowman et al., 1998) have also indicated that time to failure correlates well with steady state creep rate, independent of both the applied normalised stress and temperature within the range of temperatures investigated.

Unlike the relationship between steady state creep rate and time to failure, which is unaffected by an increase in temperature, temperature has had an effect on the relationship between steady state creep rate and log stress (MPa). This is demonstrated in Figure 4.27, where for creep at 50°C. $d\varepsilon/dt = 4.18\times10^{48}(\sigma/E)^{24.60}$, whereas at room temperature, $d\varepsilon/dt = 5.76\times10^{48}(\sigma/E)^{24.48}$. Increasing the temperature has had an effect on creep rate, as anticipated.

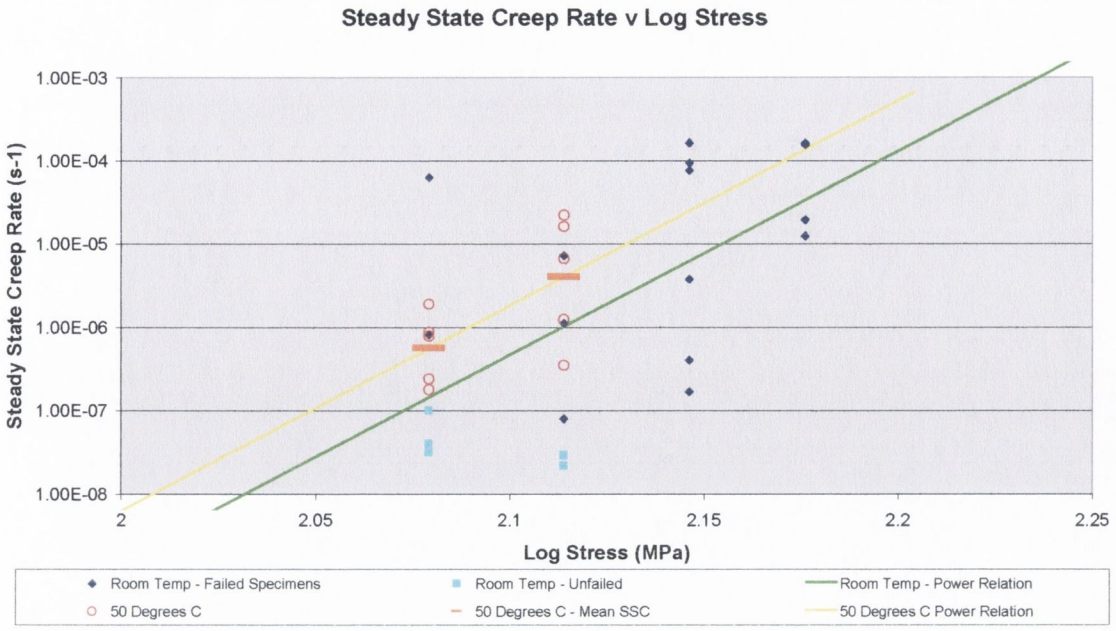

Fig. 4.27 Log – log plot of stead state creep rate (dε/dt) versus stress (σ)

For a given applied stress, the effect of increasing the operating temperature is to increase the steady state creep rate of the specimen. If this is examined from the reverse perspective, for a given steady state creep rate, the effect of increasing the operating temperature from room temperature to 50°C is to reduce the stress level by a factor of 1.06.

4.2.5 Fractography – Scanning Electron Microscopy Imaging of Creep Fracture Surfaces

The examination of room temperature creep fracture surfaces suggested that creep failure is generally associated with oblique cracking and longitudinal splitting through the structure of the bone. This is characteristic of compressive stresses leading to mainly shear components of macrocrack growth through the specimen.

Analysis of fracture surfaces suggests that as the main fracture site progresses through the structure and encounters osteons separation can occur over a relatively long distance parallel to the long axis of individual osteons. This occurs as a result of shear failure along the inner surfaces of the bone's microstructure. The oblique fracture angle also reflects crack growth parallel to lamellae at low crack velocities.

The fracture surface of failed specimens in this study was consistent with the work of Caler and Carter (1989) and demonstrated many of the features observed by Corondan and Haworth (1986) and Fleck and Eifler (2003) with regard to crack propagation through the specimen and shear mechanisms. The results presented here would suggest that the main mechanisms of failure are delamination at lamellar and osteon boundaries accompanied by limited microcracking. It is possible that, as these areas of damage coalesce, the specimen will begin to separate, resulting in complete failure. Caler and Carter (1989) suggest that, at the level of the whole bone, the observations made here would constitute crack initiation.

It can be assumed that bone fails where it is at its weakest (Evans and Bang, 1967; Evans, 1976). Corondan and Haworth showed that the fracture surface has a different histological structure to that of sections deeper into the specimen; consistently lower osteon densities were found at the fracture surface than elsewhere in the specimen. If it is assumed that the bone breaks where it is weakest, or where crack propagation is less restrained by microstructural barriers. Then the fracture plane will take an irregular course through the specimen as it follows a path of least resistance through the structure (Corondan and Haworth, 1986).

Although fracture surfaces showed surface microcracking, this was not quantified due to the possibility of artefactual cracking due to freezing of the specimen in the vacuum of the SEM. For this reason, microdamage quantification was limited to epifluorescence microscopy.

4.2.6 Microdamage formation in creep

It was not possible to measure the development of microdamage over time, or to separate pre-existing from test-induced damage. This was largely due to the inability to distinguish between two dyes: Alizarin Complexone and Xylenol Orange. Given that in the fatigue investigations a difference could be identified, this would suggest that the application of the full dye sequence (Alizarin Complexone – Xylenol Orange – Calcein – Calcein Blue) enhances differentiation between individual dyes (O'Brien, 2000).

An earlier study by O'Brien et al. (2003) quantified the percentage of *in vivo* or artefactual damage present in bovine cortical bone specimens prior to testing. Their results describe only 6 % of the total number of cracks identified (3.4 $\mu m/mm^2$, surface crack density) as being produced either *in vivo* or as a result of manufacture in transversely cut sections (pre-existing microdamage). Only one out of 54 pre-existing microcracks was observed to propagate during fatigue testing. In a control study (O'Brien et al., 2003) 25.9 % of such pre-existing damage was classified as *in vivo* damage (0.9 $\mu m/mm^2$, surface crack density). These findings were lower than *in vivo* crack densities found in human bone (Burr and Stafford, 1990; Lee et al., 1998; O'Brien, 2000). It is therefore suggested that, since the specimens used in this work are comparable with those used by O'Brien et al. (2003), and given that similar manufacturing methods were employed, it can be assumed that pre-existing damage would be of the same order (6%) and therefore negligible.

Microcrack location was considerably weighted towards interstitial rather than osteonal bone in a similar manner to the fatigue findings and published work (Schaffler et al., 1994b; Schaffler et al., 1995; Lee et al., 2000b; O'Brien et al., 2004). Microdamage primarily occurred in older bone tissue.

Statistical analysis showed a significant positive correlation between time to failure and the percentage of interstitial microcracks and a significant inverse correlation between time to failure and the percentage of osteonal microcracks. This suggests that specimens with a longer time to failure are more inclined to have an increased percentage of interstitial microcracks above the underlying trend for most microcracks to be interstitial. This may indicate that in stronger specimens with a longer time to failure, microcracks are less likely to penetrate an osteon cement line. This also implies that in weaker specimens with a shorter time to failure there is an increased likelihood of microcracks penetrating an osteon cement line. This would suggest differences in the progression to failure of different specimens. In specimens with longer times to failure, an individual microcrack may continue to grow forming a macrocrack and eventually lead to failure. Whereas in creep specimens with shorter times to failure, we may be observing failure en masse where a larger number of microcracks are able to penetrate the cement line and are therefore more dangerous.

If specimen 'b' (Table 3.12) is examined in more detail, this particular specimen has the highest incidence of microdamage and surface crack density, along with the lowest percentage of interstitial microcracks and highest percentage of osteonal cracks. This would also suggest that only as the length of cracks, or crack number, increases do we then see a corresponding increase in the number of cracks crossing osteon boundaries. This is consistent with the concept of a microstructural barrier, as described by a number of authors (Martin and Burr, 1989; Taylor and Prendergast, 1997; Taylor, 1998b; Akkus and Rimnac, 2001). The microstructure of the bone allows microcracks to initiate rapidly, but then suppresses further crack growth when microcracks encounter morphological barriers within the bone's microstructure. Only when cracks have grown in length and have more energy is there the potential for a microcrack to break through a cement line surrounding a secondary osteon. Other features of bone microstructure may also act as a similar mechanisms to crack arrest.

The current work is the first attempt to quantify microdamage in creep tested specimens; hence it is not possible to directly compare these results with those of other authors. However microcracks resulting from cycle-dependent loading, or fatigue, have been considered a number of times.

If these results are compared with the room temperature fatigue results of this study, for fatigue damage in cortical bone, it can be seen that the incidence of microdamage represented by numerical crack density is significantly lower in creep than in fatigue ($p<0.005$, two tailed Student's t-test for independent samples assuming unequal variance) with a mean crack density in creep of 0.07 cracks/mm^2 (standard deviation 0.08 cracks/ mm^2) and in fatigue across all stress levels (at 70 MPa only the six specimens used for data analysis used) a mean crack density of 0.95 cracks/mm^2 (standard deviation 1.2 cracks/ mm^2). This would suggest that far greater damage occurs in fatigue than in creep loading. Given the limited amount of microdamage observed in creep specimens, it is possible that other forms of damage, for example at an ultrastructural level, may contribute to creep in bone (Park and Lakes, 1986).

In contrast however, although far less damage is evident in creep than fatigue, microcracks are longer in creep. In fatigue loading, mean crack length was found to be 74.31 μm (standard deviation 59.36 μm) and in creep loading the mean crack length

was found to be 257 μm (standard deviation 205.24 μm). The difference in lengths between the two groups was found to be statistically significant ($p<0.0005$, 2-tailed Students t-test).

As a whole, these comparisons suggest that creep causes less damage than fatigue. However, microcracks are able to grow to a much longer length in creep than fatigue, without causing the development of a macrocrack resulting in catastrophic failure of the specimen. These observations indicate that, in creep, cracks are less dangerous as they are able to grow to greater lengths without causing failure.

At lower stress levels, cycle-dependent damage is far more significant than time-dependent damage, thus *in vivo*, fatigue is likely to be the agent responsible for the development of microdamage. At these levels, any effects resulting from creep are likely to be minimal and not detrimental to the integrity of bone.

4.2.7 Crack Length - High Temperature Creep versus Fatigue

Comparisons can be made between crack lengths in various creep and fatigue studies. Figure 4.28 compares mean crack length between the high temperature fatigue and creep studies (histological creep data is taken from the tests at 130 MPa).

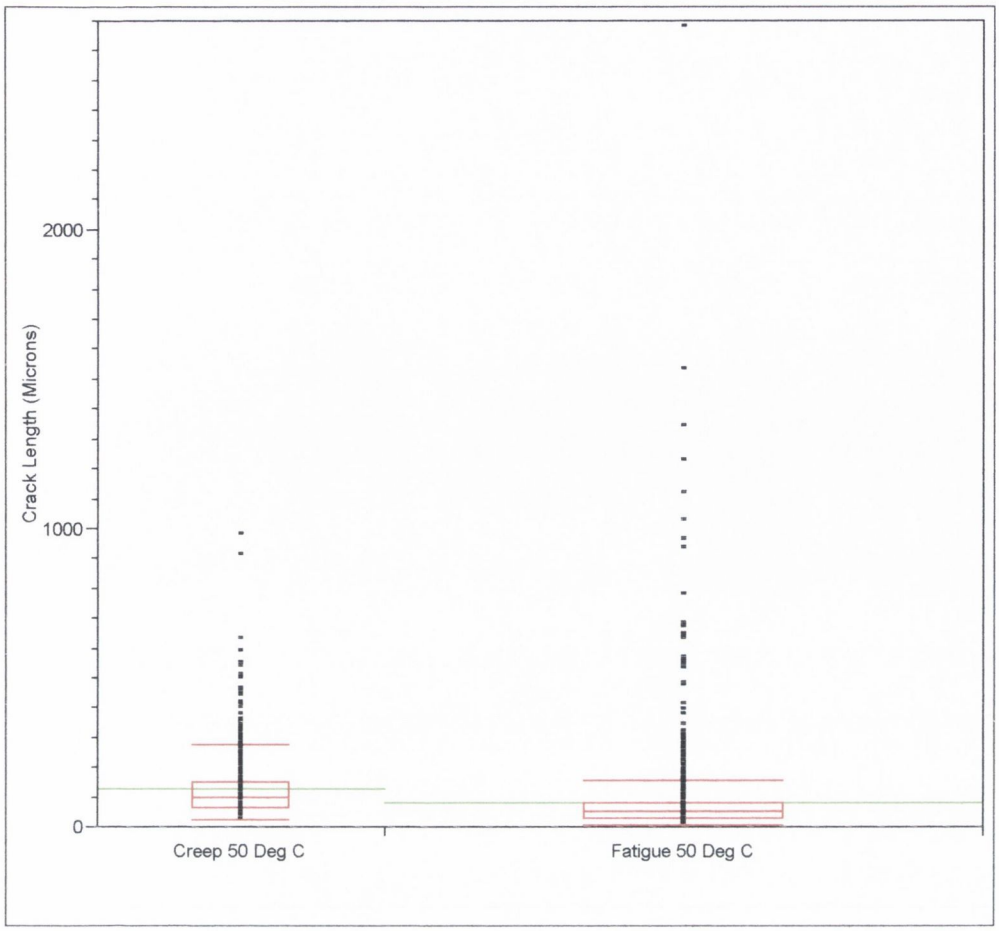

Fig. 4.28 Mean crack length – high temperature creep versus fatigue

It can be seen from the graph that, despite some outliers and extreme values (greater than 1.5 interquartile ranges from the quartiles), the bulk of the values for crack length are smaller than those in the creep study. Table 4.5 describes median and mean crack lengths for the two studies, which are also illustrated in Figure 4.28 (mean = green lines, median = line passing through the central 50% of the values).

Table 4.5 Mean and median crack length – high temperature creep and fatigue

Test Type	Mean Crack Length (μm)	Median Crack Length (μm)
Creep 130 MPa 50°C	128 (S.D 100, n = 610)	98
Fatigue 80 MPa 50°C	80 (S.D 133, n = 1275)	52

Mean and median crack lengths were greater in the creep study than in the fatigue study by factors 1.6 and 1.9 respectively. A strong and significant difference can be observed between mean high temperature creep and fatigue crack lengths ($p<0.0005$). The same pattern observed at room temperature was also observed at elevated temperatures, where mean crack length was found to be significantly longer in creep than fatigue.

Figure 4.29 compares microcrack length in both the room temperature and high temperature creep studies at a stress level of 130 MPa.

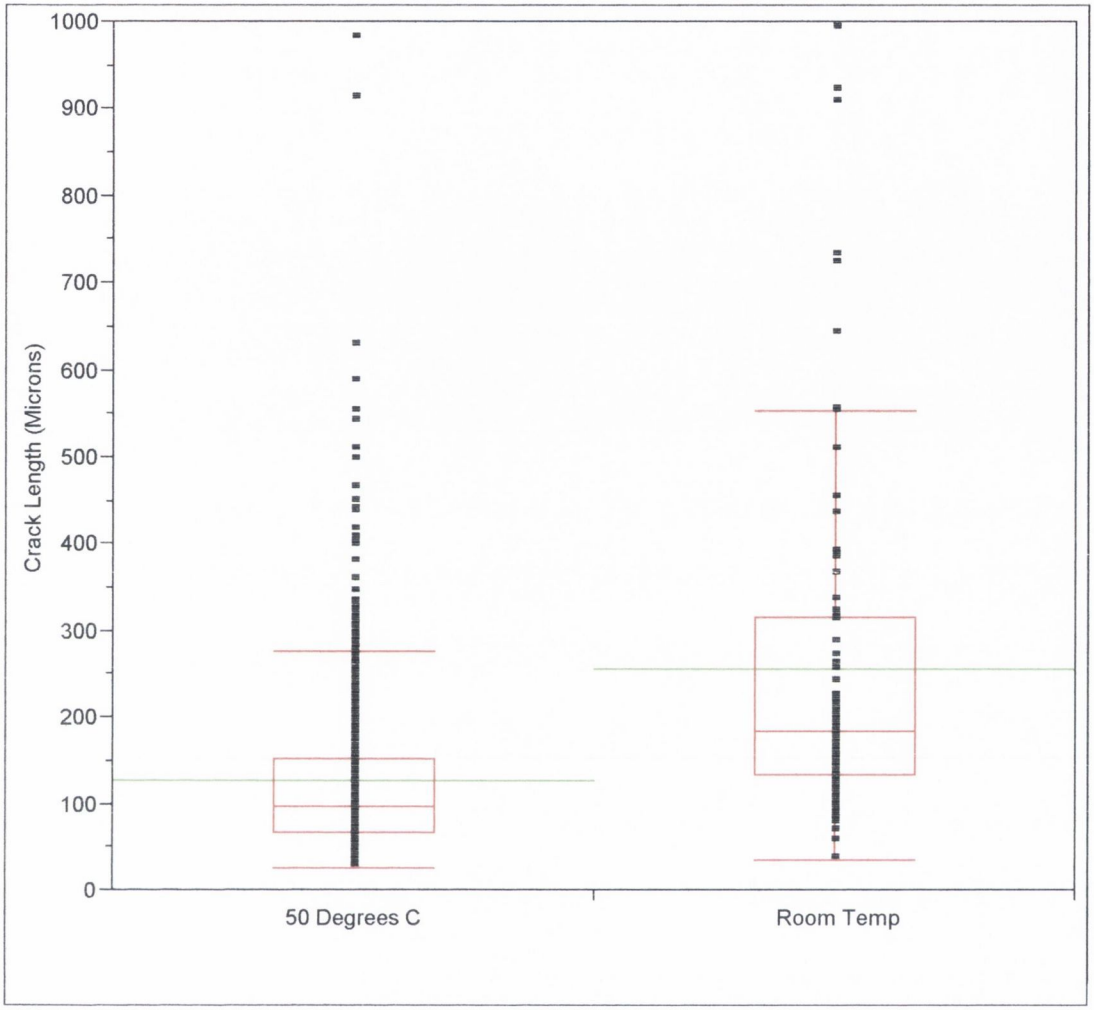

Fig. 4.29 Mean crack length – high temperature creep versus room temperature creep

The high temperature box plot shown in Figure 4.29 is based on crack measurements from 610 microcracks, whereas the room temperature box plot is based on crack measurements of 74 microcracks. The diagram demonstrates that increasing the operating temperature by approximately 28°C reduces the mean crack length by a factor of 2.01 and a statistically significant difference between crack lengths at the two operating temperatures can be observed ($p<0.0005$).

4.2.8 Thermal Effects on Microcrack Density - Creep versus Fatigue

With increased operating temperature the incidence of microdamage is once again lower in creep than fatigue with a total of 610 microcracks in the high temperature creep study and 1275 microcracks in the high temperature fatigue study. Increasing the operating temperature has increased microcrack density in creep tests in the same way in which it increased microcrack density in the fatigue study. Microcrack density has increased dramatically with a 120-fold increase in the mean crack density and a 194-fold increase in the median crack density. Mean and median crack densities are described in Table 4.6.

Table 4.6 Mean and median crack densities – high temperature versus room temperature creep

Test Type	Mean Crack Density (# cracks/mm^2)	Median Crack Density (# cracks/mm^2)
Creep 130 MPa – Room Temp	0.07	0.03
Creep 130 MPa - 50°C	4.90	3.82

The dramatic nature of these increases in microdamage are illustrated in Figure 4.30 which compares microcrack density results from the room temperature and high temperature creep studies at 130 MPa. The disparity in the range of values is vast and despite a relatively small number of samples in each operating condition a significant difference can be found between the two samples ($p<0.01$). Although a first attempt at quantifying creep microdamage, observations that the steady state creep rate, a damage accumulation parameter, is significantly related to temperature (Rimnac et al., 1993; Bowman et al., 1996a; 1998; 1999) would support the finding that an increase in temperature will result in a higher incidence of microdamage.

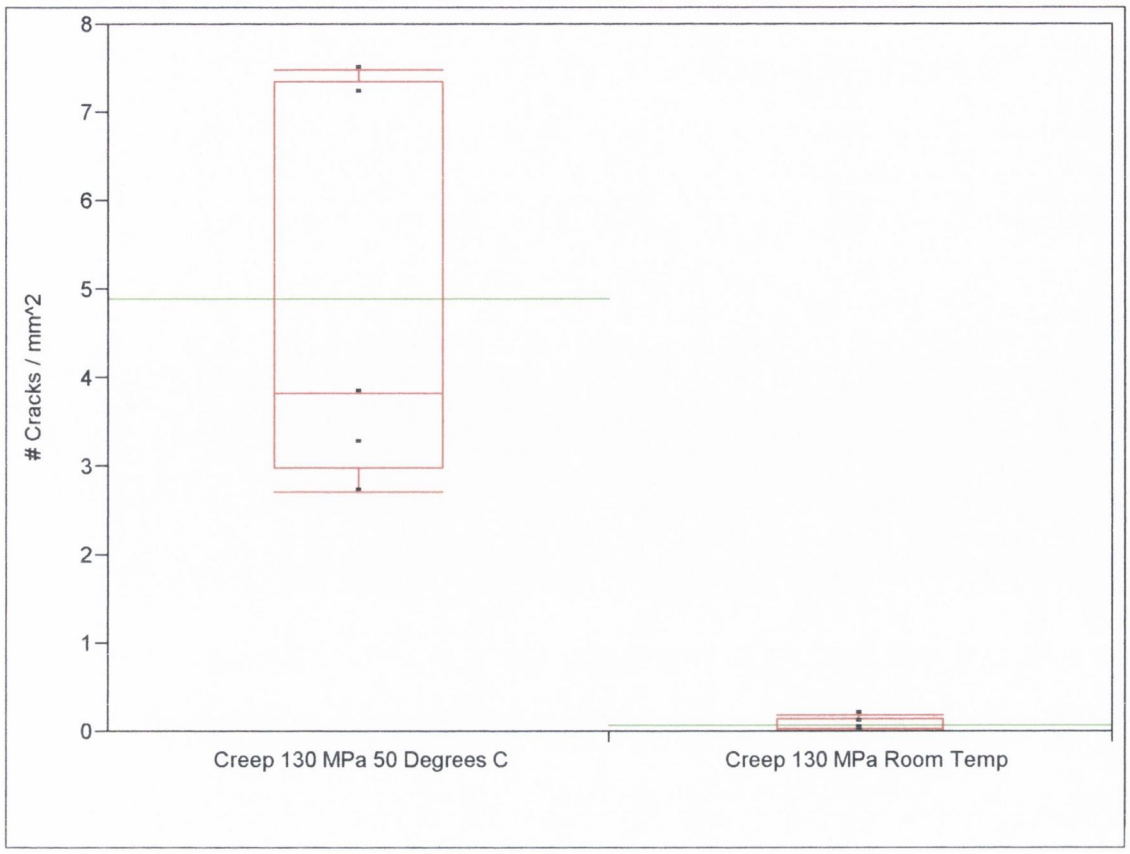

Fig. 4.30 Microcrack density – high temperature versus room temperature creep

An increase in operating temperature has clearly affected the development of microdamage in both creep and fatigue studies however, for the stress ranges and levels considered here, it still remains evident that more microdamage is present in the fatigue than creep tests. This is demonstrated in Figure 4.31, a box plot diagram of microcrack density for high temperature creep and fatigue.

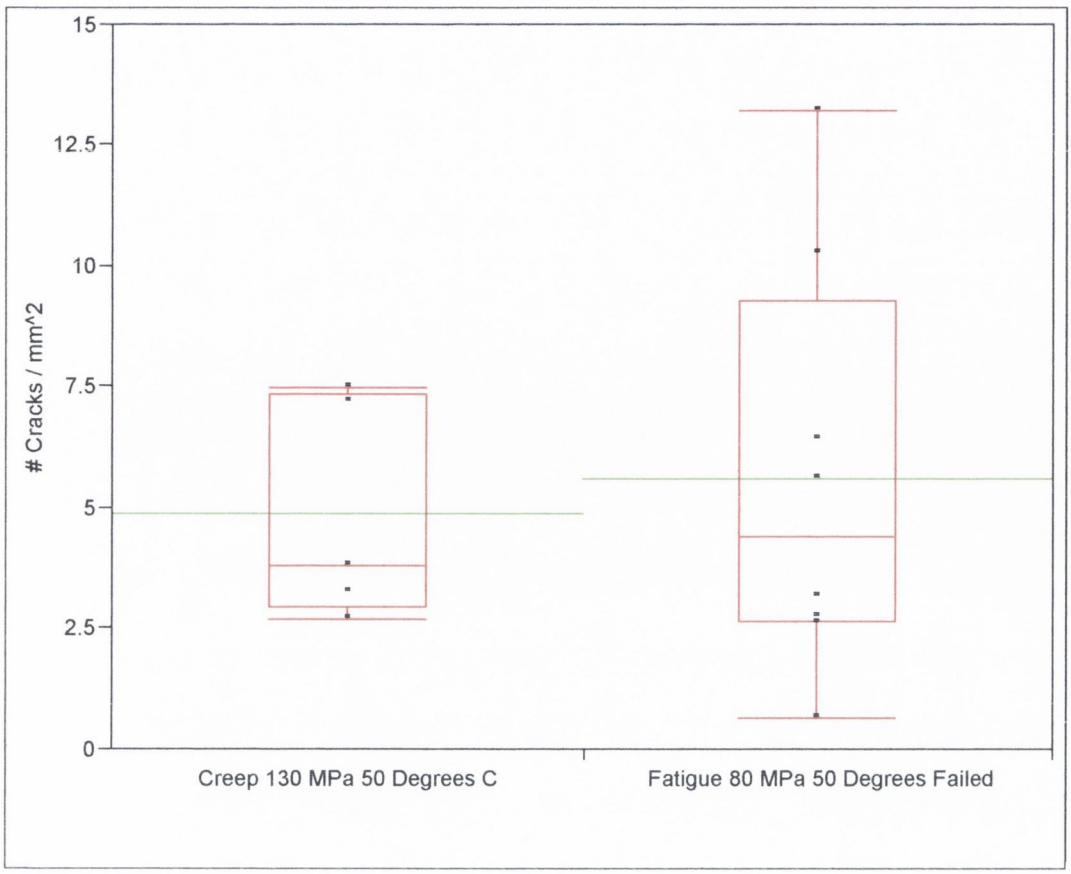

Fig. 4.31 Microcrack density – high temperature creep versus fatigue

However, the difference between the two modes of loading has narrowed, and no significant difference can be found between microcrack density in creep and fatigue ($p=0.71$ for only failed fatigue specimens, $p=0.87$ for all fatigue specimens). The effects of temperature have increased damage so substantially in creep, that despite an increase in microdamage in the fatigue study, creep microdamage approaches the levels observed in fatigue as a direct result of increased temperature. This would suggest at elevated temperatures, for the stress levels investigated (130 MPa), creep is approaching those levels where it will become the significant mechanism in microdamage development.

Comparisons between microcrack density for high temperature fatigue tests at 80 MPa and high temperature creep tests at 130 MPa show only a marginal difference. This raises the question as to whether creep damage will be significant at such elevated temperatures, but at stress levels more consistent with *in vivo* stresses. In order to examine this, the cumulative damage model employed in Section 4.2.1 is re-examined.

4.2.9 Cumulative Damage Model – The Effects of Temperature on Fatigue

In Section 4.2.1 the interaction between creep and fatigue was discussed using a cumulative damage model which considered the effects of creep and fatigue during the duration of a fatigue test. This was based largely on the work of Carter and Caler (1985) and Caler and Carter (1989). This pattern describes how, for a specimen undergoing a cyclic loading regime, damage due to generalised stress consists of both time-dependent and cycle-dependent contributions. This is described in Equation 4.11.

In Equation 4.11, D_s is the damage due to generalised stress present in the bone, and assuming a mixed mode of loading, as in a standard fatigue test, D_s will over time increase from 0 to 1, where failure will occur.

In Section 4.2.1 the analysis focused on the creep component within fatigue loading and as such all other components were neglected. With limited data available regarding any interaction between creep and fatigue, D_t will not be considered and bone fracture will occur after N_f cycles at a time t_f (seconds). This will occur under the following conditions described in Equation 4.20. A, B, F and G are constants determined from previous creep and fatigue studies, ω is the fatigue loading frequency in Hz.

4.20

$$\int_0^{t_f} \frac{1}{A\left(\frac{\sigma(t)}{E}\right)^{-B}} + \frac{\omega t_f}{F\left(\frac{\Delta\sigma}{E}\right)^{-G}} = 1$$

The first term is the creep damage contribution discussed in Section 4.2.1 and the second term is the fatigue damage contribution (Carter and Caler, 1985; Caler and Carter, 1989). Dividing Equation 4.20 by N_f, where $N_f = \omega t_f$, Equation 4.20 can be re-written as shown in Equation 4.21, or alternatively Equation 4.22.

4.21

$$\int_0^{\frac{1}{\omega}} \frac{1}{A\left(\frac{\sigma(t)}{E}\right)^{-B}} dt + \frac{1}{F\left(\frac{\Delta\sigma}{E}\right)^{-G}} = \frac{1}{N_f}$$

4.22

$$d_c + d_f = \frac{1}{N_f}$$

The symbols d_c and d_f represent the damage per loading cycle due to time-dependent creep and cycle-dependent fatigue effects. For a sinusoidal loading profile as used in these studies, the stress history is the same as discussed in Section 4.2.1. Hence d_c can be re-written according to Equation 4.23 where $\Delta\sigma$ is the applied stress range and E is the Young's Modulus of the material.

4.23

$$d_c = \frac{M}{A\left(\frac{\Delta\sigma}{2E}\right)^{-B}}, M = \int_0^{\frac{1}{\omega}} (1 + \sin(2\pi\omega t))^B dt$$

On the basis that in the low cycle regime the effects of creep will dominate and in the high cycle regime the effects of fatigue will dominate, then the constants A, B, F and G can be taken from previous creep and fatigue test. In high cycle fatigue test for a cyclic stress range $\Delta\sigma$; the number of cycles to failure N_f can be predicted according to Equation 4.24 where F and G are empirical constants determined from curve fits for experimental data.

4.24

$$N_f = F\left(\frac{\Delta\sigma}{E}\right)^G$$

Using fatigue data from O'Brien (2000),which provided data concerning the number of cycles to failure at two different stress ranges, values for F and G have been calculated for compressive fatigue tests at room temperature. F = 2.11×10^{-13} and G = 7.32.

Section 4.2.3 developed a modified equation for time to failure (Equation 4.19) in creep specimens based on predicted values for time to failure for un-failed specimens. Where $A = 4.14 \times 10^{-50}$ and $B = 24.20$.

Substituting these values for A, B, F, G and $\omega = 3$ Hz into Equation 4.21 enables the number of cycles to failure N_f to be predicted for a given cyclic stress range. This model predicts fatigue failure at a stress range of 80 MPa in 87,808 cycles for room temperature conditions. In the high temperature fatigue work investigated here, the mean number of cycles to failure for all specimens, including those that did not fail but failure was taken to be the point where testing was interrupted, the mean number of cycles to failure was calculated as 57,317 cycles. The mean number of cycles to failure for only failed specimens was 38,611 cycles. For the model to predict the same fatigue life for a room temperature test, as achieved in the tests at 50°C, it would require stress ranges of 84.8 MPa and 89.5 MPa for the two respective number of cycles. These suggest that a temperature decrease from 50°C to room temperature (approximately 22°C) has a multiplying factor of between 1.06 and 1.12 on the fatigue strength, depending upon which mean fatigue life is used from the high temperature fatigue studies. In Taylor's 1998 paper, a change from physiological temperature (37°C) to room temperature was said to have the effect of a multiplying factor of 1.16 on the fatigue strength. This represents a greater figure than that calculated from the current analysis over what is a smaller temperature difference. Clearly the factors calculated here are based on a temperature difference of approximately 28°C rather than 15°C used by Taylor (1998a) which examined a number of different sources. In their 1976 study, Carter and Hayes demonstrated that when tested as rotating cantilevers, a temperature reduction of 24°C (45°C to 21°C) was shown to increase the fatigue life of bone by a factor of three (Carter and Hayes, 1976), which corresponds to a multiplying factor of 1.16 on the fatigue strength using their model. Over a temperature difference of 28°C the methods described by Carter and Hayes would predict a multiplying factor of 1.2 on the fatigue strength, far greater than the factor shown here for axial compressive fatigue. Thus identifying that the effects of temperature were less in compression than that observed by Carter and Hayes in rotating beam fatigue tests.

Figure 4.32 describes the relationship between time to failure in seconds and normalised stress using a variety of models for both room temperature and high temperature creep and fatigue.

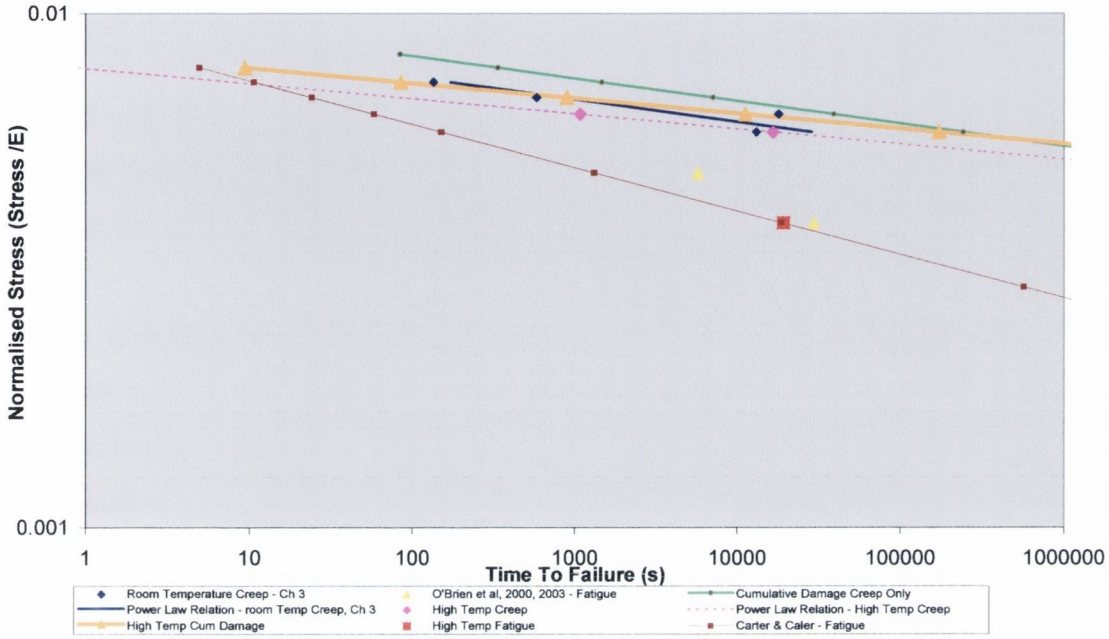

Fig. 4.32 Time to failure – creep and fatigue

Firstly, the reduction in time to failure from increasing the fatigue operating temperature can be observed by the horizontal displacement between the lower data point from the room temperature fatigue work of O'Brien et al. (2003) and the data point for the high temperature fatigue work described here. Further up the graph are illustrations of the various creep data from the room temperature and high temperature studies. The blue data points represent the mean time to failure at each creep stress for the room temperature creep experiments. The dark blue line running through the data represents Equation 3.4 which describes the creep life of specimens of bovine compact bone loaded in axial compressive creep at room temperature. The green line represents the contribution of creep in a cyclic loading regime at room temperature as described by Equation 4.17. This approach considers the time taken to initiate failure in a fatigue specimen based solely upon the effects of creep.

Equation 3.7 ($t_f = 1.201 \times 10^{-72} (\sigma/E)^{-34.137}$) describes a power law relationship for time to failure as a function of the applied creep stress at an operating temperature of 50°C.

Using this relationship, predictions can be made regarding the creep life of bone at an elevated operating temperature. This is represented in the graph by the pink dashed line. It should be noted that this equation is based only on the creep life results from two stress levels, 120 MPa and 130 MPa. However, when considering this function alongside a similar function developed for room temperature creep (Equation 3.4, $t_f = 2.77 \times 10^{-47} (\sigma/E)^{-22.87}$), the position of the line in Figure 4.32 and the creep exponent correspond with the effects of temperature that would be anticipated. The exponents are of the same magnitude as the room temperature study, but reflect the shorter time to failure from increased temperatures.

Using the constants from Equation 3.7, the cumulative damage function can be modified to reflect failure resulting from the effects of creep in a high temperature fatigue specimen. The orange line in the graph represents this function. Comparisons of the cumulative damage models for both room temperature and 50°C demonstrates that, with an increase in operating temperature, as stress increases the difference between room temperature failure and high temperature failure increases. However the position of this line suggests that despite such elevated operating temperatures, in compression at fatigue stresses investigated here, the contribution of creep in a cyclic loading regime will be relatively small compared to the damage caused by fatigue. The graph would indicate that only at considerably higher fatigue stress ranges (approx 140 – 150 MPa) would a transition be observed. To confirm this, additional high temperature fatigue data would be required at different stress ranges in order to develop a prediction for fatigue life based on high temperature operating conditions.

Using linear regression of fatigue data for human femoral compact bone loaded in axial compression at an operating temperature of 37°C, Caler and Carter (1989) demonstrated the relationship between normalised stress and time to failure to be of the form shown in Equation 4.25.

4.25

$$t_f = 4.79 \times 10^{-25} (\sigma / E)^{-11.88}$$

All of the studies shown in Figure 4.32, with the exception of Caler and Carter's work, are for tests on bovine bone; therefore Equation 4.25 is represented in Figure 4.32 using

a value of E = 20.4 GPa more appropriate to tests on bovine rather than on human bone. Therefore, in theory, the only difference between any predictions made using Caler and Carter's model and the other tests illustrated is that Caler and Carter's model has an operating temperature of 37°C. The graph demonstrates that the high temperature work conducted here coincides very well with Caler and Carter's fatigue function. Their model crosses the cumulative damage model at approximately 150 MPa. Therefore, in fatigue tests with a stress range in excess of 150 MPa tested at an elevated operating temperature, creep will be the dominant failure mechanism. However at stresses below this level the effects of fatigue will clearly dominate damage formation. This supports the observations of microcrack density in high temperature creep and fatigue, where microcrack density in creep tests at 130 MPa tested at 50°C, approached the levels measured in fatigue tests at 50°C.

Increasing the operating temperature has, for creep specimens, reduced the time to failure, increased the incidence of microdamage and at the same time reduced the mean crack length with an increased number of smaller microcracks. However it still remains evident that creep causes far less damage than fatigue at *in vivo* stress levels, despite an operating temperature far greater than human body temperature. This confirms that *in vivo*, fatigue and not creep will be responsible for the development of microdamage.

5 Conclusions

The mechanisms by which fatigue induced microdamage accumulates in bone at physiological stresses are different to those observed at higher stresses. Under *in vivo* loading, larger amounts of damage can accumulate without indication of failure, whereas at higher stress levels microdamage accumulation develops more rapidly, without reaching the higher densities observed after prolonged testing. This change in behaviour may be attributable to a threshold mechanism for damage accumulation in compact bone, as identified elsewhere in the literature.

This study has found that in normal bone tissue *in vitro* fatigue failure of compact bone is unlikely to occur under physiological loading.

At fatigue stresses consistent with physiological levels there is a natural population of microcracks that will develop in such a way that will not have a detrimental effect on the structure of bone. In conjunction with the rate of damage accumulation, this damage target level is seen to increase with increasing stress. Models have been developed to describe damage accumulation in compressive fatigue over a range of stresses from physiological loading levels, to those associated with overload conditions. Agreements have been found between these models and literature reported data.

The majority of microcracks formed *in vivo* have been shown not to be dangerous as they are unlikely to propagate to failure. Cumulative density functions for microcrack length identified the low probability of finding a large potentially dangerous microcrack under physiological loading. It is proposed that failure will be dominated in fatigue by the propagation of a small number of individual microcracks and therefore a more appropriate predictor of failure should involve the identification of those longer, more dangerous microcracks.

Bone microstructure was seen to influence microcrack growth and initiation. The majority of microcracks were found in interstitial bone and microcrack lengths were lower than those associated with osteon separation.

Increasing the operating temperature for fatigue specimens to 50°C was observed to more than halve the fatigue life of specimens. A combined fatigue – creep model enables such differences to be compared to a reduction in fatigue strength of up to 12%. Considerable increases in microcrack density have also been identified as a result of testing at elevated temperatures; microcrack density increased by a factor of 10.38.

Characterisation of the compressive creep behaviour of compact bone identified a nonlinear reduction in creep life with increasing stress. Examination of the creep fatigue interaction using a cumulative damage model demonstrated that the contribution of creep during cyclic loading is insignificant when compared to the damage caused by fatigue. The process of fatigue has been shown to be far more significant than creep at physiological loading levels where time dependent effects will be negligible. This has been found for both room temperature and elevated temperature studies. This study identified that a transition point from fatigue to creep dominated compressive loading of normal bone is unlikely, with creep dominated loading only occurring at stress levels far greater than those experienced under normal *in vivo* loading.

Examination of creep induced microdamage established that significantly less microdamage is caused by creep than fatigue loading. It has also been demonstrated that creep induced microdamage is less dangerous than fatigue induced microdamage; as microcracks are able to grow to much longer lengths without causing failure.

The examination of creep fracture surfaces suggested that failure is generally associated with oblique cracking and longitudinal splitting through the structure of the bone. At the micro structural level, the fracture surfaces indicate shear failure and delamination at the boundaries of morphological features.

Increases in temperature have been observed to have a considerable impact upon creep life. Increasing the operating temperature from room temperature to 50°C was found to reduce the creep life of specimens by a factor of 2.3 at 120 MPa and 25.3 at 130 MPa. Creep rate, a damage accumulation parameter was also seen to rise with increased temperature and hence a higher incidence of microdamage was observed; a 120 fold increase in mean crack density was observed for an engineering stress of 130 MPa.

Both creep and fatigue observed dramatic increases in microcrack density as a result of increasing the operating temperature, nevertheless microdamage remains greater in fatigue than creep. It has been established that creep causes far less damage than fatigue at *in vivo* stress levels, despite an operating temperature far greater than human body temperature. This confirms that *in vivo*, fatigue and not creep will be responsible for the development of microdamage.

6 Future Work

This study has found that in normal bone tissue *in vitro* fatigue failure of compact bone does not occur under physiological loading. However practical limitations were imposed upon testing with regard to the number of fatigue cycles studied. Confirmation of this assertion needs further study to higher fatigue cycles.

Further work in this area is also needed to consider the fatigue behaviour of whole bones, where it is anticipated that larger bones will fail sooner due to increased probability of weaker regions being present, subsequently leading to dangerous, failure inducing cracks. This will confirm that the requirements of bone remodelling at physiological loading, whose purpose would remain questionable based solely upon specimen test data.

In whole bone experiments stress distribution and hence microdamage will not be uniform. The size effect will introduce further variability into fatigue data, however it may be possible to describe this as a function of the variability of small elements of the specimen and the specimen size (Weibull, 1951). This approach was considered for compressive fatigue by Taylor and colleagues (Taylor, 1998a; Taylor et al, 1999). It may therefore be possible to predict the results of whole bones from tests on specimens following experimental validation.

Bone microstructure was seen to influence microcrack growth and initiation. Various features of bone microstructure such as vascular canals will influence microcrack growth and arrest. These experiments are limited to bovine bone which is described by large areas of secondary and plexiform bone. It is important to expand this work to examine such effects on bone of different microstructures. This could be done by conducting tests on bone from humans and other animals. This will enable differences between species and therefore correlated with differences in microstructure.

Comparisons of creep and fatigue failure have demonstrated that the process of fatigue will be far more significant than creep at physiological loading levels. Future work should attempt to investigate the influence of ratcheting during fatigue loading bone, as

this may account for some of the creep like effects identified elsewhere during fatigue loading.

The current work has quantified damage accumulation during creep and fatigue for *in vitro* testing of bone, and using these findings, models have been developed to predict damage accumulation. Further work is required to fully validate and refine these models. These have not included the effects of the remodelling and repair processes that occur in living bone. As such the clinical implications of this work must be interpreted with some caution. Future work should attempt to include terms describing the effects of remodelling on microdamage and therefore more accurately predict damage accumulation in living tissue.

7 References

Aaron, J.E., Maleins, N.B., Francis, R.B. and Peacock, M. (1984) Staining of the calcification front in human bone using contrasting fluorochromes *in vitro*. *Journal of Histochemistry and Cytochemistry,* **32:** 1251-1261.

Agarwal, B.D. and Broutman, L.J. (1980) *Analysis and performance of fiber composites*. New York: John Wiley and Sons.

Akkus, O., Jepsen, K.J. and Rimnac, C.M. (2000) Microstructural aspects of the fracture process in human cortical bone. *Journal of Materials Science,* **35:** 6065-6074.

Akkus, O. and Rimnac, C.M (2000) Short fatigue crack growth in human cortical bone. *Personal communication.*

Akkus, O. and Rimnac, C.M. (2001) Cortical bone tissue resists fatigue fracture by deceleration and arrest of microcrack growth. *Journal of Biomechanics,* **34:** 757-764.

American Association of Orthopaedic Surgeons (1993) *A position statement: prevention of hip fractures.* Rosemount, IL: American Academy of Orthopaedic Surgeons.

Andrade, E.N. da C. (1914) Creep and Recovery. *Proceedings of the Royal Society of London,* **90(A):** 329-342.

Ashby, M.F. and Jones, D.R.H. (1996) *Engineering materials 1: An introduction to their properties and applications*. Oxford: Pergamon Press. ISBN 0750630817

Bazett, H.C., Love, L., Newton, M., Eisenberg, L., Day, R. and Forster, R. II (1948) Temperature changes in blood flowing in arteries and veins in man. *Journal of Applied Physiology,* **1:** 1-39.

Bazett, H.C. (1949) In: Newburgh, L.H. (Ed.) (1949) *Physiology of Heat Regulation and the Science of Clothing,* p.109. Philadelphia, PA: Saunders. ISBN 002849640X

Bentolila, V., Boyce, T.M., Fyhrie, D.P., Drumb, R., Skerry, T.M. and Schaffler, M.B. (1998) Intracortical remodelling in adult rat long bones after fatigue loading. *Bone,* **23:** 275-281.

Biewener, A.A., Thomason, J., Goodship, A. and Lanyon, L.E. (1983) Bone stress in the horse forelimb during locomotion at different gaits: a comparison of two experimental methods. *Journal of Biomechanics,* **16:** 565-576.

Biewener, A.A., Swartz, S.M. and Bertram, J.E.A. (1986) Bone modelling during growth: dynamic strain equilibrium in the chick tibiotarsus. *Calcified Tissue International,* **39:** 390-395.

Biewener, A.A. and Taylor, C.R. (1986) Bone strain: a determinant of gait and speed? *Journal of Experimental Biology,* **123:** 383-400.

Biewener, A.A. (1991) Musculoskeletal design in relation to body size. *Journal of Biomechanics,* **24 (Suppl. 1):** 19-29.

Bonar, L.C. and Glimcher, M.J. (1970) Thermal denaturation of mineralised and demineralised bone collagen. *Journal of Ultrastructure Research,* **32:** 545-551.

Bonfield, W. and Li, C.H. (1968) The temperature dependence of the deformation of bone. *Journal of Biomechanics,* **1:** 323-329.

Bowman, S. M., Keaveny, T. M., Gibson, L. J., Hayes, W. C. and McMahon, T. A. (1994) Compressive creep behaviour of bovine trabecular bone. *Journal of Biomechanics,* 27: 301-310.

Bowman, S.M., Gibson, L.J., Hayes, W.C. and McMahon, T.A. (1996a) The creep behaviour of trabecular bone is temperature dependent. *Transactions of the Orthopaedic Research Society,* **20:** 80.

Bowman, S.M., Zeind, J., Gibson, L.J., Hayes, W.C. and McMahon, T.A. (1996b) The tensile behaviour of demineralised bovine cortical bone. *Journal of Biomechanics,* **29:** 1497-1501.

Bowman, S.M., Guo, X.E., Cheng, D.W., Keaveny, T.M., Gibson, L.J., Hayes, W.C. and McMahon, T.A. (1998) Creep contributes to the fatigue behaviour of bovine trabecular bone. *Journal of Biomechanical Engineering,* **120:** 647-654.

Bowman, S. M., Gibson, L. J., Hayes, W. C. and McMahon, T. A. (1999) Results from demineralized bone creep tests suggest that collagen is responsible for the creep behaviour of bone. *Journal of Biomechanical Engineering,* 121: 253-258.

Boyce, T.M., Fyhrie, D.P., Glotkowski, M.C., Radin, E.L. and Schaffler, M.B. (1998) Damage type and strain mode associations in human compact bone bending fatigue. *Journal of Orthopaedic Research,* **16:** 322-329.

Boyde, A. (1980) Electron microscopy of the mineralising front. *Metabolic bone disease and related research,* **2 (Suppl.):** 69-78.

Brennan, O. (2001) *Secondary Osteons and Microcracks in Compact Bone.* MSc Thesis, University of Dublin.

Brown, C. U., Norman, T. L., Wang, Z. (1996) Microdamage Influences Fracture Toughness of Human Cortical Bone. *42nd Annual Meeting, Orthopaedic Research Society,* **58**:10

Burr, D.B., Martin, R.B., Schaffler, M.B. and Radin, E.L. (1985) Bone remodelling in response to *in vivo* fatigue microdamage. *Journal of Biomechanics,* **18**: 189-200.

Burr, D.B., Schaffler, M.B. and Fredrickson, R.G. (1988) Composition of the cement line and its possible mechanical role as a local interface in human compact bone. *Journal of Biomechanics,* **21:** 939-945.

Burr, D.B. and Stafford, T. (1990) Validity of the bulk-staining technique to separate artifactual from *in vivo* bone microdamage. *Clinical Orthopaedics and Related Research,* **260**: 305-308.

Burr, D.B. and Martin, R.B. (1993) Calculating the probability that microcracks initiate resorption spaces. *Journal of Biomechanics,* **26**: 613-616.

Burr, D.B. and Hooser, M. (1995) Alterations to the en bloc basic fuchsin staining protocol for the demonstration of microdamage produced *in vivo*. *Bone,* **17**: 431-433.

Burr, D.B., Milgrom, C., Fyhrie, D., Forwood, M., Nyska, M., Finestone, A., Hoshaw, S., Saiag, E. and Simkin, A. (1996) *In vivo* measurement of human tibial strains during vigorous activity. *Bone,* **18:** 405-410.

Burr, D.B., Turner, C.H., Naick, P., Forwood, M.R., Ambrosius, W., Hassan, M.S. and Pidaparti, R. (1998) Does microdamage accumulation affect the mechanical properties of bone? *Journal of Biomechanics,* **31:** 337-345.

Burr, D.B. (2000) *Damage detection and behaviour in bone.* 12th Conference of the European Society of Biomechanics, Dublin, Ireland: 38-39. ISBN 0953880907

Cannon, W. R. and Langdon, T. G. (1983) Review of creep of ceramics. Part 1: mechanical characteristics. *Journal of Materials Science,* 18: 1-50.

Caler, W.E. and Carter D.R. (1986) Time dependent and cycle dependent bone fracture. In: Christel, P., Meunier, A. and Lee, A. J. C (Eds.) *Biological and Biomechanical Performance of Biomaterials, Elsevier, Amsterdam.* ISBN 0444426663

Caler, W.E. and Carter D.R. (1989) Bone creep–fatigue damage accumulation. *Journal of Biomechanics* 22: 625-635.

Carter, D.R. and Hayes, W.C. (1976) The fatigue life of compact bone. I: Effects of stress amplitude, temperature and density. *Journal of Biomechanics,* ***9:*** 27-34.

Carter, D.R. and Hayes, W.C. (1977a) The compressive behaviour of bone as a two-phase porous structure. *Journal of Bone and Joint Surgery,* **59(A):** 954-962.

Carter, D.R. and Hayes, W.C. (1977b) Compact bone fatigue damage: a microscopic examination. *Clinical Orthopaedics and Related Research,* **127:** 265-274.

Carter, D.R. and Spengler, D.M. (1978) Mechanical properties and composition of cortical bone. *Clinical Orthopaedics and Related Research,* **135:** 192-217.

Carter, D.R., Harris, W.H., Vasu, R. and Caler, W.E. (1981a) The mechanical and biological response of cortical bone to *in vivo* strain histories. In: Cowin, S.C. (Ed.) *Mechanical Properties of Bone.* New York, NY: American Society of Mechanical Engineers. ISBN 0686344774

Carter, D.R., Caler, W.E., Spengler, D.M. and Frankel, V.H. (1981b) Uniaxial fatigue of human cortical bone: the influence of tissue physical characteristics. *Journal of Biomechanics,* **14:** 461-470.

Carter, D.R. and Caler, W.E. (1983) Cycle-dependant and time-dependant bone fracture with repeated loading. *Journal of Biomechanical Engineering,* **105:** 166-170.

Carter, D.R. and Caler, W.E. (1985) A cumulative damage model for bone fracture. *Journal of Orthopaedic Research,* **3:** 84-90.

Chamay, A. (1970) Mechanical and morphological aspects of experimental overload and fatigue in bone. *Journal of Biomechanics,* **3:** 263-270.

Chamay, A. and Tschantz, P. (1972) Mechanical influences in bone remodelling: Experimental research on Wolff's Law. *Journal of Biomechanics,* **5:** 173-180.

Cohen, R.E., Hooley, C.J. and McCrum, N.G. (1976) Viscoelastic creep of collagenous tissue. *Journal of Biomechanics,* **9:** 175-184.

Corondan, G. and Haworth, W.L. (1986) A fractographic study of human long bone. *Journal of Biomechanics,* **19:** 207-218.

Cotton, J.R., Zioupos, P., Winarood, K. and Taylor, M. (2003) Analysis of creep strain during tensile fatigue of cortical bone. *Journal of Biomechanics,* **36:** 943-949.

Cowin, S.C. (1989) *Bone Mechanics.* Boca Raton: CRC Press

Cowin, S.C., Weinbaum, S. and Zeng, Y. (1995) A case for bone canaliculi as the anatomical site of strain generated potentials. *Journal of Biomechanics,* **28**: 1281-1297.

Currey, J.D. (1965) Anelasticity in bone and echinoderm skeletons. *Journal of Experimental Biology,* **43:** 279-292.

Currey, J.D. and Brear, K. (1974). Tensile yield in bone. *Calcified Tissue research,* **15:** 173-179.

Currey, J.D. and Butler, G. (1975) The mechanical properties of bone tissue in children. *Journal of Bone and Joint Surgery,* **57(A):** 810-814.

Currey J.D. (1984) *The Mechanical Adaptations of Bones.* Princeton, NJ: Princeton University Press. ISBN 0691083428

Currey, J.D. (2002) *Bones: Structure and mechanics.* Princeton, NJ: Princeton University Press.

Danova, N. A, Colopy, S. A., Radtke, C. L., Kalsceur, V. L., Marker, M. D., Vanderby, R. Jr., McCabe, R. P., Escarcega, A. J., Muir, P. (2003) Degradation of bone structural properties by accumulation and coalescence of microcracks. *Bone,* **33**: 197 – 205.

Deligianni, D. D., Maris, A. and Missirlis, Y.F. (1994) Stress relaxation behaviour of trabecular bone specimens. *Journal of Biomechanics,* **27**: 1469-1476.

Dieter, G.E. (1986) Creep and stress rupture. In: Rao, S. (Ed.) *Mechanical Metallurgy.* New York, NY: McGraw-Hill. ISBN 0070168938

Donahue, S.W., Sharkey, N.A., Modanlou, K.A., Sequeira, L.N. and Martin, R.B. (2000) Bone strain and microcracks at stress fracture sites in human metatarsals. *Bone,* **27(6):** 827-833.

Evans, F.G. and Bang, S. (1967) Differences and relationships between the physical properties and the microscopic structure of human femoral, tibial and fibular cortical bone. *American Journal of Anatomy,* **120:** 78-88.

Evans, F.G. (1958) Relations between the microscopic structure and tensile strength of human bone. *Acta Anatomica*, **35:** 285-301.

Evans, F.G. and Riolo, M.L. (1970) Relations between the fatigue life and histology of adult femoral bone. *Journal of Bone and Joint Surgery,* **52(A):** 1579-1586.

Evans, F.G. (1973) *Mechanical properties of bone.* Springfield, IL: Charles C. Thomas.

Evans, F.G. (1976) Mechanical properties and histology of cortical bone from younger and older men. *The Anatomical Record,* **185(1):** 1-11.

Fazzalari, N.L., Forwood, M.R., Manthey, B.A., Smith, K. and Kolesik, P. (1998) Three-dimensional confocal images of microdamage in cancellous bone. *Bone,* **23:** 373-378.

Fleck, C. and Eifler, D. (2003) Deformation behaviour and damage accumulation of cortical bone specimens from equine tibia under cycle loading. *Journal of Biomechanics,* **36:** 179-189.

Fondrk, M., Bahniuk, E., Davy, D.T. and Michaels, C. (1988) Some viscoplastic characteristics of bovine bone and human cortical bone. *Journal of Biomechanics,* **21:** 623-630.

Forwood, M.R. and Parker, A.W. (1989) Microdamage in response to repetitive torsional loading in the rat tibia. *Calcified Tissue International,* **45:** 47-53.

Frank, J.D., Ryan, M., Kalschew, V.L., Ruax-Mason, C.P., Hozak, R.R. and Muir, P. (2002) Aging and accumulation of microdamage in canine bone. *Bone,* **30(1):** 201-206.

Fraser, W.D., Stamp, T.C., Creek, R.A., Sawyer, J.P. and Picot, C. (1997) A double-blind, multicentre, placebo-controlled study of tiludronate in Paget's disease of bone. *Postgraduate Medical Journal,* **73:** 496-502.

Fritton, S.P., McLeod, K.J. and Rubin, C.T. (2000) Quantifying the strain history of bone: spatial uniformity and self-similarity of low magnitude strains. *Journal of Biomechanics,* **33(3):** 317-325.

Frost, H.M. (1958) Preparation of thin undecalcified bone sections by rapid manual method. *Stain Technology,* **33:** 273-277.

Frost, H.M. (1960) Presence of microscopic cracks *in vivo* in bone. *Henry Ford Hospital Bulletin,* **8**: 25-35.

Frost, H.M. (1966) *Bone Dynamics in Osteoporosis and Osteomalacia.* Springfield, IL: Charles C. Thomas.

Frost, H.M. (1973) *Bone remodelling and its relationship to metabolic bone diseases.* Springfield, IL: Charles C. Thomas.

Frost, H.M. (1985) The skeletal intermediary organisation: a synthesis. In: Peck, W.A. (Ed.) Bone and Mineral Research 3, pp49-107. Amsterdam: Elsevierer. ISBN 044490347X

Fyhrie, D.P. and Schaffler, M.B. (1994) Failure mechanisms in human vertebral cancellous bone. *Bone,* **15:** 607-614.

Garofalo, F. (1965) *Fundamentals of creep and creep-rupture in metals.* New York, NY: MacMillan.

Gibson, L.J. and Ashby, M.F. (1997) *Cellular Solids - structures and properties, 2nd Edition.* Cambridge: Cambridge University Press.

Glimcher, M.J. and Katz, E.L. (1965) The organisation of collagen in bone: the role of noncovalent bonds in the relative insolubility of bone collagen. *Journal of Ultrastructure Research,* **12:** 705-729.

Guo, X.C., Liang, L.C. and Goldstein, S.A. (1998) Micromechanics of osteonal cortical bone fracture. *Journal of Biomechanical Engineering,* **120(1):** 112-117.

Gustavson, K.H. (1956) *The Chemistry and Reactivity of Collagen,* p.211. New York, NY: Academic Press.

Hayes, W.C. and Bouxsein, M.L. (1997) Biomechanics of cortical and trabecular bone: Implications for assessment of fracture risk, pp.69-107. In: Maow, V.C. and Hayes, W.C. (Eds.) *Basic Orthopaedic Biomechanics.* Philadelphia, PA: Lippincott-Raven Publishers. ISBN 0397516843

He, M.Y. and Hutchinson, J.W. (1989) Crack deflection at an interface between dissimilar elastic materials. *International Journal of Solids and Structures,* **25(9): 1053-1067.**

Holden, J. L., Clement, J. G. and Phakey, P. P. (1995) Age and temperature related changes to the ultrastructure and composition of human bone mineral. *Journal of Bone and Mineral Research,* **10:** 1400-1409.

Johnson, L.C. (1966) The kinetics of skeletal remodelling. *Birth Defects Original Article Series,* **2:** 66-142.

Junqueira, L.C., Carneiro, J. and Kelley, R.O. (1992) *Basic Histology.* Morwalk, CT: Appleton and Lange.

Kachanov, L. M. (1958) On the time to failure under creep conditions. *Izv Akad Nauk SSSR,* 8: 26-31.

Kachanov, L. M. (1961) Problems of continuum mechanics (contributions in honour of seventieth birthday of N. I Muskhelishvili, 16 Feb 1961). pp.202-218 Ed. by J.R.M. Radok, Philadelphia, Society of Industrial and Applied Mathematics, Published simultaneously by the Academy of Sciences of the U.S.S.R.

Kaplan, F.S., Hayes, W.C., Keaveny, T.M., Boskey, A., Einhorn, T.A. and Iannotti, J.P. (1994) Form and function of bones. In: Simon, S.R. (Ed.) *Orthopaedic basic science.* Rosemount, IL: American Academy of Orthopaedic Surgeons. ISBN 0892030593

Keaveny, T.M., Wachtel, E.F., Guo, X.E. and Hayes, W.C. (1994a) Mechanical behaviour of damaged trabecular bone. *Journal of Biomechanics,* **27**: 1309-1318.

Keaveny, T.M., Guo, X.E., Wachtel, E.F., McMahon, T.A. and Hayes, W.C. (1994b) Trabecular bone exhibits fully linear elastic behaviour and yields at low strains. *Journal of Biomechanics,* **27**: 1127-1136.

Kendall, K. (1975) Control of cracks by interfaces in composites. *Proceedings of the Royal Society of London*, **341:** 409-428.

Kimmel, D.B., Heaney, R.P., Avioli, L.V., Chesnut, C.H., Recker, R.R., Lappe, J.M. and Brandenburger, G.H. (1991) Patellar ultrasound velocities in osteoporotic and normal subjects of equal forearm or spinal bone density. *Journal of Bone and Mineral Research,* **6:** S169.

Knets, I. V. and Vilks, Y.K. (1975) Creep of compact human bone tissue under tension. Translated from *Mekhanika Polimerov,* **4:** 634-638.

Lakes, R. and Saha, S. (1979) Cement line motion in bone. *Science,* **204:** 501-503.

Landis, W.J. (1995) The strength of a calcified tissue depends in part on the molecular structure and organization of its constituent mineral crystals in their organic matrix. *Bone,* **16:** 533-544.

Lane, J.M., Riley, E.H. and Wirganowicz, P.Z. (1996) Osteoporosis: diagnosis and treatment. *Journal of Bone and Joint Surgery,* **78(A):** 618-632.

Lanyon, L.E., Goodship, A.E., Pye, C.J. and MacFie, J.H. (1982) Mechanically adaptive bone remodelling. *Journal of Biomechanics,* **15:** 141-154.

Lanyon, L.E. (1991) Biomechanical properties of bone and response of bone to mechanical stimuli: functional strain as a controlling influence on bone modelling and remodelling behaviour. In: Hall, B.K. (Ed.) *Bone, Volume 3.* Boca Raton: CRC Press. ISBN 0849388236

Lee, T.C. (1997) *Detection and accumulation of microdamage in bone.* M.D. Thesis, University of Dublin.

Lee, T.C., Myers, E.R. and Hayes, W.C. (1998) Fluorescence-aided detection of microdamage in compact bone. *Journal of Anatomy,* **193**: 179-184.

Lee, T.C., Noelke, L., McMahon, G.T., Mulville, J.P. and Taylor, D. (1999) Functional adaptation in bone. In: Pedersen, P. and Bendsoe, M.P. (Eds.) *Synthesis in BioSolid Mechanics.* Dortrecht: Kluwer Academic Publishers. ISBN 0792356152

Lee, T.C., Arthur, T.L., Gibson, L.J. and Hayes, W.C. (2000a) Sequential labelling of microdamage in bone using chelating agents. *Journal of Orthopaedic Research,* **18:** 322-325.

Lee, T.C., O'Brien, F.J. and Taylor, D. (2000b) The nature of fatigue damage in bone. *International Journal of Fatigue,* **22:** 847-853.

Liberman, U.A., Weiss, S.R., Broll, J., Minne, H.W., Quan, H., Bell, N.H., Rodriguez-Portales, J., Downs, R.W.Jr., Dequeker, J., Favus, M., Seeman, E., Recker, R.R., Capizzi, T., Santora, A.C., Lombardi, A., Shah, R.V., Hirsch, L.J. and Karpf, D.B. (1995) Effect of oral alendronate on bone mineral density and the incidence of fractures in postmenopausal osteoporosis. *New England Journal of Medicine,* **333:** 1437-1443.

Liu, D., Wagner, H.D. and Weiner, S. (2000) Bending and fracture of compact circumferential and osteonal lamellar bone of the baboon tibia. *Journal of Materials Science – Materials in Medicine,* **11:** 49-60.

Martin, R.B. and Burr, D.B. (1982) A hypothetical mechanism for the stimulation of osteonal remodelling by fatigue damage. *Journal of Biomechanics,* **15**: 137-139.

Martin, R.B. and Burr, D.B. (1989) *Structure, function and adaptation of compact bone*. New York, NY: Raven Press. ISBN 0881675008

Martin, R.B. and Boardman, D.L. (1993) The effects of collagen fiber orientation, porosity, density, and mineralization on bovine cortical bone bending properties. *Journal of Biomechanics,* **26:** 1047-1054.

Martin, R.B., Burr, D.B. and Sharkey, N.A. (1998) *Skeletal Tissue Mechanics*. New York, NY: Springer-Verlag. ISBN 0387984747

Martin, R.B. (2000) Toward a unifying theory of bone remodelling. *Bone,* **26:** 1-6.

Martin, R.B. (2002) Is all cortical bone remodelling initiated by microdamage? *Bone,* **30(1):** 8-13.

Martini, F.H. (1998) *Fundamentals of Anatomy and Physiology.* New Jersey: Prentice Hall.

Mashiba, T., Hirano, T., Turner, C.H., Forwood, M.R., Johnston, C.C. and Burr, D.B. (2000) Suppressed bone turnover by bisphosphonates increases microdamage accumulation and reduces some biomechanical properties in dog ribs. *Journal of Bone and Mineral Research,* **15:** 613-620.

Mellors, R.C. (1999) *Bone IV: Metabolic bone diseases*. Weill Medical College of Cornell University.
http://edcenter.med.cornell.edu/cumc_pathnotes/skeletal/Bone_03.html
Accessed: 11/09/2004

Melton, L.J., Kan, S.H., Fyre, M.A., Wahner, H.W., O'Fallon, W.M. and Riggs, B.L. (1989) Epidemology of vertebral fractures in women. *American Journal of Epidemology*, **129:** 1000-1011.

Melton, L.J.III (1996) Epidemiology of hip fractures: Implications of the exponential increase with age. *Bone,* **18 (Suppl.):** 121S-125S.

Moore, T.L.A. and Gibson, L.J. (2003a) Fatigue microdamage in bovine trabecular bone. *Journal of Biomechanical Engineering,* **125:** 769-776.

Moore, T.L.A. and Gibson, L.J. (2003b) Fatigue of bovine trabecular bone. *Journal of Biomechanical Engineering,* **125:** 761-768.

Moore, T.L.A. and Gibson, L.J. (2003c) A fatigue endurance limit for bovine trabecular bone tested in compression (in press).

Moore, T.L.A., O'Brien F.J. and Gibson, L.J. (2004) Creep does not contribute to fatigue in bovine trabecular bone. *Journal of Biomechanical Engineering,* **126:** 321-329.

Morcio, R. and Ciferru, A. (1969) The role of calcium and of *in vitro* aging on the creep behaviour of collagen tendons. *Biophysik,* **5:** 327-330.

Mori, S. and Burr, D.B. (1993) Increased intracortical remodelling following fatigue damage. *Bone,* **14**: 103-109.

Mori, S., Harruff, R., Ambrosius, W. and Burr, D.B. (1997) Trabecular bone volume and microdamage accumulation in the femoral heads of women with and without femoral neck fractures. *Bone,* **21(6):** 521-526.

Morris, J.M. and Blickenstaff, L.D. (1967) *Fatigue Fractures.* Springfield, IL: Charles C. Thomas.

Mow, V.C., Kuei, S.C., Lai, W.M. and Armstrong, C.G. (1980) Biphasic creep and stress relaxation of articular cartilage in compression: theory and experiments. *Transactions of the ASME: Journal of Biomechanical Engineering,* **102:** 73-84.

Moyle, D.D., Welborn, J.W. III and Cooke, F.W. (1978) Work to fracture of canine femoral bone. *Journal of Biomechanics,* **11:** 435-440.

Muir, P., Johnson, K.A. and Ruax-Mason, C.P. (1999) *In vivo* matrix microdamage in a naturally occurring canine fatigue fracture. *Bone,* **25:** 571-576.

Mulhern, D.M. and Ubelaker, D.H. (2001) Differences in osteon bonding between human and nonhuman bone. *Journal of Forensic Science,* **46(2):** 220-222.

National Osteoporosis Foundation (2004) 1232 22nd Street, N.W. Washington, D.C. 20037-1292

http://www.nof.org/osteoporosis/diseasefacts.htm
Accessed: 11/09/2004

Nesbitt, S.A. and Horton, M.A. (1997) Trafficking of matrix collagens through bone-resorbing osteoclasts. *Science,* **276:** 266-269.

Newburgh, L.H. (Ed.) (1949) *Physiology of Heat Regulation and the Science of Clothing.* Philadelphia, PA: Saunders.

Nunamaker, D.M., Butterwerk, D.M. and Provost, M.T. (1990) Fatigue fractures in thoroughbred racehorses: relationships with age. *Journal of Orthopaedic Research,* **8:** 604-611.

O'Brien, F.J. (2000) *Microcracks and the Fatigue Behaviour of Compact Bone.* PhD Thesis, Trinity College, University of Dublin.

O'Brien, F.J., Taylor, D, Dickson, G.R. and Lee, T.C. (2000) Visualisation of three-dimensional microcracks in compact bone. *Journal of Anatomy,* **197:** 413-420.

O'Brien, F.J., Taylor, D. and Lee, T.C. (2002) An improved labelling technique for monitoring microcrack growth in compact bone. *Journal of Biomechanics,* **35:** 523-526.

O'Brien, F.J., Taylor, D. and Lee, T.C. (2003) Microcrack accumulation at different intervals during fatigue testing of compact bone. *Journal of Biomechanics,* **36:** 973-980.

O'Brien, F.J., Taylor, D. and Lee, T.C. (2004) The effects of bone microstructure on the initiation and growth of microcracks (in press).

O'Reilly, P. (2002) *Torsional Fatigue of Cortical Bone.* MSc Thesis, Trinity College, University of Dublin.

Pankhurst, K.G.A. (1947) *Nature,* **159:** 538.

Parfitt, A.M. (1993) Bone age, mineral density and fatigue damage. *Calcified Tissue International,* **53 (Suppl.):** S82-S86.

Park, H.C. and Lakes, R.S. (1986) Cosserat micromechanics of human bone: strain redistribution by a hydration sensitive constituent. *Journal of Biomechanics,* **19**: 385-397.

Parkesh, R. (2003) *Selective fluorescent chemosensors and iodinated contrast agents: biological evaluation for cellular zinc detection, microdamage detection and imaging.* PhD Thesis, University of Dublin.

Pattin, C.A., Caler, W.E. and Carter, D.R. (1996) Cyclic mechanical property degradation during fatigue loading of cortical bone. *Journal of Biomechanics,* **29(1):** 69-79.

Pidaparti, R. M., Wang, Q.Y. (2001) Modeling fatigue damage evolution in bone. *Bio-Medical materials and engineering.* 11:69-78.

Prendergast, P.J. and Taylor, D. (1994) Prediction of bone adaptation using damage accumulation. *Journal of Biomechanics,* **27**: 1067-1076.

Prendergast, P.J. and Huiskes, R. (1996) Microdamage and osteocyte-lacuna strain in bone: a microstructural finite element analysis. *Journal of Biomechanical Engineering,* **118:** 240-246.

Rahn, B.A. (1977) Polychrome fluorescence labelling of bone formation, instrumental aspects and experimental use. *Zeiss Information,* **22(85)**: 36-39.

Reifsnider, K.L. and Jaminson, R.D. (1982) Fracture of fatigue-loaded composite laminates. *International Journal of Fatigue,* **4(4):** 187-198.

Reifsnider, K.L., Henneke, E.G., Stinchcomb, W.W. and Duke, J.C. (1983) Damage, Mechanics and NDE of Composite Laminates. In: Hashin, Z. and Herakovich, C.T. (Eds.) *Mechanics of Composite Materials: Recent Advances,* pp.399-420. New York, NY: Pergamon Press. ISBN 0080293840

Reilly, G.C. and Currey, J.D. (1999) The development of microcracking and failure in bone depends on the loading mode to which it is adapted. *Journal of Experimental Biology,* **202:** 543-552.

Reilly, G. (2000) Observations of microdamage around osteocyte lacunae in bone. *Journal of Biomechanics,* **33:** 1131-1134.

Riggs, B.L. and Melton, L.J.III (1995) The worldwide problem of osteoporosis: Insights afforded by epidemiology. *Bone,* **17 (Suppl.)**: 505S-511S.

Rimnac, C.M., Petko, A.A. and Wright, T.M. (1991) Creep of compact bone: effects of temperature and stress on bovine lamellar microstructure. *Transactions of the Orthopaedic Research Society,* **18:** 152.

Rimnac, C.M., Petko, A.A., Santner, T.J. and Wright, T.M. (1993) The effect of temperature, stress, and microstructure on the creep of compact bone. *Journal of Biomechanics,* **26:** 219-22.

Robinson, S. (1949). In: Newburgh, L.H. (Ed.) (1949) *Physiology of Heat Regulation and the Science of Clothing,* p.338. Philadelphia, PA: Saunders. ISBN 002849640X

Ross, P.D., Davis, J.W., Epstein, R.S. and Wasnich R.D. (1993) Pre-existing fractures and bone mass predict vertebral fracture incidence in women. *Annals of Internal Medicine,* **114:** 919-923.

Rubin, C.T. and Lanyon, L.E. (1982) Limb mechanics as a function of speed and gait: a study of functional strains in the radius and tibia of horse and dog. *Journal of Experimental Biology,* **101:** 187-211.

Salo, J., Lehenkan, P., Mulan, M., Metsikkö, K. and Väänänen, H.K. (1997) Removal of osteoclast bone resorption products by transcytosis. *Science,* **276:** 270-273.

Schaffler, M.B., Radin, E.L. and Burr, D.B. (1989) Mechanical and morphological effects of strain rate on fatigue in compact bone. *Bone,* **10**: 207-214.

Schaffler, M.B., Radin, E.L. and Burr, D.B. (1990) Long-term fatigue behaviour of compact bone at low strain magnitude and rate. *Bone,* **11**: 321-326.

Schaffler, M.B., Choi, K. and Milgrom, C. (1994a) Microcracks and aging in human femoral compact bone. *Proceedings of the Orthopaedic Research Society,* **19:** 190.

Schaffler, M.B., Pitchford, W., Choi, K. and Riddle, J.M. (1994b) Examination of compact bone microdamage using back-scattered electron microscopy. *Bone,* **15**: 483-488.

Schaffler, M.B., Choi, K. and Milgrom, C. (1995a) Aging and matrix microdamage accumulation in human compact bone. *Bone,* **17**: 521-525.

Schaffler, M.B., Boyce, T. M., Lundin-Cannon, K. D., Milgrom, C. and Fyrie, D. P., (1995b) Age related architectural changes and microdamage accumulation in the human femoral neck cortex. In: *41st Annual Meeting, Orthopedic Research Society* **549**

Schaffler, M.B., Boyce, T.M. and Fyhrie, D.P. (1996) Tissue and matrix failure modes in human compact bone during tensile fatigue. *Transactions of the Orthopaedic Research Society,* **21:** 57.

Schiller, A.L. (1994) Bone and joints. In: Rubin, E. and Farber, J.L. (Eds.) *Pathology, 2nd edn.* Philadelphia: J.B. Lippincott. ISBN 0397510470

Schmidt, M.B., Mow, V.C., Chun, L.E. and Eyre, D.R. (1990) Effects of proteoglycon extraction on the tensile behaviour of articular cartilage. *Journal of Orthopaedic Research,* **8:** 353-363.

Sedlin, E. D. (1965) A rheologic model for cortical bone. *Acta Orthopaedica Scandinavia* (Suppl.), **83:** 1-77.

Shultz, R.W. and Reifsnider, K.L. (1984) Fatigue of composite laminates under mixed tension-compression loading. *Proceedings of the 2nd International Conference on Fatigue and Fatigue Thresholds, (Fatigue 84)* University of Birmingham (September 1-7).

Simon, B.R., Coats, R.S. and Woo, S.L.Y. (1984) Relaxation and creep quasilinear viscoelastic models for normal articular cartilage. *Transactions of the ASME: Journal of Biomechanical Engineering,* **106:** 159-164.

Siris, E.S. (1998) Paget's disease of bone. *Journal of Bone and Mineral Research,* **13(7):** 1061-1065.

Smith, J. W. and Walmsley, R. (1959) Factors affecting the elasticity of bone. *Journal of Anatomy,* 503-523.

Stover, S.M., Martin, R.B., Pool, R.R., Taylor, K.T. and Harrington, T.M. (1993) *In vivo* labelling of microdamage in cortical bone tissue. *Proceedings of the Orthopaedic Research Society,* **18:** 541.

Taylor, D. and Prendergast, P.J. (1995) Damage accumulation in compact bone - a fracture mechanics approach to estimate damage and repair rates. In: *Advances in Bioengineering* BED- vol. 13, pp. 337-338. New York: American Society of Mechanical Engineers. ISBN 0791817229

Taylor, D. (1997) Bone maintenance and remodelling: a control system based on fatigue damage. *Journal of Orthopaedic Research,* **15:** 601-606.

Taylor, D. and Prendergast, P.J. (1997) A model for fatigue crack propagation and remodelling in compact bone. *Journal of Engineering in Medicine (Proceedings, Institution of Mechanical Engineers Part H),* **211:** 369-375.

Taylor, D. (1998a) Fatigue of bone and bones: an analysis based on stressed volume. *Journal of Orthopaedic Research,* **16:** 163-169.

Taylor, D. (1998b) Microcrack growth parameters for compact bone deduced from stiffness variations. *Journal of Biomechanics,* **31**: 587-592.

Taylor, D. (1999) Fatigue damage in bone: links to adaption. In: Pedersen, P. and Bendsoe, M.P. (Eds.) *Synthesis in BioSolid Mechanics.* Dortrecht: Kluwer Academic Publishers.

Taylor, D., O'Brien, F.J., Prina Mello, A., Ryan, C., O'Reilly, P. and Lee, T.C. (1999) Compression data on bovine bone confirms that 'stressed volume' principle explains the variability of fatigue strength results. *Journal of Biomechanics* **32:** 1199-1203.

Taylor, M., Verdanschott, N., Huiskes, R. and Zioupos, P. (1999) A combined finite element method and continuum damage mechanics approach to simulate the *in vitro* fatigue behaviour of human cortical bone. *Journal of Materials Science: Materials in Medicine,* **10:** 841-846.

Taylor D; O'Brien F. and Lee, TC (2002) A theoretical model for the simulation of microdamage accumulation and repair in compact bone. *Meccanica* **3179** : 1-10.

Tschantz P. and Rutishauser E. (1967) La surcharge mecanique de l'os vivant. Les deformations plastiques initiales et l'hypertrophie de l'adaptation. *Annales d'Anatomie Pathologique,* **12:** 223-248.

Van Rietbergen, B., Weinans, H., Huiskes, R. and Odgaard, A. (1995) A new method to determine trabecular bone elastic properties and loading using micromechanical finite-element models. *Journal of Biomechanics,* **28:** 69-81.

Verborgt, O., Gibson, G.J. and Schaffler, M.B. (2000) Loss of osteocyte integrity in association with microdamage and bone remodelling after fatigue *in vivo. Journal of Bone and Mineral Research,* **15:** 60-67.

Vogel, H.G. (1977) Strain of rat skin at constant load (creep experiments), influence of age and desmotropic agents. *Gerontology,* **23:** 77-86.

Wallbridge N., Dowson D. (1982) The walking activity of patients with artificial hip joints. *Engineering in medicine,* **11:** 95 – 96.

Wang, S. S., Chim, E. S. M. (1983) Fatigue damage and degradation in random short-fibre SMC composite. *Journal of Composite Materials,* **17**: 114-134.

Wang, S. S., Suemasu, H. and Chim E. S. M. (1987) Analysis of fatiguedamage evolution and associated anisotropic elastic property degradation in random short – fibre composite. *Journal of Composite Materials,***21**: 1084-1105.

Weibull, W. (1951) A statistical distribution function of wide applicability. *Journal of Applied Mechanics,* **18:** 293-305.

Weir, C.E. (1949) Rate of shrinkage of tendon collagen – heat, entropy and free energy of activation of the shrinkage of untreated tendons, effect of acid salt, pickle and tannage on the activation of tendon collagen. *Journal of the American Leather Chemists Association,* **44:** 108.

Wenzel, T. E., Schaffler, M. B. and Fyhrie, D. P. (1994) In vivo trabecular trabecular microcracks in human vertebral bone. *41st Annual Meeting, Orthopaedic Research Society,* 57:10.

World Health Organisation (WHO) Study Group on Assessment of Fracture Risk and Its Application to Screening for Post-menopausal Osteoporosis (1994) *Assessment of fracture risk and application to screening for postmenopausal osteoporosis: report of a WHO study group (Series 843).* Geneva, Switrzerland: WHO Technical Report Series.

Wright, T.M. (1976) *Tensile properties and fracture mechanics of bone.* PhD Thesis, Stanford University.

Yeni, Y.N., Brown, C.U., Wang, Z. and Norman, T.L. (1997) The influence of bone morphology on fracture toughness of the human femur and tibia. *Bone,* **21(5):** 453-459.

Yoshino, H. (2000) *Temperature dependent behaviour in fracture toughness of bovine compact bone.* MSc Thesis, The Graduate School of Science and Technology, Niigata University, Japan.

Zioupos, P. and Currey, J.D. (1994) The extent of microcracking and the morphology of microcracks in damaged bone. *Journal of Materials Science,* **29**: 978-986.

Zioupos, P., Currey, J.D. and Sedman, A.J. (1994) An examination of the micromechanics of failure in bone and antler by acoustic emission tests and laser scanning confocal microscopy. *Medical Engineering and Physics,* **16**: 203-212.

Zioupos, P., Wang, X.T. and Currey, J.D. (1996) Experimental and theoretical quantification of the development of damage in fatigue tests of bone and antler. *Journal of Biomechanics,* **29**: 989-1002.

Zioupos, P. and Currey, J.D. (1998) Changes in the stiffness, strength and toughness of human cortical bone with age. *Bone,* **22(1):** 57-66.

8 Appendix

1 Room Temperature Fatigue

Appendix 1.1 Microcrack Accumulation During Testing - 50 MPa				
Specimen	0 - 100,000 Cycles	0 - 200,000 Cycles	0 - 300,000 Cycles	
1	9.000	25.000	28.000	Number of Cracks
	0.140	0.389	0.435	Numerical Crack Density (No./mm^2)
	29.408	46.858	53.391	Surface Crack Density (microns crk. Lgt/mm^2)
2	5.000	13.000	16.000	Number of Cracks
	0.077	0.200	0.246	Numerical Crack Density (No./mm^2)
	8.372	20.321	25.280	Surface Crack Density (microns crk. Lgt/mm^2)
3	6.000	16.000	18.000	Number of Cracks
	0.093	0.247	0.278	Numerical Crack Density (No./mm^2)
	4.719	15.790	17.516	Surface Crack Density (microns crk. Lgt/mm^2)
4	19.000	30.000	38.000	Number of Cracks
	0.284	0.448	0.568	Numerical Crack Density (No./mm^2)
	11.538	31.358	47.286	Surface Crack Density (microns crk. Lgt/mm^2)
5	0.000	0.000	1.000	Number of Cracks
	0.000	0.000	0.016	Numerical Crack Density (No./mm^2)
	0.000	0.000	1.600	Surface Crack Density (microns crk. Lgt/mm^2)
6	4.000	8.000	8.000	Number of Cracks
	0.060	0.120	0.120	Numerical Crack Density (No./mm^2)
	3.383	8.103	8.103	Surface Crack Density (microns crk. Lgt/mm^2)
7	0.000	0.000	1.000	Number of Cracks
	0.000	0.000	0.015	Numerical Crack Density (No./mm^2)
	0.000	0.000	1.019	Surface Crack Density (microns crk. Lgt/mm^2)
8	0.000	2.000	3.000	Number of Cracks
	0.000	0.030	0.046	Numerical Crack Density (No./mm^2)
	0.000	0.764	1.556	Surface Crack Density (microns crk. Lgt/mm^2)
9	0.000	0.000	0.000	Number of Cracks
	0.000	0.000	0.000	Numerical Crack Density (No./mm^2)
	0.000	0.000	0.000	Surface Crack Density (microns crk. Lgt/mm^2)
10	0.000	5.000	7.000	Number of Cracks
	0.000	0.077	0.108	Numerical Crack Density (No./mm^2)
	0.000	6.443	9.714	Surface Crack Density (microns crk. Lgt/mm^2)

Appendix 1.2 Microcrack Accumulation During Testing - 60 MPa				
Specimen	0 - 100,000 Cycles	0 - 200,000 Cycles	0 - 300,000 Cycles	
1	4.000	20.000	38.000	Number of Cracks
	0.061	0.305	0.579	Numerical Crack Density (No./mm^2)
	4.628	29.198	43.260	Surface Crack Density (microns crk. Lgt/mm^2)
2	2.000	20.000	30.000	Number of Cracks
	0.030	0.304	0.456	Numerical Crack Density (No./mm^2)
	1.440	30.677	42.784	Surface Crack Density (microns crk. Lgt/mm^2)
3	0.000	30.000	32.000	Number of Cracks
	0.000	0.456	0.486	Numerical Crack Density (No./mm^2)
	0.000	28.914	32.189	Surface Crack Density (microns crk. Lgt/mm^2)
4	17.000	103.000	120.000	Number of Cracks
	0.250	1.514	1.764	Numerical Crack Density (No./mm^2)
	7.892	77.132	89.917	Surface Crack Density (microns crk. Lgt/mm^2)
5	21.000	104.000	116.000	Number of Cracks
	0.309	1.529	1.706	Numerical Crack Density (No./mm^2)
	15.502	107.151	116.466	Surface Crack Density (microns crk. Lgt/mm^2)
6	1.000	12.000	13.000	Number of Cracks
	0.015	0.179	0.193	Numerical Crack Density (No./mm^2)
	0.488	12.178	13.785	Surface Crack Density (microns crk. Lgt/mm^2)
7	0.000	28.000	33.000	Number of Cracks
	0.000	0.469	0.553	Numerical Crack Density (No./mm^2)
	0.000	39.726	44.465	Surface Crack Density (microns crk. Lgt/mm^2)
8	2.000	222.000	222.000	Number of Cracks
	0.031	3.415	3.415	Numerical Crack Density (No./mm^2)
	0.582	180.437	180.437	Surface Crack Density (microns crk. Lgt/mm^2)
9	1.000	21.000	29.000	Number of Cracks
	0.015	0.319	0.441	Numerical Crack Density (No./mm^2)
	0.492	25.979	37.639	Surface Crack Density (microns crk. Lgt/mm^2)

Appendix 1.3 Microcrack Accumulation During Testing - 70 MPa				
Specimen	0 - 100,000 Cycles	0 - 200,000 Cycles	0 - 300,000 Cycles	
1	3.000	255.000	279.000	Number of Cracks
	0.045	3.839	4.200	Numerical Crack Density (No./mm^2)
	2.313	216.581	236.672	Surface Crack Density (microns crk. Lgt/mm^2)
	0 - 100,000 Cycles	0 - 120,000 Cycles		
2 Outlier	0.000	520.000		Number of Cracks
	0.000	16.821		Numerical Crack Density (No./mm^2)
	0.000	1333.794		Surface Crack Density (microns crk. Lgt/mm^2)
	0 - 100,000 Cycles	0 - 200,000 Cycles	0 - 300,000 Cycles	
3	0.000	5.000	63.000	Number of Cracks
	0.000	0.071	0.898	Numerical Crack Density (No./mm^2)
	0.000	5.693	43.597	Surface Crack Density (microns crk. Lgt/mm^2)
	0 - 100,000 Cycles	0 - 200,000 Cycles	0 - 300,000 Cycles	
4	2.000	21.000	61.000	Number of Cracks
	0.030	0.310	0.901	Numerical Crack Density (No./mm^2)
	1.084	22.239	47.624	Surface Crack Density (microns crk. Lgt/mm^2)
	0 - 100,000 Cycles	0 - 200,000 Cycles	0 - 300,000 Cycles	
5	2.000	108.000	113.000	Number of Cracks
	0.029	1.568	1.640	Numerical Crack Density (No./mm^2)
	0.635	52.931	56.612	Surface Crack Density (microns crk. Lgt/mm^2)
	0 - 100,000 Cycles	0 - 200,000 Cycles	0 - 450,000 Cycles	
6	0.000	126.000	137.000	Number of Cracks
	0.000	3.681	4.002	Numerical Crack Density (No./mm^2)
	0.000	394.168	434.949	Surface Crack Density (microns crk. Lgt/mm^2)
	0 - 100,000 Cycles	0 - 200,000 Cycles	0 - 1,000,000 Cycles	
7	0.000	19.000	33.000	Number of Cracks
	0.000	0.884	1.535	Numerical Crack Density (No./mm^2)
	0.000	128.295	215.764	Surface Crack Density (microns crk. Lgt/mm^2)
			0 - 2,000,000 Cycles	
8			1099.000	Number of Cracks
			15.655	Numerical Crack Density (No./mm^2)
			1104.278	Surface Crack Density (microns crk. Lgt/mm^2)
			0 - 2,000,000 Cycles	
9			405.000	Number of Cracks
			6.050	Numerical Crack Density (No./mm^2)
			562.876	Surface Crack Density (microns crk. Lgt/mm^2)
			0 - 2,000,000 Cycles	
10			160.000	Number of Cracks
			2.318	Numerical Crack Density (No./mm^2)
			159.280	Surface Crack Density (microns crk. Lgt/mm^2)

Appendix 1.4 Microcrack Length Across all Specimens (Data for Fig. 2.20)

Stress Range	0 - 100,000 Cycles	0 - 200,000 Cycles	0 - 300,000 Cycles	
50 MPa	86.91	85.46	90.13	Mean Crack Length (microns)
	115.67	84.46	95.88	Standard Dev.
60 MPa	43.59	62.50	62.55	Mean Crack Length (microns)
	37.21	50.41	49.21	Standard Dev.
70 MPa	38.68	68.03	64.57	Mean Crack Length (microns)
	17.93	60.14	59.80	Standard Dev.

Appendix 1.5 Microcrack Location 50 MPa

Interstitial Touching Cement Line	Interstitial	Penetrating	Osteonal	Period of Formation
3	34	0	1	0-100,000 cycles
11	44	1	0	100,000 - 200,000 cycles
6	14	1	0	200,000 - 300,000 cycles
2	2	0	0	Propagating *

* Slide with 5th propagating microcrack could not be located for analysis of microcrack location

Appendix 1.6 Microcrack Location 60 MPa

Interstitial Touching Cement Line	Interstitial	Penetrating	Osteonal	Period of Formation
6	50	0	2	0-100,000 cycles
34	442	4	33	100,000 - 200,000 cycles
23	43	0	7	200,000 - 300,000 cycles
1	16	0	3	Propagating

Appendix 2.7 Microcracks and bone microstructure, the effect of osteon density

Specimen	Fatigue Stress Range (MPa)	Numerical Crack Density (# cracks / mm^2)	Surface Crack Density (mirons of crack length / mm^2)	Osteon Density (# Osteons / mm^2)	Mean Crack Length (microns)	Percentage of Microcracks by Location %			
						Intersistial Touching Cement	Interstitial	Penetrating	Osteonal
1	50	0.435	53.391	14.005	122.631				
2	50	0.246	25.280	14.541	102.676				
3	50	0.278	17.516	18.512	62.924				
4	50	0.568	47.286	16.746	83.280				
5	50	0.016	1.600	3.502	102.650				
6	50	0.120	8.103	9.113	67.254				
7	50	0.015	1.019	12.255	67.420				
8	50	0.046	1.556	14.158	34.020				
9	50	0.000	0.000	0.448	0.000				
10	50	0.108	9.714	4.016	90.206				
1	60	0.579	43.260	19.440	74.659	59	22	3	16
2	60	0.466	42.784	0.212	93.859	7	90	0	3
3	60	0.486	32.189	2.371	66.194	19	75	3	3
4	60	1.764	89.917	2.239	50.966	13	81	0	7
5	60	1.706	116.466	3.157	68.277	1	83	0	16
6	60	0.193	13.785	8.589	71.247	50	50	0	0
7	60	0.563	44.465	0.923	80.416	0	82	6	12
8	60	3.415	180.437	1.492	52.834	0	98	0	2
9	60	0.441	37.639	11.701	85.423	28	72	0	0

2 Room Temperature Creep

Appendix 2.1 Mechanical Test Data - Creep

Specimen Number	Creep Stress Level σ (MPa)	Normalized Stress (σ/E)	Time to Failure t_f (s)	Steady state creep Rate dε/dt (s^{-1})	Failure Yes / No
1	88	0.00431	45032	1.715E-07	Yes
2	120	0.00588	83	6.271E-05	Yes
3	120	0.00588	8657	8.123E-07	Yes
4	120	0.00588	2235	Error	Yes
5	120	0.00588	109377	Error	No
6	120	0.00588	76615	4.005E-08	No
7	120	0.00588	67296	9.973E-08	No
8	120	0.00588	74302	3.165E-08	No
9	130	0.00637	79039	2.912E-08	No
10	130	0.00637	77196	2.185E-08	No
11	130	0.00637	59355	7.986E-08	Yes
12	130	0.00637	5638	1.114E-06	Yes
13	130	0.00637	897	7.247E-06	Yes
14	140	0.00686	111	7.595E-05	Yes
15	140	0.00686	55	9.342E-05	Yes
16	140	0.00686	16442	4.055E-07	Yes
17	140	0.00686	27302	1.684E-07	Yes
18	140	0.00686	779	3.795E-06	Yes
19	140	0.00686	18	1.63E-04	Yes
20	150	0.00735	293	1.243E-05	Yes
21	150	0.00735	81	1.618E-04	Yes
22	150	0.00735	582	1.943E-05	Yes
23	150	0.00735	24	1.555E-04	Yes

Appendix 2.2 Histological Data – Creep 130 MPa

Section A

Section	Section Surface Area (mm^2)	Crack Number	Crack Length (μm)	Crack Location
1	82.02	1	100.9	Interstitial
		2	106.6	Osteonal
2	49.98	-		
3	28.86	1	201.3	Interstitial
		2	124.1	Interstitial
		3	553.1	Interstitial
4	24.33	-		
5	47.98	-		
6	79.76	-		

Section B

Section	Section Surface (mm^2)	Crack Number	Crack Length (μm)	Crack Location
1	33.27	1	335.4	Interstitial
		2	162.1	Interstitial
		3	170.1	Interstitial
		4	225.6	Interstitial
2	24.85	1	159.1	Interstitial
		2	145.7	Interstitial
		3	92	Osteonal
		4	259.5	Osteonal
		5	287.1	Interstitial
		6	220.6	Interstitial
		7	200.1	Osteonal
3	15.8	1	390.8	Interstitial
		2	181.7	Interstitial
		3	148.8	Interstitial
		4	134.8	Interstitial
4	10.3	1	270.4	Osteonal
		2	185.6	Interstitial
		3	210.4	Interstitial
		4	162.3	Osteonal
		5	318.7	Interstitial
		6	203.6	Interstitial
5	36.03	1	142.1	Osteonal
6	58.81	1	992.1	Interstitial
		2	552.2	Interstitial
		3	365.8	Osteonal
		4	174.3	Osteonal
		5	311.5	Interstitial
		6	921.3	Osteonal
		7	732.4	Interstitial
		8	335.5	Interstitial
		9	315	Interstitial
		10	508.6	Interstitial
		11	435.1	Interstitial
		12	641.5	Interstitial
		13	906	Osteonal

Section C

Section	Section Surface (mm^2)	Crack Number	Crack Length (µm)	Crack Location
1	28.45	-		
2	14.66	-		
3	17.34	1	34.6	Osteonal
		2	132.9	Interstitial
4	19.35	1	138.4	Interstitial
		2	178.3	Interstitial
		3	15.5	Interstitial
		4	175.7	Interstitial
		5	128.63	Interstitial
		6	88.8	Interstitial
		7	113.8	Interstitial
		8	76.1	Interstitial
		9	159.2	Interstitial
		10	241	Osteonal
		11	159.4	Interstitial
5	48.73	1	155.2	Interstitial
		2	383.3	Interstitial
		3	222.3	Interstitial
		4	142.8	Interstitial
6	54.65	1	452.4	Interstitial
		2	722.9	Interstitial

Section D

Section	Section Surface (mm^2)	Crack Number	Crack Length (µm)	Crack Location
1	49.08	1	218.2	Interstitial
2	56.51	1	203.6	Interstitial
3	56.14	-		
4	55.11	1	192.3	Interstitial
		2	98.9	Interstitial
5	56.17	-		
6	56.19	1	185.7	Interstitial

Section E

Section	Section Surface (mm^2)	Crack Number	Crack Length (µm)	Crack Location
1	49.28	1	88.4	Interstitial
2	48.56	1	321.1	Osteonal
		2	56.8	Interstitial
		3	11.96	Interstitial
3	50.28	1	84.8	Interstitial
		2	100.5	Interstitial
4	47.5	1	68.7	Interstitial
5	51.83	1	84.1	Interstitial
		2	255.7	Interstitial
6	57.02	-		

Appendix 2.3

Pearson's Correlation Histological Data - Creep 130 MPa (% Interstitial)

(2 – tailed)

Correlations

		Time to Failure	Incidence of Microdamage	Crack Length	Numerical Crack Density	Surface Crack Density	% Interstitial
Time to Failure	Pearson Correlation	1	-.423	-.775	-.437	-.523	.873
	Sig. (2-tailed)	.	.478	.124	.462	.366	.053
	N	5	5	5	5	5	5
Incidence of Microdamage	Pearson Correlation	-.423	1	.831	.998**	.982**	-.671
	Sig. (2-tailed)	.478	.	.081	.000	.003	.215
	N	5	5	5	5	5	5
Crack Length	Pearson Correlation	-.775	.831	1	.847	.907*	-.773
	Sig. (2-tailed)	.124	.081	.	.071	.034	.126
	N	5	5	5	5	5	5
Numercial Crack Density	Pearson Correlation	-.437	.998**	.847	1	.981**	-.661
	Sig. (2-tailed)	.462	.000	.071	.	.003	.225
	N	5	5	5	5	5	5
Surface Crack Density	Pearson Correlation	-.523	.982**	.907*	.981**	1	-.720
	Sig. (2-tailed)	.366	.003	.034	.003	.	.170
	N	5	5	5	5	5	5
% Interstitial	Pearson Correlation	.873	-.671	-.773	-.661	-.720	1
	Sig. (2-tailed)	.053	.215	.126	.225	.170	.
	N	5	5	5	5	5	5

**. Correlation is significant at the 0.01 level (2-tailed).

*. Correlation is significant at the 0.05 level (2-tailed).

(1 – tailed)

Correlations

		Time to Failure	Incidence of Microdamage	Crack Length	Numerical Crack Density	Surface Crack Density	% Interstitial
Time to Failure	Pearson Correlation	1	-.423	-.775	-.437	-.523	.873*
	Sig. (1-tailed)	.	.239	.062	.231	.183	.027
	N	5	5	5	5	5	5
Incidence of Microdamage	Pearson Correlation	-.423	1	.831*	.998**	.982**	-.671
	Sig. (1-tailed)	.239	.	.040	.000	.001	.108
	N	5	5	5	5	5	5
Crack Length	Pearson Correlation	-.775	.831*	1	.847*	.907*	-.773
	Sig. (1-tailed)	.062	.040	.	.035	.017	.063
	N	5	5	5	5	5	5
Numercial Crack Density	Pearson Correlation	-.437	.998**	.847*	1	.981**	-.661
	Sig. (1-tailed)	.231	.000	.035	.	.002	.112
	N	5	5	5	5	5	5
Surface Crack Density	Pearson Correlation	-.523	.982**	.907*	.981**	1	-.720
	Sig. (1-tailed)	.183	.001	.017	.002	.	.085
	N	5	5	5	5	5	5
% Interstitial	Pearson Correlation	.873*	-.671	-.773	-.661	-.720	1
	Sig. (1-tailed)	.027	.108	.063	.112	.085	.
	N	5	5	5	5	5	5

*. Correlation is significant at the 0.05 level (1-tailed).

**. Correlation is significant at the 0.01 level (1-tailed).

Pearson's Correlation Histological Data - Creep 130 MPa (% Osteonal)

(2 – tailed)

Correlations

		Time to Failure	Incidence of Microdamage	Crack Length	Numerical Crack Density	Surface Crack Density	% Osteonal
Time to Failure	Pearson Correlation	1	-.423	-.775	-.437	-.523	-.873
	Sig. (2-tailed)	.	.478	.124	.462	.366	.053
	N	5	5	5	5	5	5
Incidence of Microdamage	Pearson Correlation	-.423	1	.831	.998**	.982**	.671
	Sig. (2-tailed)	.478	.	.081	.000	.003	.215
	N	5	5	5	5	5	5
Crack Length	Pearson Correlation	-.775	.831	1	.847	.907*	.773
	Sig. (2-tailed)	.124	.081	.	.071	.034	.126
	N	5	5	5	5	5	5
Numercial Crack Density	Pearson Correlation	-.437	.998**	.847	1	.981**	.661
	Sig. (2-tailed)	.462	.000	.071	.	.003	.225
	N	5	5	5	5	5	5
Surface Crack Density	Pearson Correlation	-.523	.982**	.907*	.981**	1	.720
	Sig. (2-tailed)	.366	.003	.034	.003	.	.170
	N	5	5	5	5	5	5
% Osteonal	Pearson Correlation	-.873	.671	.773	.661	.720	1
	Sig. (2-tailed)	.053	.215	.126	.225	.170	.
	N	5	5	5	5	5	5

**. Correlation is significant at the 0.01 level (2-tailed).

*. Correlation is significant at the 0.05 level (2-tailed).

(1 – tailed)

Correlations

		Time to Failure	Incidence of Microdamage	Crack Length	Numerical Crack Density	Surface Crack Density	% Osteonal
Time to Failure	Pearson Correlation	1	-.423	-.775	-.437	-.523	-.873*
	Sig. (1-tailed)	.	.239	.062	.231	.183	.027
	N	5	5	5	5	5	5
Incidence of Microdamage	Pearson Correlation	-.423	1	.831*	.998**	.982**	.671
	Sig. (1-tailed)	.239	.	.040	.000	.001	.108
	N	5	5	5	5	5	5
Crack Length	Pearson Correlation	-.775	.831*	1	.847*	.907*	.773
	Sig. (1-tailed)	.062	.040	.	.035	.017	.063
	N	5	5	5	5	5	5
Numercial Crack Density	Pearson Correlation	-.437	.998**	.847*	1	.981**	.661
	Sig. (1-tailed)	.231	.000	.035	.	.002	.112
	N	5	5	5	5	5	5
Surface Crack Density	Pearson Correlation	-.523	.982**	.907*	.981**	1	.720
	Sig. (1-tailed)	.183	.001	.017	.002	.	.085
	N	5	5	5	5	5	5
% Osteonal	Pearson Correlation	-.873*	.671	.773	.661	.720	1
	Sig. (1-tailed)	.027	.108	.063	.112	.085	.
	N	5	5	5	5	5	5

*. Correlation is significant at the 0.05 level (1-tailed).

**. Correlation is significant at the 0.01 level (1-tailed).

Appendix 2.4 Student's T-Test Numerical Crack Density – Room Temperature Creep versus Fatigue

Group Statistics

	VAR00002	N	Mean	Std. Deviation	Std. Error Mean
VAR00001	Fatigue	25	.9535	1.19621	.23924
	Creep	5	.0731	.08035	.03593

Independent Samples Test

		Levene's Test for Equality of Variances		t-test for Equality of Means						
									95% Confidence Interval of the Difference	
		F	Sig.	t	df	Sig. (2-tailed)	Mean Difference	Std. Error Difference	Lower	Upper
VAR00001	Equal variances assumed	4.814	.037	1.622	28	.116	.8804	.54275	-.23141	1.99215
	Equal variances not assumed			3.639	25.019	.001	.8804	.24192	.38214	1.37861

Appendix 2.5 Student's T-Test Mean Crack Length – Room Temperature Creep (130 MPa) Versus Fatigue (50, 60, 70 MPa)

Group Statistics

	VAR00001	N	Mean	Std. Deviation	Std. Error Mean
CREEP	Creep	74	257.9122	205.23612	23.85821
	Fatigue	3001	74.3079	59.35931	1.08357

Independent Samples Test

		Levene's Test for Equality of Variances		t-test for Equality of Means						
									95% Confidence Interval of the Difference	
		F	Sig.	t	df	Sig. (2-tailed)	Mean Difference	Std. Error Difference	Lower	Upper
CREEP	Equal variances assumed	337.739	.000	23.415	3073	.000	183.6043	7.84128	168.22963	198.97899
	Equal variances not assumed			7.688	73.301	.000	183.6043	23.88281	136.00924	231.19938

3 Elevated Temperature Fatigue & Creep

Appendix 3.1 Microcrack Accumulation During High Temperature Fatigue Testing – 80 MPa 50°C

Specimen	0 - 10,000 cyles	0 - 18,748 Cycles		
1	0.533	1.000		N/Nf
	0.000	5.640		Numerical Crack Density (No./mm^2)
	0.000	453.578		Surface Crack Density (microns crk. Lgt/mm^2)
	0.000	80.418		Mean Crack Length (Microns)
	0 - 10,000 Cycles	0 - 45,973 Cycles		
2	0.218	1.000		N/Nf
	0.458	13.227		Numerical Crack Density (No./mm^2)
	18.393	1067.779		Surface Crack Density (microns crk. Lgt/mm^2)
	40.171	80.726		Mean Crack Length (Microns)
	0 - 10,000 Cycles	0 - 50,000 Cycles	0 - 184,097 Cycles	
3	0.054	0.272	1.000	N/Nf
	0.000	0.000	6.441	Numerical Crack Density (No./mm^2)
	0.000	0.000	403.334	Surface Crack Density (microns crk. Lgt/mm^2)
	0.000	0.000	62.617	Mean Crack Length (Microns)
	0 - 5,000 Cycles	0 - 6,541 Cycles		
4	0.764	1.000		N/Nf
	0.946	2.744		Numerical Crack Density (No./mm^2)
	152.363	348.734		Surface Crack Density (microns crk. Lgt/mm^2)
	160.997	127.068		Mean Crack Length (Microns)
	0 - 10,000 Cycles	0 - 50,000 Cycles	0 - 60,253 Cycles	
5	0.166	0.830	1.000	N/Nf
	0.211	0.885	3.202	Numerical Crack Density (No./mm^2)
	13.834	184.665	413.867	Surface Crack Density (microns crk. Lgt/mm^2)
	65.660	208.687	129.234	Mean Crack Length (Microns)
	0 - 5,000 Cycles	0 - 10,000 Cycles	0 - 278,317 Cycles	
6	0.018	0.036	1.000	N/Nf
	0.074	0.148	0.503	Numerical Crack Density (No./mm^2)
Test	4.340	10.995	38.210	Surface Crack Density (microns crk. Lgt/mm^2)
Interupted	58.644	74.283	75.929	Mean Crack Length (Microns)
	0 - 5,000 Cycles	0 - 10,000 Cycles	0 - 186,035 Cycles	
7	0.027	0.054	1.000	N/Nf
	0.055	0.110	10.267	Numerical Crack Density (No./mm^2)
	1.524	4.326	545.543	Surface Crack Density (microns crk. Lgt/mm^2)
	27.610	39.185	53.134	Mean Crack Length (Microns)
	0 - 5,000 Cycles	0 - 10,000 Cycles	0 - 278,355 Cycles	
8	0.018	0.036	1.000	N/Nf
	0.045	0.076	0.892	Numerical Crack Density (No./mm^2)
Test	1.220	2.267	71.165	Surface Crack Density (microns crk. Lgt/mm^2)
Interupted	26.883	29.978	79.747	Mean Crack Length (Microns)
	0 - 5,000 Cycles	0 - 10,000 Cycles	0 - 11,104 Cycles	
9	0.450	0.901	1.000	N/Nf
	0.050	0.555	0.656	Numerical Crack Density (No./mm^2)
	14.533	141.126	161.925	Surface Crack Density (microns crk. Lgt/mm^2)
	287.890	254.146	246.740	Mean Crack Length (Microns)
	0 - 10,000 Cycles	0 - 38,240 Cycles		
10	0.262	1.000		N/Nf
	0.000	2.636		Numerical Crack Density (No./mm^2)
	0.000	269.181		Surface Crack Density (microns crk. Lgt/mm^2)
	0.000	102.125		Mean Crack Length (Microns)

Appendix 3.2 High Temperature Creep Data

Sample	Creep Stress (MPa)	Time to Failure (s)	Steady State Creep Rate
1	120	25365	7.83E-07
2	120	7842	8.72E-07
3	120	58331	2.40E-07
4	120	46307	1.79E-07
5	120	2358	1.90E-06
6	130	243	2.23E-05
7	130	18268	3.50E-07
8	130	997	1.24E-06
9	130	1080	6.71E-06
10	130	309	1.62E-05

Appendix 3.3 Non- Parametric Mann-Whitney U Test – Time to Failure High Temperature Creep Tests 120 and 130 MPa

Ranks

	Stress	N	Mean Rank	Sum of Ranks
TTF	120.00	5	7.60	38.00
	130.00	5	3.40	17.00
	Total	10		

Test Statistics[b]

	VAR00002
Mann-Whitney U	2.000
Wilcoxon W	17.000
Z	-2.193
Asymp. Sig. (2-tailed)	.028
Exact Sig. [2*(1-tailed Sig.)]	.032[a]

a. Not corrected for ties.

b. Grouping Variable: Creep Stress (MPa)

Appendix 3.4 Student's T-Test Numerical Crack Density High Temperature Fatigue versus Room Temperature Fatigue

Group Statistics

	VAR00002	N	Mean	Std. Deviation	Std. Error Mean
VAR00001	80 MPa 50 Deg C	10	4.6211	4.29927	1.35955
	80 MPa Room Temp	13	.6188	.44364	.12304

Independent Samples Test

		Levene's Test for Equality of Variances		t-test for Equality of Means						
									95% Confidence Interval of the Difference	
		F	Sig.	t	df	Sig. (2-tailed)	Mean Difference	Std. Error Difference	Lower	Upper
VAR00001	Equal variances assumed	22.547	.000	3.357	21	.003	4.0023	1.19223	1.52296	6.48171
	Equal variances not assumed			2.932	9.148	.016	4.0023	1.36510	.92183	7.08284

Appendix 3.5 Student's T-Test Mean Crack Length High Temperature Fatigue versus High Temperature Creep Cracks

Group Statistics

	VAR00002	N	Mean	Std. Deviation	Std. Error Mean
VAR00001	HT Creep	610	128.0356	100.59588	4.07301
	HT Fatigue	1275	80.7679	133.46959	3.73936

Independent Samples Test

		Levene's Test for Equality of Variances		t-test for Equality of Means						
									95% Confidence Interval of the Difference	
		F	Sig.	t	df	Sig. (2-tailed)	Mean Difference	Std. Error Difference	Lower	Upper
VAR00001	Equal variances assumed	4.782	.029	7.755	1882	.000	47.2677	6.09509	35.31383	59.22151
	Equal variances not assumed			8.549	1543.641	.000	47.2677	5.52922	36.42210	58.11324

Appendix 3.6 Student's T-Test Mean Crack Length High Temperature Creep versus Room Temperature Creep Cracks

Group Statistics

	VAR00002	N	Mean	Std. Deviation	Std. Error Mean
CRACKLEN	50 Deg C	610	128.0356	100.59588	4.07301
	Room Temp	74	257.9122	205.23612	23.85821

Independent Samples Test

		Levene's Test for Equality of Variances		t-test for Equality of Means						
									95% Confidence Interval of the Difference	
		F	Sig.	t	df	Sig. (2-tailed)	Mean Difference	Std. Error Difference	Lower	Upper
CRACKLEN	Equal variances assumed	56.339	.000	-9.066	682	.000	-129.8766	14.32639	-158.006	-101.747
	Equal variances not assumed			-5.366	77.309	.000	-129.8766	24.20338	-178.069	-81.68459

Appendix 3.7 Student's T-Test Microcrack Density High Temperature Creep versus Room Temperature Creep

Group Statistics

	VAR00002	N	Mean	Std. Deviation	Std. Error Mean
VAR00001	Creep 50 Deg C	5	4.9020	2.27511	1.01746
	Creep Room Temp	5	.0731	.08035	.03593

Independent Samples Test

		Levene's Test for Equality of Variances		t-test for Equality of Means						
									95% Confidence Interval of the Difference	
		F	Sig.	t	df	Sig. (2-tailed)	Mean Difference	Std. Error Difference	Lower	Upper
VAR00001	Equal variances assumed	49.564	.000	4.743	8	.001	4.8289	1.01809	2.48117	7.17663
	Equal variances not assumed			4.743	4.010	.009	4.8289	1.01809	2.00499	7.65281

Appendix 3.8 Student's T-Test Microcrack Density High Temperature Creep versus High Temperature Fatigue

All Fatigue Specimens

Group Statistics

	VAR00002	N	Mean	Std. Deviation	Std. Error Mean
VAR00001	HT Creep	5	4.9020	2.27511	1.01746
	HT Fat All Specimen	10	4.6211	4.29927	1.35955

Independent Samples Test

		Levene's Test for Equality of Variances		t-test for Equality of Means						
									95% Confidence Interval of the Difference	
		F	Sig.	t	df	Sig. (2-tailed)	Mean Difference	Std. Error Difference	Lower	Upper
VAR00001	Equal variances assumed	1.803	.202	.135	13	.895	.2809	2.07767	-4.20764	4.76943
	Equal variances not assumed			.165	12.841	.871	.2809	1.69811	-3.39227	3.95406

Only Failed Fatigue Specimens

Group Statistics

	VAR00002	N	Mean	Std. Deviation	Std. Error Mean
VAR00001	HT Creep	5	4.9020	2.27511	1.01746
	HT Fat Failed	8	5.6019	4.27279	1.51066

Independent Samples Test

		Levene's Test for Equality of Variances		t-test for Equality of Means						
									95% Confidence Interval of the Difference	
		F	Sig.	t	df	Sig. (2-tailed)	Mean Difference	Std. Error Difference	Lower	Upper
VAR00001	Equal variances assumed	1.407	.261	-.334	11	.745	-.6999	2.09465	-5.31021	3.91036
	Equal variances not assumed			-.384	10.875	.708	-.6999	1.82135	-4.71432	3.31446